Universidade de São Paulo
Instituto de Astronomia, Geofísica e Ciências Atmosféricas
Departamento de Astronomia

Pedro Ticiani dos Santos

Searching for Be stars using multi-band photometry: Case study of NGC 330 using SOAR and S-PLUS data

São Paulo

2023

Pedro Ticiani dos Santos

Searching for Be stars using multi-band photometry: Case study of NGC 330 using SOAR and S-PLUS data

Dissertação apresentada ao Departamento de Astronomia do Instituto de Astronomia, Geofísica e Ciências Atmosféricas da Universidade de São Paulo como requisito parcial para a obtenção do título de Mestre em Ciências.

Área de Concentração: Astronomia
Orientador: Prof. Dr. Alex Cavaliéri Carciofi

Versão Corrigida. O original encontra-se disponível na Unidade.

São Paulo
2023

Aos meus pais, os pilares da minha formação.

À minha querida irmã, cuja minha admiração é infinita.

À minha amada, que esteve sempre por perto nos momentos mais difíceis.

Ao meu orientador, pela excelência acadêmica e bom companheirismo.

A todos que defendem uma sociedade justa governada pela classe trabalhadora.

Acknowledgements

Começo os meus agradecimentos citando as pessoas mais importantes na minha vida: a minha família. Aos meus pais, agradeço imensamente o carinho e o cuidado desde pequeno, sendo inteiramente responsáveis pela minha caminhada. À minha irmã, pelo companheirismo de sempre e uma das minhas principais referências como pessoa. À minha noiva, na qual divido os meus dias, e experienciou de perto as angústias durante a dissertação, ajudando a sempre seguir em frente. Dedico também aos meus *pets*: Fafá e Bibo, minhas lindas calopsitas que recentemente viraram pais, e à Cacazinha, Meli, Chiara e Boninho.

Agradeço também os meus amigos pessoais, em especial o Gabriel, uma das pessoas em que mais confio e que possuo um enorme carinho.

Ao meu orientador, Prof. Alex, agradeço não somente as incríveis discussões científicas em nossas reuniões individuais e de grupo, mas também pelos momentos de camaradagem. Considero-o um grande amigo. Agradeço também o relator deste projeto, o Prof. Laerte, pelos comentários de alto valor e por ter aceitado participar da banca avaliadora.

Aos colegas de grupo, em especial Tajan, Amanda e Ariane, agradeço pelos momentos de construção científica, a toda ajuda que recebi e também pelas distrações.

Aos pesquisadores Jonathan e Felipe, os pós-docs que trouxeram para mim uma visão de ciência e trabalho complementar àquela obtida durante a graduação e o mestrado.

A todos os docentes do Instituto, em especial às Profas. Silvia e Beatriz, e ao Prof. Reinaldo, que foram figuras especiais durante as disciplinas realizadas. Aproveito este parágrafo para citar também o grupo de atendimento astronômico às escolas, na qual agradeço aos monitores na qual realizei atendimento em conjunto e à Rose e Luciana.

Aos colegas do IAG, que sempre ajudaram a superar os obstáculos durante a dura graduação e também na pós-graduação, em especial a Luciana e o Guilherme – grandes ouvintes dos meus

longos desabafos.

À CAPES, agradeço imensamente pelo apoio financeiro do programa PROEX, sob o processo de n^o 88887.604774/2021-00. Este trabalho foi também baseado em observações obtidas no telescópio SOAR (Southern Astrophysical Research), que é um projeto conjunto do Ministério da Ciência, Tecnologia e Inovações (MCTI/LNA), da fundação NOIRLab (US National Science Foundation), da University of North Carolina, localizada em Chapel Hill (UNC), e da Michigan State University (MSU).

Ao Instituto como um todo, inclusive aqueles na qual não tive direto contato, pela qualidade no ensino e formação dos alunos de forma geral. Agradeço também aos funcionários e servidores, cujo trabalho foi e continua sendo crucial para o pleno funcionamento das atividades do instituto.

Por fim, dedico os meus agradecimentos a todos aqueles organizados para a construção do poder popular, e pela luta por uma vida digna para a classe trabalhadora.

Esta tese/dissertação foi escrita em LaTeX com a classe IAGTESE, para teses e dissertações do IAG.

“*Though frontiers and mountains stand between us, Proletarians of the whole world come together as one family.*”

Nguyen Tat Thanh

“*It makes unavoidably necessary an entirely new organization of society in which production is no longer directed by mutually competing individual industrialists but rather by the whole society operating according to a definite plan and taking account of the needs of all.*”

Friedrich Osvald

Resumo

Devido a grande quantidade de diferentes classes de objetos astronômicos, responsáveis por contribuições científicas relevantes para todo o campo da astronomia, múltiplas técnicas observacionais e métodos de classificação de objetos foram desenvolvidos ao longo da história.

No caso das estrelas Be clássicas (CBe) – objetos de tipo espectral B de alta rotação (próxima do limite crítico), não supergigantes e que apresentam ou já apresentaram um disco kepleriano ejetado pela própria estrela – a técnica observacional pioneira foi a espectroscopia, na qual as epônimas linhas espectrais em emissão se tornaram as características mais marcantes. Porém, através do uso de outras técnicas observacionais como a fotometria e a polarimetria, outras manifestações foram detectadas, como um excesso de emissão no contínuo e polarização linear não nula.

Uma das tarefas ainda ativas no campo de CBes é encontrar formas acuradas de classificar estes objetos em uma dada população estelar jovem. Por exemplo, no aglomerado estelar jovem NGC 330, localizado na Pequena Nuvem de Magalhães, foi encontrada uma alta fração de CBes, a partir da década de 70, através de levantamentos espectroscópicos. Dos anos 80 em diante, houve a descoberta de que CBes em um aglomerado estelar poderiam ser classificadas utilizando fotometria, especialmente com o uso de filtros de banda estreita centralizados na linha espectral Hα. Porém, há uma forte limitação no método: apenas CBes com um disco ativo, e suficientemente denso, são passíveis de classificação.

Visando contornar este problema, este trabalho utilizou modelos realistas de estrelas B e CBes a fim de produzir aglomerados sintéticos e sua subsequente fotometria sintética para modelar NGC 330 com os algoritmos de aprendizado de máquina supervisionado *k-Nearest Neighbors* (k-NN) e *Decision Tree* (DT). Os dados utilizados foram fotometria do levantamento S-PLUS e do imageador SAMI/SOAR, ambos contendo um filtro estreito em Hα.

Os modelos k-NN e DT treinados nas magnitudes do aglomerado sintético foram utilizados para realizar predições inéditas nos dados, resultando na classificação dos objetos presentes em três diferentes classes: estrelas de sequência principal pertencentes ao aglomerado, estrelas Be clássicas pertencentes ao aglomerado, e estrelas não pertencentes à sequência principal ou não membros do aglomerado, como objetos de fundo e/ou estrelas evoluídas. O resultado obtido foi de 44 e 47 estrelas classificadas como CBes pelos respectivos modelos k-NN e pelo DT no conjunto de magnitudes do S-PLUS, e um total de 206 e 289 objetos classificados como CBes no conjunto do SOAR, considerando o k-NN e o DT, respectivamente. No conjunto do SOAR, o modelo DT estima uma fração mínima $\mathrm{CBe}/(\mathrm{B}+\mathrm{CBe})$ de 26%. Em ambos algoritmos, quase toda estrela CBe com emissão em Hα foi classificada como candidata a CBe. Um dos resultados mais impressionantes diz respeito ao fato de que os modelos classificaram as candidatas a CBe na região mais "avermelhada" da sequência principal, local já conhecido de estrelas CBes inativas e de sistemas com discos pouco densos (por exemplo, no começo ou fim das respectivas fases de construção e dissipação de um disco). Como o primeiro trabalho a ter considerado propriedades conhecidas dos discos de estrelas CBe na formulação de um aglomerado estelar sintético, é possível afirmar que nossa metodologia desenvolvida é promissora, visto que as análises preliminares aqui contidas resultaram na predição de uma fração de CBes ainda maior do que em estimativas prévias da literatura, incluindo levantamentos espectroscópicos de alta resolução quando considerada a mesma profundidade observacional.

Abstract

Due to the complex variety of astronomical classes, each responsible for relevant scientific contributions to Astronomy, multiple observational techniques and object classification methods have been developed throughout history.

In the case of Classical Be stars (CBe) – B spectral type objects with high rotation rates (close to the critical limit), non-supergiant and that have or already had a Keplerian disk ejected by the star itself – the pioneering observational technique was spectroscopy, in which the eponymous emission lines became their most notable feature. However, through other techniques such as photometry and polarimetry, different manifestations were detected, such as continuum excess and non-zero linear polarization.

One of the still ongoing tasks in the field of CBes is finding accurate ways to classify these objects in a given young stellar population. For example, in the young stellar cluster NGC 330, located in the Small Magellanic Cloud, a high fraction of CBes was found through spectroscopic surveys starting in the 1970s. From the 1980s onwards, it was discovered that CBes in a star cluster could be detected using photometry, specifically by means of narrow-band filters centered in Hα. However, there is a strong limitation in the method: only classical Be stars with an active and sufficiently dense disks can be detected with this technique.

In order to circumvent this problem, this work uses realistic models of B and CBe stars to produce synthetic clusters and the subsequent synthetic photometry to model NGC 330 with the supervised machine learning algorithms k-Nearest Neighbors (k-NN) and Decision Tree (DT). As input data we use photometry from the S-PLUS survey and the SAMI/SOAR imager, both using narrow band Hα filters.

The k-NN and DT models trained on the synthetic cluster magnitudes were applied to make unseen predictions, resulting in the classification of the observed sources into three different

classes: main-sequence and CBe stars belonging to the cluster and stars not belonging to the main sequence nor members of the cluster, such as foreground objects and/or evolved stars. The obtained result consisted of 44 and 47 stars classified as CBes in the S-PLUS magnitudes set, and a total of 206 and 289 objects classified as CBes in the SOAR set, for k-NN and DT predictions, respectively. In the SOAR ensemble, the DT model estimated a minimum CBe/(B + CBe) fraction of 26%. For both estimators, almost every CBe with Hα emission was classified as a candidate. One of the remarkable results also lies on the prediction of CBe candidates in the "redder" side of the MS, location of inactive CBes or systems with less dense disks (e.g., the beginning of building-up or end of dissipation phases). As the first work to consider every known properties of CBe disks in the formulation of the synthetic cluster, it can be stated that our developed methodology is promising as a preliminary analysis resulted in a higher CBe content than previous estimates, including high resolution spectroscopic surveys, when taking into account the same magnitude depth.

List of Figures

List of Tables

Acronyms

MS Main Sequence

IMF Initial Mass Function

ZAMS Zero Age Main Sequence

TAMS Terminal Age Main Sequence

CNO Carbon-Nitrogen-Oxygen

RGB Red Giant Branch

AGB Assymptotic Giant Branch

CBe Classical Be star

tMS main sequence lifetime

Teff Effective temperature

UV Ultraviolet

YSC Young Stellar Cluster

YOC Young Open Cluster

MSTO Main Sequence Turn-Off

SSP Simple Stellar Population

SFR Stellar Formation Rate

HPC High Performance Clusters

NLTE Non-Local Thermodynamical Equilibrium

VDD Viscous Decretion Disk

AM Angular Momentum

PDF Probability Density Function

SMC Small Magellanic Cloud

LMC Large Magellanic Cloud

SED Spectral Energy Distribution

HST Hubble Space Telescope

sdO sub-dwarf O star

sdB sub-dwarf B star

NRP Non Radial Pulsation

MCPC Magellanic Clouds Photometric Catalog

BSG Blue Supergiant

RSG Red Supergiant

FWHM Full Width at Half Maximum

LGS Laser Guide Star

ST Spectral Type

DR Data Release

ADQL Astronomical Data Query Language

SQL Structured Query Language

KH Kelvin-Helmholtz

SNR Signal-to-Noise Ratio

AI Artificial Intelligence

ML Machine Learning

k-NN k-Nearest Neighbors

DT Decision Tree

CV Cross Validation

Contents

Chapter 1

Introduction

Stars are astronomical objects that drew attention since the beginning of humanity's social manifestations. Our knowledge about them and what is done with it has changed dynamically throughout millennia.

Even with great advances in sky mapping, with parallax measurements and stellar classifications based on the apparent brightness and spectroscopic characteristics (e.g., Pickering 1890), the physical description of a star started to flourish only at the beginning of the last century, due to a series of events such as the establishment of quantum mechanics as a fundamental field in physics, technological progress of observing equipment, and advances in thermodynamics and statistical mechanics.

A variety of pioneering works in stellar spectral classification, before the definition of the modern MK system (Morgan et al., 1943), were published without a good understanding of the connection between physical and observational properties of stars, such as Pickering and Fleming (1905) and Cannon and Pickering (1912). While spectral classification had previously identified the existence of atomic lines, it wasn't until the 1920s that scientists uncovered the predominant chemical composition of stars to be primarily hydrogen and helium (Payne, 1925). The physics behind the stellar structure, stellar evolution and stellar atmospheres (and the associated theoretical models) were still being slowly developed.

The astronomer Hans Rosenberg, in 1910, identified, for the first time in astronomy, a relation between color (obtained using methods of comparison of spectroscopic lines) and luminosity[1], through the apparent photographic magnitude of the stars in the open cluster Pleiades (Rosenberg, 1910). In this case, the apparent magnitude is connected to the luminosity since the distance

---

[1] Luminosity is a quantity defined as the electromagnetic energy radiated per time unit, measured in watts in the S.I. units and commonly expressed in terms of Solar luminosity $L_{\odot} = 3.828 \times 10^{26}$ W.

between stars from the cluster and an observer from Earth are approximately the same, avoiding the need to measure distances. Rosenberg showed the relation in a primitive color-magnitude diagram, where the region known today as the main sequence could be seen for the first time.

Shortly afterward, Ejnar Hertzsprung and Henry N. Russell became recognized as pioneers for independently identifying again, in 1911 and 1914 respectively, the relation between color and luminosity in the articles "*Ueber die Verwendung photographischer effektiver Wellenlaengen zur Bestimmung von Farbenaequivalenten*"[2] (Hertzsprung, 1911) and "Relations between the spectra and other characteristics of the stars" (Russell, 1914). In Russell's work, there was a more careful treatment of the subject. He plotted the absolute photographic magnitude versus the spectral type of stars for four different moving groups (in a diagram that became later famously known as the Hertzsprung-Russell – hereafter HR – diagram), showing the main sequence and two isolated regions, which were later identified as being populated by giant and white dwarf stars.

In 1939, Dr. Subrahmanyan Chandrasekhar published a rigorous treatise on stellar structure (Chandrasekhar, 1939) — however, complications such as stellar variability and rotation effects were avoided. One of the crucial findings of this work is that an individual star in equilibrium can be characterized by 3 main parameters: the mass M, radius R, and luminosity L (intrinsically related to the energy generated in the stellar interior, but not yet considered in Chandrasekhar's work since nuclear fusion as the energy fuel in the interior of stars was unveiled in the same year by Bethe 1939).

It is currently known that a star, throughout its life, experiences a complex evolution, from its primordial molecular cloud to its final stages, and the main ruling factor is its mass — which governs the structure, possible nuclear reactions, and the energy transport occurring in the interior. The most stable phase of stellar evolution is the main sequence (hereafter MS), where the fusion of hydrogen into helium is the dominant energy source. Another important parameter is the initial chemical composition, usually written as the mass fraction of hydrogen, helium, and all heavier elements fractions (X, Y, and Z, respectively), so that $X + Y + Z = 1$.

Many physical parameters in astronomy are scaled to their solar values, represented with the subscript $\odot$, such as stellar radius, luminosity, mass, or metallicity. In common notation, a star with 30 times the mass of our sun has a total mass of $30\,\mathrm{M}_\odot$. In Sect. 1.1, intermediate-mass stars ($2\,\mathrm{M}_\odot \lesssim M \lesssim 8\,\mathrm{M}_\odot$) and massive stars ($M \gtrsim 8\,\mathrm{M}_\odot$) are carefully detailed, focusing when

---

[2] The paper's title can be literally translated as "On the Use of Photographic Effective Wavelengths for the Determination of Color Equivalents".

needed on B-type stars. The transition value of $\approx 8\,\mathrm{M}_\odot$ roughly corresponds to a threshold where stars below it are not capable of developing an iron core at the end of the main sequence, ending their life as white dwarfs[3].

1.1 *Intermediate-Mass and Massive Stars*

Intermediate-mass stars and massive stars have been the subject of much attention and research in astrophysics. These stars, in particular, have lifetimes ranging from few million up to billion years and play an important role in the dynamics of stellar clusters, the evolution of galaxies and the Universe.

Stars in both mass ranges share the common property of being born through the collapse of molecular clouds, leading to a protostar and eventually experiencing the MS. However, the timescale for protostar formation up to the ignition of nuclear fusion are way shorter when compared to the time spent on the MS.

1.1.1 *Intermediate-Mass Stars*

Despite not being as common as low-mass stars, as the star formation process highly favors stars with smaller masses (for more details, see Sect. 3.3 of McKee and Ostriker 2007), intermediate-mass stars live for long periods and contribute in many ways to the cosmos. For example, when considering a distribution sampled from an Initial Mass Function[4] (hereafter IMF) of the derived power law from Kroupa (2001), brown dwarfs can represent 37% of the population in number, yet contributing to only 4.3% of the total mass. In contrast, intermediate-mass and massive stars constitute together $\approx$ 6% of the population and contribute with 51% of the mass.

As every other star, the evolution of an intermediate-mass star can be tracked back to the Zero Age Main Sequence (ZAMS), the instant of time where hydrogen nuclear fusion starts in the central region of the star, the stellar core. For the whole MS duration, the star will experience changes at its structure.

The main energy production chain on intermediate-mass stars are the carbon-nitrogen-oxygen (CNO) cycles (Salaris and Cassisi, 2005), followed by the proton-proton (p-p) chains (Iliadis,

---

[3] Considering $Z = \mathrm{Z}_\odot \approx 0.014$. As metallicity drops, the mass range shifts (e.g., in environments with $Z = 0.0001$, stars with $M > 6\,\mathrm{M}_\odot$ can end their lives as other types of stellar remnants).

[4] The IMF is an empirical function used to describe the distribution of masses for a set of stars during star formation periods (Scalo, 1986), usually expressed as a probability density function.

2007). The CNO cycle is a catalytic cycle, where four protons fuse, with carbon, nitrogen and oxygen being used as catalysts at each step of the cycle, but re-generated again. The result is one stable helium nucleus (or an α particle), two positrons and two electron neutrinos, plus electromagnetic radiation.

The final moments on the MS for intermediate-mass stars happen when the hydrogen is fully exhausted on the stellar core, and nuclear burning starts in a shell surrounding the helium core. In this period, the star expands in an attempt to achieve equilibrium because of the contracting helium core. The expansion leads to a cooling process, enabling a deeper convection layer that brings chemical products of the MS burning to the surface. This marks the onset of the Red Giant Branch (RGB) phase.

The RGB phase ends when the helium core has contracted enough to ignite helium fusion. In intermediate-mass stars, this ignition happens as they have enough mass to avoid the helium flash[5].

Helium burning, as for hydrogen, happens in a specific reaction chain, named triple-α. The chemical yield of these reactions is mainly carbon (^{12}C), which will be partially converted into oxygen (^{16}O) via α capture. The result of this phase is the formation of a carbon-oxygen core, with general characteristics highly depending on the initial stellar mass, the chemical composition and the state of the evolutionary models used for theoretical predictions. The latter will be better discussed in Sect. 1.2.

The helium burning phase ends after core helium depletion, starting the brief (when compared to the time spent on hydrogen and helium burning phases) Asymptotic Giant Branch (AGB) phase. In this phase, helium burning happens in a shell surrounding the new core composed of carbon and oxygen, being the second shell burning phase of the star. This configuration of a contracting electron-degenerate C-O core, a helium burning shell, an intershell region, the hydrogen burning shell and the stellar envelope implies a very complex structure for the star.

Although the AGB is a brief phase, it allows the production of heavy elements through a reaction called slow neutron capture (s-process), responsible for the nucleosynthesis of nearly half the elements heavier than iron (Fe), in the helium intershell. The heavy elements get mixed with the material present on the stellar surface and eventually are thrown out to the interstellar

---

[5] Helium flash is a runaway process happening when the temperature needed for He ignition is achieved in low mass stars, where the core becomes mainly degenerate and thermally unstable. This runaway explosion isn't observable, as the energy released is absorbed by the stellar envelope and outer core regions (Prialnik, 2009).

medium via stellar winds.

The end of the AGB phase is generally marked by the formation of a white dwarf, and intermediate-mass stars typically evolve to less massive white dwarfs, of a maximum mass of about $1.1\,\mathrm{M}_\odot$ according to stellar models (Karakas, 2017). Observationally, most white dwarfs fall in the mass range of $M = 0.5\,\mathrm{M}_\odot$ to $0.7\,\mathrm{M}_\odot$ (Kepler et al., 2007).

1.1.2 *Massive stars*

The basics of stellar evolution of massive stars is comparable to low- and intermediate-mass stars with respect to how energy is produced – i.e., via nuclear burning. However, massive star evolution is even more complex to understand, as stellar parameters such as rotation, magnetic fields and metallicity can significantly impact on their evolution and fate. Also, binarity becomes a common aspect on massive stars, so single stellar evolution models are not sufficient to describe many systems.

Stars having $M \gtrsim 8\,\mathrm{M}_\odot$ are also referred in the literature as *hot stars*, as their high luminosities (reaching as high as $10^7\,\mathrm{L}_\odot$ in individual stars, see Crowther et al. 2010) imply intense ionization and strong stellar winds, the latter being responsible for enriching the interstellar medium in evolutionary stages where heavy chemical elements are produced and mixed to the surface. One characteristic historically important is their visibility in the sky. Because of their high luminosities, an observer on Earth can detect massive stars with considerably further distances than the low- and intermediate-mass counterparts.

As described in Langer (2012), the theory of massive star evolution is driven by at least five (important) factors: rotation, internal mixing, mass loss, binarity, and magnetic field effects. A brief introduction to how these factors impact on stellar evolution is exposed in Sect. 1.2.

For completeness, the evolution of idealistic single non-rotating massive stars can be shortly described before we try to untangle the complexity behind the more complete theory. Unlike intermediate-mass stars, subsequent fusion reactions are possible after the C-O core formation, and carbon is the first element ignited in the contracting core.

If the initial mass is somewhat lower than $\sim 11\,\mathrm{M}_\odot$, an oxygen-neon core is produced, but central temperatures are not enough to continue nuclear burning. The fate of this case is a supernova explosion, if the core collapses by reaching the Chandrasekhar limit (Chandrasekhar, 1931), or an O-Ne white dwarf if mass loss removes sufficient mass from the envelope.

In stars with $M \gtrsim 11\,\mathrm{M}_\odot$, neon is the next nuclear fuel, generating mainly oxygen. As expected, neon burning moves to a core-surrounding shell, and oxygen plays a role when the core reaches high enough temperature. The last possible fuel element of massive stars nuclear burning history is silicon, which produces iron and chromium. The iron core represents the end of nuclear fusion, that always collapses and results into a supernova explosion. This happens due to the fact that an iron core becomes inert – no further nuclear reactions are possible, leading to a rapid collapse that cannot be reversed. Describing the explosion mechanism in beyond the scope of this work, but the interested reader is referred to Branch and Wheeler (2017) for more details.

1.2 *Modern Theory of Stellar Evolution*

The theory of stellar evolution, which explains how stars are born, evolve, and the different evolutionary pathways using known physics, has been the subject of extensive study in astrophysics for over a century. In this section, we will discuss the key modern developments in the theory of stellar evolution. Astrophysical modeling of stars is a complex and challenging task due to a variety of factors, even more for low- and intermediate-mass stars. Here are some of the challenges that exist in the field:

- Complexity of Stellar Physics: The evolution of stars involves a wide range of intricate physical processes, including nuclear reactions, radiation transfer, and hydrodynamics. The interplay between these processes is nonlinear and poses challenges for accurate modeling;
- Uncertainties in Stellar Parameters: Accurate modeling of a star requires knowledge of its initial mass, chemical composition, and other physical properties. However, there are significant uncertainties associated with determining these parameters, leading to propagated uncertainties in the resulting models;
- Treatment of Convection: Convection plays a crucial role in stellar evolution, but its modeling is still not fully understood. Different convection models exist, each incorporating its own set of assumptions and uncertainties;
- Treatment of Rotation: Rotation significantly influences the internal structure and evolution of stars. However, incorporating rotation in stellar models is complex due to the involvement of various physical processes, such as turbulence and magnetic fields;

- Numerical Challenges: Numerical methods employed in stellar modeling must accurately capture the intricate physics involved, which is challenging due to the broad range of length and time scales. This can lead to numerical instabilities and errors in the resulting models;
- Comparison with Observations: The ultimate validation of a stellar model relies on its agreement with observational data. However, observations of stars can be limited in precision and completeness, posing challenges for testing and validating models.

1.2.1 *Effects of rotation*

It is currently well understood that rotation can greatly change the evolutionary course of a star, becoming an important parameter. Moreover, it can be an ingredient for many main sequence variable stars and also for stellar remnants. Rotation can lead to three main consequences on the stellar structure: gravity darkening – that results from the centrifugal force, which lowers the effective gravity at the equator; angular momentum transport – which was found to be a crucial mechanism in rapidly rotating stars; and rotationally induced mixing – responsible for chemical enriching the stellar surface and the rejuvenating the stellar core (Maeder, 2009).

The centrifugal force effect began to be researched already in the beginning of the twentieth century. In the work of von Zeipel (1924), a classical theoretical treatment on the matter, it was argued (assuming radiative energy transport) that a rotating star is brighter and hotter at its pole, with the opposite occurring at its equator. As the centrifugal force does not have spherical symmetry, the effective gravity becomes latitude dependent, and the local surface flux has reduced intensity near the equator. The von Zeipel law has been contested in the last decades, as for extreme rotators its fixed gravity darkening exponent becomes overestimated (for more information, see Fig. 13 of Domiciano de Souza et al. 2014).

Also, due to the centrifugal force, a rotating star, while keeping all of its parameters unchanged, acts similarly to a non-rotating counterpart with less mass (see Chap. 4 of Maeder 2009) and can reach the so called critical rotation, when gravity equals the centrifugal acceleration, leading to $g_{\mathrm{eff}} = 0$ at the equator. A common parametrization of a rotating star is the Roche formalism, where the gravitational potential is described by

$$\Phi(r, \theta) = -\frac{GM_*}{r} - \frac{1}{2}\Omega^2 r^2 \sin^2\theta, \tag{1.1}$$

where M_* is the stellar mass concentrated at the center, r is the radial component, θ is the polar angle, G is the gravitational constant and Ω is the (constant) angular velocity. In this description, one can estimate for example the maximum possible oblateness for a solid body of $R_{\rm equator} = 1.5\,R_{\rm pole}$ (see Sect. 2.1.4 of Maeder 2009).

Angular momentum transport, for instance, is a physical process necessary for reestablishing equilibrium after an instability occurs in a rotating star (such as shear instability and meridional circulation) and for avoiding break-up in the stellar core, with angular momentum transport happening inside-out. For a detailed prescription of angular momentum transport, see Sect. 10.5 of Maeder (2009). This mechanism will be mentioned again in Sect. 2.1.2, highlighting its importance on the variable intermediate- and massive objects named Classical Be (CBe) stars.

One of the dynamical products arising from rotation is the rotational induced mixing, resulting from the circulation of matter throughout the star and intrinsically linked to angular momentum transport. Stellar rotation turns possible the transport of chemical ingredients from the core of the star to the surface. The opposite is also true: mixing can “rejuvenate” the core by transporting hydrogen from the upper layers to the stellar center. This effect is observed typically via spectroscopy (Dunstall et al., 2011), but abundance estimations can be strongly affected by stellar rotation itself – that renders the absorption profiles broader – and other factors such as stellar winds and magnetic fields.

1.2.2 *Binary evolution*

The effects of binarity in stellar evolution is an important subject, as modeling becomes a complex task and it needs to account for most observational constraints in order to be realistic. Also, it is connected to rotation, as a mass gainer in a binary interaction can reach critical rotation after a slight mass increase, as small as 5% (see Packet 1981). As a result, any detailed binary evolution model must take angular momentum transfer into account, besides the traditional mass transfer.

Binary systems can be composed of a pair of MS stars, a MS star plus a red giant, a MS star and a stellar remnant, or a red giant with a stellar remnant. Some configurations represent different evolutionary stages of a given pair arrangement; for example, a MS star with a red giant is an advanced stage of a system composed of two MS stars, in which the more massive star, because of its lower hydrogen burning lifetime, enters the red giant phase before its companion, leading to possible mass transfer by overflowing the Roche lobe (Paczynski, 1971).

In young stellar populations, it can be difficult to observe single O stars, as the fraction of binaries tends to be very high towards more massive stars (Langer, 2012). Moreover, very massive stars are seen in a higher proportion in very close binaries[6] (Sana and Evans, 2011), strongly supporting the need of realistic binary modeling in stellar evolution applications.

However, it is also important to highlight the observational difficulties in analyzing some binary systems. For example, there exists a class of binary systems consisting of a massive MS star plus a remnant object called Be/X-ray binaries, normally with a CBe star acting as the primary and a neutron star as the secondary[7] (Reig, 2011). In this composition, orbital solutions or mass estimates are limited by the intrinsic transient nature of the Be phenomenon, the optical contamination of the stellar flux from the CBe star in respect with its companion (including emission lines arising from the disk contribution and continuum excess towards high wavelengths), the angular resolving power, and other environmental factors (e.g., attenuation of the X-ray flux by the interstellar medium).

1.2.3 *Mass loss*

Massive stars experience significant mass loss primarily due to strong winds driven by radiative pressure, which is a consequence of their high luminosity (Smith, 2014). The mass loss has profound effects on various stellar parameters, including luminosity (L), main-sequence lifetime ($t_{\rm MS}$), effective temperature ($T_{\rm eff}$), and the final helium (He) core mass. The chosen description of the mass-loss rate can dramatically alter the fate of a massive star, including the possibility of undergoing or bypassing the luminous blue variable phase (Smith, 2014).

Stellar winds, the main cause of mass loss, are primarily initiated by radiative momentum transfer resulting from a series of absorptions and scatterings by metallic lines in the ultraviolet (UV) region of the electromagnetic spectrum (Lucy and Solomon 1970, Castor et al. 1975). The significance of UV lines in this mechanism was initially proposed by (Lucy and Solomon, 1970), although the authors could not accurately predict the magnitude of the mass loss rate due to the limited inclusion of lines in their study. In addition to the radiative mechanism, the mass loss rate in massive stars is influenced by three key parameters:

---

[6] In this context, close binaries are characterized by periods shorter than 10 days, corresponding to the majority of the systems in Sana and Evans (2011). However, one may notice that the term close binary can refer to different definitions when moving to other fields.

[7] Following Reig (2011), the primary is the most massive star in massive X-ray binaries (i.e., the donor star has a current mass above $\approx 8\,{\rm M}_\odot$), and the remnant (white dwarfs, neutron stars or black holes) in low-mass systems (i.e., the donor star has a mass below $\approx 2\,{\rm M}_\odot$).

1. The stellar luminosity in the UV, L_{UV};
2. The previously mentioned effective temperature, T_{eff};
3. The metallicity, Z.

Consequently, modern evolutionary calculations necessitate the incorporation of a comprehensive set of metallic lines, particularly in the UV range, to accurately reproduce observations.

However, from an observational point of view, the parameters that can be derived are the mass loss rate $\dot{M} = \mathrm{d}M/\mathrm{d}t$, conventionally expressed in units of $\mathrm{M}_{\odot}\,\mathrm{yr}^{-1}$, and the terminal velocity v_{∞}, which is the velocity of the wind at a large distance from the star, conventionally in $\mathrm{km\,s}^{-1}$ (Lamers and Cassinelli, 1999). The mass loss rate due to line-driven winds is generally written from the mass continuity equation as

$$\dot{M} = 4\pi r^2 \rho(r) * \left[v_0 + (v_{\infty} - v_0) \left(1 - \frac{R_*}{r} \right)^{\beta} \right] \tag{1.2}$$

where $\rho(r)$ is the mass density, v_0 is the velocity at the photosphere, v_{∞} is the asymptotic velocity, and β is the exponent controlling how fast the terminal velocity is achieved when moving outward of the star for a spherically symmetric wind and using the β velocity law. For a detailed review on the matter, see Lamers and Cassinelli (1999) and Smith (2014).

1.3 *Young Open Clusters*

Stellar clusters have been defined using different terms throughout time, with the main purpose of clearly distinguishing a simple multiple system from a cluster. Examples of definitions include a set of stars gravitationally bound to each other (Portegies Zwart et al., 2010) or a set of stars with its mass density exceeding the environmental mean (Krumholz et al., 2019); for a more classical reference on young clusters (specially old ones, to contrast with our work), see Friel (1995). A stronger criterion can be used, such as a *group of stars with a mass density large enough to resist tidal disruption and numerous enough to avoid N-body evaporation for 100 Myr* (Lada and Lada, 2003).

The astrophysical importance of studying stellar clusters is manifold:

- The detailed comprehension of stellar cluster formation;

- Stellar evolution after the formation of the first stars for a given environment;
- The interaction between the primordial gas with feedback effects from the first supernova explosions and hot star winds due to the most massive stars.

For the purpose of this work, young stellar clusters (YSC) are defined as complex systems composed of a large number of stars that form nearly simultaneously from a common molecular cloud, usually clumps (which are overdensities of an even larger and massive cloud), sharing the same chemical composition at the beginning of formation, being gravitationally bound, and consisting of masses of the order of 10^4 $M_\odot$ and age smaller than 100 Myr. Just like older clusters, there are many open questions about the observational properties of these stellar associations, such as the mass, spatial and age distributions.

The process of star formation is related to the collapse of the molecular cloud, through the conversion of gas to individual stars and multiple systems. Following the approach of McKee and Ostriker (2007), considering an initial cloud mass $M_{\rm cloud}$, the free-fall time $t_{\rm free-fall}$, and birth rate $\dot{M}_*$, the star formation rate SFR can be described as

$$\dot{M}_* = \epsilon_{\rm free-fall} \frac{M_g}{t_{\rm free-fall}}, \tag{1.3}$$

where M_g is the remaining gas mass and $\epsilon_{\rm free-fall}$ is the fraction of $M_{\rm cloud}$ to be converted into stars per free-fall instant. However, the SFR can be affected by various physical factors such as feedback effects from massive stars (stellar winds), photoionization, binarity, and supernovae. For example, feedbacks, in general, can be treated as generic winds which act with a rate of $\dot{M}_{\rm wind}$, leading to another factor in the parametrization. This is sufficient for us to understand how difficult it is to model the birth of a single cluster, or a cluster association, as observations are also limited to our current technologies. One thing is certain: the complexity of YSCs results in a diverse population, observed in nature with a variety of characteristics such as multiple MS turn-off (MSTO) points (i.e., the corresponding position on the HR diagram of a star leaving the MS) on the cluster's color-magnitude diagrams (Milone et al., 2018). After the gas exhaustion, the dynamics of a stellar cluster are ruled mainly by stellar evolution.

A stellar cluster can also suffer from external influences during its evolution, which can change stellar orbits and even remove part of the stars from their birthplace. Some examples include tidal perturbations – caused by gravitational interaction with other massive objects, such as another star cluster and giant molecular cloud; dynamical friction – a phenomenon which removes angular momentum from the cluster and directs it toward its galactic center; and also internal radial migration – caused by density waves (see Sect. 4.3 of Krumholz et al. 2019 and references therein).

To simulate the formation of a star cluster from its inception, a comprehensive set of assumptions and observational constraints is necessary. While understanding stellar evolution is fundamental to comprehending the subsequent stages of star formation, most studies focused on modeling complete clusters prioritize an initial understanding of the observed characteristics (e.g., structure, initial cluster mass function) exhibited by star clusters within the Milky Way and extragalactic environments.

A stellar cluster can be probed through many observing techniques, such as photometry, astrometry, spectroscopy or polarimetry. When photometry is used, a spatially unresolved cluster can have its integrated light fitted with simple stellar population (SSP) models, revealing possible descriptions for the IMF, the SFR and even chemical enrichment evolution. A resolved cluster, on the other hand, can have its age, metallicity, interstellar extinction, distance and rotation rates obtained via isochrone fitting (which needs a few stars already at the MSTO point, as considering just MS stars can lead to degeneracies) using evolutionary tracks (Mints and Hekker 2018, Gontcharov et al. 2019).

If other observational techniques are used, such as spectroscopy, individual stellar fitting with atmosphere models can yield effective temperature and surface gravity estimates, and with high resolution, a better knowledge of chemical abundance with precise fitting of spectral lines, which are useful for studies as chemical tagging (Yu et al., 2021). For astrometry, as we will see in Chap. 3, measures such as the sky position (right ascension, declination) and parallax can be estimated.

However, there is something not yet fully concerned in evolutionary tracks and spectral libraries, and that may lead to unpredictable consequences. As YSCs are known to host many CBe stars (Milone et al. 2018; Hastings et al. 2020), extremely complex objects, modeling needs to take into account effects of very rapid rotation (including the consideration of changing viewing angles when observing a star, due to the already described limb and gravity darkening effects), binary evolution taking into account observational constraints of CBe stars and also the presence of a circunstellar disk, composed of mainly hydrogen. In the next section, CBes are briefly described, as they are the major object of this dissertation.

1.4 *Classical Be stars*

CBe stars can be defined on the following terms: a B-type main sequence star possessing a high rotation rate which has (or already had in any moment of its life) a viscous decretion disk composed of matter ejected by the star (Rivinius et al., 2013). However, these terms can *slightly* vary, as stars near main sequence and late A-type plus early O-type stars may show the Be phenomenon (e.g., Oey et al. 2023) – as long as they share the other attributes: the high rotation rate and the *ability* to produce its circunstellar disk.

Although CBes have been observed since the nineteenth century (Secchi, 1867), the comprehension of these objects only reached a solid ground on the last two decades. Due to their circunstellar disk, CBes manifest themselves through emission lines in their spectra (specially on Balmer lines, such as Hα and Hβ, but not restricted to these), a continuum emission excess (mainly on longer wavelengths, as the presence of the disk does not significantly change the strong UV emission of intermediate-mass/massive stars), non-zero linear polarization and broadened photospheric lines caused by the rapid rotation (Slettebak, 1956). The general properties of the central star and the disk will be further discussed in Chap. 2.1, when the BeAtlas model grid is introduced. In the context of YSC and stellar clusters in general, the rest of this section briefly introduces our knowledge on CBe stars in different environments.

As a class, CBes are common objects, representing 17% of galactic B-type stars (rising to a total of 34% when considering only the B1 spectral sub-type, likely due to observational biases; for more, see Zorec and Briot 1997). However, when analyzing stellar populations sharing common properties (e.g., age and metallicity), this fraction becomes even higher, specially in sufficiently young clusters in which the earliest types of B stars can still be observed. Some good examples are the open cluster NGC 330, with recent works finding a lower fraction of CBe stars as high as $\mathrm{CBe}/(\mathrm{B}+\mathrm{CBe}) = 32\%$ (Bodensteiner et al., 2020), the open cluster NGC 220 with $\mathrm{CBe}/(\mathrm{B}+\mathrm{CBe}) = 31.3\%$ (Iqbal and Keller, 2013) and $\mathrm{CBe}/(\mathrm{B}+\mathrm{CBe}) = 33\%$ for NGC 1856 (Bastian et al., 2016).

For this reason, CBe stars are regularly indirectly observed in astronomical surveys, such as all-sky photometric surveys [e.g., SDSS (Aihara et al., 2011), MCPS (Zaritsky et al., 2002), SkyMapper (Wolf et al., 2018) or S-PLUS (Mendes de Oliveira et al., 2019)], whole sky astrometric missions [e.g., Hipparcos (Perryman et al., 1997) or GAIA (Gaia Collaboration et al., 2016)], spectroscopic surveys [e.g., LAMOST Yan et al. (2022)], and high cadence photometric missions [e.g., OGLE (Udalski et al., 1992), KELT (Pepper et al., 2018) or TESS (Ricker et al., 2015)].

Up to the present day, CBe stars have been observed in many galactic stellar clusters, in the Magellanic Clouds, in the Andromeda galaxy (Peters et al., 2020), and even in a nearby low metallicity irregular dwarf galaxy of the Local Group, in which few B stars could be observed, but a high incidence was found when compared to the whole set of B-type stars (Bresolin et al., 2007). This repertoire makes it possible to state that CBe stars are a unique class, but still linked with the local B stars originated within the same molecular cloud. There are still some open questions regarding this class of stars, such as:

1. What is/are the definite origin(s) of the high rotation rate observed in CBe stars?
2. How do environmental properties (e.g., metallicity, binary fraction, etc) affect CBe stars, regarding for example the incidence fraction Be/(B+Be) or the disk evolution and observables?
3. Does the incidence fraction change over time in a given population? If so, how can one describe its evolution?

In order to keep feeding our understanding about them, it is first necessary to observe CBe stars in a coordinated way in one YSC or in a sample of star clusters (sharing common and different metallicities), and using as many observational techniques as possible, to reduce biases and gather useful data to help answering the mentioned current ongoing debates.

1.5 *Main goals*

The main goal of this dissertation is to develop a method to separate CBes from the normal MS objects in a given stellar cluster using synthetic multi-band photometry, through the creation of synthetic stellar populations with the addition of CBe models present in the BeAtlas grid of models, machine learning classification algorithms and real observational data.

Instead of following a linear approach, this work is structured on different fronts, with each one being necessary before the final outcome. In Chap. 2, the BeAtlas model grid is described in detail. Chap. 3 introduces the SMC open cluster NGC 330, one of the most well-studied YOC that contains many confirmed CBes. In Chap. 4, a methodology to make synthetic photometry out of SSPs with realistic B, Bn, and CBe models is outlined. For Chap. 5, NGC 330 is revisited, and two supervised classification machine learning algorithms are fitted on the synthetic cluster, and applied for SAMI and S-PLUS iDR4 observations of NGC 330 obtained for this work. The main conclusions and future perspectives are ran through in Chap. 6.

Chapter 2

BEATLAS model grid

Over the last two decades, astronomy experienced great technical developments, comprising more efficient programming languages and their base scientific libraries, software made for specific problems (stellar atmosphere fitting with high resolution spectra, radial velocity and light curve fitting for eclipsing binaries, etc), the existence of more accessible (in the context of institutional financing) High Performance Clusters (HPC), and complex data curation and analysis methods such as artificial intelligence (including its ramifications) that, together with increasing amounts of observational data and a sophisticated stellar evolution theory, allows robust analysis for a wide range of applications.

CBes, introduced in Sect. 1.4, behave almost like perfect astrophysical laboratories, as these stars lie on an intersection between many fields of study, such as stellar astrophysics, asteroseismology, extragalactic and galactic studies, and even cosmology – outlining their importance. Finding the fundamental stellar parameters of a star, as briefly mentioned in Chap. 1, is always a difficult task. For CBes, the high rotation rate of these objects, combined with their intrinsic variability and the presence of a circumstellar disk, complicate even more this problem. Complexity grows significantly when we finally realize that the central star and its disk are observationally coupled.

This happens according to the following dynamic: the disk structure (its composition, density, scale height, temperature or velocity field) depends on the matter ejection process and on the physical properties of the central star; the star, on the other hand, has modified apparent properties when observed, due to the disk dynamics.

In this context, the BEATLAS project was planned focused on finding the physical parameters of the coupled system simultaneously, based on a grid of realistic models calculated with the

3D Monte Carlo non-local thermodynamic equilibrium (NLTE[1]) radiative transfer code HDUST (Carciofi and Bjorkman 2006; Carciofi and Bjorkman 2008), capable of solving the radiative transfer problem with a reasonable description of the star, considering rotation effects (e.g., gravity darkening and rotational flattening according to the Roche model) and limb darkening. HDUST deals with the circumstellar material in full NLTE regime (considering just atomic hydrogen) with all main sources of gas opacity being available, such as Thomson scattering, bound-bound, bound-free and free-free absorptions. The output results from HDUST comprise the polarized emergent spectrum (of both continuum and emission lines) and also synthetic images for a given spectral region.

There are two main branches of the BeAtlas project, consisting of the first designed grid (dubbed Original BeAtlas) and the recent on-going update (hereafter BeAtlas v2). The basis of both projects are detailed in Sect. 2.1.

2.1 *Main BeAtlas structure*

Although BeAtlas primary subject are CBes, inactive CBes, B-type, and Bn stars in general can also be studied. This is because BeAtlas consists of two sets of models: one named the *photospheric grid*, and the other the *disk grid*.

2.1.1 *The Photospheric grid*

The photospheric set is suited for diskless stars, including inactive CBe stars (observational data of an inactive phase can be difficult to find, as weak residual emission can still be present even when the inner disk is dissipated), normal[2] B stars, and Bn stars.

Although the native HDUST parameters for the central star consist of the stellar mass M, rotation rate W, gravity darkening exponent $\beta_{\rm GD}$, luminosity L, and the polar radius $R_{\rm pole}$, the only parameters necessary to define the grid are M, W, and age, given as the fraction of time spent on the main sequence $t/t_{\rm MS}$. The BeAtlas grid uses rotating stellar evolution models from

---

[1] NLTE refers to the situation in which the energy distribution of atoms or ions differs from the LTE regime, characterized by both Boltzmann excitation and Saha ionization equations and Maxwell-Boltzmann velocities distribution. NLTE can arise due to many physical interactions (e.g., photoionization, recombination, etc), and cannot be ignored in atmosphere modelling of hot stars (Hubeny and Mihalas, 2014).

[2] Hereafter, the term normal in this case will refer to B-type stars that are not CBe stars (or have not yet been classified as such).

the Geneva group (Georgy et al. 2013b; Granada et al. 2013) to connect these 3 parameters to the full set needed for HDUST, as $R_{\rm pole}$ and L can be estimated given the other three. The gravity darkening exponent $\beta_{\rm GD}$ is obtained from W following the model described in Espinosa Lara and Rieutord (2011).

The final parameter is the inclination angle of the stellar spin axis i, important in the context of rapidly rotating objects. In Fig. 2.1, it is shown how oblateness causes a star seen at low inclination angles (near pole-on) to be brighter and bluer, while edge-on objects can appear dimmer and redder.

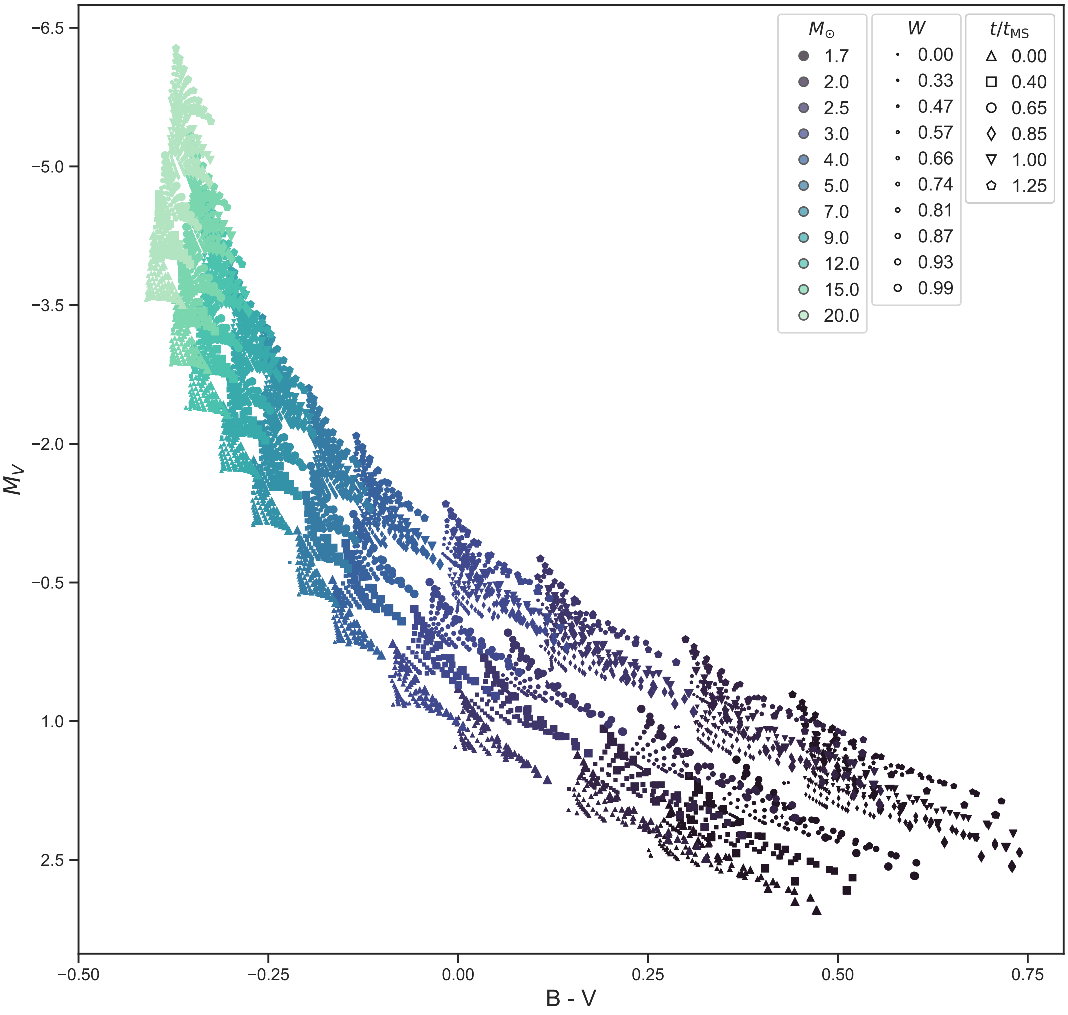

Figure 2.1: (M_V, $B - V$) color-magnitude diagram of the BeAtlas v2 photospheric grid on the Vega system. The configuration of this figure (markers' colors, types and sizes) follows Fig. 2.6. A significant feature shows up on the observational diagram, which is the cone opening caused by the different inclination angles. Models observed pole-on, when rotating fast, seem brighter, while models observed edge-on behave dimmer and redder than their non-rotating counterparts.

2.1.2 *The Disk grid*

The disk model set was designed for CBes. Besides the necessary parameters for the central star, exemplified in Sect. 2.1.1 (M, W and $t/t_{\rm MS}$), and the geometric factor coming from the inclination angle i, there are at least three other parameters needed for the disk definition, which are the radial disk density falloff exponent n, the volume number density at the base of the disk n_0 (i.e., at $r = R_{\rm eq}$), and the disk radius $R_{\rm D}$.

The theoretical basis justifying the choices of how many and which parameters are need to describe the circunstellar disk of CBes is the Viscous Decretion Disk (VDD) model (Lee et al., 1991), a formulation based on an α-disk (Shakura and Sunyaev, 1973), with the disk building from inside-out through the viscous shear between layers of material thrown into orbit by the central star.

In the VDD model, the process of material ejection from the star is followed by orbital movement. Through turbulent viscosity, matter and AM are transported outward, leading to the formation of a disk. Although HDUST is capable of dealing with only hydrogen, the disk itself is typically composed with the same material from the stellar photosphere, lacking any significant presence of dust — which sets it apart from distinctive objects like B[e] stars (Lamers et al., 1998).

Assuming an uniform mass injection rate along the stellar equator and the validity of the thin disk approximation (for more information, refer to Bjorkman and Carciofi 2005), the viscous diffusion simplifies into a one-dimensional problem. In this scenario, the density and velocity solely depend on the radial distance from the star. By further assuming that the disk is both radially and vertically isothermal and that the central star continuously loses mass over a sufficiently long period (as described in Haubois et al. 2012), it becomes possible to derive an analytical solution for the structure of the disk.

Bjorkman and Carciofi (2005) derived the following expression for the surface density based on these considerations:

$$\Sigma(r) = \frac{\dot{M} v_{\rm orb} R_{\rm eq}^{1/2}}{3\pi\alpha\, c_s^2\, r^{3/2}} \left[\left(\frac{R_0}{r} \right)^{1/2} - 1 \right] , \tag{2.1}$$

where $v_{\rm orb}$ denotes the Keplerian orbital velocity at the equator, $\dot{M}$ represents the rate of mass flowing out of the central star, α stands for the Shakura-Sunyaev viscosity parameter, R_0 is an integration constant associated with the outer, torque-free boundary condition, and $c_s =$

$\sqrt{kT/(m_{\rm H}\mu)}$ represents the sound speed in the disk (with T being the disk temperature, k the Boltzmann constant, $m_{\rm H}$ refers to the hydrogen mass, and μ is the mean molecular weight of the gas). Assuming that $R_0 \gg R_{\rm eq}$, Eq. 2.1 assumes a simple functional form $\Sigma(r) \propto \Sigma_0, r^{-2}$, where Σ_0 denotes the surface density at the base of the disk.

In the absence of radiative forces and nearby stellar companions, and under the assumption that the material is in vertical hydrostatic equilibrium, the vertical density distribution (i.e., along the direction orthogonal to the disk plane) follows a simple Gaussian profile with a scale height controlled solely by gas pressure and the gravitational field of the CBe star. As the disk extends further from the star, it flares. Hence, the scale height H takes the following form:

$$H = H_0 \left(\frac{r}{R_{\rm eq}}\right)^{\beta}, \tag{2.2}$$

where $H_0 = c_s R_{\rm eq}/v_{\rm orb}$ and β is 1.5 (where β denotes the flaring exponent, which controls the scale height profile; see Bjorkman and Carciofi 2005). The volume mass density equation of an isothermal VDD can then be obtained, considering that the surface density Σ is the vertical integral of the density. Therefore, the volume mass density can be written in terms of the scale height and the surface density as:

$$\rho(r,z) = \frac{\Sigma_0}{H\sqrt{2\pi}} \left(\frac{r}{R_{\rm eq}}\right)^{-2} \exp\left[-\frac{z^2}{2\,H^2}\right] \propto \rho_0\, r^{-n}, \tag{2.3}$$

with $n = 3.5$ and ρ_0 the base volume density of the disk. The aforementioned considerations and the power-law approximation of Eq. 2.3 hold true for an isothermal, steady-state VDD. Also, the Gaussian description of the vertical density distribution is valid for regions near the central star, which serves for the purposes of this work. For distances of hundreds of stellar radii, a more realistic distribution cannot follow $z \ll R_{\rm D}$. A more detailed 2D formulation of $\rho(r,z)$ is given in Kurfürst et al. (2018), from Eq. 31 to Eq. 39.

However, real CBe disks deviate from these ideal conditions. CBe disks are renowned for their variability across various timescales. Their existence relies on the injection of mass and angular momentum (AM) at their base, and fluctuations in the mass injection rate lead to complex effects on their properties.

If mass injection ceases for an extended period (longer than typical viscous timescales), the disk dissipates entirely, leaving the CBe star as a regular B star with fast rotation. Initially, the inner disk dissipates more rapidly, collapsing back onto the central star as it can no longer sustain itself without the influx of AM from the star. The outer disk, still receiving AM from the decaying inner disk, can persist for a longer duration but eventually dissipates over time. Disk formation and dissipation events are governed by the viscous diffusion timescale, which can be written as

$$\tau_\nu = \frac{v_{\rm orb}}{\alpha c_s^2}\sqrt{R_{\rm eq}\, r} \sim 2\,{\rm years}\,\frac{0.1}{\alpha}\sqrt{\frac{r}{R_{\rm eq}}}\,, \tag{2.4}$$

meaning that CBe disks can be completely built and lost, passing through matter ejection, orbiting and consequent dissipation in timescales ranging from months to years, as recent estimates of the viscous parameter α indicate it is usually a few tenths, ranging from ~ 0.01 to 1.00 (Rímulo et al., 2018; Ghoreyshi et al., 2018, 2021).

A CBe star undergoing the formation or dissipation of its disk does not exhibit a volume density that strictly follows the prescribed $n = 3.5$ power law. During the buildup phase, the inner region of the disk fills up more rapidly than the outer region, resulting in a higher value of n (greater than 3.5). Conversely, during the dissipation phase, the inner disk depletes at a faster rate than the outer disk, leading to a lower value of n (less than 3.5; for more, refer to Haubois et al. 2012, specially Figs. 1 and 3).

Furthermore, the situation is more intricate than described above, as the models by Haubois et al. (2012) demonstrate a significant variation in n with distance from the star (e.g., their Fig. 3 and 6). Vieira et al. (2017) utilized this information to correlate their estimates of n for a sample of 80 CBe stars with the current state of their disks, considering a range of $3.0 < n < 3.5$ as indicative of disk stability. For most of their sample, n was found to be less than 3.5, suggesting that these disks were dissipating at the time of observation, while only 45% of the disks were either in a buildup phase (24%) or considered stable (21%).

Also, the radial density falloff exponent can deviate from the isothermal value of $n = 3.5$ due to the presence of a binary companion. Early-type CBe stars (i.e., spectral classes B0-B3), which are massive stars, are often part of binary or multiple systems, as stated in Sect. 1.2.2. Approximately 80% of these stars experience interactions with a companion at some point in their lives (Sana et al., 2012). Even though the binary fraction tends to decrease when moving to lower masses (Janson et al., 2012; Sota et al., 2011), binary companions have been observed together with late-type CBe stars (spectral classes B4-B9) (e.g., κ Dra – Klement et al., 2022)). Oudmaijer and Parr (2010) reported a binary fraction of 30 ± 8% specifically for CBe stars, with a separation limitation of 0.1 to 8 arcsecs and magnitude differences up to 10 magnitudes.

The binary fraction among CBe stars remains uncertain, with estimates achieving almost 100%

(Shao and Li, 2014; Klement et al., 2019). In smoothed particle hydrodynamics simulations of binary CBe stars, tidal influences from a close companion lead to disk truncation and the accumulation of matter within the orbit (Okazaki et al., 2002). This phenomenon results in a smaller radial density falloff exponent (i.e., $n < 3.5$) as observed by (Panoglou et al., 2016; Cyr et al., 2017). This accumulation effect is also influenced by the binary separation, the disk viscosity, and the binary mass ratio, becoming a complex phenomenon.

Another possible cause for deviations of n from its isothermal state arises if the disk comprises an exceedingly non-isothermal temperature structure (Carciofi and Bjorkman, 2008; McGill et al., 2012; Kurfürst et al., 2018). The sound speed (and hence the viscosity) in the disk depends on temperature, so temporal and/or spatial temperature variations can significantly alter the density structure of the disk. Carciofi and Bjorkman (2008) found that in a non-isothermal but steady-state disk, n can range between 2 and 6 (see Fig. 4 in their study). The disk structure is also influenced by α, which can independently change both radially and temporally (Ghoreyshi et al., 2021).

Concluding, the value of n can fluctuate in time due to the dynamic state of the disk and the tidal effects of a companion, while radial variations can occur due to non-isothermality and variations in viscosity. Therefore, the power law density represented by Eq. 2.3 serves as an approximation for the majority of CBe stars. At the same time, it is a useful approximation as it allows measuring – via detailed modeling – the (average) disk density slope at a given moment in time, irrespectively of how this slope was realized.

Along with the 3 defining disk parameters previously established (n, n_0, R_D), the disk scale-height is of the same form of Eq. 2.2, with H_0 being computed with the disk temperature set to a fixed value based on a fraction of the central star temperature (a common value used in the literature is $T_\mathrm{d} = 0.60\,T_\mathrm{eff}$, as reported by findings of Carciofi and Bjorkman 2006) and with the flaring exponent fixed at the known isothermal value of $\beta = 1.5$.

2.1.3 *Observables*

To connect the input parameters to the expected HDUST results, BeAtlas needs the definition of the desired spectral coverage and also the images configuration, which we call the observables.

The spectral coverage is given in a list of continuum bands, delimited by a wavelength range, and a list of spectral lines. This takes advantage of HDUST efficiency when being ran for separate spectral regions. Each band is assigned a particular number of photon packets to be used in the

Monte Carlo sampling, which allows a better distribution of computational time, focusing on higher quantities of photon packets in the most important regions.

Spectral lines can be chosen from the optical up to the infrared domains, and their selection can occur based on their importance in the study of CBes or for specific demands. Note that the current version of HDUST only includes hydrogen lines in NLTE.

Therefore, we defined a number spectral bands, encompassing wavelengths ranging from the UV to the radio domain. Each band is then characterized by a minimum and maximum wavelength, the number of spectral bins (representing its image resolution), the spacing between bins (linear or logarithmic), and the number of photon packets used in the simulation.

Images are configured with a specific value of spectral bins, translating to the final resolution and the bin spacing. In every BeAtlas version, predefined spectral channels were designed, focusing on the reproduction of interferometric measurements – based on existent, past and future planned interferometric instruments (to be described further ahead).

2.2 *Original BeAtlas*

The first designed grid, hereafter Original BeAtlas, involved a huge effort to be designed and run, being completed near 2014/2015. The parameters chosen for the first BeAtlas grid are described in Tab. 2.1 for the disk grid and Tab. 2.2 for the photospheric subset, comprising near 1700 models with disk (which corresponds to nearly 17000 emergent spectra) and 60 photospheric-only models (600 emergent spectra).

In the original BeAtlas disk subgrid, H_0 was calculated with $T = 0.72\,T_{\rm pole}$, and only one value of age and disk radius were used. The age parameter in Original BeAtlas was characterized by the Hydrogen fraction present in the core, a value present directly in Geneva evolutionary files. The chosen value, $X_c = 0.30$, is roughly equivalent to a star at $t/t_{\rm MS} = 0.75$.

The observables in the first BeAtlas grid included the continuum from the UV (starting at $\lambda = 1000$Å) up to the infrared, plus Hα and Brγ spectral lines. Although this grid is almost 10 years old, being calculated using a much older version of HDUST (2.02, current version is 2.12), it is still very useful.

For example, the original grid was extremely important for both Masters dissertation and PhD thesis defended by Dr. Tiago Batista Souza (see Batista Souza 2015 and Batista Souza 2021, respectively). In his Masters, BeAtlas was used to fit physical parameters of 63 CBes observed

Table 2.1 - Stellar + disk parameters of the Original BeAtlas disk grid. For each rotation rate, there is only one associated value of the gravity darkening exponent. The non-rotating models are assigned with $\beta_{\rm GD} = 0.25$, and for the critically rotating models $\beta_{\rm GD} \approx 0.13$.

Symbol	Parameter	Range	Values
Fundamental parameters			
M ($M_\odot$)	Stellar Mass	3.4 - 14.6	3.4, 3.8, 4.2, 4.8, 5.5, 6.4, 7.7, 8.6, 9.6, 10.8, 12.5, 14.6
X_c	H fraction in the core	Fixed	0.30
Z	Metallicity	Fixed	0.014
W	Rotation Rate	0.45 - 0.95	0.45, 0.63, 0.78, 0.89, 0.95
R_D ($R_{\rm eq}$)	Disk radius	Fixed	50
Σ_0 (g cm^{-2})	Disk surface density	0.02 - 4.00	0.02, 0.05, 0.12, 0.28, 0.68, 1.65, 4.00
n	Density radial exponent	3.0 - 4.5	3.0, 3.5, 4.0, 4.5 + non-isothermal steady-state
$\cos i$	Inclination angle	0 - 1	0, 0.11, 0.22, 0.33, 0.44, 0.55, 0.67, 0.78, 0.89, 1
Derived parameters			
ST	Spectral Type	B9 - B0.5	B9, B8, B7, B6, B5, B4, B3, B2.5, B2, B1.5, B1, B0.5
$\beta_{\rm GD}$	Gravity darkening exponent	0.22 - 0.15	0.22, 0.20, 0.18, 0.16, 0.15

Table 2.2 - Stellar parameters of the Original BeAtlas photospheric grid. For each rotation rate, there is only one associated value of the gravity darkening exponent.

Symbol	Parameter	Range	Values
Fundamental parameters			
M ($M_\odot$)	Stellar Mass	3.4 - 14.6	3.4, 3.8, 4.2, 4.8, 5.5, 6.4, 7.7, 8.6, 9.6, 10.8, 12.5, 14.6
X_c	H fraction in the core	Fixed	0.30
Z	Metallicity	Fixed	0.014
W	Rotation Rate	0.45 - 0.95	0.45, 0.63, 0.78, 0.89, 0.95
$\cos i$	Inclination angle	0 - 1	0, 0.11, 0.22, 0.33, 0.44, 0.55, 0.67, 0.78, 0.89, 1
Derived parameters			
ST	Spectral Type	B9 - B0.5	B9, B8, B7, B6, B5, B4, B3, B2.5, B2, B1.5, B1, B0.5
$\beta_{\rm GD}$	Gravity darkening exponent	0.22 - 0.15	0.22, 0.20, 0.18, 0.16, 0.15

by the APOGEE-1 survey (the latter was part of the third release of the Sloan Digital Sky Survey; for more details of SDSS-III, refer to York et al. 2000), with the observables being focused in the H band and the Brγ spectral line ($\lambda_{\rm laboratory} = 16113.74$ Å), which was available for every star in the sample spectra. At that time, it was possible to notice some limitations of the original grid, such as the density distribution.

In his thesis, BeAtlas was applied for a wider sample of 102 stars, with also more observables besides the typical H band and the already cited Brγ spectral line, such as the whole SED and spectra obtained with FEROS, a high resolution optical spectrograph mounted in La Silla, Chile. At that time, the original grid could be used with still limited knowledge of inference techniques and a restricted grid, with only one stellar age and disk radius.

2.3 *Intermediate BeAtlas grids*

After the first tests and applications of the original grid, it was realized that the disk grid needed a wider parameter space, with the inclusion of multiple stellar ages – to better sample the parameters of the central star, and also detailed parameters of the disk itself – such as multiple values for the outer radius and a wider range for the density radial exponent and disk base densities.

For the works of Mota (2019), Rubio (2019) and Genaro (2020) (PhD thesis, Masters dissertation and Bachelor monograph, respectively), two photospheric grids were calculated, and a partial disk grid was computed aiming at studying particular stars. A low-mass star subgrid was computed to model α Col (five masses ranging from $3.0\,\mathrm{M_\odot}$ to $6.0\,\mathrm{M_\odot}$) and a higher mass subgrid for α Ara (masses ranging from $\sim 4.9\,\mathrm{M_\odot}$ to $\sim 8\,\mathrm{M_\odot}$). However, the partial disk grid was already based on a newer prescription, but with computational limitations the whole grid would not be able to be fully computed for the works of Mota (2019) and Rubio (2019).

Table 2.3 - Stellar parameters of Mota's BeAtlas photospheric grid. For each rotation rate, there is only one associated value of the gravity darkening exponent.

Symbol	Parameter	Range	Values
Fundamental parameters			
M ($\mathrm{M_\odot}$)	Stellar Mass	1.7 - 20	1.7, 2, 2.5, 3, 4, 5, 7, 9, 12, 15, 20
t/t_{MS}	Stellar age	0 - 1.02$^{(a)}$	0, 0.25, 0.5, 0.75, 1, 1.01, 1.02
Z	Metallicity	Fixed	0.014
W	Rotation Rate	0 - 0.99	0, 0.33, 0.47, 0.57, 0.66, 0.74, 0.81, 0.87, 0.93, 0.99
$\cos i$	Inclination angle	0 - 1	0, 0.11, 0.22, 0.33, 0.44, 0.55, 0.67, 0.78, 0.89, 1
Derived parameters			
ST	Spectral Type	A7 - O8	A7, A2, A0, B9.5, B7, B6, B3, B2.5, B1, B0, O8
β_{GD}	Gravity darkening exponent	0.25 - 0.13	0.25, 0.23, 0.21, 0.20, 0.19, 0.18, 0.17, 0.16, 0.15, 0.13

(a) The post-MS values of t/t_{MS} ($t/t_{\mathrm{MS}} = 1.01, 1.02$) are existent only on Mota's grid, not included in the expansion of Genaro's work.

The photospheric grid calculated by Mota (2019) covered a wider range of parameters (shown in Tab. 2.3) than the original grid, and extended the observables up to the radio domain. In the work of Genaro (2020), the photospheric grid received an expansion, focusing on the main Balmer series Hydrogen transitions (Hα, Hβ, Hγ, Hδ), but without the inclusion of post-MS stellar age values. These four spectral lines were computed with a higher resolution (and more photon packets on HDUST), plus a wider coverage from the line center of each individual line profile.

Since these works, the stellar age started to be expressed in terms of its MS lifetime. For example, in the MS the age parameter will range from a minimum of $t/t_{\rm MS} = 0$, corresponding to the H fraction in the core of $\sim 72\%$, up to $t/t_{\rm MS} = 1.0$, where the H fraction approaches 0%, with $t/t_{\rm MS}$ representing the fraction of time already spent by the star relative to the whole age span from the ZAMS to TAMS. Note that translating from $t/t_{\rm MS}$ to real age depends on the stellar mass and rotation rate.

2.4 *BeAtlas v*2

The original grid planning, execution, and testing against real CBe observational data were equally important for a better understanding how well the grid was suited for model interpolation in a wide parameter space, and how it could be improved when taking into account the most important correlations between parameters.

Works using the original grid were capable to show that the VDD framework with HDUST calculations reproduced well some CBe stars observations. However, a grid containing just one stellar age for each set of (M, W) and just one value for the disk radius does not cover the expected range for a lot of CBes. Also, we realized that the disk density values chosen for the original grid did not follow a realistic trend (in the $M - \Sigma_0$ relation) of CBes. With this prior knowledge, a new version of the grid (hereafter BeAtlas v2) was planned, and its execution is on course. Its structure (photospheric + disk subgrids and observables) is detailed ahead.

For this study, new photospheric and disk grids were designed. The photospheric grids (summarized in Tab. 2.4) were already computed for 3 metallicities, while the disk grid is currently being run.

The stellar mass was chosen in the range 1.7 to 20 $\mathrm{M}_\odot$, typically covering the spectral range from A7 to O8.5. Specifically for this work, 20 $\mathrm{M}_\odot$ models were computed to properly cover the high-mass end of the Be phenomenon, following the exact same physical description that the ones in Georgy et al. (2013b). The chosen mass range includes all typical masses of known CBe stars as well as the transition to late type Oe stars (Negueruela et al., 2004) and to early-A stars. By using the Geneva grid, the number of free parameters for a star reduces from four to three (mass, rotation rate and age).

The association between mass and spectral type are based on Martins et al. (2005), Schmidt-

Kaler (1982), and Adelman (2004), for O, B and A spectral types, respectively. The rotation rate covers the full range between a non-rotating star ($W = 0$) to a nearly-critically rotating one $W = 0.99$. The chosen steps follow $W_i = 0.99\,(i/N)^{1/2}$ with $i = 0, \dots, N$ and $N = 10$. There is one specific $\beta_{\rm GD}$ for each rotation rate, with values ranging from $\beta_{\rm GD} = 0.25$ for $W = 0$, and $\beta_{\rm GD} \approx 0.13$ for $W = 0.99$.

An important modification was made to the parameters of the central star, specifically regarding $t/t_{\rm MS}$ and can be seen in Tab. 2.4. The values assigned to $t/t_{\rm MS}$ in Tab. 2.4 were carefully selected to ensure a more comprehensive sampling of the star's trajectory along its MS track.

In Mota's work, the five values of $t/t_{\rm MS}$ (0 to 1, in steps of 0.25) did not uniformly cover the whole evolutionary trajectory throughout the MS. In Fig. 2.2, it is possible to see that the first three ages ($t/t_{\rm MS}$ = 0, 0.25, 0.50) were too concentrated towards the ZAMS. As BeAtlas uses $t/t_{\rm MS}$ to find, together with the pair (M, W), the polar radius $R_{\rm p}$ and luminosity L from the Geneva rotating models, $t/t_{\rm MS}$ must comprise a more uniform sampling. With this findings, both photospheric and disk grid values of $t/t_{\rm MS}$ were then improved, with the solution of finding a better suiting set of stellar ages.

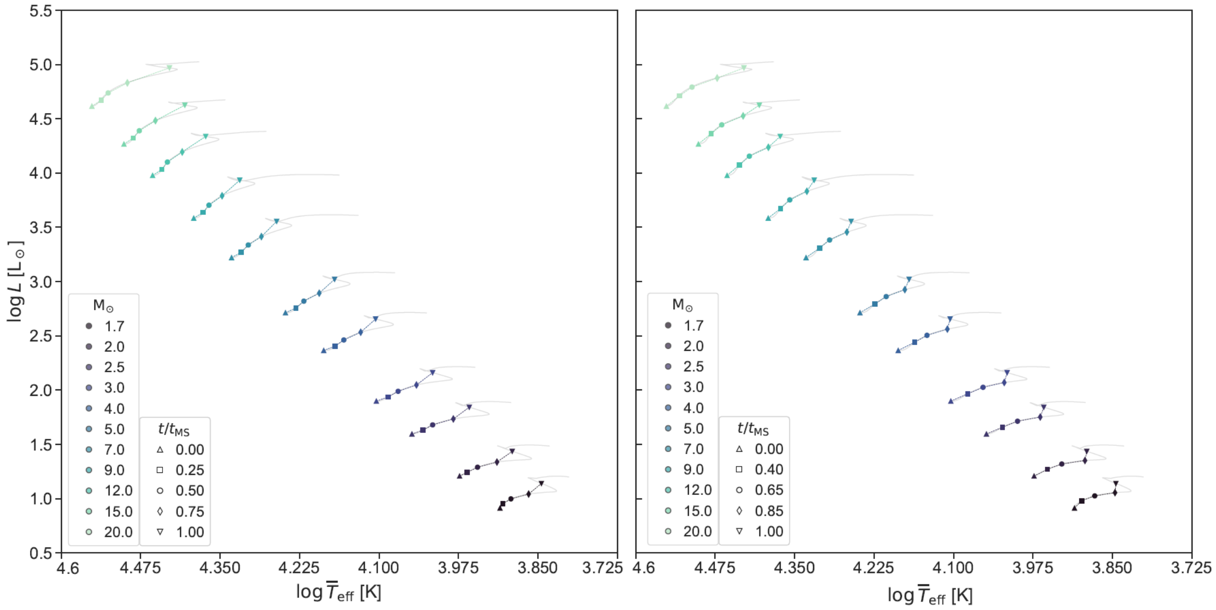

Figure 2.2: Theoretical HR diagram comprising the masses considered in the photospheric grid of BeAtlas v2, for the non-rotating case. Left: sources have the $t/t_{\rm MS}$ array used in the works of Mota and Genaro. Right: updated values of $t/t_{\rm MS}$, focusing on a better sampling of the stellar evolution. The corresponding Geneva non-rotating tracks from Georgy et al. (2013b) are shown as thin solid lines, matching each labeled stellar mass. Both panels share the same scale.

Also, it will be discussed below that the disk grid of BeAtlas v2 consists of only three values of $t/t_{\rm MS}$. Before the discovery of the ZAMS stacking problem, the disk grid $t/t_{\rm MS}$ values were planned to go from 0 to 1 with the intermediate value equal to half. Now, the intermediate value consists of $t/t_{\rm MS} = 0.65$, being closer to the evolutionary trajectory "half" in the theoretical HR diagram. The conversion from $t/t_{\rm MS}$ to real age is mass- and W-dependent within the range of $0 \leq t/t_{\rm MS} \leq 1$. Given a specific mass, rotation rate, and $t/t_{\rm MS}$, the Geneva grid is interpolated to calculate the corresponding values of $R_{\rm p}$, L, and age[3].

Another important realization is that BeAtlas was not able to correctly infer the stellar age for some CBes, such as Achernar (α Eridani, HD 10144, HR 472, HIP 7588) or α Col (α Columbae, Phact, HD 37795, HR 195). For example, in Genaro (2020), modeling of Achernar was done using BeAtlas photospheric models and observational data from the UV and three spectral lines (Hα, Hβ and Hγ) and the best estimate of the stellar age was $t/t_{\rm MS} = 0.999 \pm 0.001$, using Monte Carlo Markov Chains (Bayesian inference). The resulting probability density functions (PDF) for the other stellar parameters plus the stellar distance and reddening is shown in Fig. 2.3. It is possible to notice a "stacking" phenomenon towards $t/t_{\rm MS} = 1.0$ in the simulation corner plot.

In the case of α Col, Rubio (2019) found a value of $t/t_{\rm MS} = 0.952^{+0.013}_{-0.017}$, with a piled PDF towards $t/t_{\rm MS} = 1$, which can be seen in Fig 2.4. Instead of using UV and Balmer lines, α Col had its entire SED[4] modeled using data from IUE, Hα profiles from a variety of databases, and photometric measurements up to the radio part of the electromagnetic spectrum. For both cases, the stars are indeed in an advanced evolutionary stage as seen in different studies, and analysis should be made with care. For Achernar, Kervella et al. (2022) found $t/t_{\rm MS} = 0.90$ ($t = 63$ Myr) using the same rotating evolutionary models of Georgy et al. (2013b) – but with their estimated mass of $M = 6.4 \pm 0.2\,{\rm M}_\odot$ and considering a single track with initial rotation of 95% of the critical limit – whereas α Col has two estimates putting it at the end of the MS, with $t/t_{\rm MS} = 0.97 \pm 0.06$ being found by Zorec et al. (2016) and $t/t_{\rm MS} = 0.91$ by Levenhagen and Leister (2006).

A piled PDF of one parameter towards any limit is not ideal for two reasons; the first one is that the inference may have found the "true" solution set – in this case, the mean value and its uncertainty becomes not so precise. The second reason is that the inference could not reach the true solution, as the best set for the minimization process appears to be beyond the grid limit.

As $t/t_{\rm MS}$ is a parameter specifically used to be translated to the star $R_{\rm p}$ and L, a solution was

---

[3] In this context, *age* refers to the time elapsed since the initiation of hydrogen ignition in the core, i.e., the duration since zero-age main sequence (ZAMS) measured in years.

[4] SED is the Spectral Energy Distribution, defined as the energy emitted by an object as a function of different wavelengths.

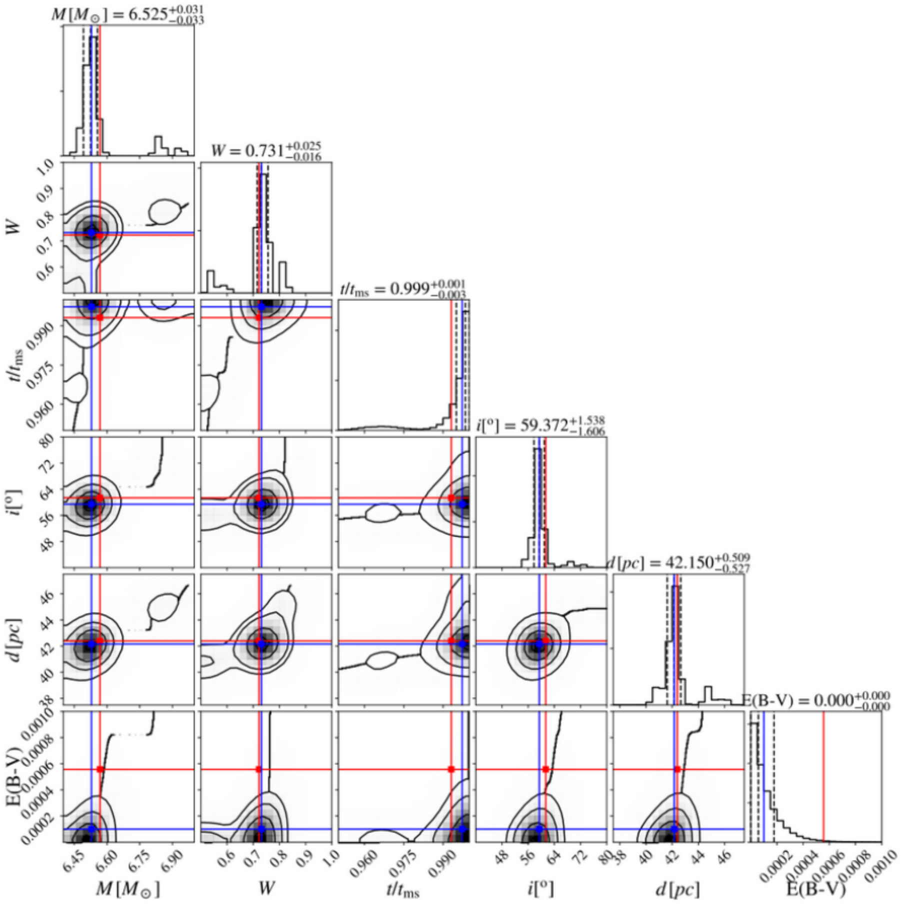

Figure 2.3: MCMC simulation made with 100 walkers and 25 000 steps using Hα, Hβ, Hγ high resolution spectral lines obtained from FEROS and a UV spectrum from the IUE satellite for the CBe Achernar. Credit: Genaro (2020).

developed. Ideally, it would be interesting to add another value of $t/t_{\rm MS}$ after the MS using the Geneva evolutionary models. However, after the Hydrogen fraction in the core becomes zero, the code does not have enough resolution (in terms of time steps) and the envelope expands too fast while rotation intensively drops. For example, in the case of Achernar, the MCMC inference is asking to go beyond the MS (according to the Geneva evolution), but it has been observed by interferometric techniques and had its radius and oblateness being measured with precision, so a parametric solution beyond Geneva is necessary.

To overcome this adversity, an additional value of $t/t_{\rm MS} = 1.25$ for the age parameter was introduced, as an extrapolation of the MS models rather than relying on the problematic post-MS models. Consequently, this particular $t/t_{\rm MS}$ value does not correspond to a real age but serves the purpose of exploring parameter ranges (the former cited $R_{\rm p}$ and L) that are consistent with stars transitioning away from the MS. These ranges extend beyond those predicted by the Geneva grid for the main sequence.

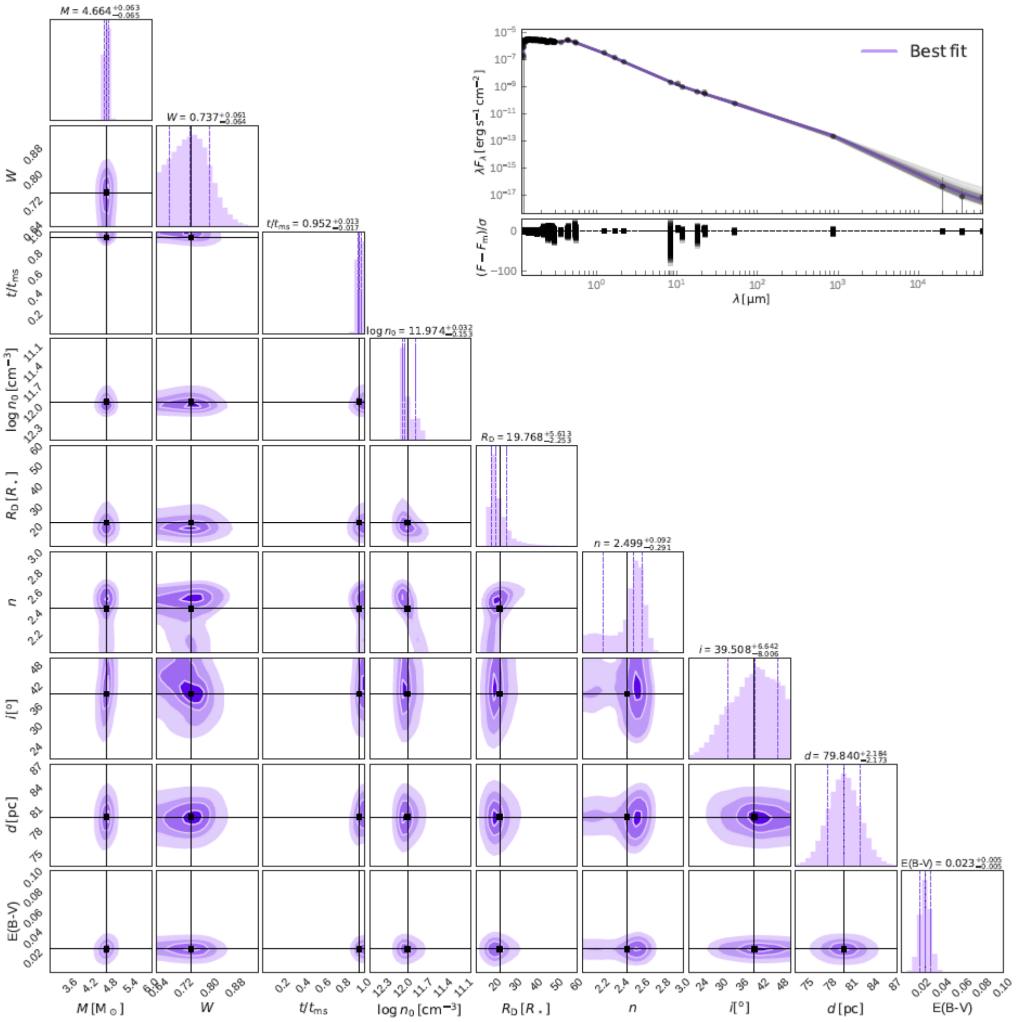

Figure 2.4: MCMC simulation made with 300 walkers and 20 000 steps using the Hα line, UV spectra from IUE, and photometric data from the visible up to the radio regime obtained through the Virtual Observatory SED Analyser. Credit: Rubio (2019).

To determine the associated values of R_p and L for each (M, W) pair, extrapolation techniques utilizing an exponential function are employed, based on the values of R_p and L for $t/t_\mathrm{MS} = 0.40, 0.65, 0.85, 1$. This approach allows us to accommodate possibilities that are not anticipated or covered by the Geneva main sequence grid, such as stars with higher luminosities but without an expanded envelope. If a simulation infers $t/t_\mathrm{MS} > 1$ for a given star, it becomes an indication that the star may not be well represented by the MS phase of the Geneva grid of evolutionary models. In Fig. 2.5, the extrapolation effects can be seen in a $(R_\mathrm{p}, \log L)$ diagram.

Finally, the last parameter of the photospheric grid is the inclination angle of the stellar spin axis with respect to the line of sight, i. For i, ten equally spaced values in $\cos i$ were chosen.

The other two implemented metallicities match the typical values associated with the LMC and SMC ($Z = 0.006$ and $Z = 0.002$, respectively). At the moment, the SMC and LMC grids

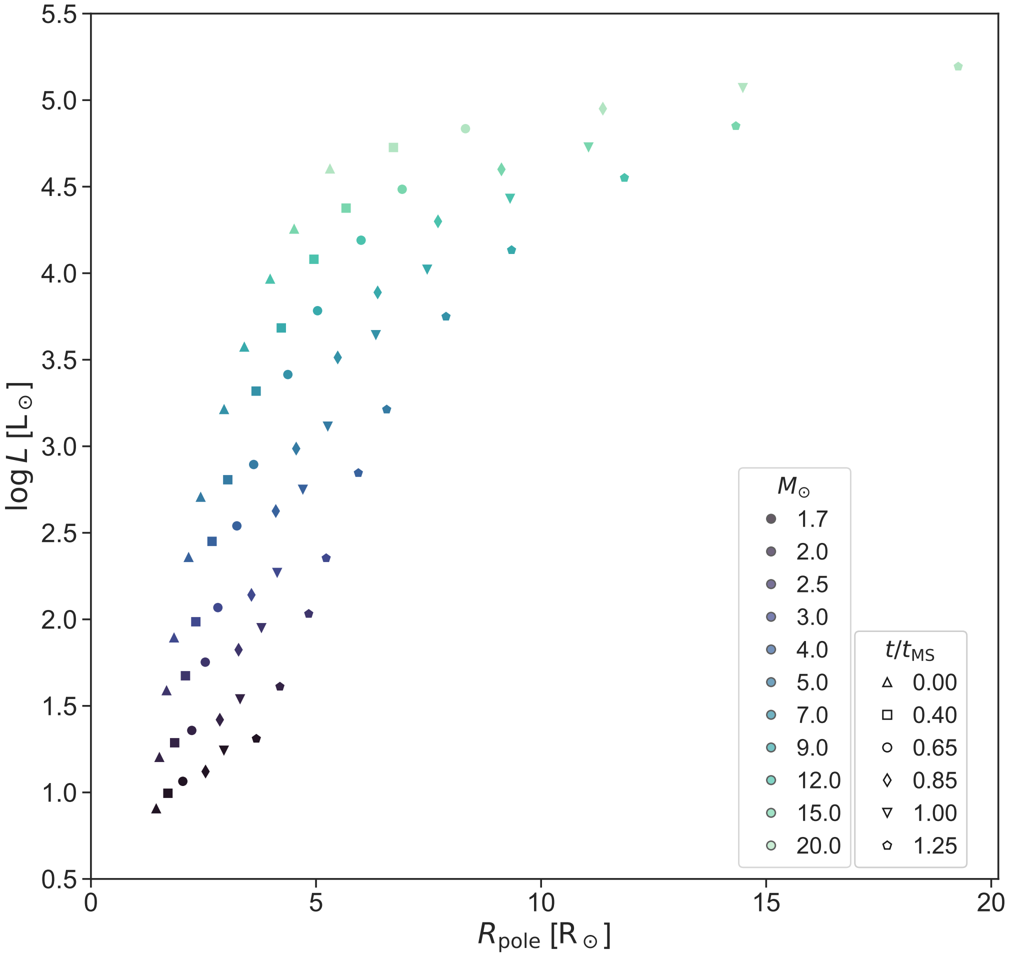

Figure 2.5: (R_{pole}, log L) diagram comprising the BeAtlas v2 stellar parameters for $Z = 0.014$. Masses are indicated by different marker colors. Values of t/t_{MS} are indicated by different marker types. Rotation rate is fixed at $W = 0.33$. The extrapolated value of $t/t_{\text{MS}} = 1.25$ is shown as a colored pentagon.

are only partially completed. They cover the SED from λ = 1000Å to ≈ 14000Å, allowing for studies that use the standard *UBVRI* and the S-PLUS bandpasses.

For the BeAtlas v2 disk grid, the selection of stellar parameters aimed at on achieving the best representation of the Be phenomenon. To maintain consistency with the mass grid of Georgy et al. (2013b), the lower limit of the mass range was set at 3 M$_\odot$, while the upper limit remained unchanged at 20 M$_\odot$.

The intention was to minimize the use of interpolated values from the Geneva grid and instead focus on an almost equivalent mass grid. A total of 11 stellar mass values were chosen for the disk grid, along with 5 values for W, ranging from $W = 0.50$ to $W = 0.99$. This choice was motivated by the absence of known slowly rotating CBe stars (refer to the compilation presented in Rivinius et al., 2013, Fig. 9). Also, 4 values of t/t_{MS} were included, including the extrapolated

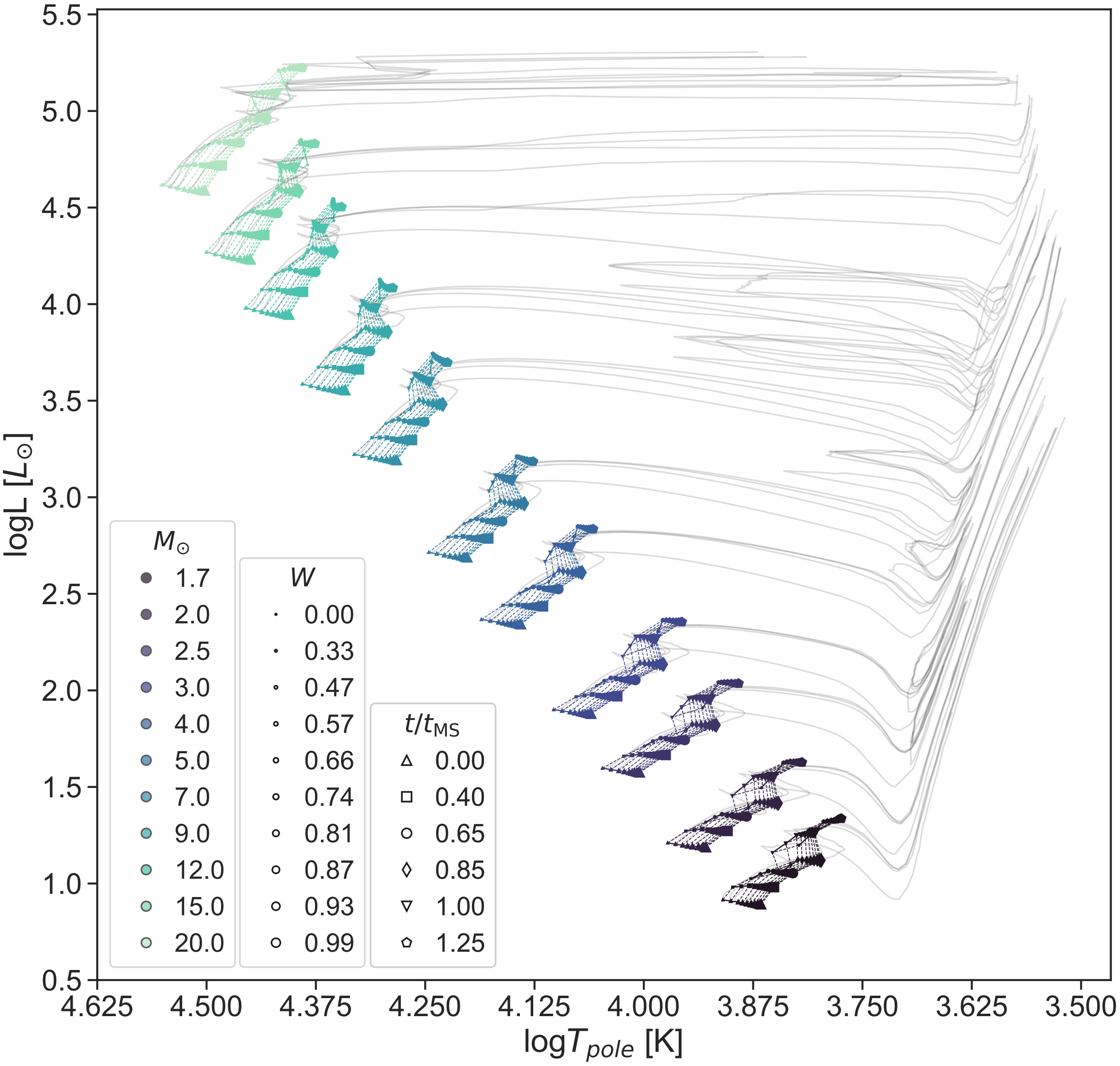

Figure 2.6: Hertzsprung–Russell diagram comprising the photospheric grid parameters. Masses are indicated by different marker colors. Marker sizes represent different rotation rates W. In gray solid lines, four complete Geneva tracks are shown, corresponding to the initial velocities of $W_{\rm Geneva} = 0,\ 0.769,\ 0.925$ and 0.998 for each stellar mass. Values of $t/t_{\rm MS}$ for each (M, W) pair are connected with dashed lines, following the tracks, indicated by different marker types; the path from ZAMS to TAMS goes from bottom left up to top right. A complete version of the photospheric grid including all metallicities is shown in App. A.1.

Table 2.4 - BeAtlas v2 stellar parameters of the photospheric grid. For each rotation rate, there is only one associated value of the gravity darkening exponent.

Symbol	Parameter	Range	Values
Fundamental parameters			
M	Mass ($M_\odot$)	1.7 - 20	1.7, 2, 2.5, 3, 4, 5, 7, 9, 12, 15, 20
W	Rotation Rate	0 - 0.99	0.00, 0.33, 0.47, 0.57, 0.66, 0.74, 0.81, 0.87, 0.93, 0.99
$t/t_{\rm MS}$	Stellar Age	0 - 1.25	0, 0.40, 0.65, 0.85, 1, 1.25
Z	Metallicity	0.002 - 0.014	0.002, 0.006, 0.014
$\cos i$	Inclination angle	0 - 1	0, 0.11, 0.22, 0.33, 0.44, 0.55, 0.67, 0.78, 0.89, 1
Derived parameters			
ST	Spec. Type	A7 - O8.5	A7, A2, A0, B9.5, B7.5, B6, B3.5, B2.5, B1, B0.5, O8.5
$\beta_{\rm GD}$	Gravity darkening exponent	0.25 - 0.13	0.25, 0.23, 0.21, 0.20, 0.19, 0.18, 0.17, 0.16, 0.15, 0.13

non-physical value of $t/t_{\rm MS} = 1.25$ present in the photospheric grid. The inclination angle distribution for the disk grid remained the same as the photospheric grid, consisting of 10 evenly spaced values.

Regarding the disk scale-height, H_0 was calculated with the disk temperature set to $T = 0.60\,T_{\rm pole}$, while β was fixed at the isothermal value of 1.5. For each M value, a grid of n_0 was constructed using 8 points equally spaced in logarithmic space, ranging between a fixed lower limit and an upper limit dependent on the mass. The upper limit was determined based on the convergence limit of HDUST models, adapted to an analytical approximation described as:

$$\ln n_0^{\rm upper}(M)\ [\mathrm{cm}^{-3}] = \begin{cases} aM^2 + bM + c, & M \leq 7\,\mathrm{M}_\odot, \\ dM + e, & M > 7\,\mathrm{M}_\odot. \end{cases} \tag{2.5}$$

The parameters in the equation are defined as follows: $a = -0.152/{\mathrm{M}_\odot}^2$, $b = 2.51/\mathrm{M}_\odot$, $c = 22.09$, $d = 0.14/\mathrm{M}_\odot$, and $e = 31.02$. Previous studies by Vieira et al. (2017) and Rímulo et al. (2018) have shown that massive stars tend to have denser disks compared to their low-mass counterparts, which aligns with the convergence limitations observed in our simulations.

The maximum value of n_0, corresponding to $M = 20\,\mathrm{M}_\odot$, was set to $n_0 = 5 \times 10^{14}\,\mathrm{cm}^{-3}$, the highest value reported in the literature for a B0 star (Carciofi and Bjorkman, 2006). As for the lower limit, we adopted a value of $10^{11}\,\mathrm{cm}^{-3}$ for all stellar masses, which roughly corresponds to the detection limit of an emission feature, even if weak, in the Hα line.

The disk radius ranges from 10 to $100\,R_{\rm eq}$. While CBe disks theoretically have the potential to expand to several hundred stellar radii, the presence of a binary companion can tidally affect and truncate the disk. In our grid, the lower limit of the disk radius corresponds to an estimate for

Table 2.5 - BeAtlas v2 parameters of the disk grid. The values for $\cos i$ are the same as in Tab. 2.4.

Symbol	Parameter	Range	Values
Fundamental parameters			
M	Mass ($M_\odot$)	3 - 20	3, 3.5, 4, 4.5, 5, 6, 7, 9, 12, 15, 20
W	Rotation Rate	0.50 - 0.99	0.50, 0.75, 0.85, 0.92, 0.99
$t/t_{\rm MS}$	Stellar Age	0 - 1.25	0, 0.65, 1, 1.25
Z	Metallicity	Fixed	0.014
$\log_{10} n_0$ (lower)	Disk base number density (cm^{-3} - dex)	Fixed	11.0
$\log_{10} n_0$ (upper)	Disk base number density (cm^{-3} - dex)	M-dependent	12.3, 12.6, 12.9, 13.2, 13.4, 13.9, 14.0, 14.2, 14.4, 14.7
$R_{\rm D}$	Disk radius ($R_{\rm eq}$)	10 - 100	10, 20, 40, 70, 100
n	Number density radial exponent	1.5 - 4.5	1.5, 2.0, 2.5, 3.0, 3.5, 4.0, 4.5
Derived parameters			
ST	Spec. Type	B9.5 - O8.5	B9.5, B9, B7.5, B6.5, B6, B4.5, B3.5, B2.5, B1, B0.5, O8.5
$\beta_{\rm GD}$	Gravity darkening exponent	0.21 - 0.13	0.21, 0.18, 0.16, 0.15, 0.13

the disk radius of the CBe star o Pup, which has the shortest period among all known binary CBe stars (Koubský et al., 2012), and thus possesses the smallest known disk radius. On the other hand, the upper limit of $100\,R_{\rm eq}$ corresponds to a disk size at which the disk emission becomes negligible across all wavelengths considered in the simulation (see Vieira et al., 2015).

The range of the exponent n in Eq. 2.3 was determined based on the findings of Vieira et al. (2017) and spans from 1.5 to 4.5. This range broadly agrees with other studies in the literature (e.g., Waters et al., 1989; Silaj et al., 2014; Touhami et al., 2014). It is worth to remember that for an isothermal, steady-state disk, $n = 3.5$ (see Eq. 2.3). A summary of the parameters for the disk grid is presented in Tab. 2.5.

Finally, in Tab. 2.6) we summarized the spectral bands planned for the final version of the BeAtlas v2 grid. The SED (first part of Tab. 2.6) ranges all the way from the UV up to the radio. Each continuum band is defined by a minimum and maximum wavelength, the number of spectral bins, their spacing, and the number of photon packets used. The second part described the planned spectral lines, whose choice was based on the lines with most data available in the literature.

For some observables, images were computed across pre-defined spectral channels aiming at reproducing interferometric observables. Our definitions include, for example, both decommissioned interferometers (e.g., AMBER and MIDI), for which large number of archival observations are available, and current interferometers at ESO (GRAVITY and MATISSE) and the Georgia State University's CHARA.

It is important to notice that the primary reason for the choice of a smaller number of stellar masses, ages and rotation rates for the disk grid was computational efficiency, as a more extensive

Table 2.6 - Definition of BeAtlas' observables.

Observable	$\lambda_{\rm min}$ [μm]	$\lambda_{\rm max}$ [μm]	$N_{\rm bins}$	Spacing	$N_{\rm phot}$	Image	Comments
UV	0.1	0.32	210	linear	4.0×10^8	No	Kurucz resolution
SED	0.32	1.05	108	log	1.0×10^9	No	–
J	1.05	1.4	30	linear	1.8×10^8	No	–
H	1.4	1.85	30	linear	1.5×10^8	Yes	PIONIER[1], MIRC[2], R~300
K	1.85	2.45	30	linear	1.5×10^8	Yes	GRAVITY[3], R~4,000
L	2.45	3.9	16	linear	1.0×10^8	Yes	MATISSE[4], R~1,000
M	3.9	8	24	linear	1.5×10^8	Yes	MATISSE, R~550
N	8	13	15	linear	1.0×10^8	Yes	MATISSE, R~250
Q1	13	18	10	linear	2.0×10^7	No	–
Q2	18	25	10	linear	2.0×10^7	No	–
IR35	25	45	10	log	2.0×10^7	No	–
IR65	45	85	10	log	2.0×10^7	No	–
IR100	85	120	10	log	2.0×10^7	No	–
IR160	120	200	10	log	2.0×10^7	No	–
IR300	200	400	10	log	2.0×10^7	No	–
IR600	400	800	10	log	2.0×10^7	No	–
MM	800	1200	10	log	2.0×10^7	No	LABOCA[5], JCMT1/2[6], IRAM[7]
CM07	6000	7500	10	log	2.0×10^7	No	VLA[8]/Q
CM13	11300	16700	10	log	2.0×10^7	No	VLA/K
CM20	16700	25000	10	log	2.0×10^7	No	VLA/Ku
CM30	25000	37500	10	log	2.0×10^7	No	VLA/X
CM60	37500	75000	10	log	2.0×10^7	No	VLA/C

Observable	$\lambda_{\rm c}$ [Å]	R	Spacing	$N_{\rm phot}$	Image	Comments
Hα	6564.61	20,000	linear	1.1×10^9	Yes	CHARA/SPICA[9], R~10,000
Hβ	4862.71	10,000	linear	3.0×10^8	No	–
Hγ	4341.69	6,000	linear	6.5×10^7	No	–
Hδ	4102.89	6,000	linear	6.5×10^7	No	–
Br11	16811.1	6,000	linear	1.0×10^8	No	APOGEE[10]
Br13	16113.7	6,000	linear	1.0×10^8	No	APOGEE
Brγ	21661.178	20,000	linear	2.0×10^8	Yes	AMBER[11], GRAVITY[3]
Pfγ	37405.6	10,000	linear	1.0×10^8	No	–
Hu14	40208.7	10,000	linear	1.0×10^8	No	–
Brα	40522.6	10,000	linear	1.0×10^8	No	–

[1] `www.eso.org/sci/facilities/paranal/instruments/pionier.html`

[2] `www.chara.gsu.edu/instrumentation/mirc`

[3] `www.eso.org/sci/facilities/paranal/decommissioned/midi.html`

[4] `www.eso.org/sci/facilities/develop/instruments/matisse.html`

[5] `www.eso.org/public/teles-instr/apex/laboca/`

[6] `www.eaobservatory.org/jcmt/`

[7] `www.iram-institute.org/`

[8] `www.public.nrao.edu/telescopes/vla/`

[9] `www.chara.gsu.edu/instrumentation/spica`

[10] `www.sdss4.org/dr12/irspec/`

[11] `www.eso.org/sci/facilities/paranal/instruments/amber/overview.html`

stellar grid would significantly increase the computational cost of generating the grid.

At the current planning, BeAtlas v2 comprises a total of 660 (11 masses × 10 rotation rates × 6 ages) photospheric models for each metallicity and 61 600 disk models (11 masses × 5 rotation rates × 4 ages × 7 density slopes × 5 disc sizes × 8 values for n_0). Each model is computed for the ten common inclination angles of both grids, so the grid effectively contains 6 600 emergent spectra of photospheric-only stars (for each Z) and 616 000 for CBes.

Given that each complete model can take on average 15 h to be calculated using 64 computing cores, to complete just the BeAtlas v2 disk grid, approximately $15 \times 61\,600 \times 64 = 59$ million core-h[5] are required, a challenging number even for modern computing standards.

Also, I was directly responsible for the managing and execution planning of the new grid, being in constant contact with external collaborators such as Dr. Armando Domiciano Souza, from the Observatoire de la Côte d'Azur (France), Dr. Michel Curé from Universidad de Valparaíso (Chile), the PhD. student Mark Suffak from the Western University (Canada), and former group members which participated in the original BeAtlas grid creation, such Dr. Daniel F. Moser and Dr. Rodrigo Vieira.

As a result of these collaborations this newest BeAtlas version has used resources from the National Laboratory of High Performance Computing (cluster Leftraru, Chile), the computing center Mésocentre of CentraleSupélec and École Normale Supérieure Paris-Saclay (France), and SHARCNET (cluster graham, Canada), besides smaller machines locally, such as Pituna (P.I., prof Carciofi) and Prof. Dr. Laerte Sodre Jr. group's TEIU machine. Also, a significant amount of computing hours was recently aproved for the Santos Dumont supercomputer, managed by the National Laboratory for Scientific Computing (LNCC/MCTI, Brazil), and there is an open request for the TGCC cluster, managed by GENCI (France), whose outcome is expected to be known in November, 2023. Currently, only $\sim 24\%$ of the disk grid was run, considering just the continuum range of $\lambda = 1000$Å to $\lambda = 10500$Å, plus the Hα line. These three simulations, summed with the hdust step 1 process, is equivalent to almost 60% of the computational time for a complete model. A scientific paper describing the grid with two applications on the CBe stars Achernar and β CMi[6] was recently approved, and is attached in App. B. For the full reference,

---

[5] The core-h is a standard unit for measuring computing time in parallel computers, and is equivalent of one hour of computing time in one computing core.

[6] For Achernar, the fully computed BeAtlas v2 photospheric grid was used, and an important result regarding $t/t_{\rm MS}$ was obtained, with a behaved PDF indicating a mean value of $t/t_{\rm MS}$ greater than one. This result is shown in Fig. 5 of the BeAtlas paper attached in App. B. For β CMi, as the BeAtlas v2 disk grid does not comprise

see Rubio et al. (2023).

Currently, the disk grid of BeAtlas v2 is already completed for $M = 3.5$ and $4.0\,\mathrm{M}_\odot$, and the disk radius ranging from $R_\mathrm{D} = 10$ to $40\,R_\mathrm{eq}$, for every other parameter in the disk set. In Fig. 2.7, an example of use of the grid is shown with a composite plot of β CMi's continuum and normalized Hα profile using the inferred parameters present in the BeAtlas paper ($M = 3.64\,\mathrm{M}_\odot$, $W = 0.74$, $t/t_\mathrm{MS} = 0.71$, $\log n_0 = 12.17$, $R_\mathrm{D} = 33\,R_\mathrm{eq}$, $n = 2.83$, and $i = 46.29°$) and a comparison with its real observations. One of the cited current limitations of HDUST can be seen in the Hα profile panel, in which the wings are not so well sampled because of the lack of electron scattering.

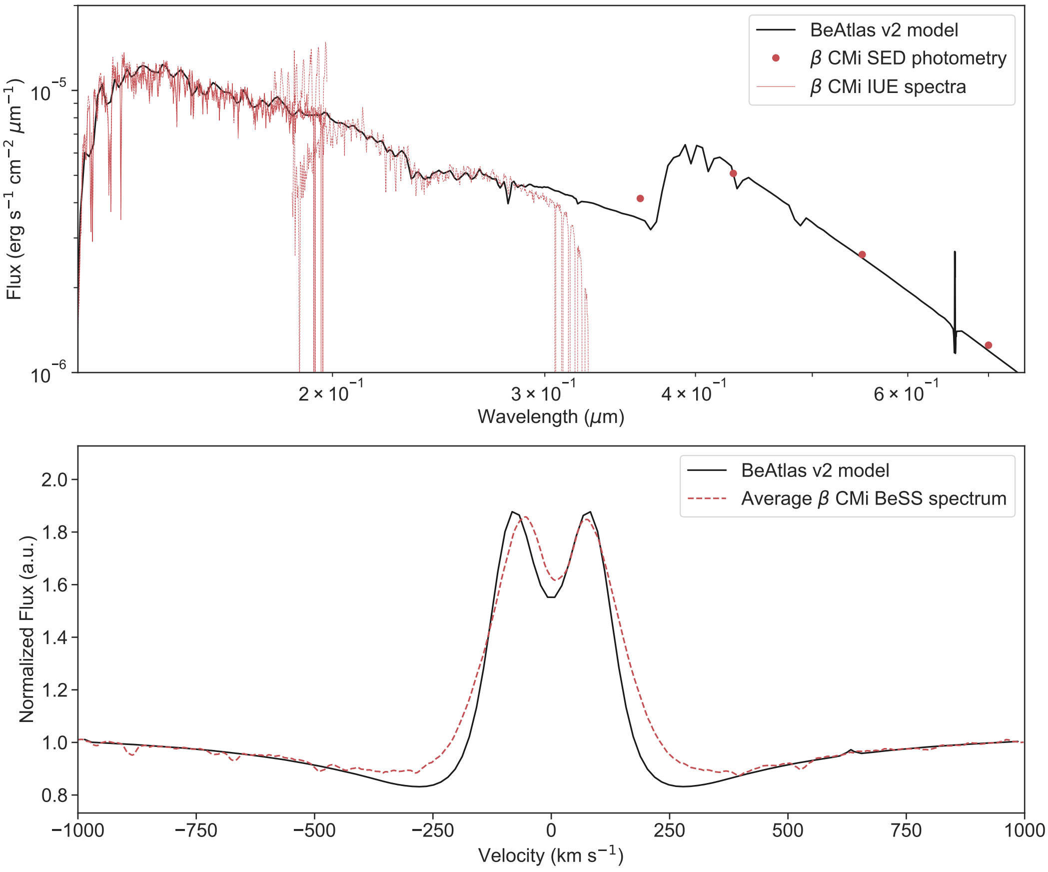

Figure 2.7: Composite plot of β CMi SED plus a normalized Hα profile computed with BeAtlas v2 using inferred parameters and compared with real observations. Upper panel: in red, the SED of β CMi from the UV up to $\lambda = 10500$Å is shown. UV spectra comes from the IUE satellite, while the red dots are photometric measurements. In black, the corresponding BeAtlas v2 interpolated flux is shown. Lower panel: normalized Hα profiles. In red, an average spectrum from the BeSS database is shown, while in black a close BeAtlas v2 model is plotted.

---

observables up to the radio regime yet, the intermediate grid computed by Rubio (2019) was used.

In the next section, I will briefly review the historical context of the SMC YOC NGC 330, highlighting its importance on the advances of the Be field and stating why it will be our object of study in Chap. 4.

Chapter 3

The Young Open Cluster NGC 330

In this chapter, the open cluster NGC 330 will be reviewed from a historical perspective, highlighting its importance to the Be field and how it is one of the most interesting objects to test our developed method for stellar content characterization using synthetic clusters, to be introduced in Chap. 4.

NGC 330, located in the Small Magellanic Cloud, is seen in the direction of Tucana, centered at α = 00h 56m 17.6s and $\delta = -72°\ 27'\ 47''$ (J2000; Rafelski and Zaritsky 2005) and was the object of study of 20+ refereed articles in the past three decades. It is classified as a young stellar cluster, with its age being recently estimated as $\approx$ 30 Myr (Bodensteiner et al., 2020), known to be a very metal-poor ($[\mathrm{Fe/H}] < -1$) cluster (Piatti et al., 2018). In Fig. 3.1, an observation from the Hubble Space Telescope (HST) Wide Field Camera 3 is shown.

3.1 *Historical perspective*

One of the first observations of NGC 330 was published by Arp (1959), still using photographic plates, and is shown in Fig. 3.2. This observation was part of a paper series focused on southern stellar clusters. Despite the technological limitations of the time, many stars were cataloged for the first time on the *UBV* Johnson's system (Johnson and Morgan, 1953), helping the observations that were to come. Arp (1959) concluded, besides cataloging many stars, that the observed (V, $B - V$) color-magnitude diagram could be different from those observed in galactic open clusters due to changes in chemical composition.

Only twelve years later, an extremely important work came out, starting to unveil the high content of CBe stars within the cluster: the first Hα survey, conduced by Feast (1972). Based on previously known MS stars, Feast (1972) found significant Hα emission in the majority of the MS

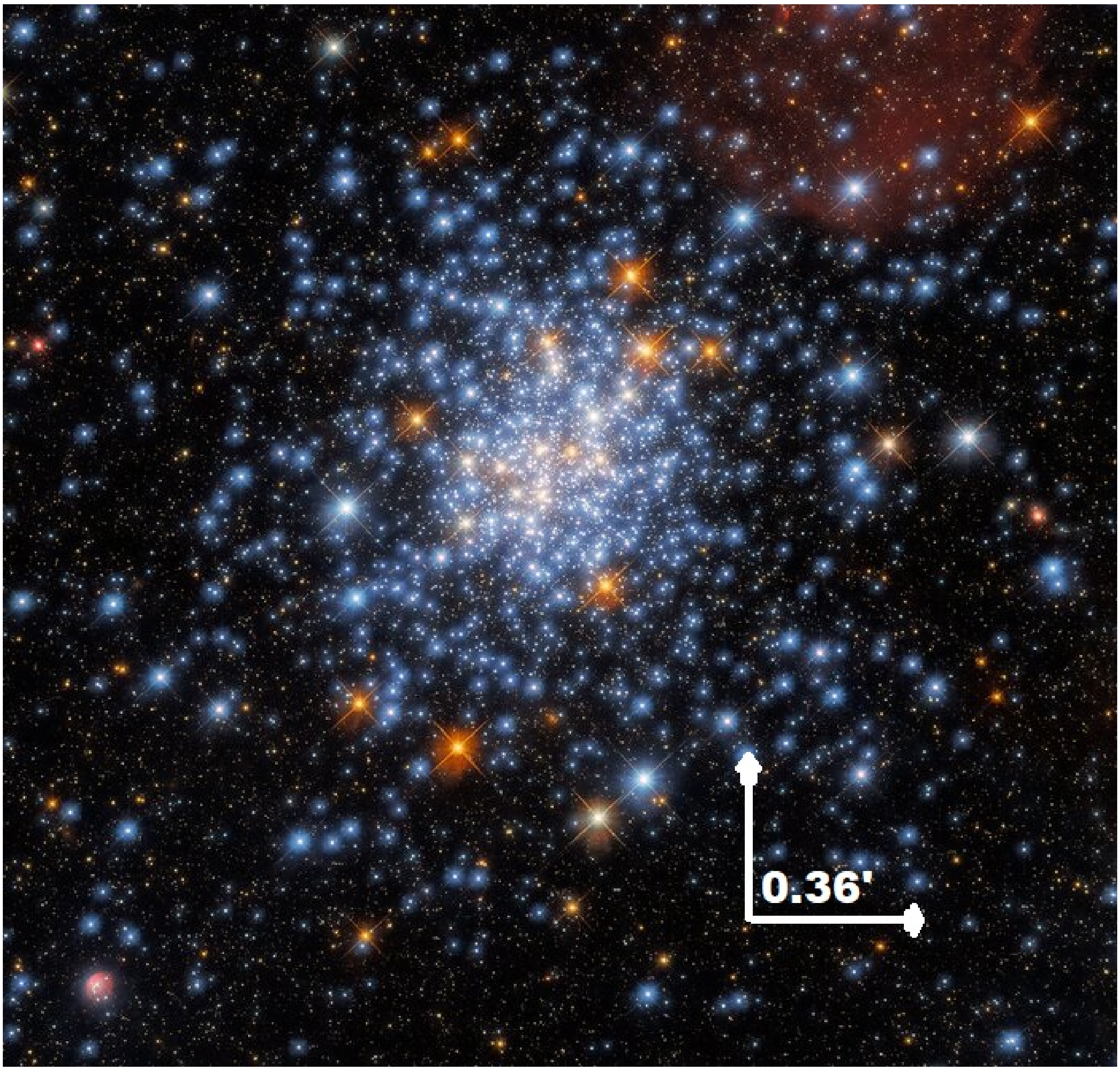

Figure 3.1: NGC 330 observed by the Wide Field Camera 3 from HST. The RGB channels are composed from the (I, Hα), (I, U) and (UV, U) bands respectively. North is 28° left of vertical. Credit: ESA/Hubble & NASA, J. Kalirai, A. Milone.

stars observed, with the equivalent width being larger (in absolute terms) than the expected for nebulosity contamination effects. A color-magnitude diagram is shown in Fig. 3.3, with probable CBe stars marked by filled circles.

Even though this was one of the first works to reveal the Be content on NGC 330, many works were to come, with developments coming side by side with technical advances in both observation and theory. In 1985, another great contribution was published on the matter. Carney et al. (1985) observed NGC 330 in *UBV* photometry (still partly using photographic techniques), low resolution spectroscopy and infrared *JHK* photometry for both cluster-centered and field stars. At that time, it was well established that NGC 330 was an important cluster, being the brightest

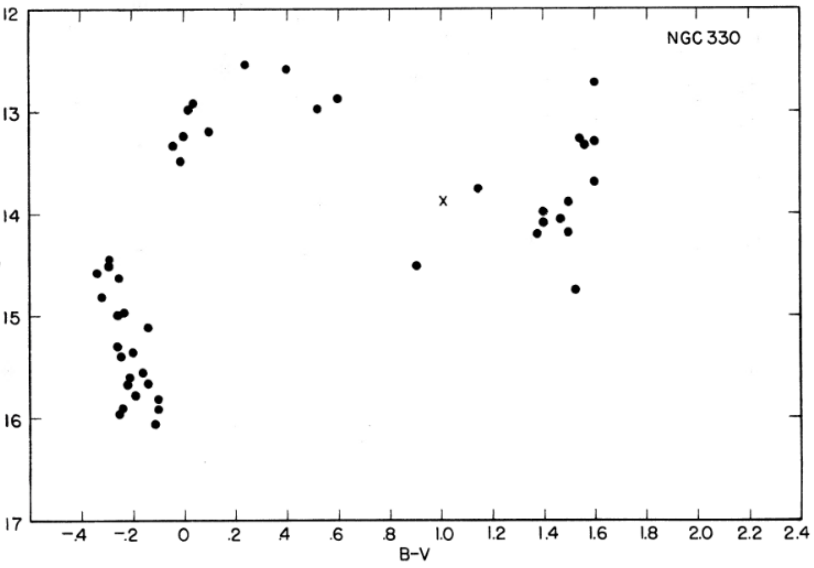

Figure 3.2: (V, $B-V$) color-magnitude diagram for NGC 330 of stars near the cluster center, indicating probable members. Credit: Arp (1959)

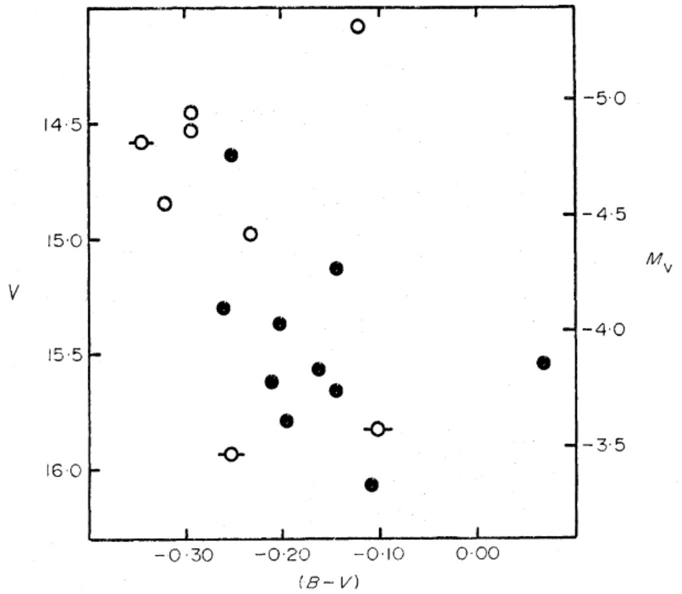

Figure 3.3: Color-magnitude diagram for MS stars observed by Feast (1972) and Arp (1959). Open circles mark stars without Hα emission, while filled circles are Hα emitters. Horizontal bars mark probable weak emission. Credit: Feast (1972).

of the SMC, very compact, and containing young (thus, also massive) stars with metallicity lower than the Galaxy. The color-magnitude $V \times (B-V)$ diagram for stars considered members of Carney et al. (1985) is shown in Fig. 3.4. The MS, red supergiant, blue supergiant and red giant population positions were recovered from previous works in the literature, but with a better data quality and completeness.

With only CCD photometry, Alcaino and Alvarado (1988) presented *UBVRI* sequences for

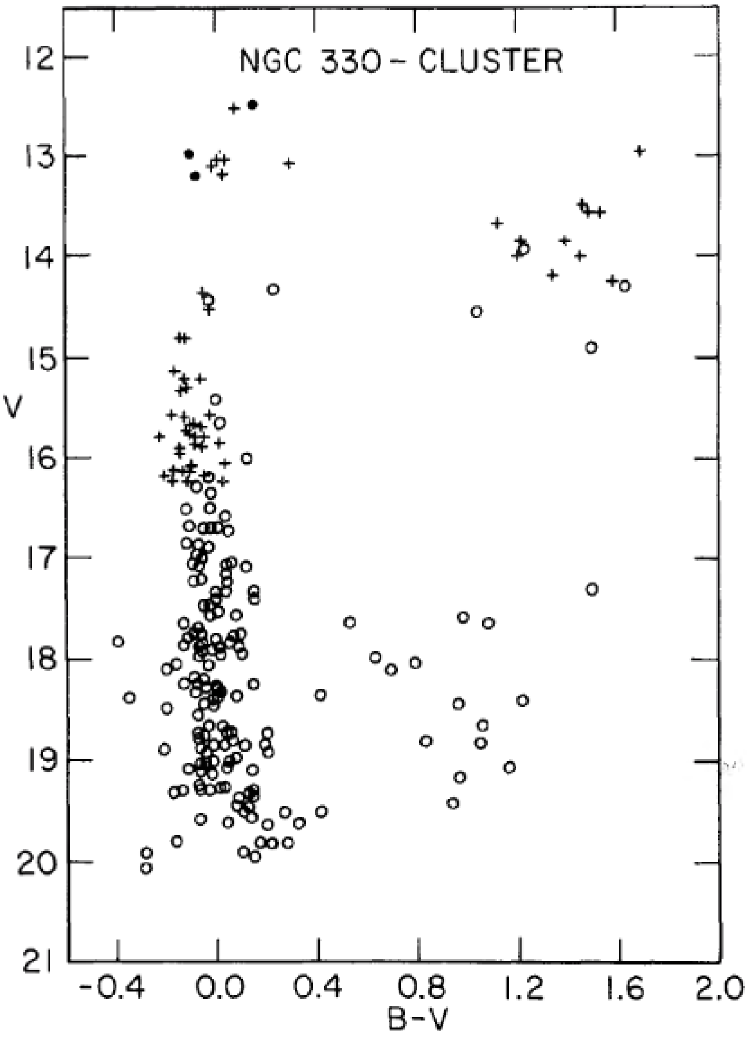

Figure 3.4: (V, $B - V$) diagram of NGC 330, showing its probable members. Filled circles are photoelectric data, open circles are photographic data, and crosses are transformed photographic data from Robertson (1974). Credit: Carney et al. (1985).

NGC 330, along with another SMC cluster and two LMC clusters. This was the first major work to provide *RI* (Kron-Cousins system; for details, see Landolt and Clem 2015) standards for NGC 330, and marks a solid ground for subsequent works using longer wavelengths; this would naturally facilitate the finding of CBe stars, considering their intrinsic IR excesses.

Grebel et al. (1992) proposed the first reliable photometric method for identifying CBe stars using the Strömgren system, with the bandpasses b (λ_c = 4670Å; Δ_λ = 180Å) and y (λ_c = 5470Å; Δ_λ = 230Å), plus a narrow Hα filter, testing it against previously classified CBe stars. It must be emphasized that at that point in time, there was still a limited understanding of the Be phenomenon. Consequently, significant efforts were underway to classify new CBe stars for subsequent study and monitoring.

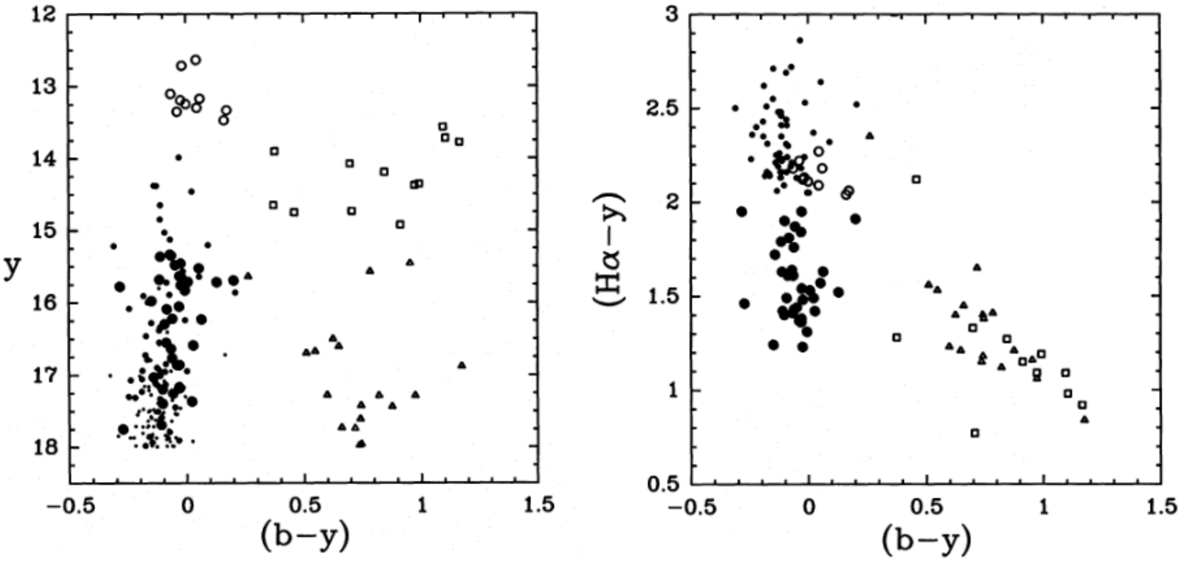

Figure 3.5: Strömgren photometric diagrams for NGC 330. Left panel: (y, $b - y$) color-magnitude diagram. Right panel: (H$\alpha - y$, $b - y$) color-color diagram. In both panels, MS objects, CBe stars, blue supergiants, yellow and red supergiants and red giants are indicated by small and medium sized dots, large filled circles, open circles, open squares and triangles, respectively. Credit: Grebel et al. (1992).

The idea behind defining a classification method based on photometry is to avoid spectroscopy, a method that still nowadays is time consuming, and the competition for telescope time has only risen. The work of Grebel et al. (1992) was, at the time, a pioneer method able to identify CBe stars using only photometric techniques.

In Fig. 3.5, two photometric diagrams are shown. It is possible to see intense Hα emitters in the color-color diagram (H$\alpha - y$, $b - y$), as Hα emitting stars are separated from the main sequence diagonal. This is also the first work to show that Hα does not need an absolute calibration, but a relative calibration is still required (one still needs to obtain the instrumental magnitude and add a zero point to it before comparing with another filter); this will be later discussed again when discussing Keller et al. (1999).

Soon after the work of Grebel et al. (1992), NGC 330 was observed (together with three other Magellanic Clouds' clusters) using the broad-band *VRI*[1] filters and a narrow band Hα filter. In Bessell and Wood (1993), it was shown that the photometric identification of CBe stars can also be done by investigating mainly the color index R−Hα. Given our current understanding, it is important to explain that emission star selection via photometry using an Hα filter requires another filter covering the nearby continuum (preferably not containing the Hα line), such as the R filter, allowing for the comparison of mainly the Balmer line with its surrounding continuum.

---

[1] It is unclear from the article whether the set is a Bessell or from Johnsons-Cousins.

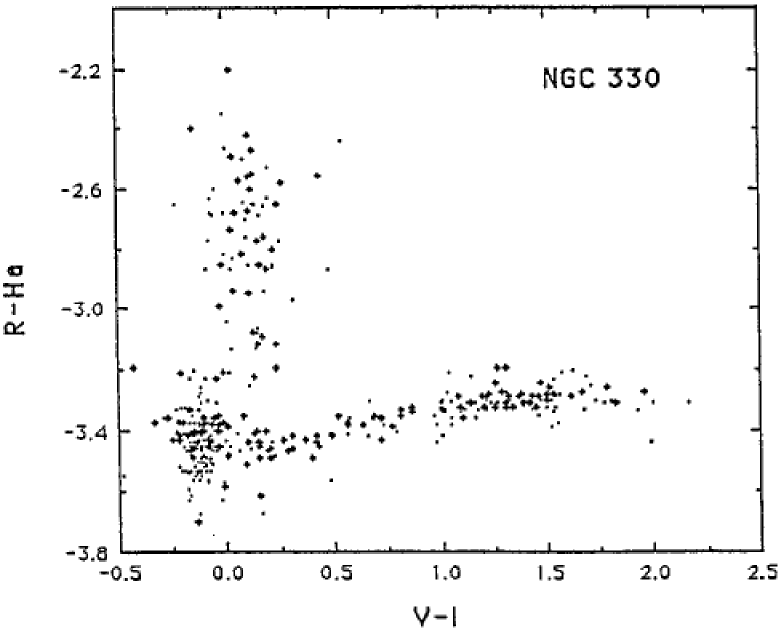

Figure 3.6: (R−Hα, $V-I$) color-color diagram of NGC 330, comprising both cluster and field stars. Stars fainter than $V = 16$mag are indicated by dots. Credit: Bessell and Wood (1993).

Bessell and Wood (1993) noticed that when plotting a color-color diagram of the form (H$\alpha-R$, $V-I$), strong emission stars "stand out very clearly" from the rest of the *normal* MS stars. In Fig. 3.6, it is possible to spot some strong emission stars near R−H$\alpha \approx -2.6$ and $V-I \approx 0.25$.

With another work supporting results in the literature bringing a high fraction of CBe stars in NGC 330, Bessell and Wood (1993) came to an intriguing conclusion, that is discussed until now – *"The higher proportion of Be stars in the SMC cluster NGC 330 presumably reflects the higher rotation of its pre-cluster material"*. This subject warrants significant attention due to its notable implications for the modeling of stellar cluster formation, particularly in relation to the dynamics of angular momentum transfer.

Vallenari et al. (1994) presented new photometric data for NGC 330, extending the completeness of Johnson B and V magnitudes and estimating physical parameters of the cluster. The article focused on finding the structural parameters of the cluster (i.e., its ellipticity, concentration, and the core/tidal radii[2]), but one of the most important contribution, in my personal historical

---

[2] The ellipticity can be defined as $e = 1 - (\mathcal{A}/\mathcal{B})$, with $\mathcal{A}$ and $\mathcal{B}$ being the semi-major and semi-minor axes of the apparent star distribution on the sky. The core radius mentioned here represents the distance which the surface brightness falls to half (some authors acknowledge it as *effective radius*, keeping the core radius as the distance where density is approximately constant). The tidal radius definition used in Vallenari et al. (1994) is the same as of King (1966) – the radius at which the stellar density drops. The concentration parameter is defined as $c = \log(r_c/r_t)$, with

analysis, was on comparing the calibration with other authors, which included old standard stars still observed on plates, and photographic photometry. As their night was photometric, with a seeing of 1.1" and using a 2.2-m telescope, it was possible to obtain a reliable new photometric dataset and a very detailed color-magnitude diagram, shown in Fig. 3.7.

With many observations of NGC 330 (and other clusters from both Magellanic Clouds), it could be learned that this cluster hosts a significant number of massive stars, helping to constrain theoretical models of single and binary evolution during the MS, rapid rotators (leading to the necessity of developing more realistic models), and a number of red and blue supergiants. However, Grebel et al. (1996) realized that some stars of NGC 330 were above the MSTO point, estimated via isochrone fitting using single star evolutionary tracks from the Geneva group (Schaller et al. 1992, Charbonnel et al. 1993), but below the expected position of blue supergiants. This is an intriguing fact, as these stars could be evolved stars (located at the Hertzsprung gap[3]) or peculiar MS stars, such as blue stragglers – MS objects with a larger luminosity than expected from its age and that are probably a product of a merger between two MS stars.

Grebel et al. (1996) first exclude the possibility of these "blue giants" being contaminating evolved field stars, as they are located near the cluster center and possess radial velocities similar to the other members. The second exclusion is on post-red supergiants, which would show helium enrichment and carbon deficiency – not observed on the blue giants. They also discarded the possibility of Case-B evolution[4], an evolutionary process where a MS star can become a blue supergiant without experiencing the red-supergiant phase; this was mainly due to the difficulty of joining this explanation, based on calculations from Brunish and Truran (1982) with the observed position of the known supergiants, not compatible with Brunish and Truran (1982). Also, in this paper, they highlight the difficulty of modeling the stars of NGC 330 with the available models of that epoch.

After all possibilities focused on evolved stars were excluded, Grebel et al. (1996) argued in favor of a mix of hypothesis to explain the existence of stars past the MSTO point. First,

---

r_c and r_t being the recently mentioned core and tidal radius, respectively.

[3] The Hertzsprung gap is an area of the HR diagram containing few or no stars. Stars located in the gap are recently evolved, experiencing envelope expansion. The main reason behind the lack of many objects in it is due to the timescale of thousand years, which is negligible next to the nuclear timescale (Hoyle, 1960).

[4] The Case-B mass transfer refers to systems with orbital periods between a few days and $\sim$ 100 days, in which the donor star fills its Roche lobe during the rapid expansion to a red giant with a He core, and the transfer stops after He ignition (Soberman et al., 1997).

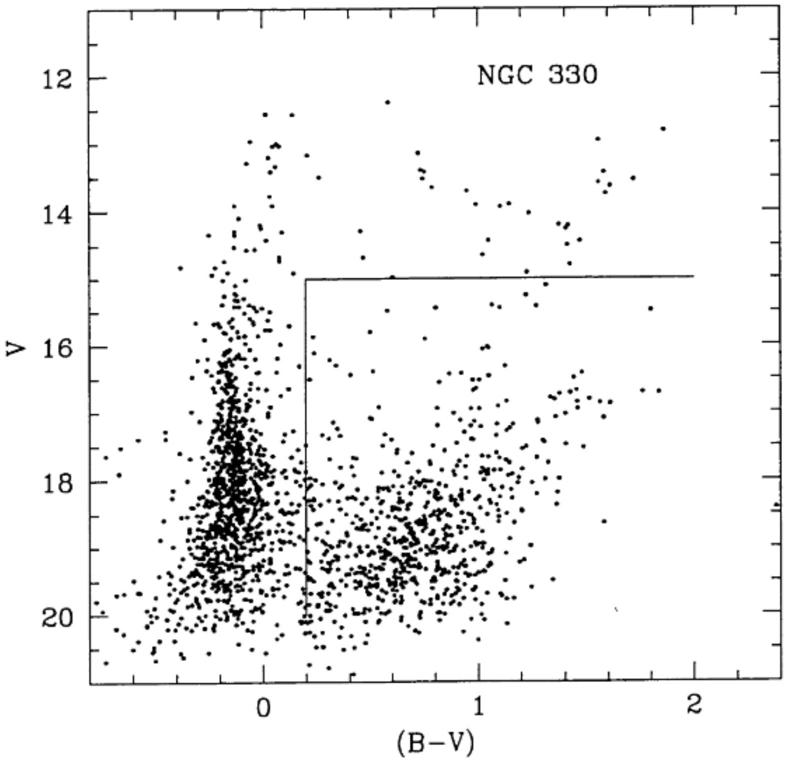

Figure 3.7: (V, $B-V$) color-magnitude diagram of NGC 330, comprising cluster and field stars. The most likely field stars are indicated inside the box at the right. Credit: Vallenari et al. (1994).

when considering fast rotation, the position of most blue giants without strong Balmer emission could to be explained by pole-on rapid rotators, which are probable CBe stars, as previous works revealed a high content of CBe stars in this cluster. However, this cannot be the unique solution, as all blue giants would have to be pole-on CBe stars, implying an extremely small probability.

The second solution is to consider the previously defined blue stragglers. Even though some blue stragglers can be indeed result of delayed formation, Grebel et al. (1996) suggested that that was not the case for NGC 330, as delayed formation results (considering single stars) in objects appearing as earlier spectral types than the earliest types of the cluster, and in NGC 330 this would imply in blue stragglers being O-type stars, which was not observed in Grebel et al. (1996). Considering the large binarity incidence in massive stars, they are better explained due to binary interactions (Stryker, 1993). Blue stragglers can be seen in ordinary photometric diagrams as either single objects, a binary system containing a stripped secondary (e.g., a helium star) or a degenerate product (such as a white dwarf or neutron star). Many blue stragglers (the primary stars) become rapid rotators due to angular momentum transfer, are capable of showing the Be phenomenon and become apparent rejuvenated stars. This is strongly supported in the current literature by direct spectroscopic observations of sub-dwarf O (sdO) and sub-dwarf B

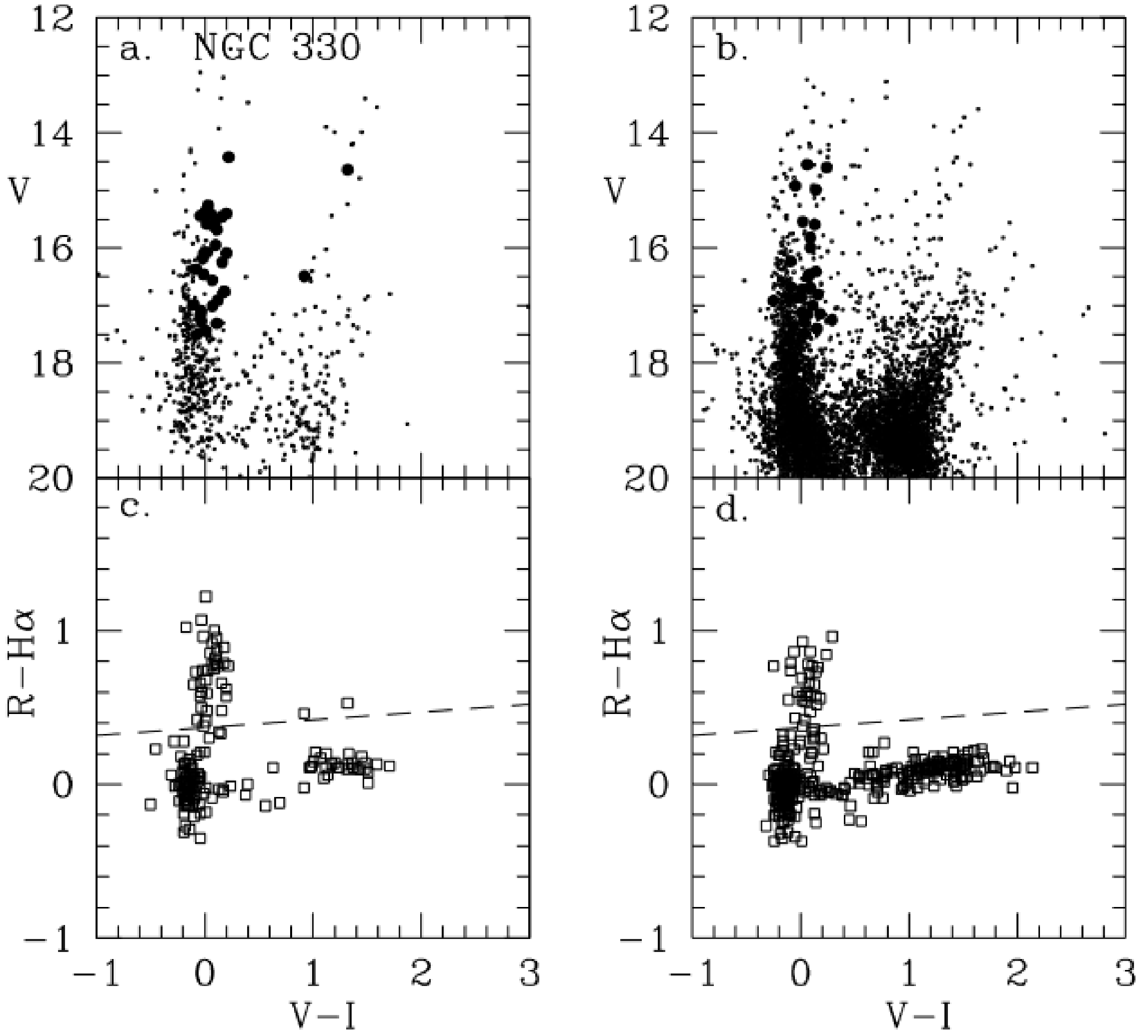

Figure 3.8: (V, $V-I$) and (R−Hα, $V-I$) diagrams for NGC 330. On the left, panels **a** and **c** show the cluster center ($15'' < r < 1'.6$). On the right, the surrounding field is shown. CBe stars are identified as the stars above the dashed line in the (R−Hα, $V-I$) diagram and shown as filled circles in (V, $V-I$). Credit: Keller et al. (1999).

(sdB) companions to CBe stars (Wang et al. 2018; Klement et al. 2022).

In Keller et al. (1999), the photometric method of using *VRI* plus Hα magnitudes to detect CBe candidates was applied for six clusters, with two located in the SMC and four in the LMC. The authors consolidated the results found in Bessell and Wood (1993) as follows: *"Be stars are redder in $V-I$ than normal main-sequence stars of similar magnitude and the redness increases with increasing Hα emission strength"*. The significance of this statement lies in the limitation of using spectroscopy to directly identify CBe stars within dense environments.

One of this method's strength is that R and Hα don't need to be absolute calibrated. For example, Keller et al. (1999) chose an arbitrary zero-point based on the position of normal MS stars, forcing them to have R−H$\alpha \approx 0$. They found that most of the identified dispersion in the

$R-\mathrm{H}\alpha$ color is due to photometric errors; in this case, a deeper survey would minimize this effect. The main limitation of this method is that separation is based on a color selection criteria – CBe stars were selected above an arbitrary line on the ($R-\mathrm{H}\alpha$, $V - I$) diagram, which can miss weak Hα emitters.

Keller and Bessell (1998) conducted a medium resolution spectroscopic follow-up of previously identified CBe stars by Keller et al. (1999) and Mazzali et al. (1996). The paper focuses on the confirmation (or not) of CBe stars and their observed rotational velocities distribution found by Mazzali et al. (1996). Even with a 2.3-m telescope, Keller and Bessell (1998) noticed that caution is needed when observing/analyzing NGC 330. First of all, to find an accurate $v\ \sin i$ value for CBe stars from an atmospheric profile fit, the observational data was fit blueward of Hβ from the Kurucz (1993) non-rotating stars library and then rotationally broadened until Hγ, Hδ and Hϵ were matched, producing a mean $v\ \sin i$. Also, in this part, some intense emitters with emission in Hγ and Hδ had to be fit ignoring the line center.

Second, being a dense field (mostly near the center), surrounding stars "act to dilute the Hα equivalent width", as the continuum flux is raised without generally increasing the Hα contribution. To deal with this, no stellar source with $r < 25''$ were observed, as they would not be able to resolve them. Last, but not least, NGC 330 is located to the SE in the direction of a diffuse HII emission (see Fig. 3.1), forcing data reduction to be made with caution as sky background subtraction might not be easy.

The paper concludes with two significant findings, as outlined below along with their contextualized transcriptions:

1. "*Within our sample, two stars, B13 and B29, show emission spectroscopically but are not flagged as Be within Paper 1. The ability of our photometric survey technique to discern Be stars relies upon the [R-Hα] color of the emission line objects being significantly different to those of the majority of non-emission objects. Photometric errors give the non-emission stars a certain dispersion in the [R-Hα] index. This presents a limit to the equivalent width discernable within our survey. [...] Three stars from the spectroscopy of Grebel et al. (1996) show emission undetectable to the photometric survey technique (A4, B24 and B33). [...] We conclude that there does not appear to be a large population of Be stars with emission levels below that detectable in Paper 1.*"

2. "*Our results (...) span a large range of W(α) and* $v\ \sin i$ *and in contrast to Mazzali et al.*

> *(1996) (their Fig. 7) show no correlation between* $v \sin i$ *and equivalent width is present. This indicates that we are observing a sample of stars with* $v \sin i$ *and disk size as randomly distributed properties. There is no sign of a preferential alignment of rotational axes nor a dependence of disk size on* v.”

Point 1) above is of relevance for this dissertation. Indeed, in the photometric method, most of CBe stars with emission were detected. However, it was still unknown how many *inactive* CBe stars are present in the cluster and if it was possible for a CBe system to host an undetectable disk in both photometry and Hα spectroscopy.

In 2), more important than correcting Mazzali et al.'s analysis, they brought back the information that the high proportion of observed CBe stars in NGC 330 is not due to a preferential pole-on alignment of the rotational axes. This was further confirmed in Hummel et al. (1999) and Hummel et al. (2001).

A very interesting work on the Be variability was published in 2002, focusing on SMC stars (Baade et al., 2002). The foundation of this article was on the finding that stellar pulsation, specifically non-radial pulsations (NRPs), could be linked to mass loss processes (Abbott et al., 1986). In Rivinius et al. (1998) for example, the authors found for the galactic CBe star μ Cen, from a significant amount of data (a total of 409 high resolution spectra taken between 1992 and 1997), two characteristic groups of periods close to 0.28 and 0.505 days, associated with radial velocities periodicity. The period group at 0.505 d showed constructive interference before line emission outbursts, which themselves indicate on-going mass transfer process. This settled for the first time that NRP could act as a trigger of the Be phenomenon (this, nowadays, is a better understood mechanism; for more details, see Labadie-Bartz et al. 2022).

Baade et al. (2002), however, did not find this low-order line profile variability signature due to NRPs in SMC stars, which raised new questions. If there were no observational issue, some possibilities for this finding are: NRPs, in some way, would not be related to the Be phenomenon and would appear as a coincidental effect; metallicity difference between SMC and Galactic stars are so extreme that pulsation would occur in a different way, and would not be a necessary ingredient for the mass ejection.

However, two significant conclusions were established for the first time regarding NRPs in CBe stars within two distinct environments, once again emphasizing the role of NGC 330 as a platform for advancing our understanding of the Be phenomenon:

- "*A possible absence of line profile variability in Be stars in the SMC would have no implications whatsoever for the interpretation of the line profile variability in Galactic Be stars*"
- "*While there are stars, in which photometric variability has not, or only hardly, been detected although the line profile variability is quite significant, the opposite does not seem to have been observed so far. Non contemporaneous photometry and spectroscopy often suggest even different periods. Accordingly, the unexpected result would not be the lack of agreement between photometry and spectroscopy but the absence of spectroscopic variability.*"

In Martayan et al. (2006) and Martayan et al. (2007), the authors found correlation between the fraction of CBe stars (field and cluster) with metallicity, indicating that the percentage of CBe stars increases when metallicity decreases, which is the opposite of the previous results of Keller et al. (1999). However, an important thing is highlighted in the discussion section, which is that the observations of Martayan et al. (2007) are from a single epoch survey. This shows how difficult it is to compare Be proportions in different galaxies, as the Be phenomenon presents long term variability. The correlation found is within theoretical predictions that in low metallicity environments stellar rotation is enhanced. The other important finding in Martayan et al. (2007) was that SMC stars indeed are pulsators, found by analyzing MACHO light curves, which confirmed multi-periodicity in 9 SMC CBe stars. Their periods fall in the expected range of slow pulsating B-type stars, corresponding to $\approx$ 0.40 to 1.60 days. This went against Baade et al. (2002), showing that for low metallicity environments, photometry was probably better suited for analyzing Be short-term variability.

Still on this matter, Schmidtke et al. (2008) studied a sample of 150 hot stars from NGC 330 to characterize *BVI* variability using OGLE II data. The results in general indicate that more than 50 stars were variable, with $\approx$ 75% being clearly periodic, and most of the periodic stars showed NRPs. Although not focusing on the Be phenomenon, $\approx$ 30% of the CBe stars of the sample exhibited NRPs. Another striking outcome was that 2/3 of stars showing moderate or strong NRPs[5] were CBe stars. It is important to notice that most CBe stars of the sample were early-type B stars, which can also result in an observational bias.

Further findings using NGC 330 stars were published in 2013 by Tanabé et al. (2013). Using

---

[5] This is a qualitative analysis made by the authors. For more details, see Schmidtke et al. (2008).

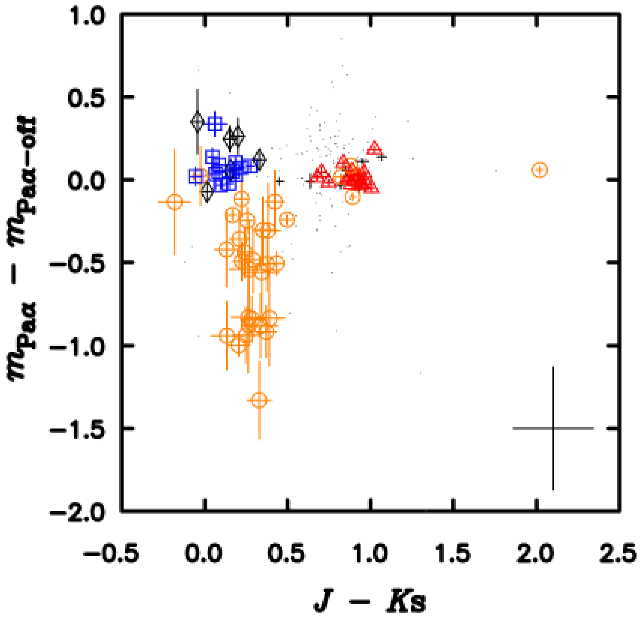

Figure 3.9: (Pa α index, $J - K$) color-color diagram towards NGC 330. Open orange circles show known emission-line stars, open blue squares and open black diamonds represent luminosity class I and less luminous O, B and A stars respectively, and open red triangles indicate red supergiants. Credit: Tanabé et al. (2013).

data from a 1-m telescope located in Chile, at an altitude of more than 5000 meters, Tanabé et al. (2013) were capable of consistently detecting for the first time Paschen series emission in known CBe stars, avoiding the strong telluric lines appearing in that spectral region. The authors observed NGC 330 in the near-infrared *JHK* filters and in two narrow-band filters near Paschen α (hereafter Pa α; $\lambda = 1.875\,\mu$m) — one being a very narrow ($\Delta\lambda = 0.0079\,\mu$m) centered exactly on the transition wavelength, and the other a wider and off-centered filter ($\lambda_c = 1.910\,\mu$m; $\Delta\lambda = 0.033\,\mu$m). Pa α emission detection was made using two photometric colors, namely the narrow bands difference $m_{\mathrm{Pa}\,\alpha} - m_{\mathrm{Pa}\,\alpha,\mathrm{off}}$ (dubbed Pa α index) and $m_{\mathrm{Pa}\,\alpha} - K$. In Fig. 3.9, it is possible to see the photometric separation between normal stars and the previously known CBe objects.

In 2013, an extension of the previous work of Keller et al. (1999) was published. Iqbal and Keller (2013) made a photometric survey of 11 and 14 young clusters in the LMC and SMC, respectively, searching for CBe stars. The idea behind the paper was to examine the effects of both metallicity and age on the Be phenomenon, so that CBe star formation channels could be probed and better understood.

The method behind CBe star classification was still using ($R-\mathrm{H}\alpha$, $V-I$) color-color diagrams, where R is the magnitude in the Cousins R band, and VI are Bessell magnitudes calibrated using

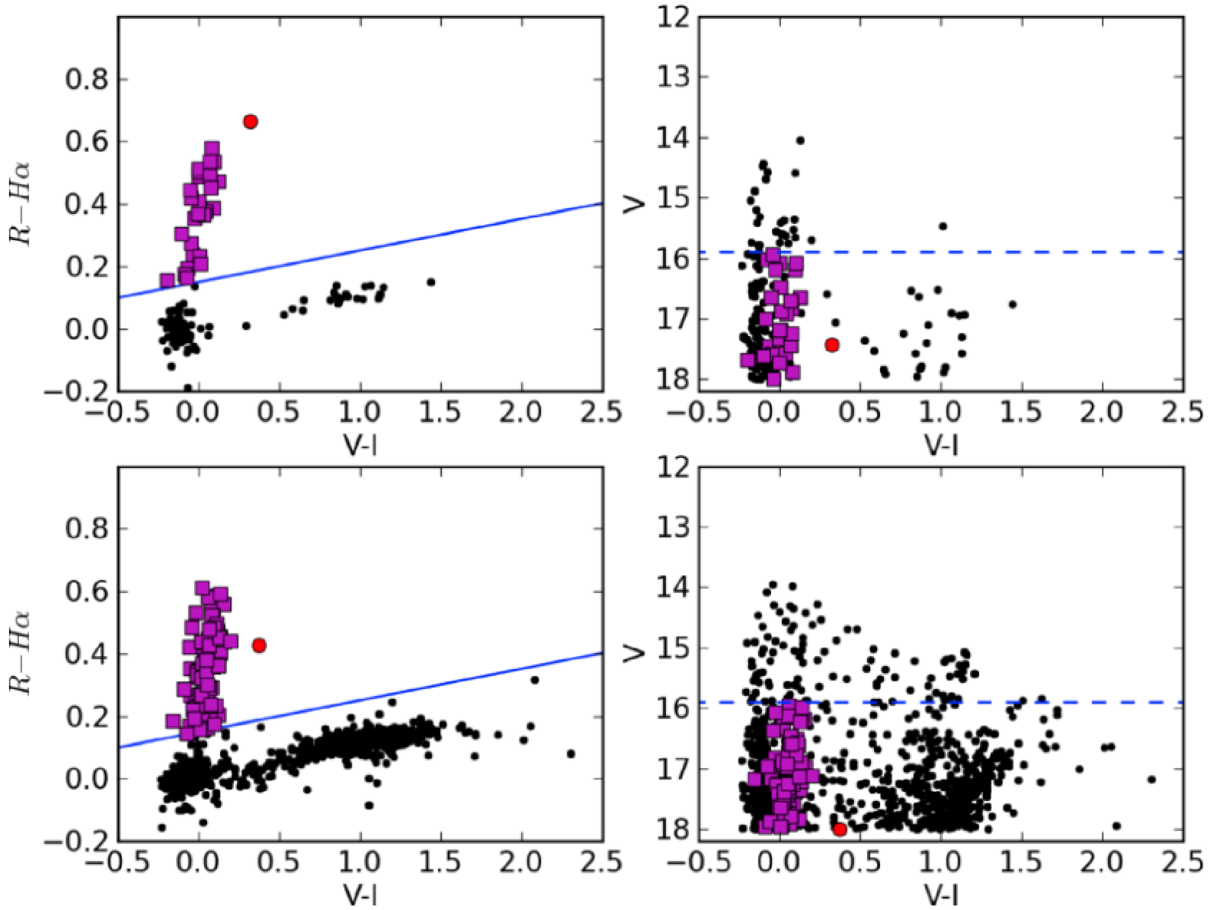

Figure 3.10: (R−Hα, $V-I$) and (V, $V-I$) color-color and color-magnitude diagrams of NGC 330. At the top panel, probable members are exhibited. At the bottom panel, the surrounding field is shown. CBe stars are identified as the ones above the solid blue line in the color-color diagram, and as purple squares in all photometric diagrams. The dashed line represents the predicted MSTO point established by the authors. The red circles indicate a cooler object presenting prominent Hα emission. Credit: Iqbal and Keller (2013).

the Magellanic Clouds Photometric Catalog (MCPC – see Zaritsky et al. 2002) from instrumental g and i magnitudes, and Hα magnitudes obtained through a narrow band filter centered at the transition wavelength with $\Delta\lambda = 300$Å. As in Keller et al. (1999), neither R nor Hα magnitudes are calibrated, but the authors set an arbitrary zero point for the R−Hα color index such that MS stars will have R−Hα = 0 for every observed cluster. Figure 3.10 shows the newer results for NGC 330, that display the same pattern found in Keller et al. (1999).

From Iqbal and Keller (2013), two main findings can be outlined:

- Some previously identified CBe stars by Keller et al. (1999) did not show strong enough emission to be separated from the MS strip in the color-color diagram. This is in agreement with the known long-term variability of CBe stars, and in a time difference of nearly a decade, it is plausible to assume that some stars may have dissipated their disks.

- In every diagram, CBe stars were located in a redder sequence in comparison with the typical MS from normal stars. This can be explained by typically three mixed scenarios, which are rapid rotation, unresolved binaries, and circumstellar disks. Some CBe stars may be associated with two or even all three scenarios. As noted by Haubois et al. (2012) and further developed by Vieira et al. (2017), reddening due to CBe disks can be generally treated by the sum of the central star and a pseudo-photosphere, with its effective size being wavelength dependent. A general trend is that CBe stars will appear redder in the $V - I$ color as they are always rapid rotators, and in a given population, it is plausible that a fraction of them will be active.

In their conclusions, Iqbal and Keller (2013) come to an overall agreement with what was being outlined in the literature, such as the metallicity dependence of the Be phenomenon, the CBe star fraction reaching its highest value near the MSTO point, and YOCs will inevitably possess a larger fraction of CBe stars, as the most massive B-type and early O-type stars are still in the main sequence.

Moving to a recent paper with NGC 330 as its main object of study, Bodensteiner et al. (2020) was able of resolving the dense cluster core using a 8.2-m unit telescope of VLT[6] supported by adaptive optics, which gave them an angular resolution between 0.4” and 0.7”. They observed NGC 330 using MUSE, an integral-field spectrograph, composed of 24 individual spectrographs. The MUSE data allowed for the stellar classification of 278 stars, despite the $V = 18.5$ mag limitation of the observations.

The majority of the MS observed sources are B-type stars (249 objects), with only 2 O-type stars. For the evolved objects, 11 red supergiants were identified (most were already known in the literature, but with differences in the spectral type) and 6 A-type supergiants (blue supergiants) were classified. From the MS stars, 80 are CBe stars and 2 were classified as Oe/B0e stars, leading to a lower CBe star fraction value of 32 ± 3%, which is a more reliable estimate than previous works because it focuses entirely on stellar content of NGC 330 core and present a significant amount of stars with good signal to noise ratio. This work shows how spectroscopy is a better technique in Be classification, when there is possibility of doing it with a large telescope, adaptive optics and with an instrument such as an integral-field spectrograph.

The already known blue stragglers present in NGC 330 were also detected, with optical magnitude brighter than the expected for stars at the MSTO point but without showing spectral

---

[6] For more details, see `www.eso.org/public/teles-instr/paranal-observatory/vlt/`.

characteristics of an evolved object. The authors estimated the age of the cluster as about 35-45 Myrs, and also confirmed previous reports on the existence of multiple sequences in YOCs, but with the explanation that the red MS appearing in a given coeval population is most likely due to CBe stars, which themselves are related to IR excess, rapid rotation and also members of binary systems in some cases.

Following the efforts of understanding the stellar content of NGC 330, Patrick et al. (2020) analyzed 15 red supergiants (RSG) in the cluster using multi-epoch HARPS and MUSE spectra in the search of binaries and to study the multiplicity in evolved RSGs. Using radial velocity variability between epochs, they were able to estimate a RSG binary fraction of 0.3 ± 0.1, and to derive luminosities of the RSG population in order to find the cluster age using a luminosity-age diagram, leading to an age of 45 ± 5 Myrs. This is an important finding, as previous works that did not focus just on evolved stars provide similar estimates

Also, Patrick et al. (2020) came into a conclusion that the luminosity spread (which leads to an age span from 15 to 50 Myr) is a strong indicator of *post-interaction binary products*. They mainly argued that the relative luminosity range of a single RSG in a coeval cluster is $\approx 5\%$, and all RSGs with high luminosities, with $\log{(L/\mathrm{L}_{\odot})} > 4.2$, were red stragglers.

In the next section, I will discuss new observations of NGC 330 made with SOAR, with data reduction, calibration and analysis being done by our research group and collaborators

3.2 *SAMI photometry of NGC* 330

The YOC NGC 330 was observed on January 5th, 2019[7], at the 4.1-m SOAR telescope in Chile, using the broad-band *BVRI* (Kron-Cousins) filters and a narrow band Hα filter. The SAM imager (hereafter SAMI) was used in conjunction with the SOAR Adaptive Module (for a detailed description of the adaptive optics of SAM, see Tokovinin et al. 2016). The SAMI detector comprises a CCD array with dimensions of 4096×4112 pixels, featuring a pixel scale of 45.5 mas, resulting in a square field-of-view of approximately $3'.1 \times 3'.1$. Also, the observation was conducted in a 2×2 binned mode, yielding a final pixel scale of 91 mas.

For the broad-band *BVRI* images, individual long-exposure frames were acquired using a three-point dither pattern, with each point separated by 15" in the E–W direction. The exposure

---

[7] Our research group had raw data of three SMC clusters (NGC 330, NGC 1847, NGC 1850). Besides NGC 330, the other observations were also reduced, but not yet calibrated and analyzed.

Table 3.1 - Log of the SAMI observations for NGC 330, made in January 5th, 2019.

Filter	MJD	N_{exp}	Exp. Time (sec)	Airmass	Seeing (”)
B	58488.05261	3	60	1.47	0.54
B	58488.05462	2	5	1.47	0.53
V	58488.04946	3	60	1.46	0.50
V	58488.04823	2	5	1.46	0.47
R	58488.05661	3	60	1.47	0.55
R	58488.05536	2	5	1.47	0.51
I	58488.05968	3	60	1.48	0.49
I	58488.06229	2	5	1.49	0.50
Hα	58488.0665	3	240	1.50	0.54
Hα	58488.06316	2	5	1.49	0.59

time for each frame was 60 s, resulting in a total of 180 s per filter. As for the Hα band, three individual exposures of 240 s were obtained, summing up to 720 s or 12 minutes of total exposure time. In addition, to prevent saturation of the brightest stars, short exposures (exposure times of 5 s per frame) were captured for all filters using a two-point dither pattern, with each point separated by 15” in the East–West direction. A summary of the SAMI observations of NGC 330 is summarized in Tab. 3.1.

The acquired data underwent processing using the SAMI PyRAF-based PySOAR pipeline[8]. In the pipeline, a master bias and master flat-field templates for each filter are generated, and after that, the raw images can be corrected for overscan, bias-subtracted, and flat-fielded.

Table 3.2 - Parameters of the PSF model for SAMI observations and the peak and maximum magnitude for each filter. N_* corresponds to the number of sources detected above a 1-σ limit in the short and long exposure frames. σ corresponds to the range of magnitude uncertainties for each filter.

Filter	FWHM (”)	N_* (short)	N_* (long)	1-σ (ADU)	m_{peak} (mag)	m_{max} (mag)	σ (mag)
B	0.40	1262	4820	1.86	21.5	22.5	0.06-0.14
V	0.38	2101	7057	2.19	21.8	23.3	0.03-0.18
R	0.35	3255	9464	3.40	22.2	24.2	0.03-0.30
Ha	0.33	424	5715	2.05	22.0	23.6	0.09-0.21
I	0.31	1840	7876	3.58	21.6	22.9	0.04-0.26

Stellar photometry was conducted using an automated point spread function fitting procedure

---

[8] `https://noirlab.edu/science/programs/ctio/instruments/sam/user-guides/`.

based on the StarFinder algorithm (Diolaiti et al., 2000). The construction of the PSF for each *BVRI*+Hα image relied on relatively isolated and bright sources. A summary of the full width at half maximum (FWHM) values for the PSF in each filter is provided in Tab. 3.2. The table highlights the exceptional performance of the Laser Guide Star (LGS) system, achieving remarkable angular resolutions as sharp as 0".33 in the Hα filter. The great resolving power of the adaptive optics of SAMI/SOAR can be seen in Fig. 3.11, where the faintest background objects and sources from the stellar cluster cannot be observed or resolved in SkyMapper, while possible with SAMI.

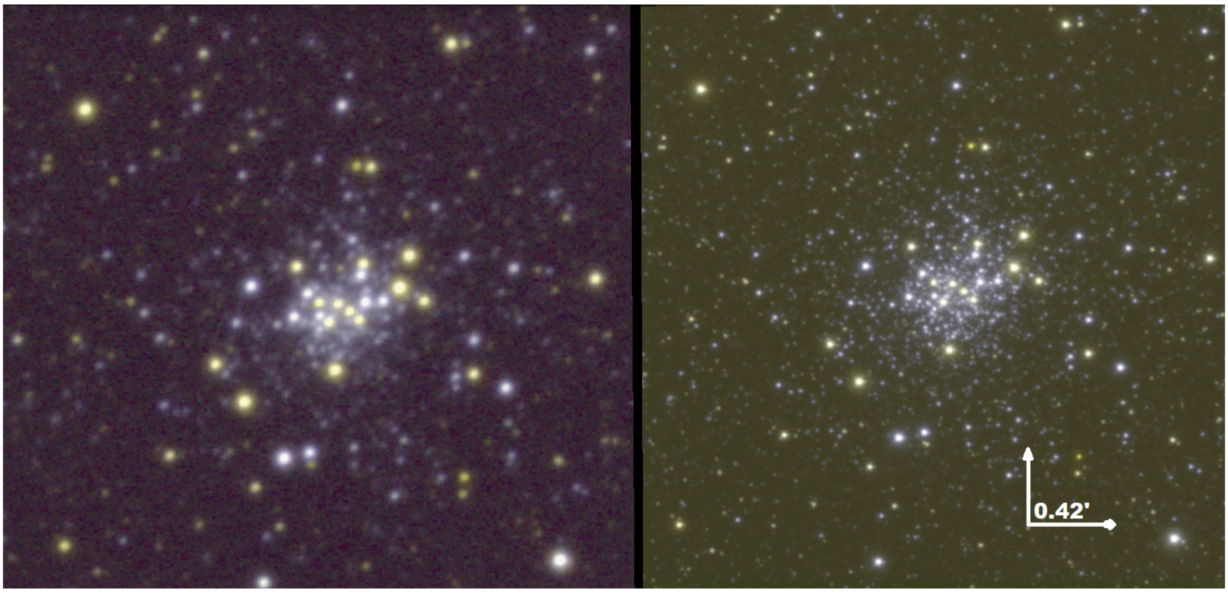

Figure 3.11: Comparison of NGC 330 observations from SkyMapper (left panel) and SAMI (right panel). Colors are not true, but a composition of each RGB channel using the existent filters from each system.

3.2.1 *Photometric calibration*

In order to calibrate the reduced data, a photometric pipeline named *stellar template fitting*, based on the calibration method used for S-PLUS DR2 (Almeida-Fernandes et al., 2022), was implemented for the SAMI *BVRI*+Hα observations. The pipeline consists of using an external catalog (hereafter, EC) with the final objective of calibrating our data in the same photometric system as the one existent in the EC. In this method, synthetic atmospheric models are used to connect the EC photometric system to our observations, as the reduced instrumental magnitudes share a common non-physical zero point.

The synthetic spectral library was provided by Coelho (2014), which offers SEDs of stellar atmospheric models spanning the wavelength range from 0.13 to 10 μm. The low resolution grid of the library has a resolution of $\Delta \log \lambda = 8 \times 10^{-4}$ and covers a wide range of stellar parameters. It includes effective temperatures ($T_{\rm eff}$) ranging from 3000 to 25000 K, surface gravity ($\log g$) from -0.5 to $+5.5$ (in increments of 0.5 dex) and metallicity from $Z = 0.0017$ to 0.049. The library encompasses 12 customized chemical mixtures, providing extensive options for stellar model analysis (for further details, refer to Tab. 1 in Coelho 2014).

For the EC, we adopted SkyMapper DR1.1 (Wolf et al., 2018), which offers a good photometric coverage of the southern hemisphere in the *uvgriz* system (similar to SDSS, but with two intersecting ultraviolet filters instead of the SDSS-like *u* band), including the Magellanic Clouds. It also provides well-defined transmission curves for all filters in the Spanish Virtual Observatory's Filter Profile Service[9], covering a broader spectral range compared to our observations. Using the template fitting method, the photometric system becomes equivalent as of the EC — in our case, the SAMI magnitudes become calibrated in the AB magnitude system[10].

The calibration happens according to the following steps:

1. The first step consists of making a crossmatch of stellar sources present in SAMI observations and in the EC. In this part, only sources with observed magnitudes in every filter (of both sets) are chosen to begin the calibration process. For the crossmatch, a maximum threshold radius of 0".30 was defined[11] between the SAMI and SkyMapper sky coordinates. This crossmatching process resulted in a total of 204 common sources found in both catalogs. Among these sources, 82 exhibited magnitudes detected in all six *uvgriz* filters.

2. The second procedure involves the creation of a synthetic magnitude library. Each spectrum of the atmospheric library was reddened following the Cardelli et al. (1989) extinction law with a fixed value of $R_V = 3.1$, and assuming $E(B-V)$ values ranging from 0 to 1, in 22 custom steps with spacing rising towards larger values. Then, the reddened spectra were convolved with the transmission curve of the filters of both the SkyMapper and the SAMI filters' transmission curves, generating an array of 11 magnitudes (*BVRI*+Hα + *uvgriz*) for each synthetic reddened spectrum.

---

[9] See `http://svo2.cab.inta-csic.es/theory/fps/` for more information.

[10] The AB magnitude system follows the definition $m_{\rm AB} = -2.5 \log_{10} f_\nu - 48.60$, with f_ν being the spectral flux density in cgs units (erg s^{-1} Hz^{-1} cm^{-2}). It represents an absolute calibration method, with a fixed zero point (Oke and Gunn, 1983).

[11] This threshold value was chosen by comparing the number obtained of common sources for a wide range of arcseconds. For radii > 0".30, the number of sources become unchanged, as the best solution was found for every SkyMapper source with non-zero magnitudes on every filter of the *uvgriz* set.

3. A loop is created for every star present in the crossmatch, in which a combination of observed colors from SkyMapper's magnitudes are compared to the corresponding colors for each atmospheric model existent in the synthetic magnitude library. The best-fitted model is the one that minimizes

$$\chi^2 = \sum_{\mathrm{i=1}}^{N} \left(\frac{\mathrm{C_{i,model}} - \mathrm{C_{i,ext}}}{\mathrm{e_{C_i}}} \right)^2 , \tag{3.1}$$

   where C_i is the i-th color, $\mathrm{e_{C_i}} = \left(\mathrm{e^2_{C_{i,model}}} + \mathrm{e^2_{C_{i,ext}}}\right)^{1/2}$ is the uncertainty of the color index, N are the number of combinations, and 'model' together with 'ext' refer to the synthetic model and the EC, respectively.

4. With the representative atmospheric model (indicated next with the subscript 'best model') at hand, the differences between the atmospheric model magnitudes and the corresponding ones from SkyMapper were evaluated as:

$$\Delta m_i = m_{i,\mathrm{ext}} - m_{i,\mathrm{best\,model}} \ \text{ for } i \in uvgriz. \tag{3.2}$$

   A mean quantity μ_Δ, dubbed mean photometric offset, and its error σ_{μ_Δ}, were calculated based on the mean and the standard deviation of all Δm_i values for $i \in uvgriz$.

5. Then, $BVRI$+Hα magnitudes are predicted by adding the recently found difference with the best atmospheric model $BVRI$+Hα magnitudes following

$$m_{i,\mathrm{pred}} = m_{i,\mathrm{best\,model}} + \mu_\Delta \ \text{ for } i \in BVRI\text{+H}\alpha \tag{3.3}$$

6. From Eq. 3.3, the residuals between the instrumental (m_{inst}) and the predicted $BVRI$+Hα magnitudes of each sources are used to infer the photometric zero point offset for each filter ($\mathrm{ZP}_{\mathrm{ext},i}$):

$$\mathrm{ZP}_{\mathrm{ext},i} = m_{i,\mathrm{inst}} - m_{i,\mathrm{pred}} \ \text{ for } i \in BVRI\text{+H}\alpha. \tag{3.4}$$

The result of Eq. (3.4) is a distribution of ZP values. A mean zero point for every filter is calculated using an outlier-resistant gaussian fit. With the final ZP available, all stars observed with SAMI have their instrumental magnitudes shifted to the predicted calibrated values by applying

$$\left.\begin{aligned} m_{i,\mathrm{ext}} &= m_{i,\mathrm{inst}} - \mathrm{ZP}_i \\ \sigma_{i,\mathrm{ext}} &= \sqrt{\sigma^2_{i,\mathrm{inst}} + \sigma^2_{\mathrm{ZP}_i}} \end{aligned}\right\} \text{ for } i \in BVRI\text{+H}\alpha. \tag{3.5}$$

Also, for an accurate calibration, the EC should have a spectral coverage similar to or broader than that of the observations, enabling proper prediction of our observed magnitudes. The detailed description of the whole data reduction process and the calibration method is described in Navarete et. al. (2023, submitted.), and attached in App. C. In the next section, the resulting calibrated magnitudes are shown and analyzed.

3.2.2 *Calibrated SAMI magnitudes*

With the calibrated magnitudes at hand, a detailed analysis was performed. For example, it is possible to check the magnitude distribution on each filter, to combine magnitudes and color indices, and even crossmatch the sources with surveys of different nature, such as GAIA, so that better astrometric solutions can be obtained. The approach of this section is to run through the final uncertainties, the photometric completeness of each filter, the plot of four color-magnitude and color-color diagrams and also the search for members using astrometric measurements.

The uncertainties of the calibrated magnitudes range from 0.03 to 0.30 mag for the broad-band *BVRI* filters, and from 0.02 to 0.19 mag for the Hα filter. The distribution of the SAMI photometry per filter is exhibited in Fig. 3.12. The peak magnitude was computed (a proxy for evaluating the photometric completeness limit), and the brightest and faintest source detected for each filter, as reported in Tab. 3.2.

The second panel of Fig. 3.12 shows the magnitude distribution for every band. At the distance of the SMC, all B9.5 or earlier objects are brighter than $V = 20.29$ mag, which is about 2 mag brighter than the completeness limit of our observations ($V_{\mathrm{peak}} = 21.79$ mag), indicating that the adopted instrumental setup is sufficient to identify all O- and B-type stars associated with NGC 330, and a limited fraction of the A-type stars. The range of magnitudes of each filter for all spectral types (ST) are calculated using BeAtlas v2 photospheric models with $Z = 0.002$, for stars critically rotating ($W = 0.99$), and seen pole- or edge-on, and with the same mass-ST relations described in Sect. 2.4. The models fluxes are placed at a representative distance of $d_{\mathrm{SMC}} = 57500$ pc, reddened with $E(B-V) = 0.11$ (Milone et al., 2018), while adopting a fixed $R_V = 3.1$ and the Fitzpatrick and Massa (1999) law, and then convoluted through SAMI *BVRI*+Hα transmission curves.

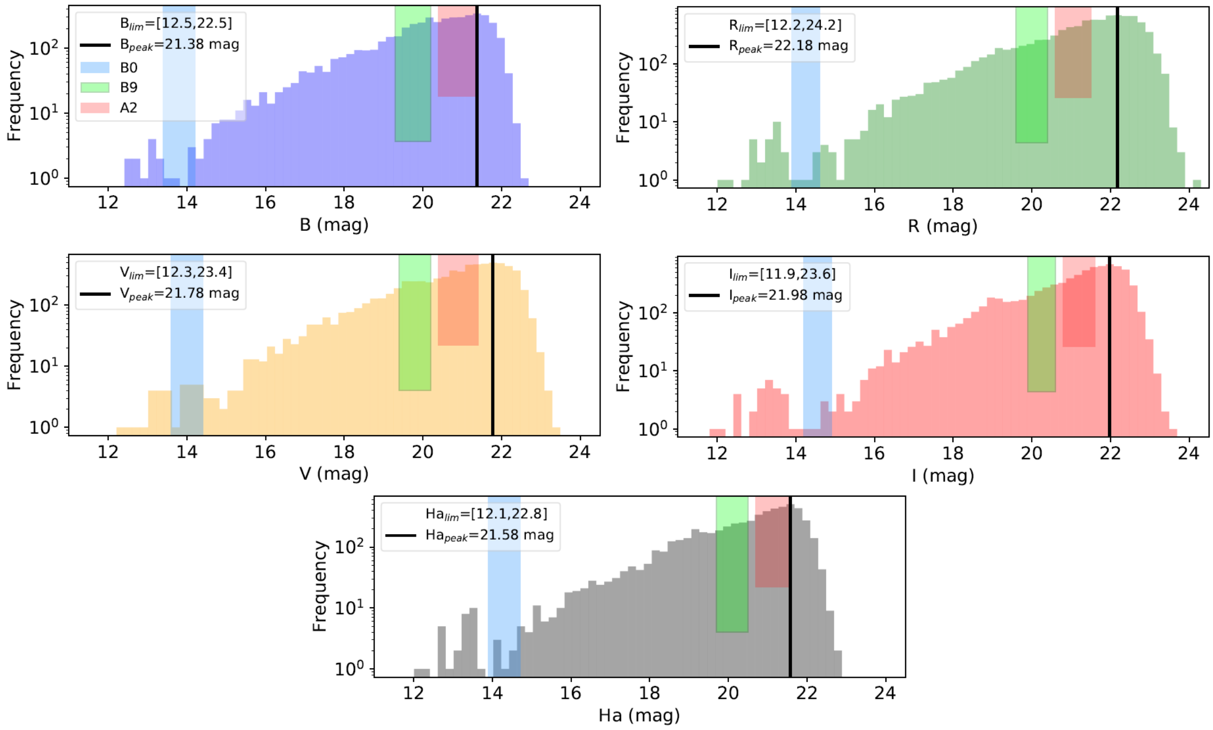

Figure 3.12: Photometric completeness for the *BVRI*+Hα filters of SAMI observations shown in five different histograms, with y-axis representing total counts. Each histogram is sampled with a bin of 0.1 mag, from 11.5 to 24 mag. The thick black solid line indicates the peak of the distribution. The brightest and faintest object detected on each filter are indicated by the min and max values, respectively. The expected magnitude intervals for B0 (blue), B9.5 (green), and A2 stars (orange) are shown for each filter.

In Fig. 3.13, four photometric diagrams are shown: $(V, V-I)$, $(R{-}\mathrm{H}\alpha, V-I)$, $(V-R, B-V)$, $(B{-}I, B{-}R)$, where 4430 sources are plotted as black dots, indicating stellar objects with extracted photometry in all five filters[12]. Following the method of Iqbal and Keller (2013), it is possible to identify the emission stars with a color criterion. All sources with $R{-}\mathrm{H}\alpha > 0.10 * (V-I) + 0.18$ are color-coded.

In order to analyze membership probability of each stellar object from the total of N = 4430 sources, and to compare the SAMI observation with previous works from the literature, a methodology based on the work of Ghosh et al. (2022) was applied. The methodology consists in two clustering selection methods, the machine learning clustering algorithm HDBSCAN (Hierarchical Density-Based Spatial Clustering of Applications with Noise; see McInnes et al. 2017) and Gaussian Mixture Modeling[13] (GMM; see Sect. 16.1 of the third edition of Press

---

[12] The whole SAMI catalog has more than 10 000 valid observations; however, less than half possess magnitudes on every filter.

[13] In this work, the implementation of SCIPY, a Python package, was used. For more details, refer to Virtanen et al. (2020).

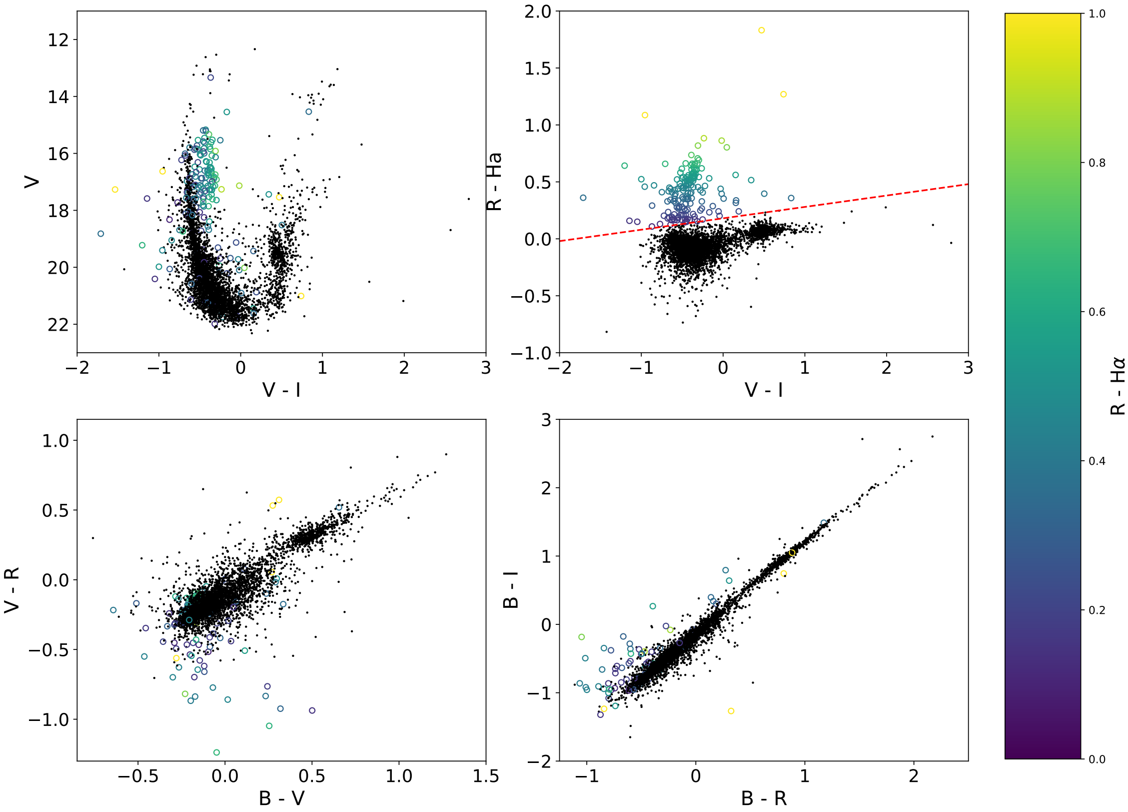

Figure 3.13: Photometric diagrams of NGC 330 SAMI observations of sources detected in every filter, color-coded based on $R - \text{H}\alpha$ for sources obeying the color criterion, shown as a red dashed line, established in Iqbal and Keller (2013).

et al. 1986) to astrometric data from the latest data release from the GAIA mission (DR3; see van Leeuwen et al. 2022). The astrometric parameters necessary to establish membership probabilities are the proper motions in both right ascension (μ_α) and declination (μ_δ), both measured in milliarcseconds per year ($\text{mas}\,\text{yr}^{-1}$) and parallax ($\omega$), measured in milliarcseconds (mas).

First, it was necessary to crossmatch our catalog with GAIA DR3 to obtain the respective astrometric solutions. Using TOPCAT (Taylor, 2011), a cone search (with a radius of 3') around NGC 330 was used to gather GAIA DR3 data, then a pair match based on the sky position (right ascension α and declination δ) of both SAMI and the GAIA DR3 was made, leading to 3107 targets.

Before applying any membership estimate method, it is important to filter the most reliable sources in terms of astrometric precision. This was done by selecting objects with valid observations in all three GAIA photometric bands and with a complete astrometric solution (position, proper motion space and parallax), while filtering sources with $G \leq 20$ (to reduce errors associated with the fainter stars) and RUWE ≤ 1.4, which stands for re-normalized unit weight error, a parameter which indicates how good the astrometric solution is (Lindegren et al., 2021). This final list comprises 867 targets. The methodology steps, after preparing the crossmatched data, are described as follows:

1. First, HDBSCAN is called over the 3D parameter space (μ_α, μ_δ, ω), with each parameter being normalized between 0 and 1, to bring the astrometric set to a same standard scale. The result will consist of a number of small clumps and a large group of stars, with the latter corresponding to be probable members of NGC 330. This first step removes the least probable stars (i.e., likely field stars), with values of (μ_α, μ_δ, ω) being considered outliers. HDBSCAN's selection consisted of 210 potential members.

2. The anticipated members selected by HDBSCAN are used to estimate preliminary mean values of μ_α, μ_δ and ω. The results were the following: $\mu_\alpha = 0.712\,\mathrm{mas\,yr^{-1}}$, $\mu_\delta = -1.276\,\mathrm{mas\,yr^{-1}}$ and $\omega = 0.020\,\mathrm{mas}$.

3. From the mean values of (μ_α, μ_δ, ω) estimated before, an extended list of stellar sources is created based on the following criteria: stars having μ_α or μ_δ between the respective mean $\pm 1.5\,\mathrm{mas\,yr^{-1}}$ and ω between its mean $\pm 0.5\,\mathrm{mas}$. This selection resulted in 847 stars, and will be used for the GMM application.

4. With the extended list in hands, a two-component GMM is called to fit the same parameter space used by HDBSCAN. These two components are related to the cluster members and the field star, each one with its three-dimensional Gaussian distribution.

The SCIPY module allows the probability estimation of each star in both fitted clusters. A total of 272 stars were selected with a confidence of at least 80%, indicating a high probability of indeed being member of NGC 330. Considering 50%, this result rises to 384 stars. The proper motion parameter space (μ_α, μ_δ) and a histogram of the parallax are shown in Fig. 3.14.

The high probability list can be used to finally determine the true mean astrometric solution of the cluster: $\mu_{\alpha,\mathrm{center}} = 0.7102(73)\,\mathrm{mas\,yr^{-1}}$, $\mu_{\delta,\mathrm{center}} = -1.2786(64)\,\mathrm{mas\,yr^{-1}}$, $\omega_{\mathrm{center}} = 0.0129(66)\,\mathrm{mas}$. The errors were evaluated as $\sigma/\sqrt{N}$, with σ representing the standard deviation and $N = 272$ stars (Altman and Bland, 2005). The mean ω roughly translates to a distance of

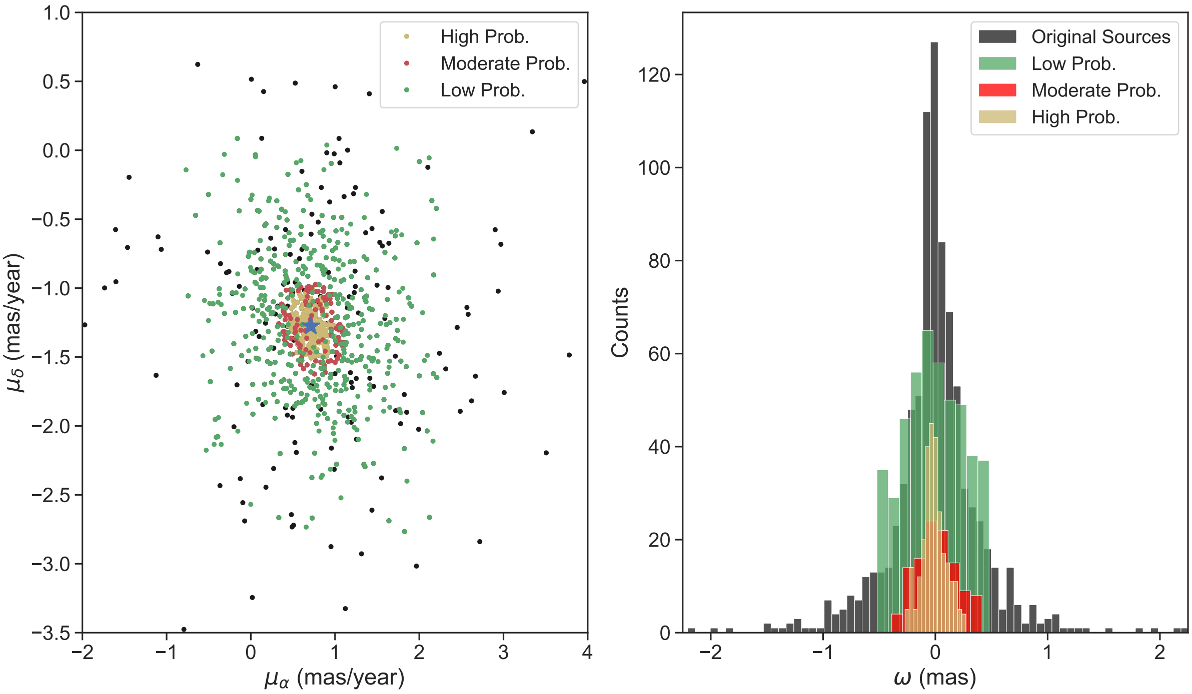

Figure 3.14: Left panel: proper motion space (μ_α, μ_δ). Right panel: parallax distribution, with the y-axis representing total counts of each bin. In black, all sources with good astrometric solutions are shown. In green, red, and yellow, it is shown the low (P < 50%), moderate (50% ≤ P ≤ 80%), and high probability (P > 80%) cluster members.

$d = 77.23$ kpc if it is inverted as $d = 1000/\omega$[14], a value ≈ 24% higher than the recent estimate of $d_{\mathrm{SMC}} = 62.44 \pm 0.47$ kpc using eclipsing binaries (Graczyk et al., 2020). However, this parallax result cannot be taken as a superb estimate, as the SMC is at a limiting distance for the GAIA mission (Vieira et al., 2021), and the uncertainty is way larger than the mean value.

In Fig. 3.15, four photometric diagrams are shown for the high probability members. It is possible to notice that some of the strongest Hα emitters were not probable members, and that the expected shape of the MS and the positions of BSG and RSG were recovered.

When analyzing stars with $V < 20$ mag, it is possible to suppose that:

- In the SAMI observations, the MS is located near $V - I \approx -0.5$ mag, with the Hα emitters being composed of the CBes present in the YOC.
- Stars with $16 \leq V \leq 20$ mag and $V - I \approx 0.5$ mag are most probably evolved stars located at the SMC with close proper motion. Isochrones from the PARSEC non-rotating

---

[14] This method is used as a simple estimate for contextualization. However, it is known that using the invert transformation is not ideal for estimating distances for small parallaxes and/or with errors higher than 20% of ω. For more information, refer to Luri et al. (2018).

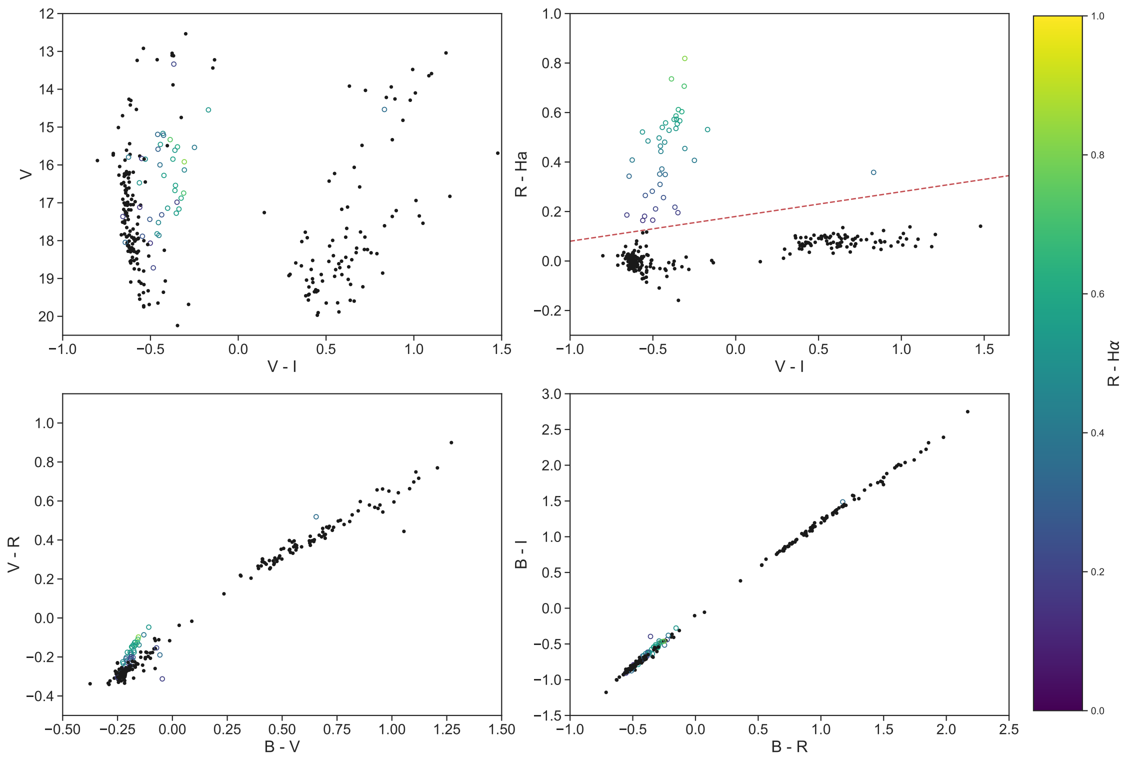

Figure 3.15: Photometric diagrams of NGC 330 SAMI observations of sources detected in every filter with high membership probability. Panels follow the same scheme of Fig. 3.13.

evolutionary models (Bressan et al., 2012) for $t \sim 800$ Myr and $Z = 0.002$ reveal that this position is compatible with red giants.

- As the membership classification does not include targets with $V \gtrapprox 20$ mag, nothing can be said, from this analysis, about the bridge-like structure connecting stars between the MS and the colder region of $V - I \approx 0.5$ mag. It may consist of young objects transitioning to the MS, foreground evolved stars, or a mix of both solutions.

3.3 *S-PLUS photometry of NGC* 330

The Southern Photometric Local Universe Survey is a photometric survey planned to image $\gtrapprox 8000$ squared degrees of the celestial sphere in twelve optical bands using a dedicated 80-cm robotic telescope at the Cerro Tololo Inter-American Observatory, in Chile. One of the primary goals of S-PLUS is to provide accurate photometric redshifts for galaxies to produce a 3D map of the local Universe. In its design, the S-PLUS survey is sliced into five small surveys: the Main Survey (with a high priority in good night conditions), the Ultra-Short Survey, the Variability

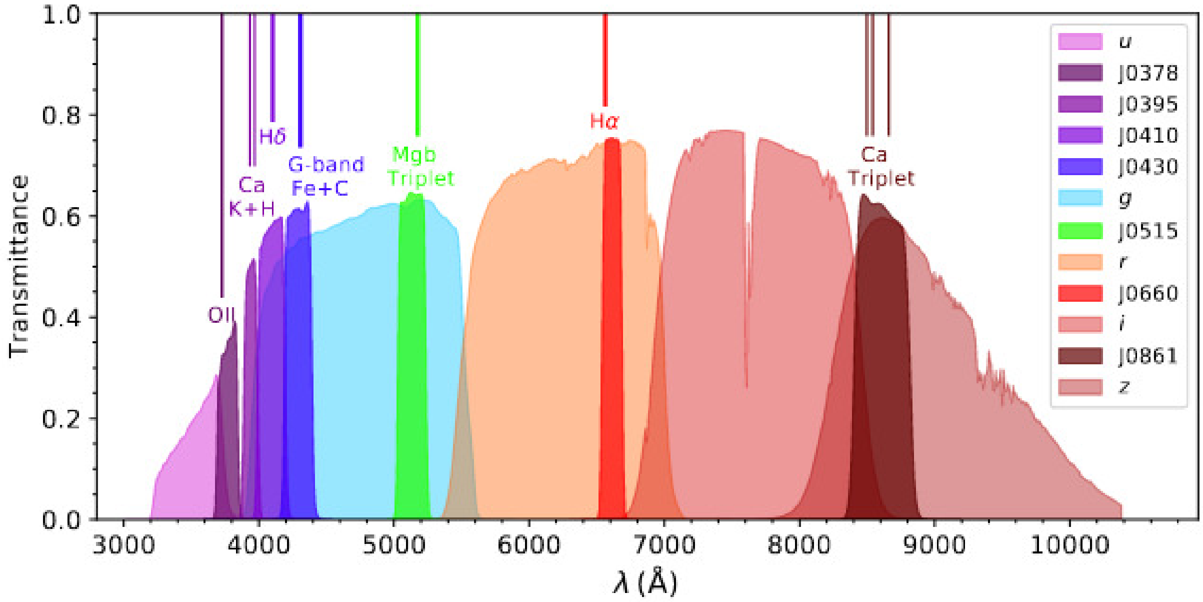

Figure 3.16: The Javalambre 12-filter system shown with the total efficiency (%) versus λ (Å). Figure extracted from Almeida-Fernandes et al. (2022).

Fields, the Galactic Survey, and the Marble Field survey (Mendes de Oliveira et al., 2019).

The filter system used in S-PLUS is the Javalambre 12-filter system, consisting of both broad-band and narrow-band filters, as shown in Fig. 3.16. This filter set is particularly well suited for this work, because the broad-band transmission curves allow probing the shape of the SED in detail, including the Balmer and Paschen discontinuities, and one of the narrow band filters is centered on Hα, important for unveiling disk emission from CBes. Besides that, the broad filters are the *ugriz* set, similar to the one used by SDSS[15] (Fukugita et al., 1996).

Data releases (DR) from S-PLUS are yearly provided to the astronomical community, with a total of six planned releases. The first three releases (DR1, DR2 and DR3) are fully available for the general public. However, data used in this work is from the internal fourth release (iDR4), being accessible only by associated members.

In general, data from the S-PLUS catalog needs to be retrieved through ADQL[16] queries from the cloud website. Also, many tools are at one's disposal, such as a cutout tool (returning cut images based on RA and DEC), the tile tool (allowing for the download of whole fields) and the catalog tool, supporting the search for any data in the available catalogs using ADQL, facilitating

---

[15] The Sloan Digital Sky Survey was designed more than two decades ago. By now, one third of the sky has been observed, and there are spectra for more than 3 million astronomical objects (e.g., stars, galaxies and quasars).

[16] The Astronomical Data Query Language (ADQL) is based on the Structured Query Language (SQL) and was created with the purpose of standardizing astronomical queries (Osuna et al., 2008).

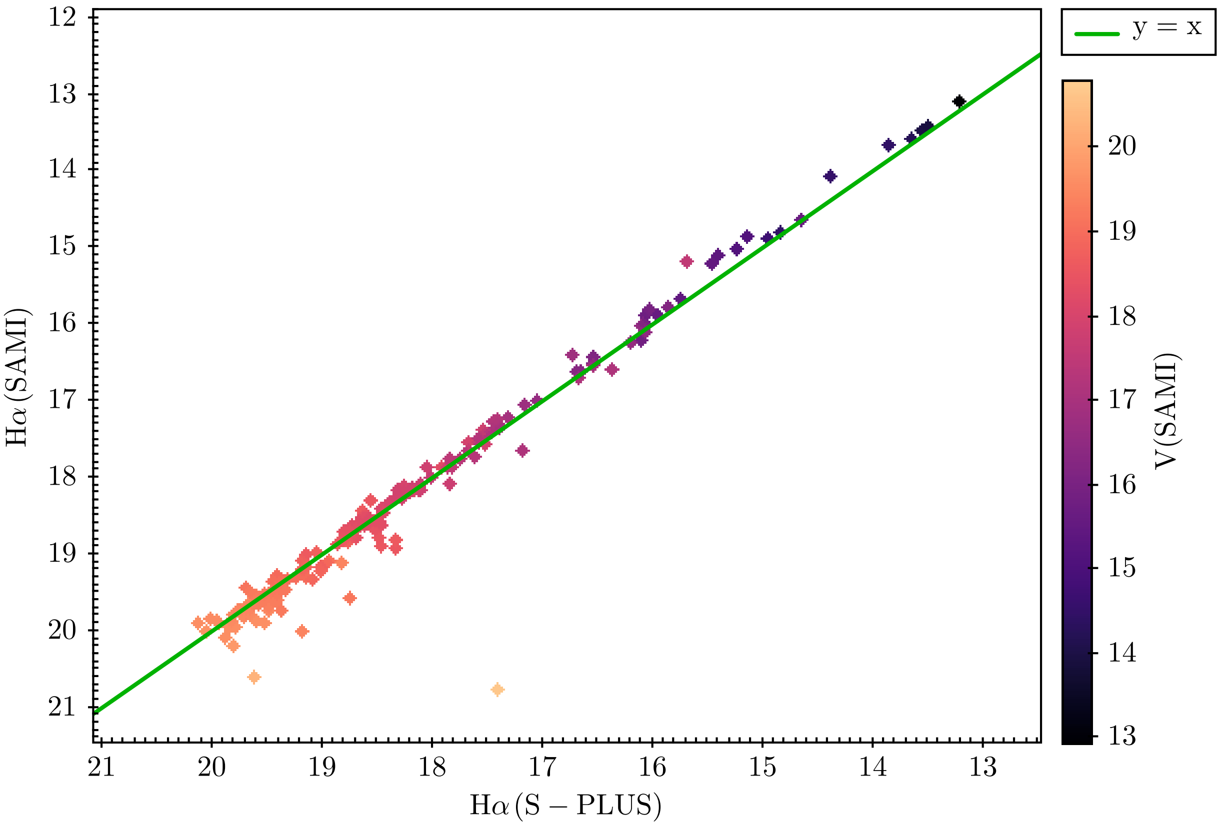

Figure 3.17: Diagram comprising the Hα SAMI magnitudes against the J660 magnitudes from the S-PLUS observations for sources present in both catalogs. All points are colored based on their V magnitude from SAMI. A linear $y(x) = x$ function is shown in a green solid line.

the selection of desired bands or even specific conditionals such as the selection of objects with a high probability of being a star.

It is important to note that the telescope used in S-PLUS cannot be compared with SOAR's 4.1-m (and also, the adaptive optics module was used for our SAMI observations). Besides the limited completeness, observations from both telescopes cannot be directly compared, as they share different filters. If one considers that both observations possess Hα narrow bands, they still cannot be strictly compared as the observational epochs do not coincide. In a Hα_{SAMI} x H$\alpha_{\mathrm{S-PLUS}}$ diagram, a straight line with small deviations is expected for identical sources in both catalogs. This plot can be seen in Fig. 3.17.

S-PLUS data was retrieved using a cone search centered on NGC 330 coordinates with a radius of 3', approximately three times the cluster estimated radius of 1.18' (Iqbal and Keller, 2013). A practical example of how T80-South is very limited compared to SAMI (with AO in usage) is that a crossmatch between both observations resulted in only 168 common stars, with almost none located in the dense cluster center. In Fig. 3.18, the $(r,\ r-i)$ color-magnitude

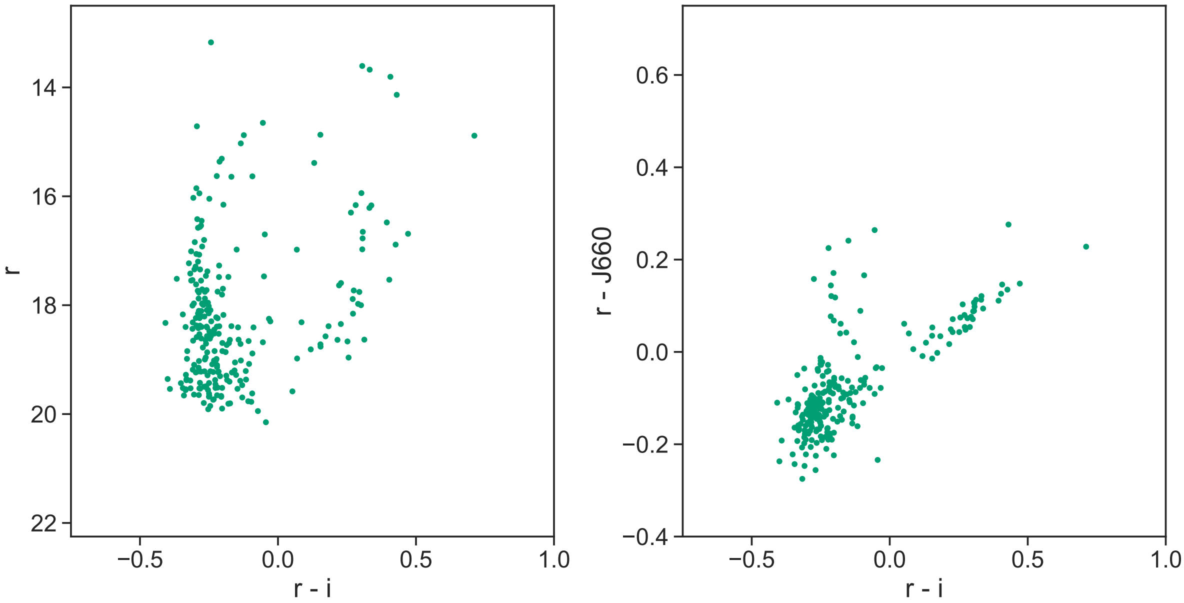

Figure 3.18: Photometric diagrams of NGC 330 from the S-PLUS iDR4. Left panel: (r, $r - i$) color-magnitude diagram. Right panel: (r − J660, $r - i$) color-color diagram.

diagram is shown. This combination is similar to the (V, $V - I$) photometric diagram, useful for identifying important regions such as the MS, the evolved stars and young pre-MS objects position.

Besides the mentioned limitations, it is clearly possible to see the MS structure on the left panel of Fig. 3.18 and also multiple stars with Hα emission in the MS $r - i$ color range ($r - i \lesssim 0$).

The procedure outlined in Sect. 3.2.2 for selecting probable members is not worthwhile for the S-PLUS observations. The number of observed sources is small, and cross-matching with GAIA results in an even smaller sample. S-PLUS can be extremely useful for nearby individual CBe stars or galactic young clusters. In the next chapter, our procedure of making synthetic YOCs with realistic CBe models is detailed.

Chapter 4

Synthetic YOC Photometry with realistic CBe models

In a first approximation, stellar clusters can be defined as groups of stars that form around the same time, share a common chemical composition, and are physically bound together by gravity. In the previous chapter, it was seen that a variety of methodologies have been proposed over the past decades to find CBe candidates in YOCs, such as multi-band photometry, individual target spectroscopy of many objects, multiple spectroscopy using instruments such as MUSE, light-curve analysis of time series data, or even alternatives not discussed yet, such as comparing magnitudes in different releases of a same survey, taking advantage of the long term variability present in this class of stars (Granada et al., 2023).

It was also shown that multi-band photometry is, observationally, the most efficient method to unveil the CBe content in a given population. In this case, combination of specific filters, in color-magnitude and color-color diagrams, for instance, allows for the separation of CBe stars from non-CBe in some cases.

However, this approach only distinguishes CBes from non-CBe stars if narrow band Hα observations are available and when CBes are active (i.e., with a circunstellar disk), and, in particular, with dense and large disks. There are several situations, however, that lead to a weak Hα emission. As an example we mention building or dissipating disks, both of which may possess a small Hα emitting area, and the common case of CBes that build intrinsically low-density disks (e.g., Vieira et al., 2017). In all these cases, CBes will likely appear mixed with the non-CBe group in photometric diagrams, even when using narrow Hα bands. Therefore, this technique cannot grasp the intrinsic multiplicity of the CBe phenomenon and classify aspects of the CBe population of the cluster. So far, no other cluster studies took into account the life cycles of CBe decretion disks.

In order to bypass this problem, a methodology was developed to make synthetic stellar

Table 4.1 - Definition of the most general properties of a synthetic stellar cluster.

	Parameter	Symbol
Intrinsic	Initial Mass Function	IMF
	Total cluster mass	M_{tot} ($M_\odot$)
	Age	t (Myr)
	Metallicity	Z ($Z_\odot$)
	Binary fraction	b_f
	Overall CBe fraction	$f_{\text{CBe}}(m)$
Extrinsic	Distance	d (pc)
	Reddening	$E(B-V)$
	Photometric noise	–

clusters using the spectral models from the BeAtlas v2 grid, introduced in Chap. 2, through an ongoing pipeline written in Python (Van Rossum and Drake, 2009). The main objective is to be able to photometrically identify the differences between normal stars and CBes (either active or inactive) in a realistic stellar population with the advantage of using CBe radiative transfer models comprising a wide range of star plus disk configurations. However, before even handling spectral models, basic assumptions must be set in order to characterize a synthetic YOC. It is important to define the intrinsic and extrinsic parameters, taking into account realistic hypotheses, exemplified in Tab. 4.1.

The IMF controls the slope of the mass distribution (number of stars in each mass bin against the different values of masses), and can be chosen by the final user as the classical form from Salpeter (1955), the broken law from Kroupa (2001) or the log normal distribution from Chabrier (2003). The total cluster mass M_{tot} represents the sum of all stellar masses, at the specific chosen age, in units of $M_\odot$. Rising the value of M_{tot} increases the number of individual masses and gives a higher chance of massive stars to be chosen. The cluster age t will control the upper and lower mass limits of the cluster, and its most significant impact is the position of the MSTO point. The metallicity Z defines which BeAtlas v2 models to use, from SMC-, LMC- and Solar-like compositions, and its impact is most seem in color differences and slightly changes in brightness[1]. The binary fraction b_f controls the total number of binary systems; although this

---

[1] The metallicity for active stars is currently fixed at $Z = 0.014$, corresponding to a solar-like value. For diskless stars (non-CBes or inactive CBes) present in the cluster, one can also ask for $Z = 0.002$ and $Z = 0.006$ (SMC- and LMC-like metallicities), besides the typical solar Z.

fraction is also seem as ST-dependent, in the currently state of our calculations every star has same chances of being in a binary system. The overall CBe fraction $f_{\mathrm{CBe}}(m)$ defines the total limit of CBe stars to exist, being equivalent to the usual ratio $\mathrm{CBe}/(\mathrm{CBe}+\mathrm{B})$, plus the probability fraction of a B-type star to be worked as a CBe per ST. This discrete probability function was based on Fig. 14 of Bodensteiner et al. (2020), with adaptations towards the high and low end of the B ST. The distance d, given in units of parsecs, impacts mostly on the magnitude shift (commonly mentioned in the literature as distance modulus). The reddening $E(B-V)$ is used to mimic total extinction effects in the line of view towards the synthetic cluster, and currently no forms of differential reddening are implemented. The last parameter, the photometric noise, is a Boolean marker that sets if the synthetic cluster will have artificial errors evaluated, based on a signal-to-noise ratio approach.

Also, multiple coeval populations are accepted, as the code allows more than one age value, which can be personalized with a different binary fraction, extinction, or any other pre-defined parameter. Below, a basic workflow is explained for a cluster containing a single coeval population.

4.1 *A Workflow for YOC models with CBes*

Given the initial cluster parameters, the individual mass values, m_i, of each star i member of the cluster are sorted using the chosen IMF law. Throughout this work, the IMF form of Kroupa (2001) was fixed in every simulation. As BeAtlas v2 has a lower mass limit of $M = 1.7\,\mathrm{M}_{\odot}$, the mass distribution behaves similarly as the classical form of Salpeter (1955).

Once a star mass is sampled, we must decide whether it is a CBe star or not. This depends on the fraction of CBe stars for each sub-spectral type and also on the overall limiting fraction. So, if m_i is within the mass range of Be stars (currently, $M = 3.5\,\mathrm{M}_{\odot}$ to $20\,\mathrm{M}_{\odot}$, but the BeAtlas v2 disk grid is planned down to $3\,\mathrm{M}_{\odot}$), the code decides whether it is a CBe star or not based on $f_{\mathrm{CBe}}(m)$.

The lower and upper limits of the mass range are age-dependent, and thus depend on the pre-defined value of the cluster age, t. The upper mass limit, M_{max}, corresponds to the mass threshold in which stars with $m_i > M_{\mathrm{max}}$ have already left the MS[2], and the lower limit corresponds to the

---

[2] As it was previously discussed, this holds true for a single coeval population, as a star in a binary system can live for a longer period than its single counterpart. Also note that rapidly rotating stars live longer than slow rotators.

mass threshold, $M_{\rm min}$, according to which stars with $m_i < M_{\rm min}$ would not have had enough time to enter the MS.

The upper mass limit is estimated based on the Geneva rotating evolutionary models introduced in Sect. 2.1. To calculate it, we computed a table of the stellar age, in Myr, when the star leaves the MS ($t/t_{\rm MS} = 1.0$), for several stellar masses (3, 4, 5, 7, 9, 12, 15, 20 $\rm M_\odot$) and for the models with initial rotation of $W = 0.998$, which corresponds to the longest MS lifetimes for a given mass. So, for a given cluster age, $M_{\rm max} = f(t)$, with f representing the fitted linear interpolating function of the previous table.

For $M_{\rm min}$, the Kelvin-Helmholtz (KH) timescale $\tau_{\rm KH} = GM^2/RL$ was considered, with G being the gravitational constant and M, R and L are the stellar mass, radius and luminosity, respectively. For example, the above thermal timescale applied to a solar mass star results in a value of $\approx$ 30 Myr, implying this minimum cluster age for its MS to contain solar-mass stars (Prialnik, 2009). Re-scaling to solar units, $\tau_{\rm KH}$ can be written as

$$\tau_{\rm KH} \approx 10^{15} \left(\frac{M}{\rm M_\odot}\right)^2 \left(\frac{\rm R_\odot}{R}\right) \left(\frac{\rm L_\odot}{L}\right) \ {\rm s}. \tag{4.1}$$

As an example, the KH timescale for $m_i = 1.7\,\rm M_\odot$ is $t = 7.67$ Myr; for this reason, a synthetic YOCs should be $t = 8$ Myr at a minimum, to make full use of the BeAtlas lowest mass models.

In the scope of this work, only masses ranging from $1.7\,\rm M_\odot \leq m_i \leq 20\,\rm M_\odot$ and $3.5\,\rm M_\odot \leq m_i \leq 20\,\rm M_\odot$ can be considered for non-CBe and CBe stars, respectively; this leads to global minima and maxima for the possible masses to be sampled. In particular, even if the cluster is extremely young, having an age in which stars with $m_i > 20\,\rm M_\odot$ are still on the MS, m_i will only be sorted up to the maximum possible value from BeAtlas. In Fig. 4.1 we show the allowed mass range for a given age for different rotation rates, based on the lower and upper values discussed above.

Before assigning a value for the rotation rate W, a minimum value must be calculated to define the workable range. $W_{\rm min}$ must exist for two main reasons:

1. CBe stars are fast rotators, being always observed with high values of W (Rivinius et al., 2013). As stated in Sect. 2.4, the lower limit of the disk grid is set to $W = 0.50$. For this reason, CBes have always this standard minimum;

2. The rotation rate is also linked to the stellar mass and age. In this case, the minimum possible rotation rate $W_{\rm min,i}$ is estimated for each source based on a linear 1D interpolation

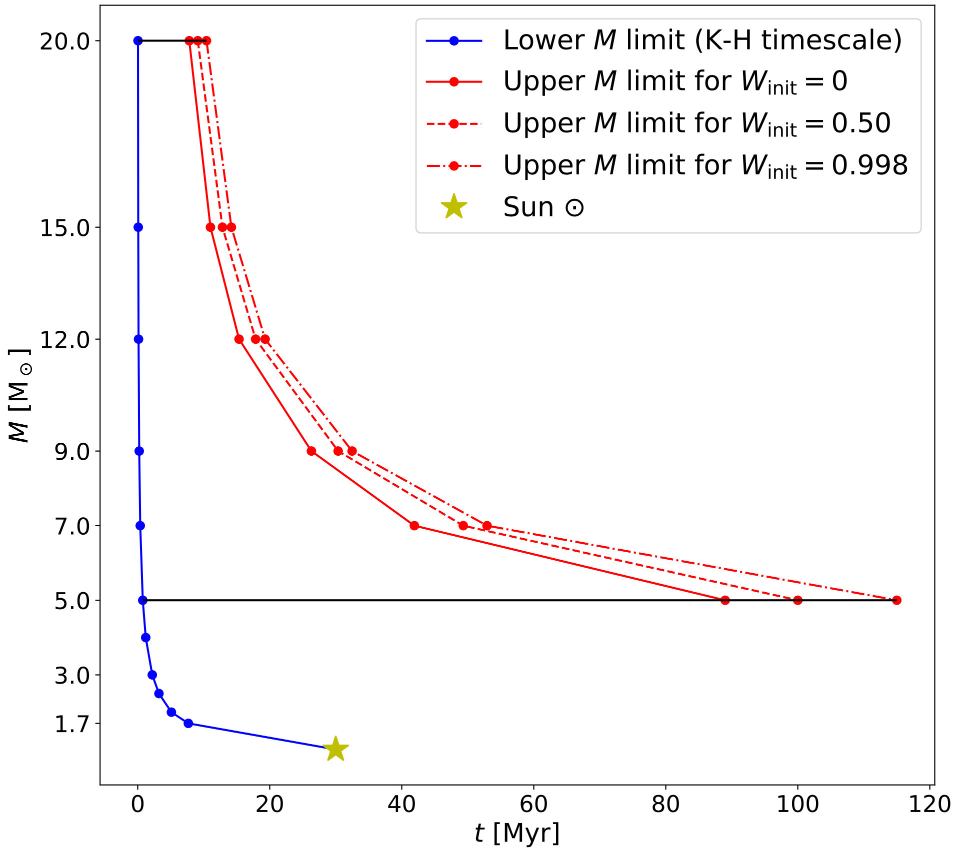

Figure 4.1: Age-dependent mass limits for a cluster composed of a single coeval population. The solid blue, solid, dashed and dot-dashed red lines represent the lower and upper mass limits (the latter for an initial W of 0, 0.16, 0.75) respectively. The upper gray line marks the maximum mass possible in BeAtlas v2, while the lower gray line represents an arbitrary limit considering YOCs having $t \leq 100$ Myr.

from a grid of M, W and age, giving rise to the function $f_{\rm W}(m_i)$. If m_i is lower than the maximum mass of the non-rotating case, the minimum W simply becomes $W_{\rm min,i} = 0$ for normal stars or $W_{\rm min,i} = 0.50$ for CBes — else, $W_{\rm min,i}$ will be estimated with $f_{\rm W}(m_i)$.

For every star, the inclination of the star[3] is chosen through an uniform distribution of $\cos i$ between 0 and 1.

With the above definitions, the workflow to build a synthetic cluster that takes into account both CBes and non-CBes is divided in two parts. First, the normal stars (non-CBe group) are worked on, iterating through each sorted mass m_i, as one may desire to generate a cluster without CBe stars; then, the pipeline moves on to the CBe group. For each non-CBe star, the following is done:

1. The rotation rate W_i is generated through an uniform distribution between $W_{\rm min,i}$ and

---

[3] In this work, the convention used is that pole- and edge-on stars are those with $i = 0°$ and $i = 90°$, respectively.

$W = 0.50$, the minimum possible for CBe stars in our synthetic clusters[4].

2. Photospheric BeAtlas v2 needs the value of $t/t_{\rm MS}$, in order to carry out the flux interpolation. As $t/t_{\rm MS}$ varies with the stellar mass and rotation rate for a given age, $t/t_{\rm MS}$ is estimated via a second degree polynomial fit. For the i-th source, with m_i and W_i, a value of stellar age is evaluated for 13 values of $t/t_{\rm MS}$ from 0 to 1, with a smaller spacing between the lowest values, from the Geneva tracks. The polynomial fit is done on the (age, $t/t_{\rm MS}$) space, and $t/t_{\rm MS,i}$ is calculated using the fitted function applied to the chosen cluster age.
3. Once all native photospheric BeAtlas v2 parameters found (M, W, $t/t_{\rm MS}$, $\cos i$), the flux F_i is linearly interpolated from the grid using the scipy function griddata, useful for unstructured squared grids (for details on the scipy Python package, see Virtanen et al. 2020).

For CBes, additional details must be taken into account to characterize each star and its disk (if present). Besides generating the central star parameters, the following procedure is adopted:

1. Every CBe has a chance of 75% and 25% to be an active or inactive CBe, respectively; This proportion is currently an arbitrary test, and reflects the observational bias existent towards active CBes; however. this is in fact a variable ratio and can be customized. In the future, it is planned to use CBes mass dependent duty cycles (Figueiredo et al., in prep).
2. Independent of the disk status (active/inactive), the rotation rate W is uniformly drawn from $W_{\rm min}$ to $W = 0.99$. Also, $t/t_{\rm MS}$ and the spin-axis inclination are estimated in the same way of a normal star. This step marks the end of the definition of the central star parameters.
3. For active CBes, the disk dynamical state is characterized as ‘dissipating’, ‘steady-state’ or ‘building-up’, according to the probabilities found by Vieira et al. (2017) – which corresponds to 55%, 24% and 21%, respectively. This is used to delimit the range from which the radial density falloff exponent is drawn; for dissipating stars, n can be sampled from the grid lower limit until $n = 3$. For steady-state disks, $3 \leq n \leq 3.5$. Building-up disks bound n between $n = 3.5$ and the grid upper limit;

---

[4] Although representing the lower limit of the BeAtlas v2 disk grid, a value of $W = 0.50$ is in agreement with observations. For more, refer to Rivinius et al. (2013).

4. The disk radius $R_{\rm D}$ can be uniformly sampled between the grid limits or have different distributions for dissipating, building-up and steady disks;

5. The normalized density is sampled through a truncated normal distribution with different μ and σ for each of the three possible disk states, being set to 0 or 1 if sampling goes beyond the lower and upper limit, respectively. This is also an internal script parameter that cannot be taken as universal for every YOC.

If $b_f > 0$, the corresponding fraction of binaries, for both groups, is accounted for. Currently, the code only simulates unresolved binaries. Following the approach of Georgy et al. (2013a), the mass of the companion is determined by $M_{\rm s} = q * M_{\rm p}$, with $M_{\rm p}$ being the primary mass and q being draw from an uniform distribution between 0.1 and 1. Then, the flux of the secondary is estimated using the photospheric grid[5]; if $M_s < 1.7\,{\rm M}_\odot$, the system is classified as a binary, but the code does not consider a flux contribution. The unresolved binary will then have a total flux consisting of only the primary star.

The interpolated flux, F_i, regardless of representing a normal or a CBe star, is then re-scaled to the chosen cluster distance d by $F_i = F_i * (10^2/d^2)$, as BeAtlas v2 models are always normalized for a distance state of 10 pc. Subsequently, the spectrum is reddened according to the chosen $E(B-V)$ following the Fitzpatrick and Massa (1999) law with $R_V = 3.1$. With the latter at hand, AB photometry is thus generated for the desired filters The AB system will be the standard in all synthetic photometry presented in this work. However, any system can be used, such as Vega or ST[6]).

The photometric noise, if present, is produced after the synthetic photometry, directly changing the *true* magnitudes, in a process where a random error is estimated, leading to an either positive or negative magnitude shift. The error evaluation of the i-th source is based on a signal-to-noise ratio (SNR) approach, in which brighter (dimmer) stars have a higher (lower) SNR, and thus a more (less) precise observation, leading to a smaller (larger) error.

---

[5] This results in considering all binary systems in the synthetic cluster to be composed of two MS stars. However, CBe stars are typically observed, when in binary systems, together with stellar remnants or sub-dwarf stars (e.g., sdO and sdB objects). Currently, the solution adopted is to consider a 5% flux contribution from the secondary if the binary system comprises a CBe as the primary.

[6] The ST system is defined such that an object with a flat spectrum characterized by $F_\lambda = 3.63 * 10^{-9}$ erg cm^{-2} s^{-1} Å^{-1} will have zero magnitude when convoluted through any transmission curve. In Vega systems, α Lyrae has, by definition, zero magnitude in any filter.

The process occurs as follows:

1. *A priori*, an array of five values are set, corresponding to the minimum magnitude, the first, second and third quartiles and the maximum magnitude, respectively. These are standardized as SNR = (125, 70, 50, 20, 5), being a good tested sequence that ensures a better controlled dispersion and produces a wider MS towards higher magnitude values. However, for future works this may be reviewed, as the error distribution is dependent on the observational quality, the calibration procedure, and also on the magnitude bands;
2. A second degree polynomial function is fit, taking the magnitudes as the independent variable. This is the expression that is used to calculate the SNR for the i-th star using its magnitudes;
3. A noisier magnitude $X_{\mathrm{noise,i}}$ is evaluated from a uniform distribution between $(X_i - \sigma, X_i + \sigma)$, with $\sigma = 1/\mathrm{SNR}$ and X_i representing the magnitude from a given band for the i-th source.
4. The error is then calculated with $eX_i = X_{\mathrm{noise,i}} - X_i$. All magnitudes of the i-th star are shifted by $\mathrm{mag}_i + eX_i$.

An example is shown in Fig. 4.2. This synthetic cluster was designed with $M_{\mathrm{tot}} = 3000\,\mathrm{M}_{\odot}$, $t = 45$ Myr, $b_f = 30\%$, $f_{\mathrm{CBe}} = 15\%$, located at $d = 1000$ pc, with a reddening of $E(B-V) = 0.1$, $Z = 0.014$ and photometric noise.

In Fig. 4.2, some interesting things can be pointed out beforehand, such as

- The CBe models are being shown in the expected positions in the color-magnitude and color-color diagrams of the upper row, with the active CBes mostly showing a redder $V - I$ and intense Hα emission;
- In the upper left panel, it is possible to see the MS being split due to binary stars;
- Some photometric diagrams cannot show clear separation between normal stars and even strong Hα emitters, such as displayed in the lower right panel. The $B - I$ color is linearly positive correlated to $B - R$, meaning that both indices present the same *contrast* between the two regions of the electromagnetic spectrum (B band having a higher flux contribution from the central star, and R/I from the whole couple system).

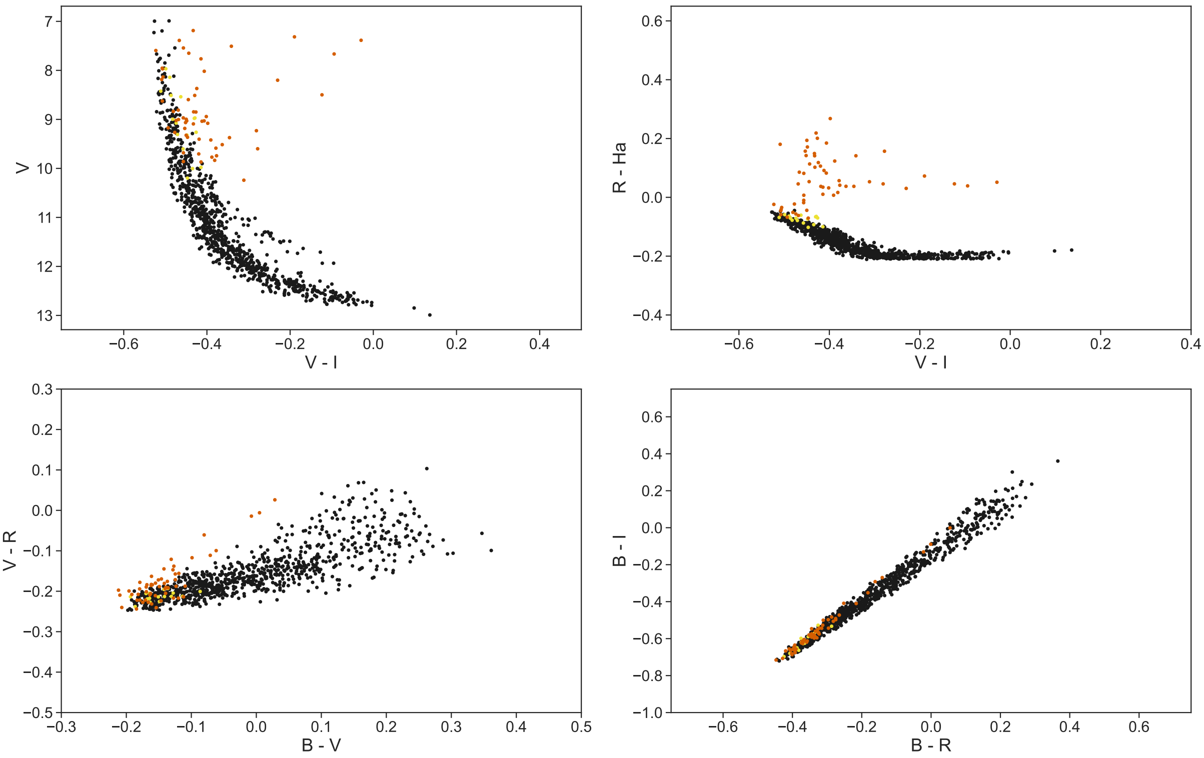

Figure 4.2: Photometric diagrams of a synthetic cluster with $M_{\rm tot} = 3000\,{\rm M}_{\odot}$, $t = 45$ Myr, $b_f = 30\%$, $f_{\rm CBe} = 0.25$, located at $d = 1000$ pc, with a reddening of $E(B-V) = 0.1$, $Z = 0.014$ and with photometric noise active. Upper left: (V, $V-I$) color-magnitude diagram. Upper right: (R−Hα, $V-I$) color-color diagram. Lower left: ($V-R$, $B-V$) color-color diagram. Lower right: ($B-I$, $B-R$) color-color diagram. Normal stars, inactive and active CBes are shown by black, yellow and red markers, respectively.

In order to see if our synthetic cluster agrees with observational and theoretical predictions, some consistency checks must be done, and are presented in the next sections.

4.2 *Initial validation of the synthetic cluster generation method*

As stated in Chap. 2, the newest disk grid is not completed yet. Stars between $3.5\,{\rm M}_{\odot} \leq m_i \leq 12\,{\rm M}_{\odot}$[7] and above $14.6\,{\rm M}_{\odot}$[8] have the most recent calculated spectra from the far-UV ($\lambda = 1000$ Å) up to the end of the optical SED ($\lambda = 10500$ Å) plus the Hα line profile; for the rest of masses, BeAtlas v1 is used.

There are two types of tests that need to be done. Initially, the internal consistency of the code (i.e., if our inputs are really creating the expected outcomes) must be checked. Secondly, a

---

[7] For stars with $4\,{\rm M}_{\odot} \leq m_i \leq 5\,{\rm M}_{\odot}$, just four rotation rates between $W = 0.50$ and $W = 0.99$. For masses ranging from $5\,{\rm M}_{\odot} \leq m_i \leq 9\,{\rm M}_{\odot}$, at most two values of W are available ($W = 0.50$ and $W = 0.75$). For $9\,{\rm M}_{\odot} \leq m_i \leq 12\,{\rm M}_{\odot}$, just rotation rates between $W = 0.50$ and 0.92 can be sampled.

[8] Only for the lowest rotation of the grid ($W = 0.50$).

comparison with external independent works must be made to confirm whether the results match for equivalent parameters of a coeval stellar population.

4.2.1 *Internal consistency*

In the initial test to evaluate internal consistency of the code, we consider two equivalent synthetic clusters (hereafter C1 and C2) containing only normal stars are compared but with different ages. Both clusters have $M_{\rm tot} = 1500\,{\rm M}_\odot$, $d = 10\,$pc, no reddening, no binaries or photometric noise, and $Z = 0.014$. C1 corresponds to a coeval population of $t = 12.5$ Myr, while for C2, $t = 275$ Myr. In Fig. 4.3, two photometric diagrams are shown [$(V, B-V)$, $(R-I, B-V)$], highlighting the differences of C1 and C2, with C1 and C2 stars being plotted as black and red markers, respectively.

Two expected features can be seen. The first one is related to the maximum mass expected in a cluster (based on its age). For C1, as $t = 12.5$ Myr, stars with up to $M = 17.3\,{\rm M}_\odot$ are still observable in the MS; in C2, the maximum mass becomes $M = 3.7\,{\rm M}_\odot$. This can be easily checked in the left panel of Fig. 4.3, as the absolute visual magnitude cut of C2 is at $M_V \approx -1.5$. The second feature is the formation of a MS tail structure towards the MSTO point of C2 (in the left panel) and a small IR excess ($R - I$ moving towards more positive values) arising near $B - V \approx -0.15$ (right panel). Stars with masses close to the cluster upper limit tend to have their age approaching $t/t_{\rm MS} = 1$.

For the second test, the effects of different inclination angles and rotation rates present in the synthetic clusters are shown with two cases:

- Case 1: a synthetic cluster with $M_{\rm tot} = 3000\,{\rm M}_\odot$, $t = 8$ Myr, $d = 10\,$pc, no reddening, no binaries or photometric noise, $Z = 0.014$, containing half of the sources with $W = 0$ and the other half rotating at $W = 0.99$ (keeping the inclination angle uniformly distributed in $\cos i$).

- Case 2: a synthetic cluster with $M_{\rm tot} = 3000\,{\rm M}_\odot$, $t = 8$ Myr, $d = 10\,$pc, no reddening, no binaries or photometric noise, $Z = 0.014$ and the rotation rate fixed at $W = 0.99$, while keeping half of the sources with $i = 0°$ and the other half viewed at $i = 90°$.

Case 1 is shown in Fig. 4.4. The expected effect is the separation of both groups – non-rotating and critically rotating stars – into a thin MS (as the observables of a static star does not change

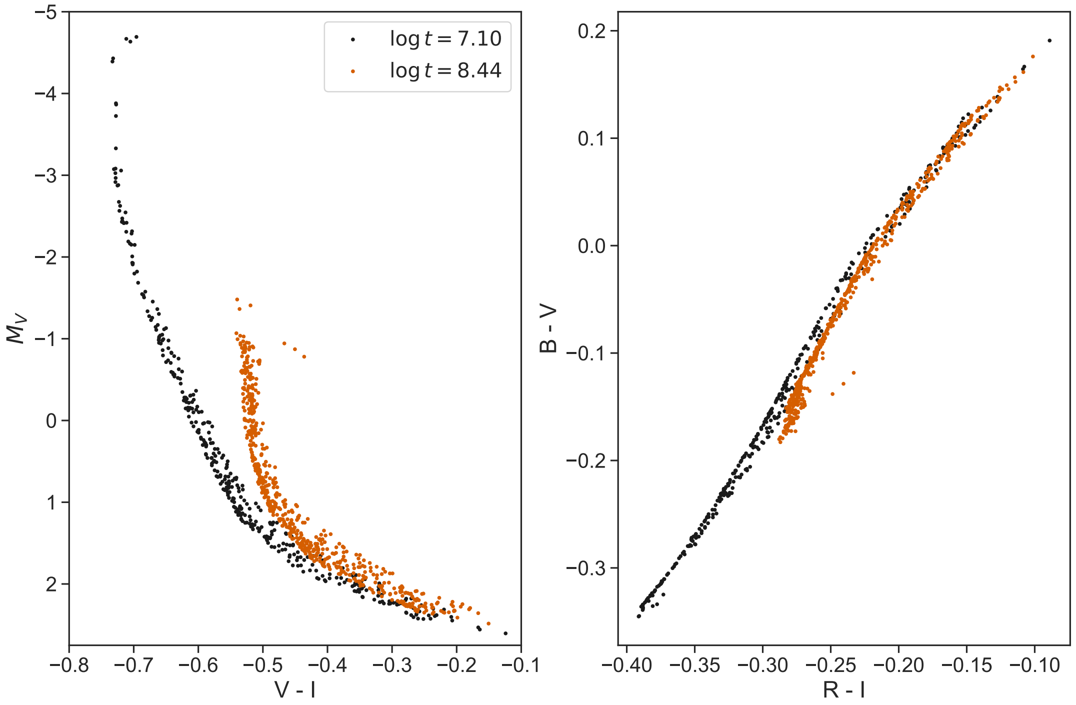

Figure 4.3: Photometric diagrams of two synthetic clusters sharing the same properties but their age. Left panel: (M_V, $V - I$) color-magnitude diagram. Right panel: ($B - V$, $R - I$) color-color diagram. The ages of $t = 12.5$ Myr and $t = 275$ Myr are plotted as black and red markers.

for different lines of sight) and a reddened scattered MS, respectively. This happens mainly due to gravity darkening effects (as explained in Sect. 1.2.1), as pole-on stars with $W = 0.99$ are typically brighter than their static counterparts, while in mid-angle and edge-on stars the observed result is a dimmer and redder flux. Another contribution to this is the uniform distribution in $\cos i$ summed to the fact that pole-on effects can be seen on extremely small inclination angles ($i < 10°$).

In Fig. 4.5, Case 2 is demonstrated, with two identical groups of critically rotating stars, differing only on their inclination angles, fixed at the extremes. While Case 1 has the purpose of testing the observables when changing rotation, Case 2 is also important, even if it highlights the effects arising from gravity darkening as Case 1, because the rotation is kept fixed. This is interesting if one wonders what are the limitations in photometry (in terms of photometric error) if rotation needs to be disentangled.

In the left panel of Fig. 4.5, it is possible to see that a star can have a ΔM_V of more than 1 mag when seen edge-on versus pole-on. The right panel better exhibits the “reddening vector” between the two groups, composed of a component based on the temperature differences ($V - I$), and the other from differences in both R magnitude and Hα profile shape.

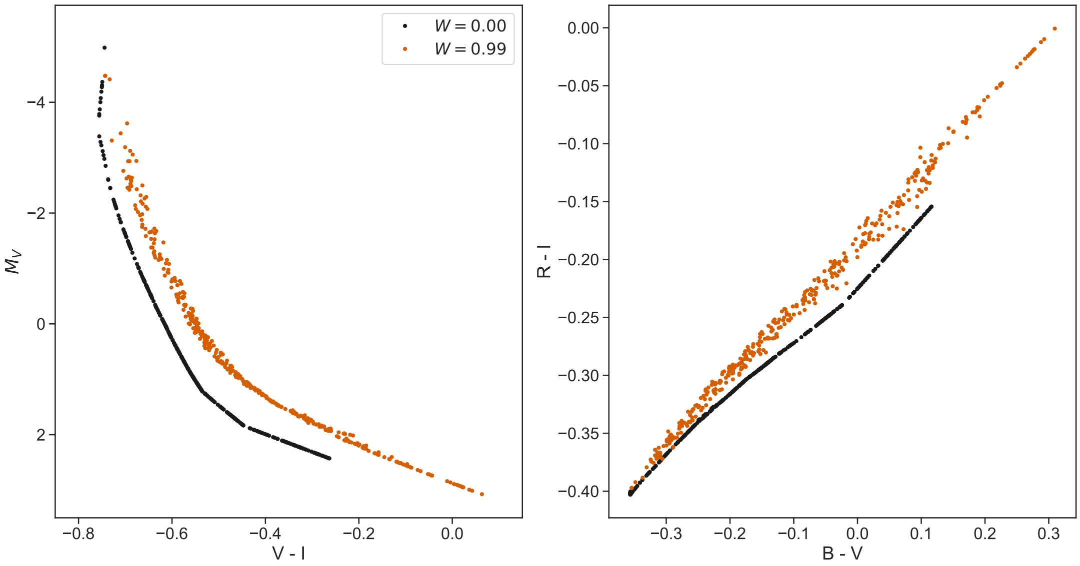

Figure 4.4: Photometric diagrams of a synthetic cluster with $M_{\rm tot}$ = 3000 $M_\odot$, t = 8 Myr, d = 10 pc, no reddening, no binaries or photometric noise, Z = 0.014 divided into two groups of non- and critically rotating stars, shown as black and red markers, respectively. Left panel: (M_V, $V - I$) color-magnitude diagram. Right panel: ($B - V$, $R - I$) color-color diagram.

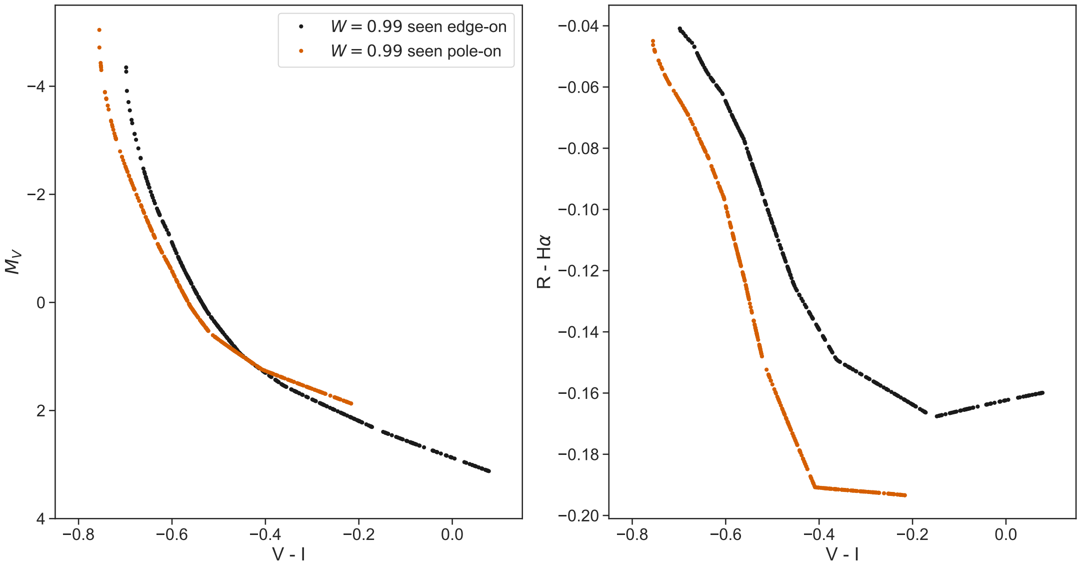

Figure 4.5: Photometric diagrams of a synthetic cluster with $M_{\rm tot}$ = 3000 $M_\odot$, t = 8 Myr, d = 10 pc, W = 0.99, no reddening, no binaries or photometric noise, Z = 0.014 divided into two groups of stars seeing pole- and edge-on, shown as red and black markers, respectively. Left panel: (M_V, $V - I$) color-magnitude diagram. Right panel: ($V - I$, R–Hα) color-color diagram.

The last two validation tests consist of checking if our $t/t_{\rm MS}$ finder routine, for a given (M, W) pair, returns the right age and if the sampled mass distribution returns the expected profile (based on the adopted IMF prescription). This is done by analyzing two histogram distributions of t and M of a given synthetic cluster, both shown in Fig. 4.6, in the left and right panel respectively.

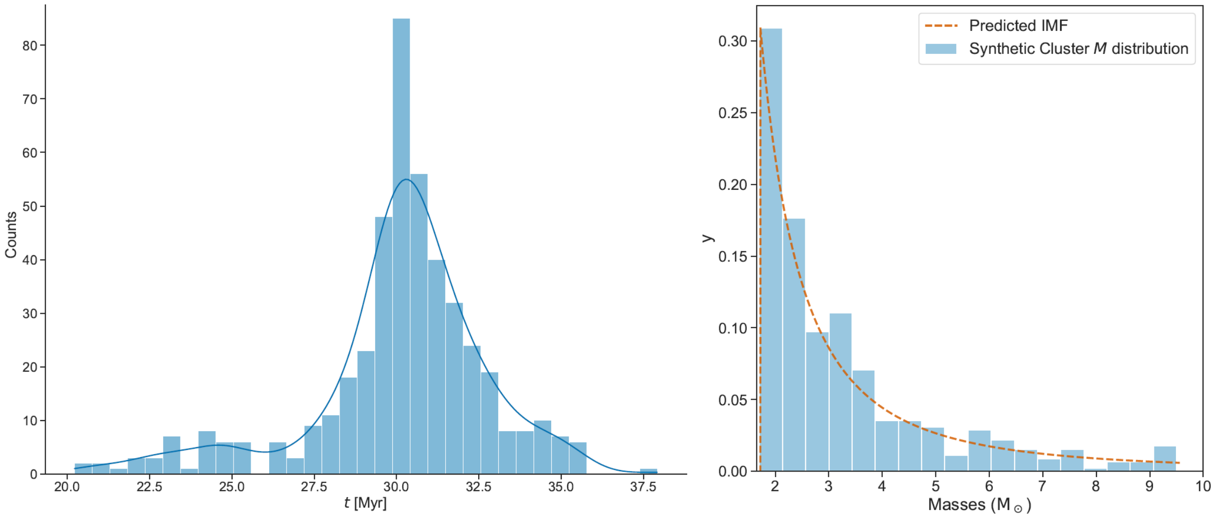

Figure 4.6: Distributions of t and M considering $t_{\rm cluster}$ = 30 Myr. Left: histogram comprising the age t distribution, with the y-axis displaying total counts of each bin. Right: histogram of the M distribution considering $M_{\rm tot}$ = 1500 M$_\odot$ following the IMF prescription of Kroupa (2001). In red dashed line, the predicted IMF, artificially broken at M = 1.7 M$_\odot$, is shown.

We see in the left panel of Fig. 4.6 that the cluster age is well recovered for most sources, with a few being sampled outside t = 30 Myr. This mainly happens due to the resolution in our linear interpolation method and in the Geneva evolutionary models themselves. However, in this test, the median of the distribution is centered at $t_{\rm med}$ = 30.3 Myr (a deviation of just 1.3% of $t_{\rm cluster}$), with a standard deviation of σ_t = 2.7 Myr.

In the right panel of Fig. 4.6, the bins are normalized so that $\sum_{i=1}^{N} y = 1$, with i denoting the i-th bin, N the number of bins, and y represents the observed fraction of masses inside the i-th bin. It is possible to see that the shape resembles the IMF slope. A more continuous form is expected if $M_{\rm tot} \rightarrow \infty$.

4.2.2 *External comparison*

A single procedure was done to check if our synthetic photometry and the cluster generation is not distant from published results. The methodology is based on the comparison of a synthetic cluster, through the photometric diagrams, with external isochrone tracks. The chosen evolutionary tracks are from the PARSEC project (Bressan et al., 2012), available at a web interface which allows custom inputs from the end user[9].

---

[9] The web interface linked to the PARSEC evolutionary models is available at `http://stev.oapd.inaf.it/cgi-bin/cmd`.

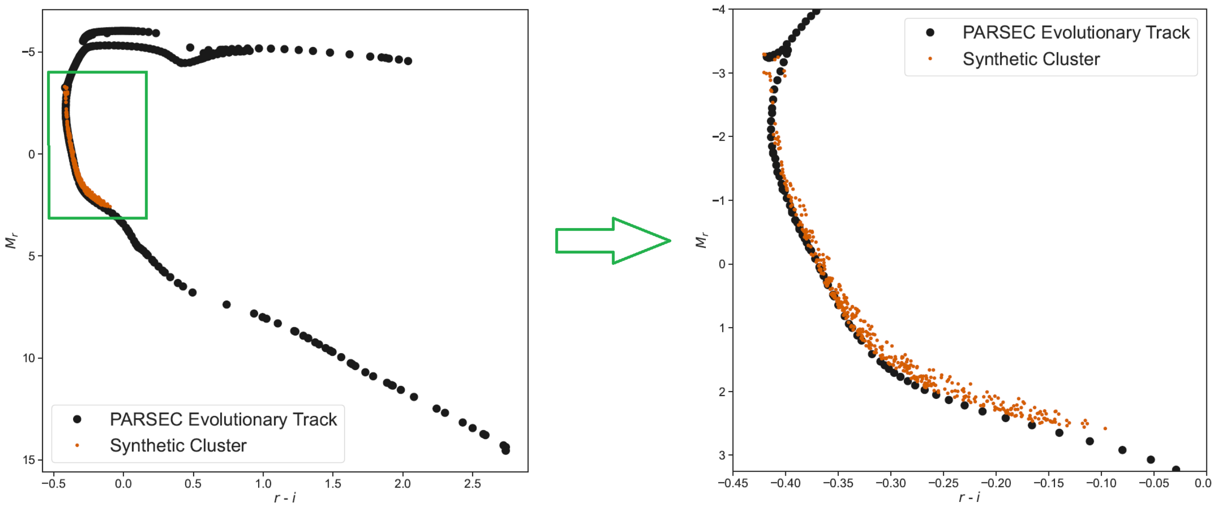

Figure 4.7: Photometric diagrams of a synthetic cluster with $M_{\mathrm{tot}} = 1500\,\mathrm{M}_\odot$ and $t = 30$ Myr compared to a PARSEC evolutionary isochrone sharing the same age, but with non-rotating models. Left: (M_r, $r - i$) color-magnitude diagram. Right: Zoom-in of the region inside the green rectangle present in the left panel. In black and red markers, PARSEC and our synthetic cluster data are respectively shown.

A synthetic cluster with $M_{\mathrm{tot}} = 1500\,\mathrm{M}_\odot$, $t = 30$ Myr, $d = 10\,\mathrm{pc}$[10], no reddening, no binaries or photometric noise, $Z = 0.014$ and containing only normal stars was generated. In order to compare it, an evolutionary track from PARSEC was requested with rotation turned off, for a scaled-solar composition (with $Z_\odot = 0.0152$), bolometric corrections as in Chen et al. (2019) using the revised Vega SED from Bohlin et al. (2020), no interstellar extinction, IMF following the two-part power law from Kroupa (2001), the same age of $t = 30$ Myr and the photometric system chosen was from SkyMapper, in AB magnitudes[11] (the same *uvgriz* system described in Sect. 3.2.1). The latter was chosen because of the available observed transmission curves of SkyMapper. The results are shown in Fig. 4.7.

In Fig. 4.7, our generated synthetic cluster is compared to the computed PARSEC isochrone using two photometric diagrams, with both data overlapping, with small systematic differences due to three things: randomness from our synthetic cluster parameters generation, the PARSEC isochrone being from non-rotating evolutionary models, and that colors and magnitudes from PARSEC are obtained from calibration methods, instead of our synthetic photometry produced via convolved spectra. The expected result was exactly this proximity between both data sets. As

---

[10] The choice of keeping the distance of 10 pc is to preserve the absolute magnitude system, standard in astronomy and used in the PARSEC evolutionary isochrones magnitudes.

[11] In the web interface service of PARSEC, many other options are available in the input form, such as the long period variability during the RGB and AGB phases prescription, or even dust compositions in M- and C-type stars. However, they do not belong in the scope of this work.

the PARSEC isochrone samples mass from $M = 0.1\,\mathrm{M}_\odot$ up to $350\,\mathrm{M}_\odot$, and takes into account post-MS evolution, the isochrone has a wider MS coverage (as our models have the low mass limit of $M = 1.7\,\mathrm{M}_\odot$) and an extension from the highest mass possible MSTO point (for models with $W = 0$).

Chapter 5

A first step towards a self-consistent model of NGC 330

In this chapter, NGC 330 is analyzed in two steps. First, a synthetic cluster using the principles presented in Chap. 4 will be created with a set of fixed parameters, such as the distance and the binary fraction, and custom values for some crucial parameters (e.g., f_{CBe}, $E(B-V)$, M_{tot}, etc) with the purpose of roughly matching NGC 330's photometric diagrams.

The second approach will make use of two machine learning supervised binary classification algorithms, to be trained and tested on synthetic clusters. Our goal here is to make a model to be trained in our synthetic NGC 330-like cluster and fitted to the observations. Besides the SAMI photometry, observations from S-PLUS iDR4 will also be analyzed, so that differences in classification due to changes in the filter set (SAMI *BVRI*+Hα and S-PLUS Javalambre system) can be highlighted. It should be pointed out that some of the results below are exploratory in nature and should be considered preliminary.

5.1 *Synthetic NGC* 330

For the cluster input, the distance is fixed at $d_{\mathrm{NGC330}} = 62.44$ kpc (Graczyk et al., 2020). The binary fraction is set to $b_f = 14\%$, based on the lower limit found by Bodensteiner et al. (2020). Also, the metallicity value of $Z = 0.002$ (Brott et al., 2011) is commonly used for SMC (e.g., Granada et al. 2013, Georgy et al. 2013b). However, as disk models from BeAtlas v2 are fixed at $Z = \mathrm{Z}_{\odot}$, an alternate approach was taken to reduce systematic differences.

The basic photometric effect of a lower metallicity is a color shift (i.e., changes on T_{eff}, resulting in a blueish color), and a slightly change in brightness, becoming brighter towards lower Z (both caused by a different stellar structure). In order to correct for this, the models from BeAtlas v2 were reddened with different values of $E(B-V)$, when compared to the literature, until the shape of the MS visually matched the observed seen in Fig. 3.15. This resulted in a custom $E(B-V) = 0.015$, with $R_V = 3.1$ and the same extinction law mentioned in Chap. 4.

Although the age of NGC 330 has been measured to be $t = 45 \pm 5$ Myr (Patrick et al., 2020), there is a significant quantity of stars with ST earlier than B3, which is not possible when considering single stellar evolution and this estimated age. To bypass this problem, the age of our synthetic NGC 330 was set to $t = 30$ Myr, allowing masses up to $M_{\rm max} = 9.56\,{\rm M}_\odot$ and still inside a 3σ confidence range. Moreover, this does not represent a physical problem, as mass sampling has a trend of generating more sources towards lower masses, which have lifetimes significantly larger than this difference of $\Delta t = 15$ Myr from the literature estimate. It is also important to notice that

1. Stars in a young cluster may not originate at the same epoch due to feedback effects and the reminiscence of molecular clumps (Krumholz et al., 2019);
2. It has being proposed in recent studies that young clusters are composed of two discrete components: a blue MS band comprising slow rotators originating in mergers and the red MS consisting of rapid rotators from disk accretion (Wang et al., 2022)
3. Binaries can evolve together throughout the MS and lead to the formation of blue stragglers, in which their structure and apparent mass are not reachable in single stellar evolutionary models.

All of the mentioned issues impact on the age inference of NGC 330, and the sole usage of single stellar evolution cannot be blindly trusted. The existence of stars more massive than the predicted MSTO point for $30 < t < 45$ Myr can be faked by relaxing the age as mentioned before, and by allowing a few stars to be sampled by the mass distribution in a range between $M_{\rm max}$ and $M = 20\,{\rm M}_\odot$.

The total cluster mass was defined as $M_{\rm tot} = 6000\,{\rm M}_\odot$, with a $f_{\rm CBe} = 0.42$, including the photometric noise. Even though a high CBe fraction was used in the synthetic representation of NGC 330, it is compatible with the recent lower limit estimate of ${\rm CBe}/({\rm CBe}+{\rm B}) = 32\%$ from Bodensteiner et al. (2020) and also agrees with the high CBe content of the cluster. In Fig. 5.1, two diagrams are shown for the SAMI filter set, with normal stars displayed as black markers, and CBe with colored markers according to the legend. Also, $\sim 5\%$ of the total stellar mass was sampled above the MSTO point, with most being considering normal stars and a few CBes.

To make the comparison visually easier, the lower panel of Fig. 5.1 contains the SAMI observations plotted in the background of the synthetic cluster magnitudes. From Fig. 5.1, the following can be concluded based on our MS modeling using BeAtlas:

1. The SAMI magnitude limit almost coincides with BeAtlas v2 lowest photospheric mass ($M = 1.7\,\mathrm{M}_\odot$) models when they are put in the NGC 330 configuration. With our models, it is possible to assume that the MS *shape* is well reproduced up to $V \sim 22$ mag;
2. The position of stars with $V - I > 0$ indeed does not represent MS objects. For $V - I > 0$ and $V < 16$ mag, known RSGs from the literature are seen. For $V > 16$ mag and the same color criterion, foreground evolved objects are the most probable explanation;
3. Stars immediately above the MSTO point ($V \sim 16$ mag) observed by SAMI are blue stragglers (for $V > 14$ mag) and known BSGs from the literature ($V < 14$ mag);

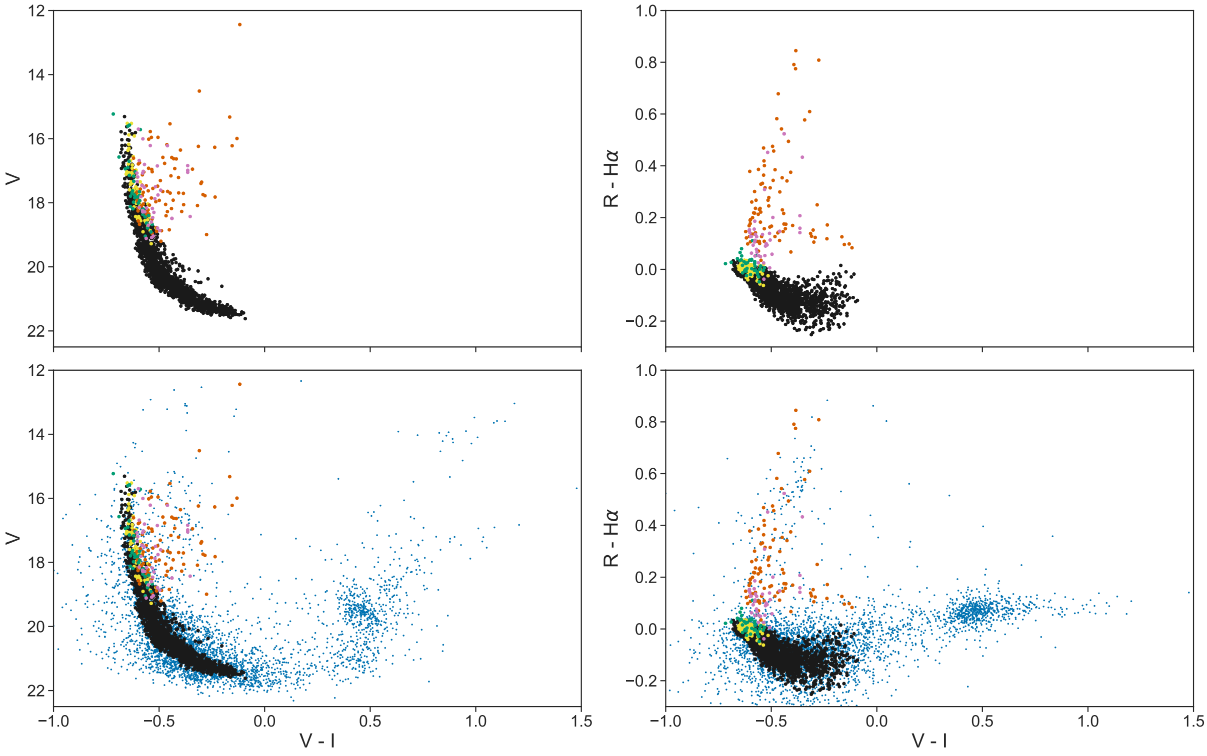

Figure 5.1: Photometric diagrams of the synthetic representation of NGC 330 using the *BVRI*+Hα transmission curves and comparison with real observations. Upper left: (V, $V - I$) color-magnitude diagram. Upper right: (R−Hα, $V - I$) color-color diagram. In the second row, the same content is shown along with the SAMI observations, represented as blue markers. Normal and inactive CBe stars are shown in black and yellow markers, respectively. Active CBes are displayed in three different colors, with dissipating, building-up and steady-state disks being represented by red, green and magenta markers.

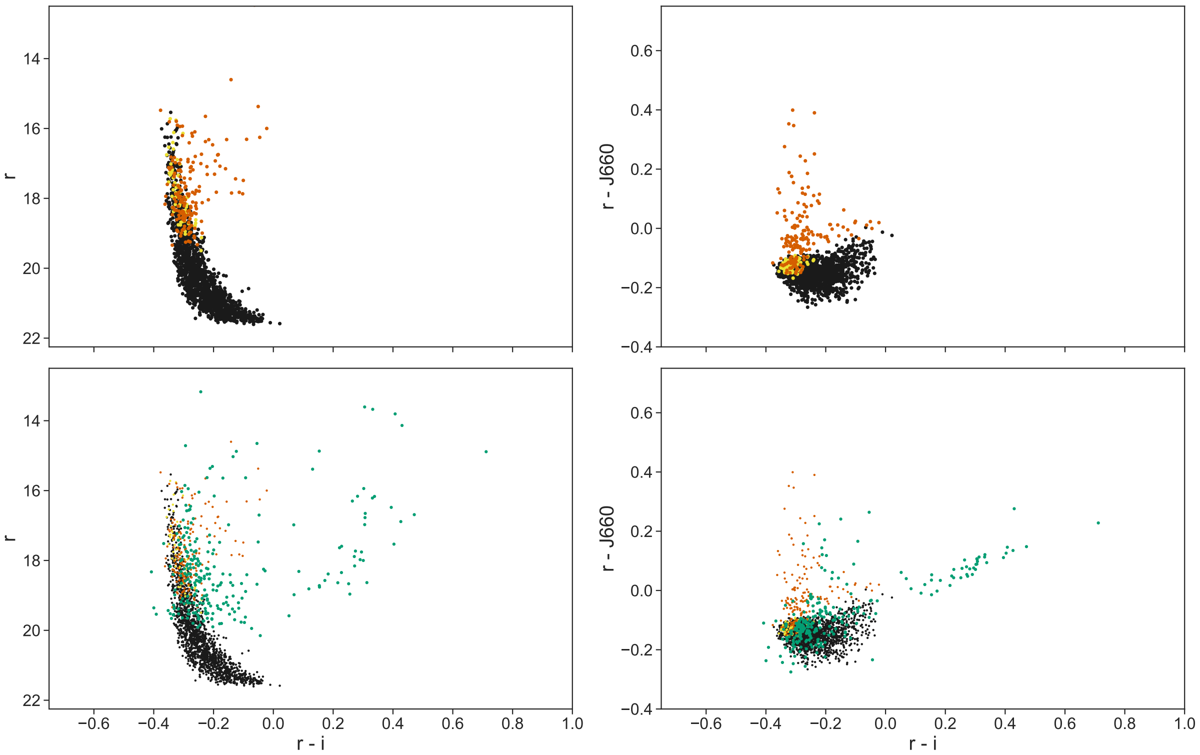

Figure 5.2: Photometric diagrams of the synthetic representation of NGC 330 using the Javalambre transmission curves. Upper left: (r, $r-i$) color-magnitude diagram. Upper right: ($r-$ J660, $r-i$) color-color diagram. In the second row, the same content is shown along with the S-PLUS observations, represented as green markers. Normal, inactive CBe and active CBe stars are shown as black, yellow and red markers, respectively.

4. The MS wider spread observed in SAMI (Fig. 3.13) cannot be mimicked using just photometric noise. As the magnitude errors of SAMI calibrated magnitudes are smaller than the observed spread, this could be interpreted in a first moment as a possible existence of other MS objects from the SMC, sharing a common field but without belonging to NGC 330.

The synthetic photometry for the S-PLUS filters is shown in Fig. 5.2, in the same scheme of two panels comprising the synthetic cluster output and the comparison between real data and observations. It is possible to see a general agreement with data.

Even though S-PLUS data consist of much fewer stars, becoming a small statistics issue, in the next section it will be shown that for our purposes, there is no need of *exactly* matching real observations, as our modeling will be scaled and normalized.

Next, the usage of ML algorithms is detailed, and the synthetic NGC 330-like cluster is used for model training.

5.2 *Machine learning algorithms with supervised classification*

Artificial Intelligence (AI) can be simply defined as a computer science and engineering field, focused in making intelligent machines, capable of solving problems. AI has proven to be significant (and indispensable) for many scientific fields, due to increasing amount of data and the ability of many algorithms to identify humanly impossible patterns in data (Feigelson and Babu 2012, Ivezić et al. 2014).

Machine learning (ML), however, is a sub-type of AI, in which an algorithm tries to *learn* from an input dataset, generating a representative model. This can happen through three different approaches:

- *Supervised learning*: a model is trained on labeled data, and becomes able to make predictions/classifications on unseen data;
- *Unsupervised learning*: a model discovers data groupings and patterns without previous human labeling;
- *Reinforcement learning*: a model learns how to solve given problems by trial and error, receiving rewards or penalties depending on its decision.

Each training method behind ML algorithms has its own strengths and weaknesses. In the past years, ML has been useful in many astrophysical fields, such as stellar atmospheric parameters estimation (Xiang et al., 2017), evaluation of photometric redshifts (Mucesh et al., 2021), galaxy morphological studies (Reza, 2021) and star/galaxy/quasar classification in photometric surveys (Wang et al., 2022).

With the synthetic cluster generation algorithm seen above, every star receives different labels depending on its configuration (e.g., an active and an inactive CBe can be easily distinguished), allowing complex class labeling. For example, a normal star can be seen as a class 0 object, while CBes as belonging to class 1. In this type of problem, a supervised ML algorithm will be dealing with a binary classification problem. However, the number of classes can be raised, with the possibility of even putting non-MS stars (such as the ones observed with SAMI for $V - I > 0$ or BSGs) as a third class, representing stars outside the BeAtlas v2 scope.

The input features, in our case, turn out to be the generated synthetic photometry, which can be also customized in many ways. For example, a model can receive as input features all magnitudes from the SAMI filterset (*BVRI*+Hα), S-PLUS (Javalambre), the union of both sets or even "stand-alone" mixed magnitudes.

In the next section, the training process of some ML algorithms on our synthetic NGC 330 is detailed, also highlighting the accuracy[1] of predictions during testing.

5.2.1 *Training and testing*

For the scope of this work, two supervised classification ML algorithms were chosen, both capable of dealing with either binary or multi-class labeling. They were:

- *k-Nearest Neighbors (k-NN)*: In classification purposes, k-NN consists of assigning one class to an object by taking into account the most common class among its k nearest neighbors, in which the distance is calculated considering all input dimensions (Kramer, 2013). k-NN needs, in general, a pre-defined value for the positive integer k, a weight function and a distance metric.

  Some pros of k-NN include the need of only one hyper parameter[2], the simple implementation for multi-class problems and that k-NN is an instance-based method, which immediately changes with new input data. Cons may include the increasing computational cost for large data sets and difficulties that can probably arise with a high number of input dimensions, suffering from the curse of dimensionality – as k-NN searches for the nearest neighbors considering every axis and may become unstable (Pestov, 2013).

- *Decision Tree (DT)*: DT consists of splitting the training data into two or more subsets by making its decision based on the input values, leading to a final *inverted* tree-like structure to be used in unseen data (Song and Lu, 2015). Before the splitting strategy, it begins with a single node, dubbed *root*, representing the entire training dataset. DT then recursively splits data by selecting the best feature and taking into account a threshold metric to split on at each node, in a repeating process ending when a stopping criterion is met (which can be the maximum tree depth or when no improvement is seen in the classification accuracy). After the stopping criterion is met, the final nodes are called leaf nodes, representing one of the possible classes.

---

[1] Accuracy is a common metric used in ML models defined as the ratio between the number of correct predictions and the total number of predictions.

[2] A hyperparameter can be defined as a parameter whole value directly controls the general behavior of training ML algorithms (Wu et al., 2019).

DT needs in general a criterion function (normally the Gini impurity, see Sect. 3.4 of Maimon and Rokach 2005), a split strategy, and the characteristics of the tree (such as the minimum number of samples to split an internal node or the minimum number of samples to create a leaf node). Some of the advantages of DTs are that data is not required to be normalized or scaled, while cons may include high calculation times in training when compared to other algorithms.

k-NN and DT were chosen because after brief initial tests, and they showed better results than Random Forests, Support Vector Machines and Naive Bayes. A more detailed exploration will be made and reported in the in-progress paper.

Before assigning the training and test samples, a larger synthetic cluster was produced, with $M_{\rm tot} = 20\ 000\,{\rm M}_{\odot}$, with a smaller CBe fraction of $f_{\rm CBe} = 0.20$ (as the chosen value of total mass results in an extreme number of MS sources), keeping the rest of the parameters the same as presented before. A higher value of $f_{\rm CBe}$ tends to lower the accuracy of the predictions, with many normal stars being wrongly classified.

In addition to the MS and CBe stars generated by the script using BeAtlas v2 models, two datasets were then created: one with the inclusion of stars observed by SAMI, and the other by S-PLUS. The selected stars were objects that clearly behaved as non-members or MS objects (e.g., objects with $V - I > 0$ or $V < 15$ mag in SAMI or $r - i > 0$ and $r < 14$ in S-PLUS magnitudes). Magnitudes of these objects received a distinct label of *non-MS stars* in both datasets, allowing multi-class classification.

The train/test ratio used was 70/30 (Gholamy et al., 2018), with the cluster being randomly split between train and test samples. The test sample in this work is used just for final validation, to inspect the overall accuracy of the trained model. Two photometric diagrams of both final train and test sets for the SAMI filters are shown in Fig. 5.3.

The implementation chosen for k-NN was the KNeighborsClassifier() and for DT was the DecisionTreeClassifier(), both from the Python package scikit-learn (Pedregosa et al., 2011). For the k-NN classifier, the optimal value for k, the weight used and the algorithm to be used were chosen through cross-validation (CV), testing in both input possibilities (SAMI/S-PLUS). Specifically for k, only $k > 2$ values were allowed in the CV, as small values of k make the estimator more susceptible to outliers and $k = 1$ generally implies in overfitting.

The details of the fine-tuning parameters ranges used in the CV for k-NN is shown in Tab. 5.1. The highest accuracy achieved, in a CV composed of 10 folds from the training set, was 94.66%

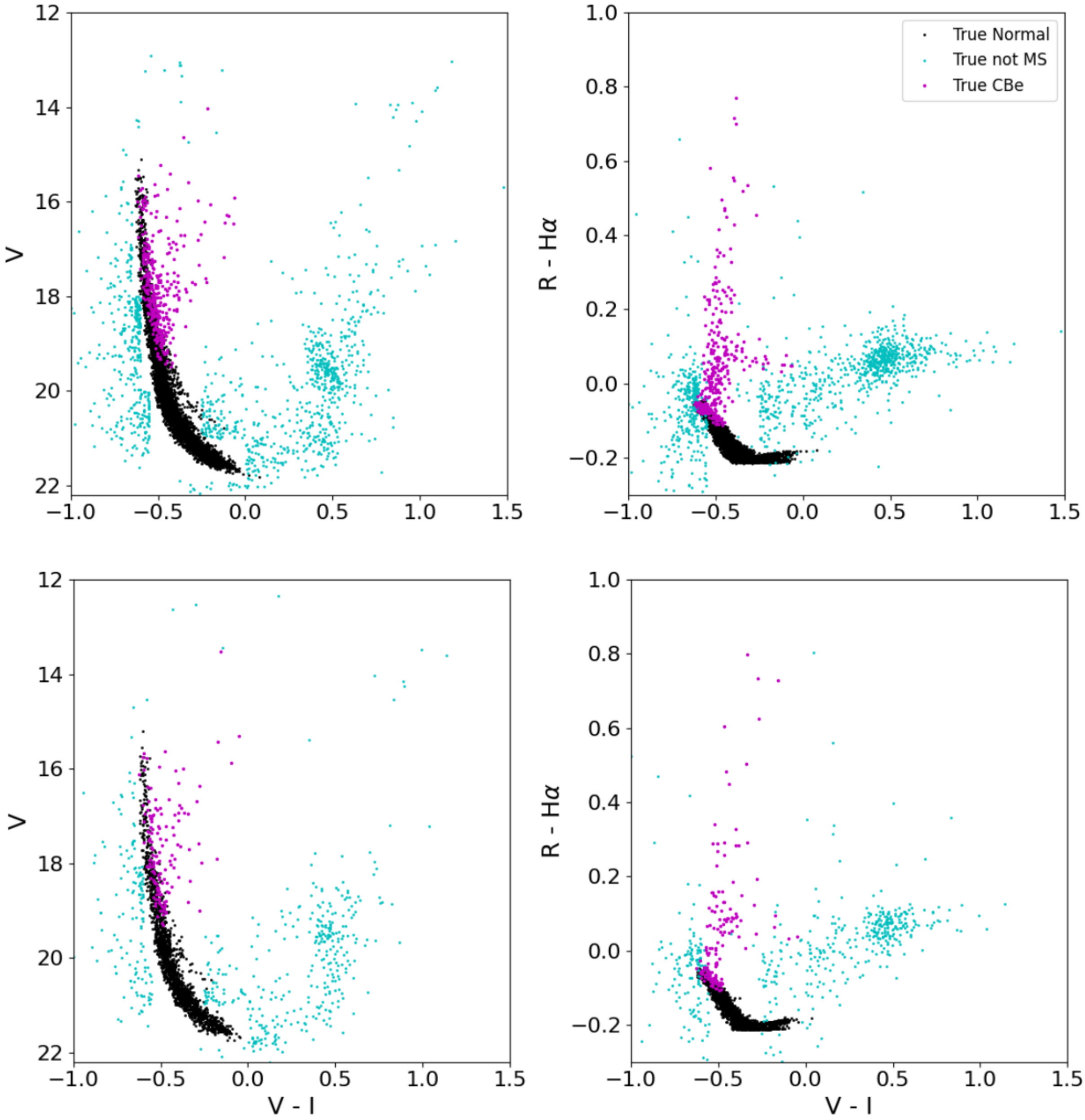

Figure 5.3: (V, $V - I$) and (R−Hα, $V - I$) photometric diagrams of the NGC 330-like synthetic cluster. Upper row: Train set, containing randomly shuffled 70% of samples. Lower row: Test set, comprising 30% of the total number of samples. True normal MS and CBe stars are showed as black and magenta markers, while non-members, blue stragglers, blue supergiants, foreground giants and red supergiants are plotted as cyan markers.

and 95.98% for SAMI and S-PLUS input features respectively, keeping $k = 4$, using the Ball Tree algorithm (Liu et al., 2006), the distance calculated using Euclidean approach and samples having weight of $1/d$, with d being the calculated distance between two neighbors (implying that closer neighbors have more influence than more distant neighbors).

As for DT, CV was also used to fine-tune the hyperparameters, such as the function that measures the split quality, the minimum number of samples to characterize a pure leaf node or

Table 5.1 - k-NN cross-validation parameters.

Parameter	Possibilities	SAMI	S-PLUS
k	3, 4, 5, 6, 7, 8, 9, 10	4	4
Weight	Uniform (equal), Distance ($1/d$)	Distance	Distance
Algorithm	Brute search, KD-Tree, Ball-Tree	Ball-Tree	Ball-Tree
Distance metric	Manhattan, Euclidean, Minkowski	Euclidean	Euclidean

Table 5.2 - Decision Tree cross-validation parameters.

Parameter	Possibilities	SAMI	S-PLUS
Criterion	Gini impurity, Shannon entropy	Gini	Entropy
Leaf Nº of samples	1, 2, 3, 4, 5, 6, 7, 8, 9, 10	1	1
Min. samples before splitting	2, 3, 4, 5, 6, 7, 8, 9, 10	3	4

the minimum number of samples to allow splitting. The allowed values in the CV are shown in Tab. 5.2. For the SAMI input features, the highest accuracy obtained was 92.56%, using the Gini impurity criterion (see Chap. 4 of Breiman et al. 1984), the minimum number of 3 samples to allow node splitting, and the minimum value of 1 sample to permit a node to become a leaf (terminal node).

The train and test samples' input features (magnitudes) were scaled using the SCIKIT-LEARN function STANDARDSCALER(), which removes the mean and scales to variance for every feature. The k-NN and DT models were fitted on the training dataset of both input groups. The final validation results from the model prediction onto the test set for the SAMI filters are shown in Fig. 5.4, and for the Javalambre transmission curves in Fig. 5.5.

It is possible to see that both models performed well in identifying the MS region, the position of unwanted stars (the ones from the not-MS group) and also in most of the CBes, with subtle differences between k-NN and DT. A slightly better accuracy was achieved, considering both classifiers, in the S-PLUS test prediction, which can be due to the existence of more features and/or the sensitivity of some features.

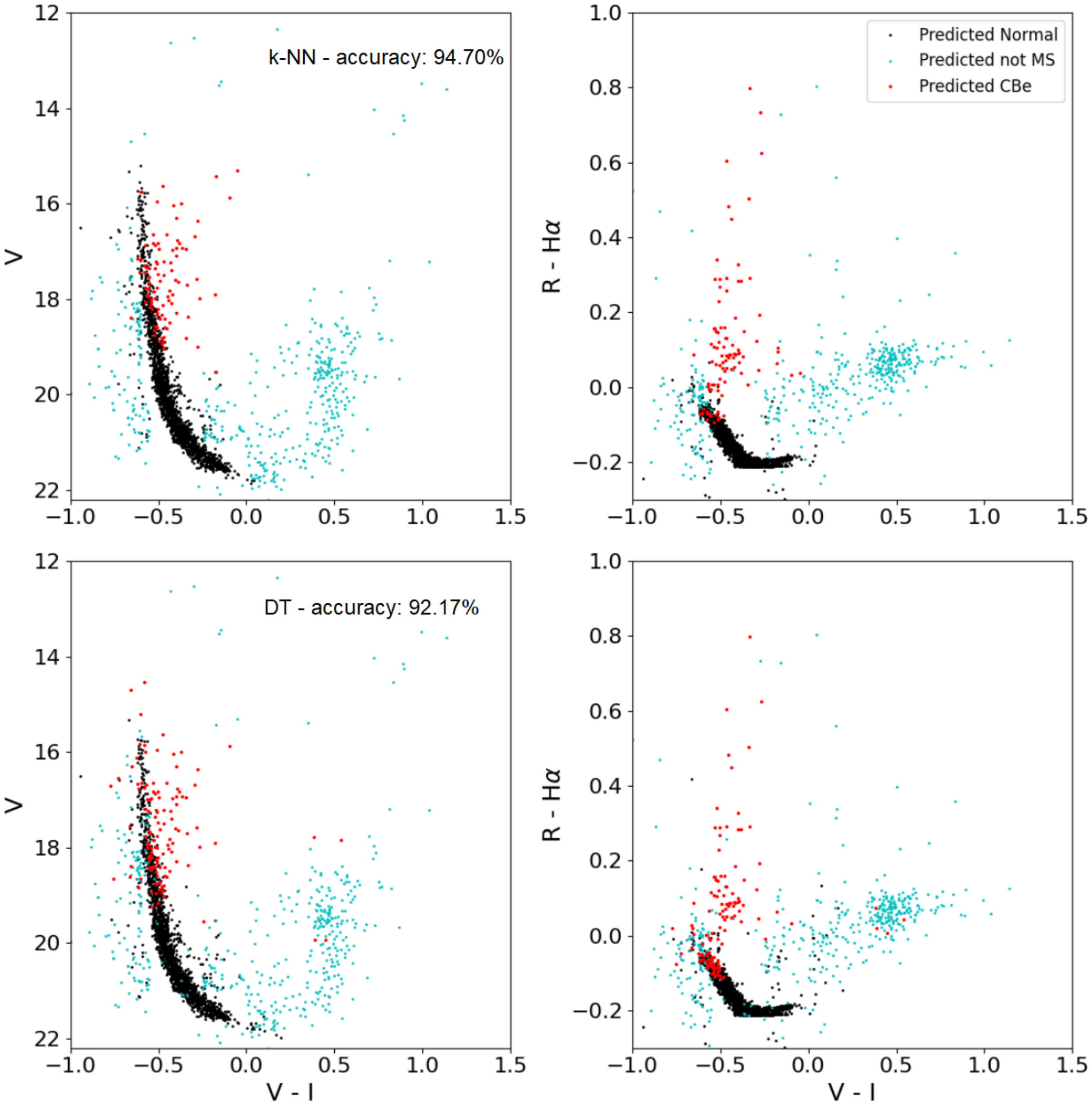

Figure 5.4: $(V, V - I)$ and $(R{-}\mathrm{H}\alpha, V - I)$ photometric diagrams of the prediction on the SAMI test sample for two different ML models. Upper row: k-NN prediction results, with an overall accuracy of $\sim 95\%$. Lower row: DT prediction results, with an accuracy of $\sim 92\%$. Predicted normal, CBe stars and objects from the *not-MS* class are respectively shown as black, red and cyan markers.

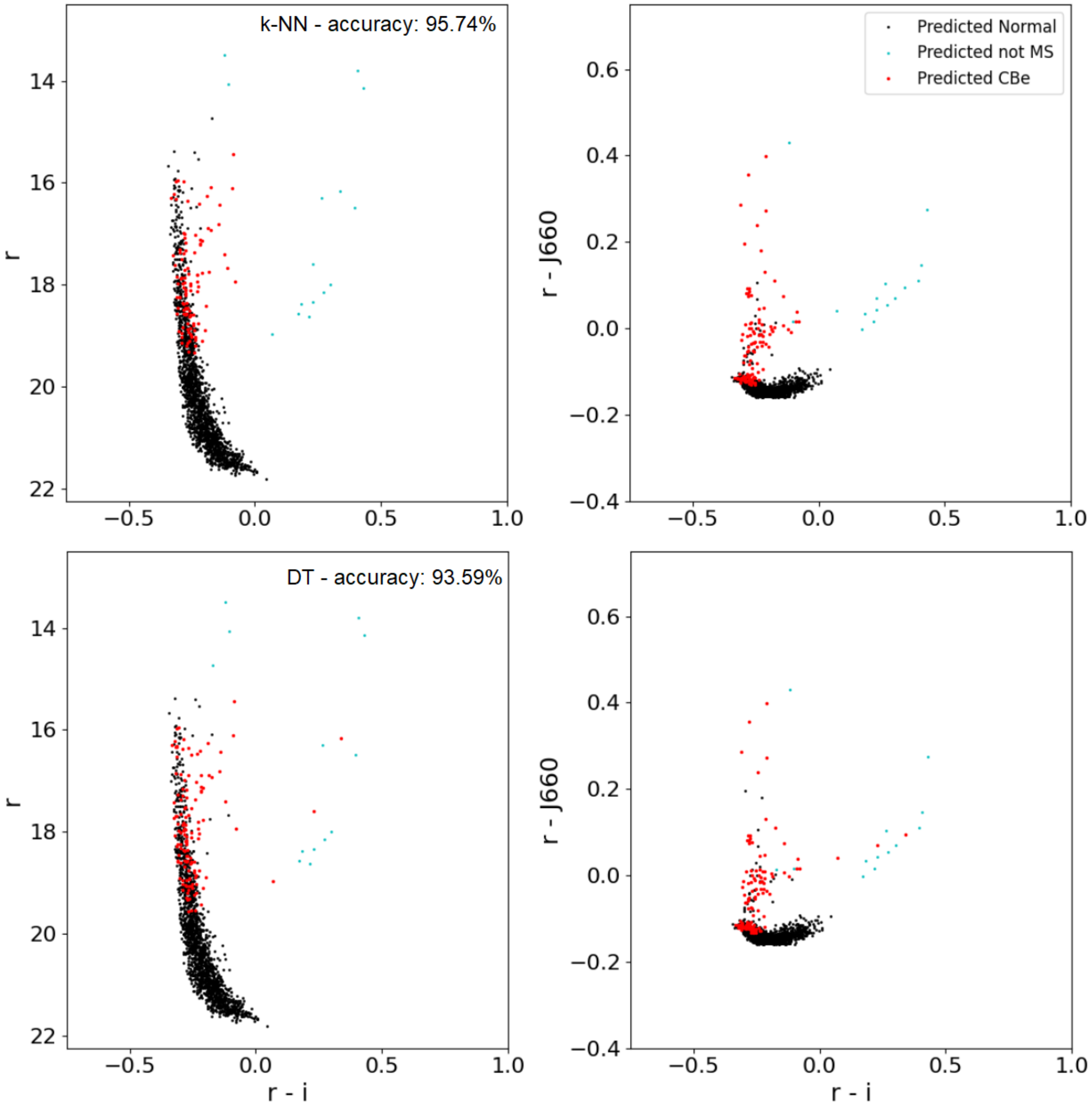

Figure 5.5: (r, $r - i$) and (r − J660, $r - i$) photometric diagrams of the prediction on the S-PLUS test sample for two different ML models. Upper row: k-NN prediction results, with an overall accuracy of ∼ 96%. Lower row: DT prediction results, with an accuracy of ∼ 94%. Predicted normal, CBe stars and objects from the *not-MS* class are respectively shown as black, red and cyan markers.

5.3 Application to real data

With both models fitted and validated for the two input possibilities, NGC 330 can finally be used for prediction, in which the model performances will be tested against unseen data. Although k-NN showed better results in the test validation, DT will not be discarded – instead, CBes classified in both predictions are more likely to be probable CBe star. Starting with the observations with lesser samples, the prediction results for the S-PLUS iDR4 observations can be seen in Fig. 5.6.

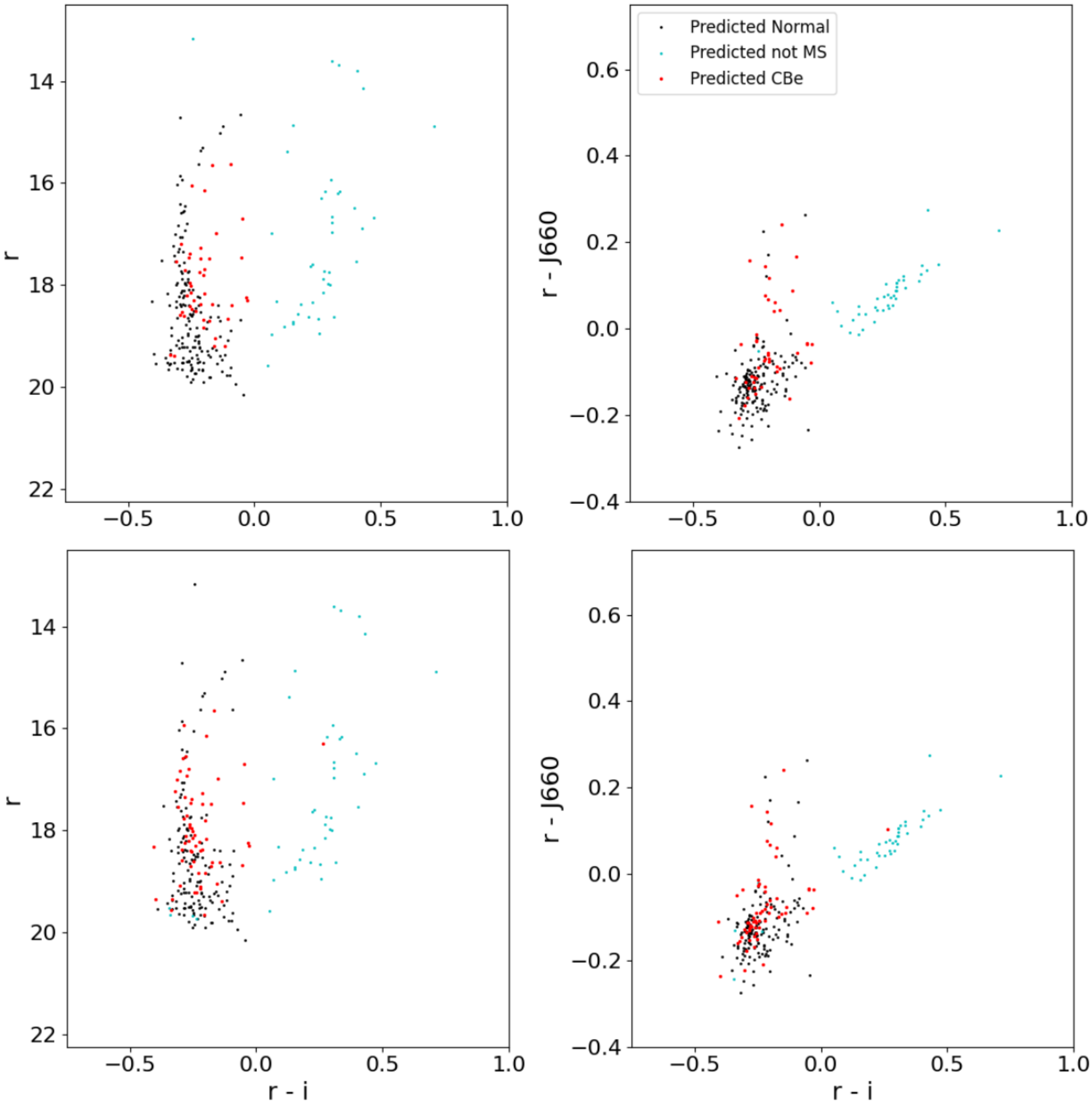

Figure 5.6: $(r, r-i)$ and $(r - \mathrm{J660}, r-i)$ photometric diagrams of the prediction on the S-PLUS iDR4 observation of NGC 330 for two different ML models. Upper row: k-NN prediction results. Lower row: DT prediction results. Predicted normal, CBe stars and objects from the *not-MS* class are respectively shown as black, red and cyan markers.

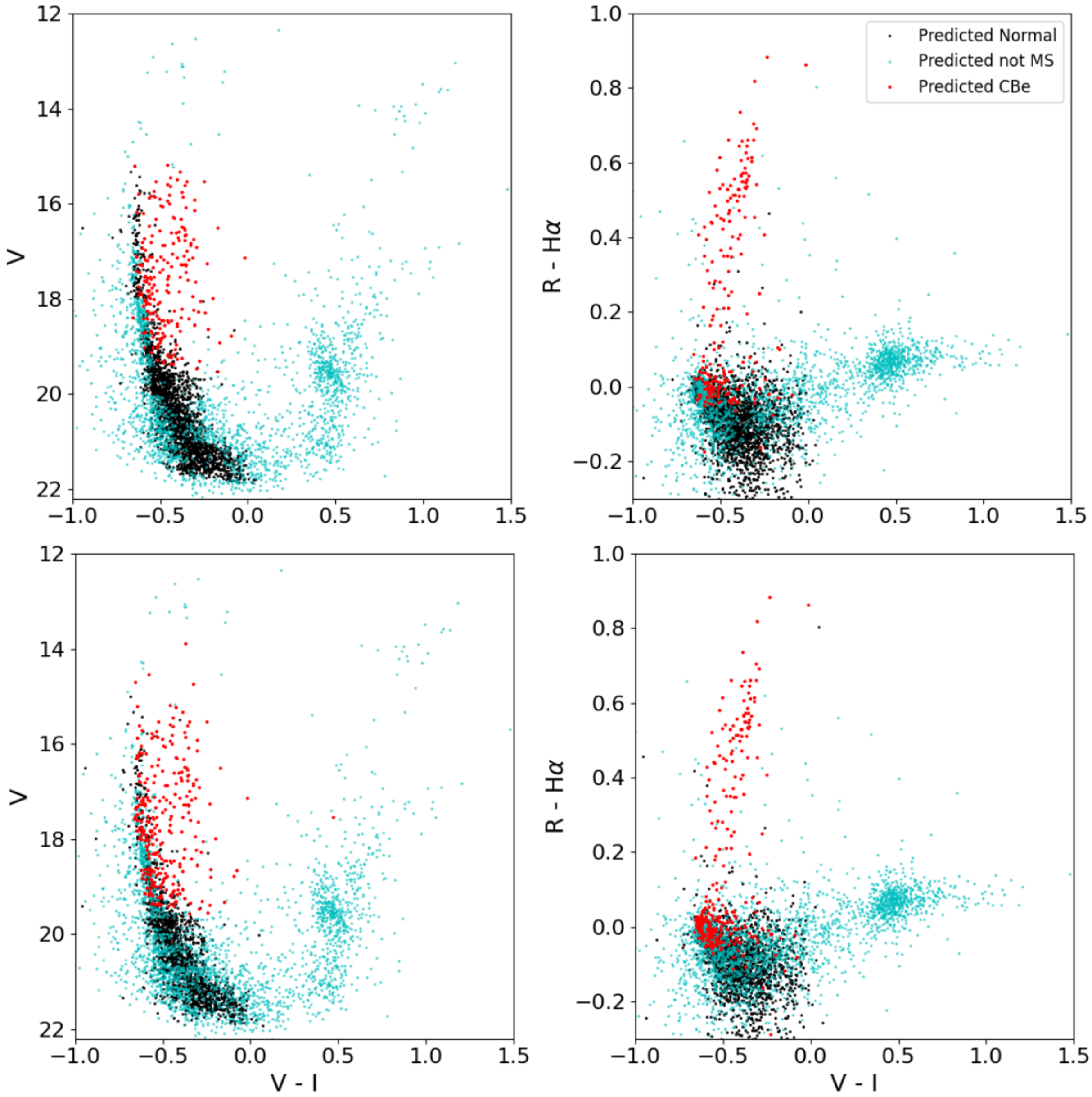

Figure 5.7: $(V, V - I)$ and $(R{-}\mathrm{H}\alpha, V - I)$ photometric diagrams of the prediction on the SAMI observation of NGC 330 for two different ML models. Upper row: k-NN prediction results. Lower row: DT prediction results. Predicted normal, CBe stars and objects from the *not-MS* class are respectively shown as black, red and cyan markers.

Applying the models to the S-PLUS observations, 44 and 47 sources, out of 250 (17.6% and 18.8%) are classified as probable CBe stars for the k-NN and the DT estimators, respectively. Even if SAMI observations did not exist in this case, the result on S-PLUS data is already of interest, as this type of prediction can help spectroscopic follow-ups and both models did not restrict the CBe classification to only Hα emitters, as the traditional photometric methods discussed in Chap. 3.

Moving on, the prediction results for the SAMI observations are shown in Fig. 5.7. From a total sample of 4430 stars from SAMI (as stated in Chap. 3, this is the quantity of sources with observed magnitudes in all five filters), 206 and 289 were classified as probable CBe stars by the k-NN and the DT estimators, corresponding to 4.6% and 6.5% of the total sample.

In order to compare with literature estimates, the predicted $\mathrm{CBe}/(\mathrm{CBe}+\mathrm{B})$ fraction must be evaluated, hereafter $f_{\mathrm{CBe,predicted}}$. Considering the expected magnitude range for the B spectral type, for objects located at NGC 330, the fraction rises to $f_{\mathrm{CBe,predicted}} = 19 \pm 2\%$ and $f_{\mathrm{CBe,predicted}} = 28 \pm 3\%$ for k-NN and DT, respectively. Fig. 5.8 shows the CBe fraction *versus* each ST bin.

However, this result can still be contaminated by foreground less massive stars classified in the MS range. The more recent fraction estimate using high resolution spectroscopy is 32 ± 3% (Bodensteiner et al., 2020), but with a sample limited to stars brighter than $V = 18.48$ mag (AB). If we consider only stars brighter than this same visual magnitude, our fraction rises even more to $f_{\mathrm{CBe,predicted}} = 51 \pm 3\%$ and $f_{\mathrm{CBe,predicted}} = 57 \pm 4\%$ for k-NN and DT, respectively – which shows that the number of CBe stars up to $V = 18.48$ mag is predicted to become larger than MS B-type objects.

In Bodensteiner et al. (2020), there is also a second evaluation considering just stars up to

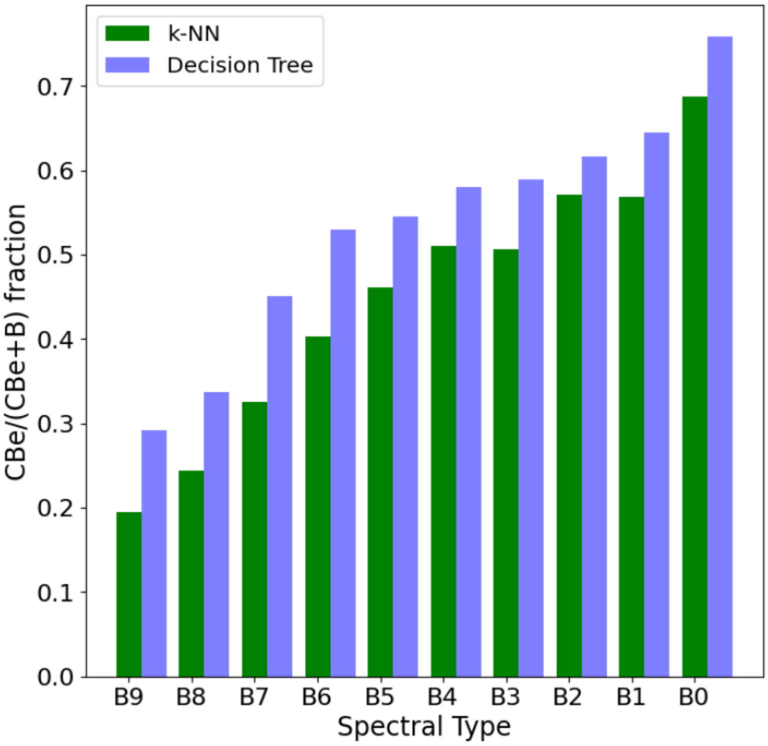

Figure 5.8: $f_{\mathrm{CBe,predicted}}$ histogram for the B spectral type range by k-NN and DT for SAMI observations. Magnitudes considered for each ST bin were calculated using BeAtlas v2 photospheric models for the SMC metallicity. The error in ST is of The predictions from k-NN and DT are shown as green and blue bars, respectively.

V = 16.98 mag (AB), with a resulting fraction of 46 ± 10%. Repeating this same condition, our fraction estimate becomes $f_{\mathrm{CBe,predicted}} = 57 \pm 3\%$ and $f_{\mathrm{CBe,predicted}} = 64 \pm 4\%$ for k-NN and DT, respectively. The lower fraction for DT shows that the model is finding more CBes in lower masses than k-NN, which can also be one of the sources for its lower accuracy in the testing phase.

When making magnitude cuts, the CBe fraction tends to naturally rise as the number of stars grows significantly towards the faintest end. For example, considering the whole sample of 4430 stars, there are 1480 stars just between $V = 18.48$ and ~ 20.22 mag (from the magnitude cut of Bodensteiner et al. (2020) up to the B9.5V limit for stars observed in NGC 330). From the B9.5 limit up to the faintest star in the source (moving to A-type stars), there are 2296. This means that 85% of the sample is composed of stars fainter than $V = 18.48$ mag, for example.

It is also possible to see, as in the S-PLUS data, that both estimators classified some non-Hα emitters as CBe stars, satisfying one of the initial purposes of this work – not needing to rely on arbitrary selection of stars by tracing a straight line in the (R−Hα, $V - I$) color-color diagram (in the case of the $BVRI$+Hα filterset).

5.4 *Discussion*

The final result, presented in Figs.5.6 and 5.7, showed the potential of the developed method to find CBe candidates using photometry. The method represents a major step forward from previous studies that employed a visual inspection on color-magnitude and color-color diagrams.

It is important to notice that the method worked without the need of finding stars with high membership probability with just few prior knowledge about the cluster – such as distance and age values or the position of non-MS/foreground objects in color-magnitude and color-color diagrams. Even without this kind of information, a meaningful analysis on the SAMI data of NGC 330 could have been done, by fitting isochrones on the population, for example.

Also, it is possible to see that both k-NN and DT were able to correctly identify the majority of sources expected in each of the three possible classes in the SAMI observation, even for the large list of 4430 sources, only filtered by the criterion of observed magnitudes in every filter.

k-NN and DT correctly learned from our synthetic cluster that CBe stars, when inactive or with less dense disks, tend to be on the right side of the MS, because of the fast rotation or the combination of fast rotation plus a binary. Our CBe fraction results (which are also a lower limit estimate, as inactive CBe stars can still be classified as MS objects) of 19 ± 2% and 28 ± 3%, for k-NN and DT predictions. When making the same magnitude cut at $V = 18.48$ mag as Bodensteiner et al. (2020), the fraction is evaluated with a higher value for both predictors (51 ± 3% and 57 ± 4% for k-NN and DT, respectively).

The predicted CBe fraction in our method is expected to be higher than the lower limit estimates obtained from photometric methods [e.g., using just visual separation on the $(V - I, R{-}\mathrm{H}\alpha)$ diagram], but can also be higher or lower when compared to high resolution spectroscopic observations with the same magnitude depth. Thus, one plausible conclusion is that our method becomes interesting to be used before extensive spectroscopic follow-up, allowing better usage of the available (and expensive) telescope time.

Moreover, this is the first work to consider every known properties of CBe disks (according to the VDD formulation) – such as different values of the disk density, the radial fall-off exponent, the disk radius or the proportion between active and inactive stars – to suitably estimate the CBe population of a stellar cluster, finding higher CBe content than previous estimates when the same conditions are met.

However, even with an important positive result, it is necessary to point out existent limitations in the current developed method. First, BeAtlas v2 consists of hdust models and also is highly structured on the Geneva single evolution tracks for rotating stars. Although hdust still deals with only the Hydrogen atom in the system composition, uses Kurucz LTE spectra to derive intensity tables for the rotating star, supports only single star + disk systems, and does not consider electron scattering when calculating line spectra, these technical limitations do not represent a problem for the synthetic photometry.

For example, other atomic species are useful for some of the S-PLUS spectral features or in photometric surveys with a large number of narrow bands. The usage of LTE spectra has a greater impact on the far-UV region, only observable by space missions. In our method, binary stars could be mimicked by calculating two MS stars (in the case of non-CBes) or adding a flux equivalent to a fixed percentage of the primary flux. Among the explained limitations, the missing electron scattering in line profiles do not interfere in our synthetic cluster, as the Sobolev method (Sobolev, 1960) used by hdust ensures that the total Hα flux is correct.

When considering the Geneva evolutionary tracks, in which the stellar structure of a star is based of for a set of $(M, W, t/t_{\mathrm{MS}})$, the stellar ages provided in the tracks helped to construct a bonafide MS. However, whenever BeAtlas receives new updates, a parametric grid may be a better solution, even if more computationally costly, as some CBes cannot be represented by the TAMS (or near TAMS) values of $R_{\rm p}$ and L.

In addition to the HDUST latest version and Geneva grid limitations, the disk grid BEATLAS v2 is not entirely computed yet, with just the far-UV and the optical SED plus the Hα line profile calculated, and with some missing values of rotation rate W and disk radius $R_{\rm D}$.

The second limitation is the complexity of parameters, either pre-defined inputs by the user or internal conditions of the cluster generator. For example, an analysis of another cluster may require a custom touch, changing the proportion of active and inactive CBes, the density distribution or even the CBe fraction for each spectral type bin.

Many future works are possible with the synthetic cluster generation script, such as building an optimized version to be used together with MCMC methods to infer an observed cluster parameters (by for example, making a grid of synthetic clusters to be interpolated and fitted to the data) or even creating a sample of YOCs and adding their composite spectra to simulate a young galaxy, which would be useful for identifying the impacts of CBes in SSPs fitting methods over observed galaxy spectra. Another possibility is the creation of probability maps in a photometric diagram, indicating in a grid the probability of membership to each class for a certain bin. In every future projects related with this material, the addition of polarimetric information (present in BEATLAS) can also be of extreme value.

Before ending the discussion, a table containing the sky position (α, δ), the SAMI magnitudes (if existent, also the S-PLUS magnitudes) and the class label predicted by k-NN and DT for every star in the 4430 list is available as online extra material. In the next chapter, the conclusions and future perspectives are ran through.

Chapter 6

Conclusions

The study of CBe stars continues to flourish as time passes by, with many open questions regarding the origin of the fast rotation, the disk evolution in single and binary systems, disk dynamics in misaligned and/or eccentric orbits in multiple systems, metallicity effects on the CBe class and on the disk itself and even stronger confirmations of the VDD formulation as the bastion of the physical formulation or of NRPs as the main source of instability before mass ejection.

However, CBe stars can only be deeply investigated if they are observed and *classified* as CBes. The classification of large samples of unknown CBe stars can appear as a difficult subject, as developed photometric methods could only correctly identify candidate CBe stars in a given population using narrow band Hα filters and by pre-selecting probable cluster members, resulting in the selection of just strong Hα emitters – in this situation, inactive CBes or tenuous disks are generally invisible to the classification – and spectroscopic surveys can be costly, as CBes are naturally variable in a wide range of timescales and depending on the instrumental setup, many nights have to be spent to observe all B stars of a YOC, for example.

Our developed method tried to tie realistic normal and CBe stars models from the BeAtlas grid, computed with NLTE 3D radiative transfer, to stellar population synthesis, in order to be able to construct a YOC, from a given set of hypotheses (e.g., the IMF form, the total cluster mass, distance, reddening, metallicity, rotation and viewing angle distribution of each star, and others), containing representative CBe stars, and then generate workable outputs – such as synthetic photometry, calculated with flux convolution for the transmission curves of different filter sets and magnitude systems.

One extensively studied YOC was the stellar cluster NGC 330, about which pioneer articles showing photometric methods of separating CBes from normal stars using color-magnitude and color-color diagrams were published. Specifically for this work, we aimed to build a synthetic cluster to represent NGC 330, based on prior knowledge of the cluster, such as the adopted SMC distance of 62.44 kpc and its binary fraction of 14%, allowing photometric noise and the inclusion of non-MS and foreground objects, trying to mimic observations from the SOAR telescope (obtained with adaptive optics) and the S-PLUS survey. The generated output, saved in a table format, also contains data labeling, in order to simplify the distinction between normal and CBe stars.

The main idea was to use the synthetic photometry as input data to train machine learning classification algorithms, and then predict candidate CBe stars from observed magnitudes. The chosen ML algorithms were k-Nearest Neighbors and Decision Tree, both supervised estimators capable of dealing with multi-class prediction. The hyperparameters of both algorithms were fine-tuned using cross-validation in the train set, and final evaluation was done using a test set.

After k-NN and DT were trained in the synthetic NGC 330 input data, both models were used to predict to which class each star, from the SAMI and S-PLUS observations, belonged to. For the S-PLUS data, $\sim$ 20% of the sample was classified as CBe candidates on both estimators (44 and 47 sources for k-NN and DT, respectively). However, as the sample contained few stars (a total of 250 objects), the result is not so impressive as for SAMI magnitudes.

For the SAMI observation, which consists of 4430 objects observed in all filters, 206 and 289 stars were classified as CBe candidates, for k-NN and DT. These values represent a CBe fraction of 19 ± 2% and 28 ± 3% over the B spectral type magnitude range. For both estimators, almost every CBe with Hα emission was classified as such; but the most remarkable result lies on the prediction of CBe candidates in the “redder” side of the MS, location of inactive CBes or systems with less dense disks.

The developed and presented method in this work is easily reproducible for other YOCs, and is mostly suitable to study main sequences composed of O8.5V to A7V type stars. The next step is making the process more user-friendly, to assist other students of our group and external collaborators, and then make it accessible to the astronomical community together with BeAtlas. Our results are to be included in Navarete et al. 2023 (submitted), the first paper of a planned series, with it being focused on presenting the SAMI data reduction pipeline, the calibration methodology (template fitting), plus the analysis and detection of CBe candidates using our synthetic cluster along with supervised ML classification models.

There is an extense list of alternate usages of our synthetic cluster generation script, such as calculating composite spectra of a YOC (to either study unresolved spectra) or a sample of YOCs (to analyze galaxy spectra) or even extending to a MCMC inference approach, in which a stellar cluster has its parameters fitted from a grid of calculated synthetic clusters.

Bibliography

Abbott D., Garmany C., Hansen C., Henrichs H., Pesnell W., The connection between nonradial pulsations and stellar winds in massive stars, Publications of the Astronomical Society of the Pacific, 1986, vol. 98, p. 29

Adelman S. J., The physical properties of normal A stars. In The A-Star Puzzle , vol. 224 of IAU Symposium, 2004, p. 1

Aihara H., Allende Prieto C., An D., Anderson S. F., Aubourg É., Balbinot E., Beers T. C., Berlind A. A., Bickerton S. J., Bizyaev D., Blanton M. R., Bochanski J. J., Bolton A. S., Bovy J., Brandt W. N., Brinkmann J., et al. The Eighth Data Release of the Sloan Digital Sky Survey: First Data from SDSS-III, ApJS, 2011, vol. 193, p. 29

Alcaino G., Alvarado F., Photoelectric UBVRI Sequences in the Magellanic Cloud Clusters Kron 3, NGC 330, NGC 1841, and NGC 2257, AJ, 1988, vol. 95, p. 1724

Almeida-Fernandes F., SamPedro L., Herpich F. R., Molino A., Barbosa C. E., Buzzo M. L., Overzier R. A., de Lima E. V. R., Nakazono L. M. I., Oliveira Schwarz G. B., Perottoni H. D., Bolutavicius G. F., Gutiérrez-Soto L. A., Santos-Silva T., Vitorelli A. Z., Werle A., Whitten e., Data Release 2 of S-PLUS: Accurate template-fitting based photometry covering 1000 deg^2 in 12 optical filters, MNRAS, 2022, vol. 511, p. 4590

Altman D. G., Bland J. M., Standard deviations and standard errors, BMJ, 2005, vol. 331, p. 903

Arp B. H., Southern Hemisphere Photometry VII. The color-magnitude diagram of NGC 330 and the adjoining region of the Small Magellanic Cloud., AJ, 1959, vol. 64, p. 254

Baade D., Rivinius T., Štefl S., Kaufer A., A spectroscopic search for variability of Be stars in the SMC, A&A, 2002, vol. 383, p. L31

Bastian N., Cabrera-Ziri I., Niederhofer F., de Mink S., Georgy C., Baade D., Correnti M., Usher C., Romaniello M., A high fraction of Be stars in young massive clusters: evidence for a large population of near-critically rotating stars, Monthly Notices of the Royal Astronomical Society, 2016, vol. 465, p. 4795

Batista Souza T., Modelizacao de estrelas Be Classicas na regiao do infravermelho proximo observadas no levantamento APOGEE, Observatório Nacional, 2015, Masters' dissertation

Batista Souza T., Estudo espectroscópico, fotométrico e interferométrico de estrelas Be Clássicas, Observatorio Nacional, 2021, Ph.D. Thesis

Bessell M. S., Wood P. R., , 1993 in Baschek B., Klare G., Lequeux J., eds, , Vol. 416, New Aspects of Magellanic Cloud Research. p. 271

Bethe H. A., Energy Production in Stars, Physical Review, 1939, vol. 55, p. 434

Bjorkman J. E., Carciofi A. C., Modeling the Structure of Hot Star Disks. In The Nature and Evolution of Disks Around Hot Stars , vol. 337 of Astronomical Society of the Pacific Conference Series, 2005, p. 75

Bodensteiner J., Sana H., Mahy L., Patrick L. R., de Koter A., de Mink S. E., Evans C. J., Götberg Y., Langer N., Lennon D. J., Schneider F. R. N., Tramper F., The young massive SMC cluster NGC 330 seen by MUSE. I. Observations and stellar content, A&A, 2020, vol. 634, p. A51

Bodensteiner J., Shenar T., Sana H., Investigating the lack of main-sequence companions to massive Be stars, A&A, 2020, vol. 641, p. A42

Bohlin R. C., Hubeny I., Rauch T., New Grids of Pure-hydrogen White Dwarf NLTE Model Atmospheres and the HST/STIS Flux Calibration, AJ, 2020, vol. 160, p. 21

Branch D., Wheeler J. C., Supernova Explosions, 2017

Breiman L., Friedman J., Stone C. J., Olshen R. A., Classification and Regression Trees. Chapman and Hall/CRC, 1984

Bresolin F., Urbaneja M. A., Gieren W., Pietrzyński G., Kudritzki R.-P., VLT Spectroscopy of Blue Supergiants in IC 1613, ApJ, 2007, vol. 671, p. 2028

Bressan A., Marigo P., Girardi L., Salasnich B., Dal Cero C., Rubele S., Nanni A., PARSEC: stellar tracks and isochrones with the PAdova and TRieste Stellar Evolution Code, MNRAS, 2012, vol. 427, p. 127

Brott I., Evans C. J., Hunter I., de Koter A., Langer N., Dufton P. L., Cantiello M., Trundle C., Lennon D. J., de Mink S. E., Yoon S. C., Anders P., Rotating massive main-sequence stars. II. Simulating a population of LMC early B-type stars as a test of rotational mixing, A&A, 2011, vol. 530, p. A116

Brunish W. M., Truran J. W., The evolution of massive stars. II. The influence of initial composition and mass loss., ApJS, 1982, vol. 49, p. 447

Cannon A. J., Pickering E. C., Classification of 1,688 southern stars by means of their spectra, Annals of Harvard College Observatory, 1912, vol. 56, p. 115

Carciofi A. C., Bjorkman J. E., Non-LTE Monte Carlo Radiative Transfer. I. The Thermal Properties of Keplerian Disks around Classical Be Stars, ApJ, 2006, vol. 639, p. 1081

Carciofi A. C., Bjorkman J. E., Non-LTE Monte Carlo Radiative Transfer. II. Nonisothermal Solutions for Viscous Keplerian Disks, ApJ, 2008, vol. 684, p. 1374

Cardelli J. A., Clayton G. C., Mathis J. S., The relationship between infrared, optical, and ultraviolet extinction, ApJ, 1989, vol. 345, p. 245

Carney B. W., Janes K. A., Flower P. J., The young SMC cluster NGC 330., AJ, 1985, vol. 90, p. 1196

Castor J. I., Abbott D. C., Klein R. I., Radiation-driven winds in Of stars., ApJ, 1975, vol. 195, p. 157

Chabrier G., Galactic Stellar and Substellar Initial Mass Function, PASP, 2003, vol. 115, p. 763

Chandrasekhar S., The Maximum Mass of Ideal White Dwarfs, ApJ, 1931, vol. 74, p. 81

Chandrasekhar S., An introduction to the study of stellar structure, 1939

Charbonnel C., Meynet G., Maeder A., Schaller G., Schaerer D., Grids of stellar models. III. From 0.8 to 120 Msolar at Z=0.004, A&AS, 1993, vol. 101, p. 415

Chen Y., Girardi L., Fu X., Bressan A., Aringer B., Dal Tio P., Pastorelli G., Marigo P., Costa G., Zhang X., YBC: a stellar bolometric corrections database with variable extinction coefficients. Application to PARSEC isochrones, A&A, 2019, vol. 632, p. A105

Coelho P. R. T., A new library of theoretical stellar spectra with scaled-solar and α-enhanced mixtures, MNRAS, 2014, vol. 440, p. 1027

Crowther P. A., Schnurr O., Hirschi R., Yusof N., Parker R. J., Goodwin S. P., Kassim H. A., The R136 star cluster hosts several stars whose individual masses greatly exceed the accepted 150M_{solar} stellar mass limit, MNRAS, 2010, vol. 408, p. 731

Cyr I. H., Jones C. E., Panoglou D., Carciofi A. C., Okazaki A. T., Be discs in binary systems - II. Misaligned orbits, MNRAS, 2017, vol. 471, p. 596

Diolaiti E., Bendinelli O., Bonaccini D., Close L., Currie D., Parmeggiani G., Analysis of isoplanatic high resolution stellar fields by the StarFinder code, A&AS, 2000, vol. 147, p. 335

Domiciano de Souza A., Kervella P., Moser Faes D., Dalla Vedova G., Mérand A., Le Bouquin J. B., Espinosa Lara F., Rieutord M., Bendjoya P., Carciofi A. C., Hadjara M., Millour F., Vakili F., The environment of the fast rotating star Achernar. III. Photospheric parameters revealed by the VLTI, A&A, 2014, vol. 569, p. A10

Dunstall P. R., Brott I., Dufton P. L., Lennon D. J., Evans C. J., Smartt S. J., Hunter I., The VLT-FLAMES survey of massive stars: Nitrogen abundances for Be-type stars in the Magellanic Clouds, A&A, 2011, vol. 536, p. A65

Espinosa Lara F., Rieutord M., Gravity darkening in rotating stars, A&A, 2011, vol. 533, p. A43

Feast M. W., The cluster NGC 330 in the SMC (Paper II): Halpha emission in main sequence stars., MNRAS, 1972, vol. 159, p. 113

Feigelson E. D., Babu G. J., Big Data in Astronomy, Significance, 2012, vol. 9, p. 22

Fitzpatrick E. L., Massa D., Determining the Physical Properties of the B Stars. I. Methodology and First Results, ApJ, 1999, vol. 525, p. 1011

Friel E. D., The Old Open Clusters Of The Milky Way, ARA&A, 1995, vol. 33, p. 381

Fukugita M., Ichikawa T., Gunn J. E., Doi M., Shimasaku K., Schneider D. P., The Sloan Digital Sky Survey Photometric System, AJ, 1996, vol. 111, p. 1748

Gaia Collaboration Prusti T., de Bruijne J. H. J., Brown A. G. A., Vallenari A., Babusiaux C., Bailer-Jones C. A. L., Bastian U., Biermann M., Evans D. W., et al. The Gaia mission, A&A, 2016, vol. 595, p. A1

Genaro M., Inferência Bayesiana de Parâmetros Fundamentais de Estrelas Be por meio de Observações Espectroscópicas, Universidade de São Paulo, IAG/USP, 2020, Bachelor's monograph

Georgy C., Ekström S., Granada A., Meynet G., Mowlavi N., Eggenberger P., Maeder A., Populations of rotating stars. I. Models from 1.7 to 15 $M_\odot$ at $Z = 0.014$, 0.006, and 0.002 with Ω/Ω_{crit} between 0 and 1, A&A, 2013a, vol. 553, p. A24

Georgy C., Ekström S., Granada A., Meynet G., Mowlavi N., Eggenberger P., Maeder A., Populations of rotating stars. I. Models from 1.7 to 15 $M_\odot$ at $Z = 0.014$, 0.006, and 0.002 with Ω/Ω_{crit} between 0 and 1, A&A, 2013b, vol. 553, p. A24

Gholamy A., Kreinovich V., Kosheleva O., Why 70/30 or 80/20 Relation Between Training and Testing Sets: A Pedagogical Explanation., International Journal of Intelligent Technologies & Applied Statistics, 2018, vol. 11

Ghoreyshi M. R., Carciofi A. C., Jones C. E., Faes D. M., Baade D., Rivinius T., A Multi-Observing Technique Study of the Dynamical Evolution of the Viscous Disk around the Be Star ω CMa, ApJ, 2021, vol. 909, p. 149

Ghoreyshi M. R., Carciofi A. C., Rímulo L. R., Vieira R. G., Faes D. M., Baade D., Bjorkman J. E., Otero S., Rivinius T., The life cycles of Be viscous decretion discs: The case of ω CMa, MNRAS, 2018, vol. 479, p. 2214

Ghosh E. M., Sulistiyowati Tucio P., Fajrin M., Membership and age determination of M67 open cluster using GAIA EDR3 data, Journal of Physics: Conference Series, 2022, vol. 2214, p. 012009

Gontcharov G. A., Mosenkov A. V., Khovritchev M. Y., Isochrone fitting of Galactic globular clusters - I. NGC 5904, MNRAS, 2019, vol. 483, p. 4949

Graczyk D., Pietrzyński G., Thompson I. B., Gieren W., Zgirski B., Villanova S., Górski M., Wielgórski P., Karczmarek P., Narloch W., Pilecki B., Taormina M., Smolec R., Suchomska K., Gallenne A., Nardetto N., Storm J., Kudritzki R.-P., Kałuszyński M., Pych W., A Distance Determination to the Small Magellanic Cloud with an Accuracy of Better than Two Percent Based on Late-type Eclipsing Binary Stars, ApJ, 2020, vol. 904, p. 13

Granada A., Ekström S., Georgy C., Krtička J., Owocki S., Meynet G., Maeder A., Populations of rotating stars. II. Rapid rotators and their link to Be-type stars, A&A, 2013, vol. 553, p. A25

Granada A., Ghoreyshi M. R., Jones C. E., Eenmäe T., New Method to Detect and Characterize Active Be Star Candidates in Open Clusters, Galaxies, 2023, vol. 11

Grebel E. K., Richter T., de Boer K. S., Be star surveys with CCD photometry. I. NGC 330 and its high Be star content., A&A, 1992, vol. 254, p. L5

Grebel E. K., Roberts W. J., Brandner W., On the nature of the blue giants in NGC 330., A&A, 1996, vol. 311, p. 470

Hastings B., Wang C., Langer N., The single star path to Be stars, A&A, 2020, vol. 633, p. A165

Haubois X., Carciofi A. C., Rivinius T., Okazaki A. T., Bjorkman J. E., Dynamical Evolution of Viscous Disks around Be Stars. I. Photometry, ApJ, 2012, vol. 756, p. 156

Hertzsprung E., Ueber die Verwendung photographischer effektiver Wellenlaengen zur Bestimmung von Farbenaequivalenten, Publikationen des Astrophysikalischen Observatoriums zu Potsdam, 1911, vol. 63

Hoyle F., On the Main-Sequence Band and the Hertzsprung GAP $\star$, Monthly Notices of the Royal Astronomical Society, 1960, vol. 120, p. 22

Hubeny I., Mihalas D., Theory of Stellar Atmospheres, 2014

Hummel W., Gässler W., Muschielok B., Schink H., Nicklas H., Conti G., Mattaini E., Keller S., Mantel K. H., Appenzeller I., Rupprecht G., Seifert W., Stahl O., Tarantik K., Hα emission line spectroscopy in NGC 330. On the hybrid model for global oscillations in Be star circumstellar disks, A&A, 2001, vol. 371, p. 932

Hummel W., Szeifert T., Gässler W., Muschielok B., Seifert W., Appenzeller I., Rupprecht G., A spectroscopic study of Be stars in the SMC cluster NGC 330, A&A, 1999, vol. 352, p. L31

Iliadis C., Nuclear Physics of Stars, 2007

Iqbal S., Keller S. C., A study of Be stars in the Magellanic Clouds, Monthly Notices of the Royal Astronomical Society, 2013, vol. 435, p. 3103

Ivezić Z., Connolly A. J., VanderPlas J. T., Gray A., Statistics, Data Mining, and Machine Learning in Astronomy: A Practical Python Guide for the Analysis of Survey Data stu - student edition edn. Princeton University Press, 2014

Janson M., Hormuth F., Bergfors C., Brandner W., Hippler S., Daemgen S., Kudryavtseva N., Schmalzl E., Schnupp C., Henning T., The AstraLux Large M-dwarf Multiplicity Survey, ApJ, 2012, vol. 754, p. 44

Johnson H. L., Morgan W. W., Fundamental stellar photometry for standards of spectral type on the Revised System of the Yerkes Spectral Atlas., ApJ, 1953, vol. 117, p. 313

Karakas A. I., Low- and Intermediate-Mass Stars, 2017, 461

Keller S. C., Bessell M. S., Spectroscopy of Be stars in the Small Magellanic Cloud cluster NGC 330, A&A, 1998, vol. 340, p. 397

Keller S. C., Wood P. R., Bessell M. S., Be stars in and around young clusters in the Magellanic Clouds, A&AS, 1999, vol. 134, p. 489

Kepler S. O., Kleinman S. J., Nitta A., Koester D., Castanheira B. G., Giovannini O., Costa A. F. M., Althaus L., White dwarf mass distribution in the SDSS, Monthly Notices of the Royal Astronomical Society, 2007, vol. 375, p. 1315

Kervella P., Borgniet S., Domiciano de Souza A., Mérand A., Gallenne A., Rivinius T., Lacour S., Carciofi A., Faes D. M., Le Bouquin J.-B., Taormina M., Pilecki B., Berger J.-P., Bendjoya P., Klement R., Millour F., Janot-Pacheco E., Spang A., Vakili F., The binary system of the spinning-top Be star Achernar, A&A, 2022, vol. 667, p. A111

King I. R., The structure of star clusters. III. Some simple dynamical models, AJ, 1966, vol. 71, p. 64

Klement R., Baade D., Rivinius T., Gies D. R., Wang L., Labadie-Bartz J., Ticiani dos Santos P., Monnier J. D., Carciofi A. C., Mérand A., Anugu N., Schaefer G. H., Le Bouquin J.-B., Davies C. L., Ennis J., Gardner T., Kraus S., Setterholm B. R., Labdon A., Dynamical Masses of the Primary Be Star and Secondary sdB Star in the Single-lined Binary κ Dra (B6 IIIe), ApJ, 2022, vol. 940, p. 86

Klement R., Carciofi A. C., Rivinius T., Ignace R., Matthews L. D., Torstensson K., Gies D., Vieira R. G., Richardson N. D., Domiciano de Souza A., Bjorkman J. E., Hallinan G., Faes D. M., Mota B., Gullingsrud A. D., de Breuck C., Kervella P., Curé M., Gunawan D., Prevalence of SED Turndown among Classical Be Stars: Are All Be Stars Close Binaries?, ApJ, 2019, vol. 885, p. 147

Koubský P., Kotková L., Votruba V., Šlechta M., Dvořáková Š., o Puppis: another Be+sdO binary?, A&A, 2012, vol. 545, p. A121

Kramer O., Dimensionality Reduction with Unsupervised Nearest Neighbors. Springer Publishing Company, Incorporated, 2013

Kroupa P., On the variation of the initial mass function, MNRAS, 2001, vol. 322, p. 231

Krumholz M. R., McKee C. F., Bland-Hawthorn J., Star Clusters Across Cosmic Time, ARA&A, 2019, vol. 57, p. 227

Kurfürst P., Feldmeier A., Krtička J., Two-dimensional modeling of density and thermal structure of dense circumstellar outflowing disks, A&A, 2018, vol. 613, p. A75

Kurucz R., ATLAS9 Stellar Atmosphere Programs and 2 km/s grid., ATLAS9 Stellar Atmosphere Programs and 2 km/s grid. Kurucz CD-ROM No. 13. Cambridge, 1993, vol. 13

Labadie-Bartz J., Carciofi A. C., Henrique de Amorim T., Rubio A., Luiz Figueiredo A., Ticiani dos Santos P., Thomson-Paressant K., Classifying Be Star Variability With TESS. I. The Southern Ecliptic, AJ, 2022, vol. 163, p. 226

Lada C. J., Lada E. A., Embedded Clusters in Molecular Clouds, ARA&A, 2003, vol. 41, p. 57

Lamers H. J. G. L. M., Cassinelli J. P., Introduction to Stellar Winds, 1999

Lamers H. J. G. L. M., Zickgraf F.-J., de Winter D., Houziaux L., Zorec J., An improved classification of B[e]-type stars, A&A, 1998, vol. 340, p. 117

Landolt A. U., Clem J. L., The Definitive Johnson Kron-Cousins UBVRI Photometric System. In IAU General Assembly , vol. 29, 2015, p. 2229744

Langer N., Presupernova Evolution of Massive Single and Binary Stars, Annual Review of Astronomy and Astrophysics, 2012, vol. 50, p. 107

Lee U., Osaki Y., Saio H., Viscous excretion discs around Be stars, MNRAS, 1991, vol. 250, p. 432

Levenhagen R. S., Leister N. V., Spectroscopic analysis of southern B and Be stars, MNRAS, 2006, vol. 371, p. 252

Lindegren L., Klioner S. A., Hernández J., Bombrun A., Ramos-Lerate M., Steidelmüller H., Bastian U., Biermann M., de Torres A., Gerlach E., Geyer R., Hilger T., Hobbs D., Lammers U., McMillan P. J., Stephenson C. A., Castañeda J., Davidson M., Fabricius C., Gracia-Abril G., Portell J., Rowell N., Teyssier D., Torra F., et al., Gaia Early Data Release 3. The astrometric solution, A&A, 2021, vol. 649, p. A2

Liu T., Moore A. W., Gray A., New Algorithms for Efficient High-Dimensional Nonparametric Classification, J. Mach. Learn. Res., 2006, vol. 7, p. 1135–1158

Lucy L. B., Solomon P. M., Mass Loss by Hot Stars, ApJ, 1970, vol. 159, p. 879

Luri X., Brown A. G. A., Sarro L. M., Arenou F., Bailer-Jones C. A. L., Castro-Ginard A., de Bruijne J., Prusti T., Babusiaux C., Delgado H. E., Gaia Data Release 2. Using Gaia parallaxes, A&A, 2018, vol. 616, p. A9

McGill M. A., Sigut T. A. A., Jones C. E., THE EFFECT OF DENSITY ON THE THERMAL STRUCTURE OF GRAVITATIONALLY DARKENED Be STAR DISKS, The Astrophysical Journal Supplement Series, 2012, vol. 204, p. 2

McInnes L., Healy J., Astels S., hdbscan: Hierarchical density based clustering, The Journal of Open Source Software, 2017, vol. 2

Maeder A., Physics, Formation and Evolution of Rotating Stars, 2009

Maimon O., Rokach L., Data Mining and Knowledge Discovery Handbook. Springer-Verlag Berlin, Heidelberg, 2005

Martayan C., Floquet M., Hubert A. M., Gutiérrez-Soto J., Fabregat J., Neiner C., Mekkas M., Be stars and binaries in the field of the SMC open cluster NGC 330 with VLT-FLAMES, A&A, 2007, vol. 472, p. 577

Martayan C., Frémat Y., Hubert A. M., Floquet M., Zorec J., Neiner C., Effects of metallicity, star-formation conditions, and evolution in B and Be stars. I. Large Magellanic Cloud, field of NGC 2004, A&A, 2006, vol. 452, p. 273

Martayan C., Frémat Y., Hubert A.-M., Floquet M., Zorec J., Neiner C., Effects of metallicity, star-formation conditions, and evolution in B and Be stars. II. Small Magellanic Cloud, field of NGC 330, A&A, 2007, vol. 462, p. 683

Martins F., Schaerer D., Hillier D. J., A new calibration of stellar parameters of Galactic O stars, A&A, 2005, vol. 436, p. 1049

Mazzali P. A., Lennon D. J., Pasian F., Marconi G., Baade D., Castellani V., Properties of the Be stars in the field of the Small Magellanic Cloud cluster NGC 330., A&A, 1996, vol. 316, p. 173

McKee C. F., Ostriker E. C., Theory of Star Formation, ARA&A, 2007, vol. 45, p. 565

Mendes de Oliveira C., Ribeiro T., Schoenell W., Kanaan A., Overzier R. A., Molino A., Sampedro L., Coelho P., Barbosa C. E., Cortesi A., Costa-Duarte M. V., Herpich F. R., Hernandez-Jimenez J. A., Placco V. M., Xavier H. S., Abramo L. R., Saito R. K., Chies-Santos A. L., Ederoclite A., Lopes de Oliveira R., Gonçalves D. R., Akras S., et al., The Southern Photometric Local Universe Survey (S-PLUS): improved SEDs, morphologies, and redshifts with 12 optical filters, MNRAS, 2019, vol. 489, p. 241

Milone A. P., Marino A. F., Di Criscienzo M., D'Antona F., Bedin L. R., Da Costa G., Piotto G., Tailo M., Dotter A., Angeloni R., Anderson J., Jerjen H., Li C., Dupree A., Granata V., Lagioia E. P., Mackey A. D., Nardiello D., Vesperini E., Multiple stellar populations in Magellanic Cloud clusters – VI. A survey of multiple sequences and Be stars in young clusters, Monthly Notices of the Royal Astronomical Society, 2018, vol. 477, p. 2640

Mints A., Hekker S., Isochrone fitting in the Gaia era, A&A, 2018, vol. 618, p. A54

Morgan W. W., Keenan P. C., Kellman E., An atlas of stellar spectra, with an outline of spectral classification, 1943

Mota B. C., BeAtlas: A grid of synthetic spectra for Be stars, IAG-USP <ORCID>0000-0002-7851-4242</ORCID>, 2019, Ph.D. Thesis

Mucesh S., Hartley W. G., Palmese A., Lahav O., Whiteway L., Bluck A. F. L., Alarcon A., Amon A., Bechtol K., Bernstein G. M., Carnero Rosell A., Carrasco Kind M., Choi A., Eckert K., Everett S., Gruen D., Collaboration) D., A machine learning approach to galaxy properties: joint redshift–stellar mass probability distributions with Random Forest, Monthly Notices of the Royal Astronomical Society, 2021, vol. 502, p. 2770

Negueruela I., Steele I. A., Bernabeu G., On the class of Oe stars, Astronomische Nachrichten, 2004, vol. 325, p. 749

Oey M. S., Castro N., Renzo M., Vargas-Salazar I., Suffak M. W., Ratajczak M., Monnier J. D., Szymanski M. K., Phillips G. D., Calvet N., Chiti A., Micheva G., Rasmussen K. C., Townsend R. H. D., Strong Variability in AzV 493, an Extreme Oe-type Star in the SMC, ApJ, 2023, vol. 947, p. 27

Okazaki A. T., Bate M. R., Ogilvie G. I., Pringle J. E., Viscous effects on the interaction between the coplanar decretion disc and the neutron star in Be/X-ray binaries, MNRAS, 2002, vol. 337, p. 967

Oke J. B., Gunn J. E., Secondary standard stars for absolute spectrophotometry., ApJ, 1983, vol. 266, p. 713

Osuna P., Ortiz I., Lusted J., Dowler P., Szalay A., Shirasaki Y., Nieto-Santisteban M. A., Ohishi M., O'Mullane W., VOQL-TEG Group VOQL Working Group., 2008 IVOA Astronomical Data Query Language Version 2.00 IVOA Recommendation 30 October 2008

Oudmaijer R. D., Parr A. M., The binary fraction and mass ratio of Be and B stars: a comparative Very Large Telescope/NACO study, MNRAS, 2010, vol. 405, p. 2439

Packet W., On the spin-up of the mass accreting component in a close binary system, A&A, 1981, vol. 102, p. 17

Paczynski B., Evolutionary Processes in Close Binary Systems, Annual Review of Astronomy and Astrophysics, 1971, vol. 9, p. 183

Panoglou D., Carciofi A. C., Vieira R. G., Cyr I. H., Jones C. E., Okazaki A. T., Rivinius T., Be discs in binary systems - I. Coplanar orbits, MNRAS, 2016, vol. 461, p. 2616

Patrick L. R., Lennon D. J., Evans C. J., Sana H., Bodensteiner J., Britavskiy N., Dorda R., Herrero A., Negueruela I., de Koter A., Multiplicity of the red supergiant population in the young massive cluster NGC 330, A&A, 2020, vol. 635, p. A29

Payne C. H., Stellar Atmospheres; a Contribution to the Observational Study of High Temperature in the Reversing Layers of Stars., Radcliffe College, 1925, Ph.D. Thesis

Pedregosa F., Varoquaux G., Gramfort A., Michel V., Thirion B., Grisel O., Blondel M., Prettenhofer P., Weiss R., Dubourg V., Vanderplas J., Passos A., Cournapeau D., Brucher M., Perrot M., Duchesnay E., Scikit-learn: Machine Learning in Python, Journal of Machine Learning Research, 2011, vol. 12, p. 2825

Pepper J., Stassun K. G., Gaudi B. S., , 2018 in Deeg H. J., Belmonte J. A., eds, , Handbook of Exoplanets. p. 128

Perryman M. A. C., Lindegren L., Kovalevsky J., Hoeg E., Bastian U., Bernacca P. L., Crézé M., Donati F., Grenon M., Grewing M., van Leeuwen F., van der Marel H., Mignard F., Murray C. A., Le Poole R. S., Schrijver H., Turon C., Arenou F., Froeschlé M., Petersen C. S., The HIPPARCOS Catalogue, A&A, 1997, vol. 323, p. L49

Pestov V., Is the k-NN classifier in high dimensions affected by the curse of dimensionality?, Computers & Mathematics with Applications, 2013, vol. 65, p. 1427

Peters M., Wisniewski J. P., Williams B. F., Lomax J. R., Choi Y., Durbin M., Johnson L. C., Lewis A. R., Lutz J., Sigut T. A. A., Wallach A., Dalcanton J. J., The Hubble Space Telescope Advanced Camera for Surveys Emission Line Survey of Andromeda. I. Classical Be Stars, AJ, 2020, vol. 159, p. 119

Piatti A. E., Pietrzyński G., Narloch W., Górski M., Graczyk D., Metallicity estimates of young clusters in the Magellanic Clouds from Strömgren photometry of supergiant stars, Monthly Notices of the Royal Astronomical Society, 2018, vol. 483, p. 4766

Pickering E. C., The Draper Catalogue of stellar spectra photographed with the 8-inch Bache telescope as a part of the Henry Draper memorial, Annals of Harvard College Observatory, 1890, vol. 27, p. 1

Pickering E. C., Fleming W. P., Stars having peculiar spectra. Spectra of known variables., ApJ, 1905, vol. 22, p. 87

Portegies Zwart S. F., McMillan S. L. W., Gieles M., Young Massive Star Clusters, ARA&A, 2010, vol. 48, p. 431

Press W. H., Flannery B. P., Teukolsky S. A., Numerical recipes. The art of scientific computing, 1986

Prialnik D., An Introduction to the Theory of Stellar Structure and Evolution, 2009

Rafelski M., Zaritsky D., The Star Clusters of the Small Magellanic Cloud: Age Distribution, AJ, 2005, vol. 129, p. 2701

Reig P., Be/X-ray binaries, Ap&SS, 2011, vol. 332, p. 1

Reza M., Galaxy morphology classification using automated machine learning, Astronomy and Computing, 2021, vol. 37, p. 100492

Ricker G. R., Winn J. N., Vanderspek R., Latham D. W., Bakos G. Á., Bean J. L., Berta-Thompson Z. K., Brown T. M., Buchhave L., Butler N. R., Butler R. P., Chaplin W. J., Charbonneau D., Christensen-Dalsgaard J., Clampin M., Deming D., Doty J., De Lee N., Dressing C., Dunham E. W., Endl M., Fressin F., Ge J., Transiting Exoplanet Survey Satellite (TESS), Journal of Astronomical Telescopes, Instruments, and Systems, 2015, vol. 1, p. 014003

Rímulo L. R., Carciofi A. C., Vieira R. G., Rivinius T., Faes D. M., Figueiredo A. L., Bjorkman J. E., Georgy C., Ghoreyshi M. R., Soszyński I., The life cycles of Be viscous decretion discs: fundamental disc parameters of 54 SMC Be stars, MNRAS, 2018, vol. 476, p. 3555

Rivinius T., Baade D., Stefl S., Stahl O., Wolf B., Kaufer A., Stellar and circumstellar activity of the Be star MU Centauri. I. Line emission outbursts, A&A, 1998, vol. 333, p. 125

Rivinius T., Carciofi A. C., Martayan C., Classical Be stars. Rapidly rotating B stars with viscous Keplerian decretion disks, A&A Rev., 2013, vol. 21, p. 69

Robertson J. W., Core-Helium Stars in Young Clusters in the Large Magellanic Cloud, ApJ, 1974, vol. 191, p. 67

Rosenberg H., Über den Zusammenhang von Helligkeit und Spektraltypus in den Plejaden, Astronomische Nachrichten, 1910, vol. 186, p. 71

Rubio A. C., Eyes on Phact: unraveling a Be star and its disk, Universidade de São Paulo, IAG/USP, 2019, Masters' dissertation

Rubio A. C., Carciofi A. C., Ticiani P., Mota B. C., Vieira R. G., Faes D. M., Genaro M., de Amorim T. H., Klement R., Araya I., Arcos C., Curé M., de Souza A. D., Georgy C., Jones C. E., Suffak M. W., Silva A. C. F., Bayesian sampling with BeAtlas, a grid of synthetic Be star spectra I. Recovering the fundamental parameters of α Eri and β CMi, Monthly Notices of the Royal Astronomical Society, 2023, p. stad2652

Russell H. N., Relations Between the Spectra and Other Characteristics of the Stars, Popular Astronomy, 1914, vol. 22, p. 275

Salaris M., Cassisi S., Evolution of Stars and Stellar Populations, 2005

Salpeter E. E., The Luminosity Function and Stellar Evolution., ApJ, 1955, vol. 121, p. 161

Sana H., de Mink S. E., de Koter A., Langer N., Evans C. J., Gieles M., Gosset E., Izzard R. G., Le Bouquin J.-B., Schneider F. R. N., Binary Interaction Dominates the Evolution of Massive Stars, Science, 2012, vol. 337, p. 444

Sana H., Evans C. J., The multiplicity of massive stars. In Active OB Stars: Structure, Evolution, Mass Loss, and Critical Limits , vol. 272, 2011, p. 474

Scalo J. M., The Stellar Initial Mass Function, Fund. Cosmic Phys., 1986, vol. 11, p. 1

Schaller G., Schaerer D., Meynet G., Maeder A., New Grids of Stellar Models from 0.8-$M_\odot$ to 120-$M_\odot$ at Z=0.020 and Z=0.001, A&AS, 1992, vol. 96, p. 269

Schmidt-Kaler T., , 1982 4.1.2 Intrinsic colors and visual absolute magnitudes (calibration of the MK system): Datasheet from Landolt-Börnstein - Group VI Astronomy and Astrophysics · Volume 2B: "Stars and Star Clusters" in SpringerMaterials, publisher="Springer-Verlag Berlin Heidelberg

Schmidtke P. C., Chobanian J. B., Cowley A. P., Hot Variable Stars in the SMC Cluster NGC 330, AJ, 2008, vol. 135, p. 1350

Secchi A., Schreiben des Herrn Prof. Secchi, Dir. der Sternwarte des Collegio Romano, an den Herausgeber, Astronomische Nachrichten, 1867, vol. 68, p. 63

Shakura N. I., Sunyaev R. A., Black holes in binary systems. Observational appearance., A&A, 1973, vol. 24, p. 337

Shao Y., Li X.-D., On the Formation of Be Stars through Binary Interaction, ApJ, 2014, vol. 796, p. 37

Silaj J., Jones C. E., Sigut T. A. A., Tycner C., The Hα Profiles of Be Shell Stars, ApJ, 2014, vol. 795, p. 82

Slettebak A., Line Broadening in the Spectra of o- and Early B-Type Stars., ApJ, 1956, vol. 124, p. 173

Smith N., Mass Loss: Its Effect on the Evolution and Fate of High-Mass Stars, Annual Review of Astronomy and Astrophysics, 2014, vol. 52, p. 487

Soberman G. E., Phinney E. S., van den Heuvel E. P. J., Stability criteria for mass transfer in binary stellar evolution., A&A, 1997, vol. 327, p. 620

Sobolev V. V., Moving Envelopes of Stars, 1960

Song Y., Lu Y., Decision tree methods: applications for classification and prediction, Shanghai Archives of Psychiatry, 2015, vol. 27, p. 130

Sota A., Maíz Apellániz J., Walborn N. R., Alfaro E. J., Barbá R. H., Morrell N. I., Gamen R. C., Arias J. I., The Galactic O-Star Spectroscopic Survey. I. Classification System and Bright Northern Stars in the Blue-violet at R ~2500, ApJS, 2011, vol. 193, p. 24

Stryker L. L., Blue Stragglers, PASP, 1993, vol. 105, p. 1081

Tanabé T., Motohara K., Tateuchi K., Matsunaga N., Ita Y., Toshikawa K., Konishi M., Kato N., Yoshii Y., Paschen α Observations of Be Stars Toward the SMC Cluster NGC 330, PASJ, 2013, vol. 65, p. 55

Taylor M., , 2011 TOPCAT: Tool for OPerations on Catalogues And Tables Astrophysics Source Code Library, record ascl:1101.010

Tokovinin A., Cantarutti R., Tighe R., Schurter P., Martinez M., Thomas S., van der Bliek N., SOAR Adaptive Module (SAM): Seeing Improvement with a UV Laser, PASP, 2016, vol. 128, p. 125003

Touhami Y., Gies D. R., Schaefer G. H., Richardson N. D., McAlister H. A., Ridgway S. T., Brummelaar T. A. t., Goldfinger P. J., Sturmann L., Sturmann J., Turner N. H., Farrington C. D., A CHARA Array Long Baseline Interferometric Survey of Circumstellar Disks of Be Stars. In Resolving The Future Of Astronomy With Long-Baseline Interferometry , vol. 487 of Astronomical Society of the Pacific Conference Series, 2014, p. 395

Udalski A., Szymanski M., Kaluzny J., Kubiak M., Mateo M., The Optical Gravitational Lensing Experiment, Acta Astron., 1992, vol. 42, p. 253

Vallenari A., Ortolani S., Chiosi C., Photometry of the young cluster NGC 330 in the Small Magellanic Cloud., A&AS, 1994, vol. 108, p. 571

van Leeuwen F., de Bruijne J., Babusiaux C., Busso G., Castañeda J., Ducourant C., Fabricius C., Hambly N., Hobbs D., Luri X., Marrese P. M., Mora A., Muinonen K., Pourbaix D., Rimoldini L., Roegiers T., et al.,, 2022 Gaia DR3 documentation Gaia DR3 documentation, European Space Agency; Gaia Data Processing and Analysis Consortium. Online at https://gea.esac.esa.int/archive/documentation/GDR3/index.html, id. 1

Van Rossum G., Drake F. L., Python 3 Reference Manual. CreateSpace Scotts Valley, CA, 2009

Vieira K., García-Varela A., Sabogal B., Rímulo L. R., Hernández J., Red Be stars in the Magellanic Clouds?, MNRAS, 2021, vol. 505, p. 5567

Vieira R. G., Carciofi A. C., Bjorkman J. E., The pseudo-photosphere model for the continuum emission of gaseous discs, MNRAS, 2015, vol. 454, p. 2107

Vieira R. G., Carciofi A. C., Bjorkman J. E., Rivinius T., Baade D., Rímulo L. R., The life cycles of Be viscous decretion discs: time-dependent modelling of infrared continuum observations, MNRAS, 2017, vol. 464, p. 3071

Virtanen P., Gommers R., Oliphant T. E., Haberland M., Reddy T., Cournapeau D., Burovski E., Peterson P., Weckesser W., Bright J., van der Walt S. J., Brett M., Wilson J., Millman K. J., Mayorov N., Nelson A. R. J., Jones E., Kern R., Larson E., Carey C. J., Polat İ., Feng Y., Moore E. W., VanderPlas J., Laxalde D., Perktold J., Cimrman R., Henriksen I., Quintero E. A., Harris C. R., Archibald A. M., Ribeiro A. H., Pedregosa F., van Mulbregt P., SciPy 1.0 Contributors SciPy 1.0: Fundamental Algorithms for Scientific Computing in Python, Nature Methods, 2020, vol. 17, p. 261

von Zeipel H., The radiative equilibrium of a slightly oblate rotating star, MNRAS, 1924, vol. 84, p. 684

Wang C., Bai Y., López-Sanjuan C., Yuan H., Wang S., Liu J., Sobral D., Baqui P. O., Martín E. L., Andres Galarza C., Alcaniz J., Angulo R. E., Cenarro A. J., Cristóbal-Hornillos D., Dupke R. A., Ederoclite A., Hernández-Monteagudo C., Marín-Franch A., Moles M., Sodré L., Vázquez Ramió H., Varela J., J-PLUS: Support vector machine applied to STAR-GALAXY-QSO classification, A&A, 2022, vol. 659, p. A144

Wang C., Langer N., Schootemeijer A., Milone A., Hastings B., Xu X.-T., Bodensteiner J., Sana H., Castro N., Lennon D. J., Marchant P., de Koter A., de Mink S. E., Stellar mergers as the origin of the blue main-sequence band in young star clusters, Nature Astronomy, 2022, vol. 6, p. 480

Wang L., Gies D. R., Peters G. J., Detection of Additional Be+sdO Systems from IUE Spectroscopy, ApJ, 2018, vol. 853, p. 156

Waters L. B. F. M., Boland W., Taylor A. R., van de Stadt H., Lamers H. J. G. L. M., Millimeter observations of the Be stars Psi Persei and Gamma Cassiopeiae, A&A, 1989, vol. 213, p. L19

Wolf C., Onken C. A., Luvaul L. C., Schmidt B. P., Bessell M. S., Chang S.-W., Da Costa G. S., Mackey D., Martin-Jones T., Murphy S. J., Preston T., Scalzo R. A., Shao L., Smillie J., Tisserand P., White M. C., Yuan F., SkyMapper Southern Survey: First Data Release (DR1), PASA, 2018, vol. 35, p. e010

Wu J., Chen X.-Y., Zhang H., Xiong L.-D., Lei H., Deng S.-H., Hyperparameter Optimization for Machine Learning Models Based on Bayesian Optimizationb, Journal of Electronic Science and Technology, 2019, vol. 17, p. 26

Xiang M. S., Liu X. W., Shi J. R., Yuan H. B., Huang Y., Luo A. L., Zhang H. W., Zhao Y. H., Zhang J. N., Ren J. J., Chen B. Q., Wang C., Li J., Huo Z. Y., Zhang W., Wang J. L., Zhang Y., Hou Y. H., Wang Y. F., Estimating stellar atmospheric parameters, absolute magnitudes and elemental abundances from the LAMOST spectra with Kernel-based principal component analysis, MNRAS, 2017, vol. 464, p. 3657

Yan H., Li H., Wang S., Zong W., Yuan H., Xiang M., Huang Y., Xie J., Dong S., Yuan H., Bi S., Chu Y., Cui X., Deng L., Fu J., Han Z., Hou J., Li G., Liu C., Liu J., Liu X., Luo A., Shi J., Wu X., Zhang H., Zhao G., Zhao Y., Overview of the LAMOST survey in the first decade, The Innovation, 2022, vol. 3, p. 100224

York D. G., Adelman J., Anderson John E. J., Anderson S. F., Annis J., Bahcall N. A., Bakken J. A., Barkhouser R., Bastian S., Berman E., Boroski W. N., Bracker S., Briegel C., Briggs J. W., SDSS Collaboration The Sloan Digital Sky Survey: Technical Summary, AJ, 2000, vol. 120, p. 1579

Yu J., Tang B., Fernández-Trincado J. G., Geisler D., Yan H., Soto M., Chemical Tagging N-rich Field Stars with High-resolution Spectroscopy, The Astrophysical Journal, 2021, vol. 913, p. 23

Zaritsky D., Harris J., Thompson I. B., Grebel E. K., Massey P., The Magellanic Clouds Photometric Survey: The Small Magellanic Cloud Stellar Catalog and Extinction Map, AJ, 2002, vol. 123, p. 855

Zorec J., Briot D., Critical study of the frequency of Be stars taking into account their outstanding characteristics., A&A, 1997, vol. 318, p. 443

Zorec J., Frémat Y., Domiciano de Souza A., Royer F., Cidale L., Hubert A.-M., Semaan T., Martayan C., Cochetti Y. R., Arias M. L., Aidelman Y., Stee P., Critical study of the distribution of rotational velocities of Be stars. I. Deconvolution methods, effects due to gravity darkening, macroturbulence, and binarity, A&A, 2016, vol. 595, p. A132

Appendix

Appendix A

Additional plots of the BeAtlas v2 grid

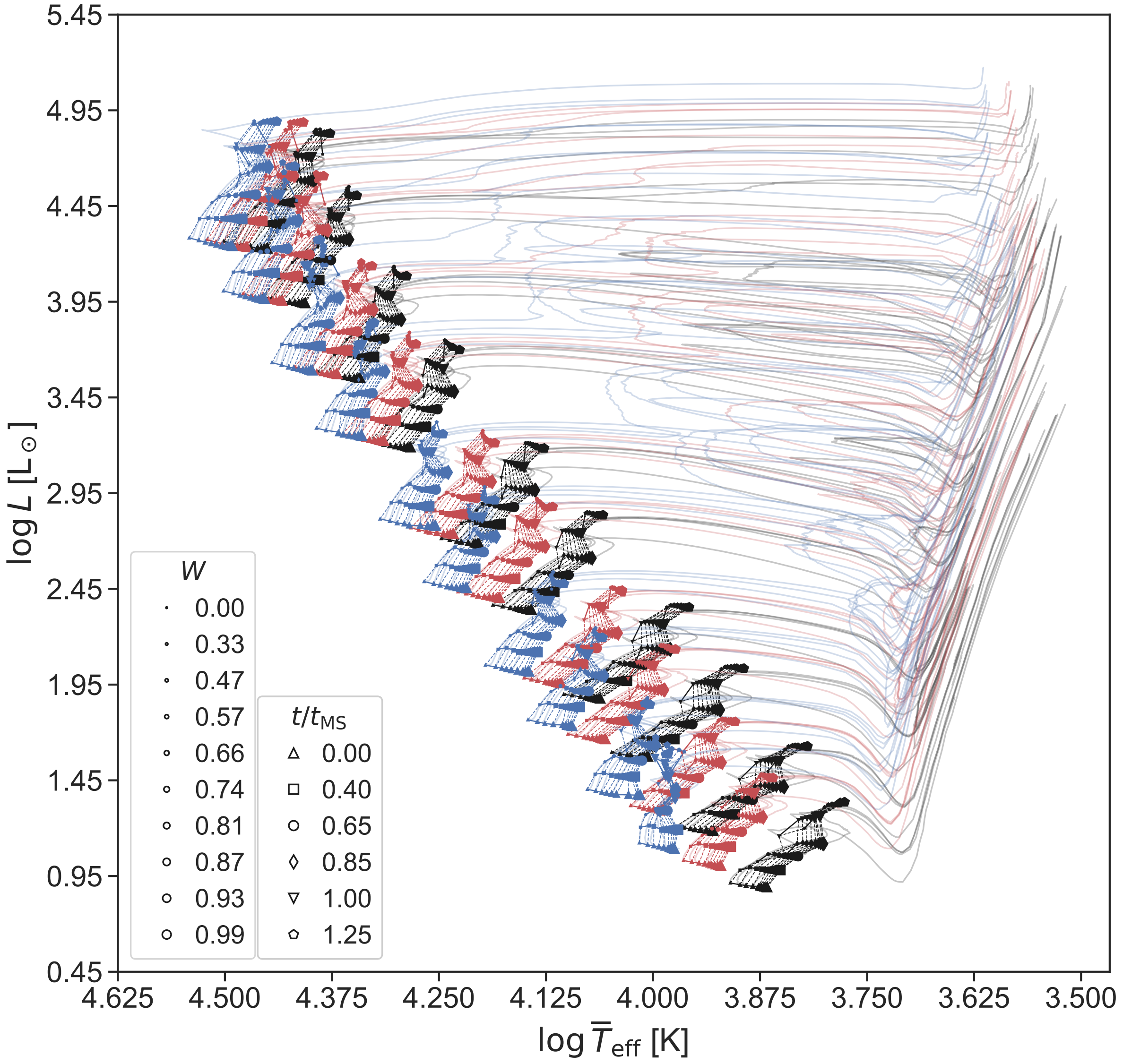

Figure A.1: Hertzsprung–Russell diagram comprising the photospheric grid parameters for masses up to $M = 15\,\mathrm{M}_\odot$. Metallicities are indicated by different marker colors, with $Z = 0.014$, 0.006 and 0.002 being respectively shown in black, red and blue. Marker sizes represent different rotation rates W. In solid lines following the same coloring for each Z, four complete Geneva tracks are shown, corresponding to the initial velocities of $W_{\rm Geneva} = 0$, 0.769, 0.925 and 0.998 for each stellar mass. Values of $t/t_{\rm MS}$ for each (M, W) pair are connected with dashed lines, following the tracks, indicated by different marker types; the path from ZAMS to TAMS goes from bottom left up to top right.

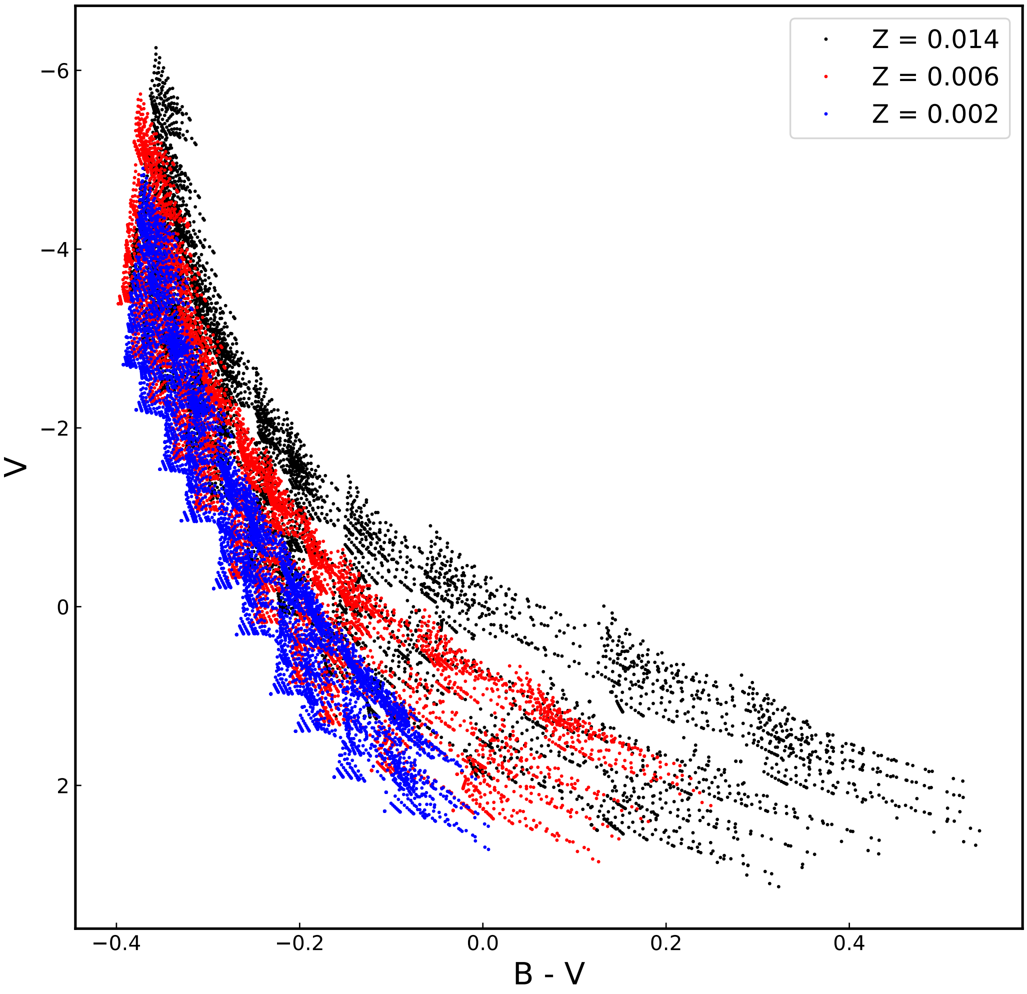

Figure A.2: (M_V, $B-V$) color-magnitude diagram of the BeAtlas v2 photospheric grid on the Vega system for every value of Z. In black, red and blue markers, models with Z = 0.014, Z = 0.006 and Z = 0.002. The configuration of this figure (markers' types and sizes) follows Fig. 2.6

Appendix B

BeAtlas paper

MNRAS 000, 1–34 (2023) Preprint 23 May 2023 Compiled using MNRAS LATEX style file v3.0

Bayesian sampling with BeAtlas, a grid of synthetic Be star spectra I. Recovering the fundamental parameters of α Eri and β CMi

A. C. Rubio[1,2⋆], A. C. Carciofi[1], P. Ticiani[1], B. C. Mota[1], R. G. Vieira[3], D. M. Faes[4], M. Genaro[5], T. H. de Amorim[1], R. Klement[6], I. Araya[7], C. Arcos[8], M. Curé[8], A. Domiciano de Souza[9], C. Georgy[10] C. E. Jones[11], M. W. Suffak[11], A. C. F. Silva[1]

[1] *Instituto de Astronomia, Geofísica e Ciências Atmosféricas, Universidade de São Paulo, Rua do Matão 1226, 05508-900 São Paulo, Brazil*
[2] *European Organisation for Astronomical Research in the Southern Hemisphere (ESO), Karl-Schwarzschild-Str. 2, 85748 Garching b. München, Germany*
[3] *Departamento de Física, Universidade Federal de Sergipe, Av. Marechal Rondon, S/N, 49100-000, São Cristóvão, SE, Brazil*
[4] *National Radio Astronomy Observatory, 1003 Lopezville Road, Socorro, NM 87801, USA*
[5] *Instituto de Física, Universidade de São Paulo, Rua do Matão 1371, 05508-090 São Paulo, Brazil*
[6] *European Organisation for Astronomical Research in the Southern Hemisphere (ESO), Casilla 19001, Santiago 19, Chile*
[7] *Centro de Óptica e Información Cuántica, Vicerrectoría de Investigación, Universidad Mayor, Santiago, Chile*
[8] *Instituto de Física y Astronomía, Facultad de Ciencias, Universidad de Valparaíso, Casilla 5030, Valparaíso, Chile*
[9] *Université Côte d'Azur, Observatoire de la Côte d'Azur, CNRS, UMR7293 Lagrange, 28 Av. Valrose, F-06108 Nice Cedex 2, France*
[10] *Geneva Observatory, Geneva University, Chemin des Maillettes 51, 1290 Versoix, Switzerland*
[11] *Department of Physics and Astronomy, Western University, London, ON N6A 3K7, Canada*

Accepted XXX. Received YYY; in original form ZZZ

ABSTRACT

Classical Be stars are fast rotating, main sequence B-type stars. The rotation and the presence of circumstellar discs profoundly modify the observables of active Be stars. Our goal is to infer stellar and disc parameters, as well as distance and interstellar extinction, using the currently most favoured physical models for these objects. We present BeAtlas, a grid of 61 600 NLTE radiative transfer models for Be stars, calculated with the hdust code. The grid was coupled with a Monte Carlo Markov chain code to sample the posterior distribution. We test our method on two well-studied Be stars, α Eri and β CMi, using photometric, polarimetric and spectroscopic data as input to the code. We recover literature determinations for most of the parameters of the targets, in particular the mass and age of α Eri, the disc parameters of β CMi, and their distances and inclinations. The main discrepancy is that we estimate lower rotational rates than previous works. We confirm previously detected signs of disc truncation in β CMi and note that its inner disc seems to have a flatter density slope than its outer disc. The correlations between the parameters are complex, further indicating that exploring the entire parameter space simultaneously is a more robust approach, statistically. The combination of BeAtlas and Bayesian-MCMC techniques proves successful, and a game-changing new tool for the field: the fundamental parameters of any Be star can now be estimated in a matter of hours or days.

Key words: Stars: emission-line, Be – β CMi, HD58715, HR2845 – α Eri, HD10144, HR472 – Methods: statistical

1 BE STARS IN THE ERA OF BIG DATA

Over the last decade, astrophysics has been flooded with all types of observational data. At the same time, high performance computing clusters grew more powerful, smaller and cheaper, calculating ever more sophisticated physical models. A single human, or even dozens, cannot go through and make sense of all the data and models available today. In order to organise, classify, analyse and systematically compare data and models, methods such as Monte Carlo, machine learning, artificial intelligence, deep learning have proven invaluable, and are now indispensable tools for astronomers (for a review, see Baron 2019).

Among the objects with a profusion of observational data are classical B emission (Be) stars: Main Sequence (MS) stars with large rotation rates, characterised by emission lines in the Balmer hydrogen series, infrared excess and linear polarisation. These ob-

---

[⋆] E-mail: amanda.rubio@usp.br

servational characteristics originate from a gaseous circumstellar disc formed from matter expelled episodically and usually unpredictably by the central star. Be stars are popular targets for many reasons. Firstly, many are bright: four of the seven sisters on the Pleiades cluster are Be stars. Achernar (α Eri), with $V = 0.46$ is the 9th brightest star in the night sky, while η Cen ($V = 2.35$) is the 79th. In fact, the first detection of an emission line in a star was on the prototypical Be star γ Cas (Secchi 1866), the 89th brightest star in the sky. Secondly, most Be stars are rather variable in photometry and spectroscopy, in time-scales from hours to decades. There are tens or so Be stars with observing histories ranging more than a century. Aside from them, large photometric surveys, such as OGLE and TESS, are bound to have a large number of Be stars in them simply because Be stars are common: in the Galaxy, they represent 17% of B stars, going up to 34% for spectral type B1 (Zorec & Briot 1997), and in open clusters at lower metallicities, the lower fraction of Be stars can be as high as 32% (Bodensteiner et al. 2020).

Finding the fundamental parameters of Be stars (i.e., mass, size, rotation rate) is challenging due to the effects of their fast rotation (oblateness and gravity darkening), the disc and its variability. The star and the disc are coupled – the apparent stellar parameters are changed by the disc, while the disc structure depends on the stellar characteristics. Some Be stars, such as Achernar (Domiciano de Souza et al. 2014), have had their intrinsic properties measured with great precision via interferometry, but the fundamental parameters of the majority of Be stars are still poorly known, with estimates in the literature differing by several spectral sub-types, and sometimes not even being recognised as Be stars (e.g., ν Gem - B5V, OB, B7IV, B6III; α Col - B9Ve, B7III, B5p, B8Vn, B7IV, B8Vevar; β Psc - B6Ve, B4V, B5p, B7IV/V, B5Ve)[1].

Efforts to model Be star discs have found success after the viscous decretion disc (VDD) model of Lee et al. (1991) began to be systematically tested against observations in the last two decades or so. Being an α-disc (Shakura & Sunyaev 1973), a VDD builds from inside-out through the viscous shear between layers of material thrown into orbit by the central star. While the engine of the mass ejection mechanism itself is still unclear, models have been generally successful to describe the structure of the disc at large. Works such as Carciofi et al. (2006). Tycner et al. (2008) and Klement et al. (2015) created realistic physical models for Be stars in the VDD framework using the non-local thermodynamic equilibrium (non-LTE) radiative transfer codes BEDISK (Sigut & Jones 2007) and HDUST (Carciofi & Bjorkman 2006) and successfully compare the synthetic observables with data.

The solid foundation of the VDD model opens the door to the systematic modelling of Be stars, using their wealth of data to obtain more reliable parameters of individual stars or populations of stars. However, detailed modelling of even one star is a time-consuming effort. The usual approach is to compare models to observational data by manual searches through the parameter space. To date, the most comprehensive model of a Be star is Klement et al. (2015, 2017b)'s work with β CMi. The authors use a tailor-made grid of dozens of HDUST radiative transfer models and a wide range of observations, such as photometric, polarimetric, interferometric and spectroscopic data. This approach, however, misses nuances of the coupled star+disc system, as many parameters are fixed and their degeneracies are, in many cases, not accounted for. The results of "manual" searches cannot be blindingly trusted as they overlook the correlations between the physical parameters of the system, and may entirely miss regions of the parameter space that provide adequate (or even better) descriptions of the observations. Furthermore, calculating radiative transfer models in non-local thermodynamic equilibrium (NLTE), such as is done by HDUST, is a slow and computationally expensive process.

Even with so much data available, it is difficult to study large samples of Be stars because of their variability and diversity. The favoured approach so far has been to use simplified models rather than detailed radiative transfer calculations, as is the case of Vieira et al. (2015, 2017). Although this approach may provide important insights on the properties of the sample, they also suffer from biases originating from the simplifications to the model.

Data are available; a well-tested, substantiated physical model exists. To connect them and contemplate all the drawbacks of traditional modelling, we need 1) an extensive grid of detailed, state-of-the-art radiative transfer models that consider all quirks of Be stars and is cemented in the VDD theory and 2) a statistical engine to compare observational data and models, considering the coupled nature of the system. In this work, we provide and test such an alternative modelling method. We present BEATLAS, a comprehensive grid of radiative transfer Be star models that covers all the relevant stellar and disc parameters present in the Be class. We compare models to observational data using Bayesian Monte Carlo Markov chain (MCMC) methods, also taking prior information on the Be star into account, such as parallax measurements. The analysis is done simultaneously for all parameters, so that the degeneracy of the model parameters is fully considered, and their correlations can be quantified. The results consist not in a set of best-fitting parameters, but in probability density functions (PDFs) for each parameter, allowing for robust error estimates. We apply this method to two well-studied Be stars, α Eri and β CMi, and compare our results with their rich literature.

2 OVERVIEW OF THE VDD MODEL

The observational characteristics of Be discs are well established: continuum excess (starting in the visible and growing towards the infrared and radio domain), linear polarisation and double peaked emission lines (when the disc is seen at inclinations different than pole-on). Over the years, observations made it clear that the disc must be relatively thin, and rotating in a quasi-Keplerian fashion (Porter 1997, Okazaki 1991; more recently, Meilland et al. 2007, Oudmaijer & Parr 2010). In the 90's, several disc models were proposed to explain Be discs, such as the wind compressed disc (WCD) (Bjorkman & Cassinelli 1993) and the VDD model (Lee et al. 1991; see also Porter 1999; Okazaki 2001; Bjorkman & Carciofi 2005; Kritička et al. 2011). It soon became clear that only the VDD model could provide an adequate description of the global picture presented by observations, and it has been the favoured model for Be star discs ever since. The VDD has been successfully employed in the study of individual Be stars, modelling either snapshots (e.g., Carciofi et al. 2006; Tycner et al. 2008; Klement et al. 2015) or the temporal evolution of the disc (e.g., Carciofi et al. 2012; Ghoreyshi et al. 2018, 2021). Studies of samples of Be stars were also carried out (e.g., Touhami et al. 2013; Vieira et al. 2015, 2017; Rímulo et al. 2018).

The disc is formed because Be stars expel matter into orbit.

---

[1] Buscombe (1962), Hardorp et al. (1965), Borgman (1960), Lesh (1968), Levenhagen & Leister (2006), Arcos et al. (2018), Cannon & Pickering (1993), Molnar (1972), Hiltner et al. (1969), Buscombe (1962), Lesh (1968), Arcos et al. (2018), Cannon & Pickering (1993), Houk & Swift (1999), Buscombe (1962), respectively.

The mechanism behind this mass ejection is not fully defined, although fast rotation, ubiquitous in Be stars, plays an important part. However, since Be stars are fast, but not critical rotators (see Rivinius et al. 2013a, for a review), the mass ejection needs additional elements to be triggered and sustained; common suggestions are non-radial pulsations (Baade et al. 2016) and small-scale magnetic fields (Cassinelli et al. 2002; Brown et al. 2008).

In the VDD model, once the material is ejected and enters orbit, turbulent viscosity transports mass and angular momentum (AM) outwards, building up the disc. A VDD is similar to protostellar and accretion discs (Pringle 1981), the difference being that VDDs switch between *outflowing* and *inflowing*, while pre-MS and accretion discs are always *inflowing*. These discs are also completely dust- and molecule-free, being composed mostly of hydrogen.

If one assumes that mass is lost from the stellar equator at a constant rate, that the thin disc approximation is valid (Bjorkman & Carciofi 2005, for further details) the viscous diffusion effectively reduces to a one-dimensional problem, with the density and velocity depending only on the radial distance to the star. If we further assume that the disc is radially and vertically isothermal, and that mass is lost by the central star at a constant rate for a sufficiently long time (see Haubois et al. 2012), an analytical solution for the disc structure can be derived. Considering this, Bjorkman & Carciofi (2005) obtained the following expression for the surface density

$$\Sigma(r) = \frac{\dot{M} v_{\rm orb} R_{\rm eq}^{1/2}}{3\pi\alpha\, c_s^2\, r^{3/2}} \left[\left(\frac{R_0}{r} \right)^{1/2} - 1 \right], \tag{1}$$

where $R_{\rm eq}$ is the equatorial radius of the central star, $v_{\rm orb}$ is the Keplerian orbital velocity at the equator, $\dot{M}$ is the rate of mass flowing out of the central star, α is the Shakura-Sunyaev viscosity parameter, R_0 is an integration constant, associated with the outer, torque-free boundary condition, and the sound speed in the disc is $c_s = (kT/m_{\rm H}\mu)^{1/2}$ (T is the disc temperature, k is the Boltzmann constant, $m_{\rm H}$ is the hydrogen mass, and μ is the mean molecular weight of the gas). Given that $R_0 \gg R_{\rm eq}$, Eq. 1 assumes a simple functional form $\Sigma(r) \propto \Sigma_0\, r^{-2}$, where Σ_0 is the surface density at the base of the disc.

In the absence of radiative forces and nearby stellar companions, and assuming that the material is in vertical hydrostatic equilibrium, the vertical (i.e., along the direction orthogonal to the disc plane) density distribution is a simple Gaussian with a scale height controlled solely by gas pressure and by the gravitational field of the Be star: as the disc grows further from the star, it will flare. Thus, the scale height H has the form

$$H = H_0 \left(\frac{r}{R_{\rm eq}} \right)^{\beta}, \tag{2}$$

where $H_0 = c_s R_{\rm eq}/v_{\rm orb}$ and β, the flaring exponent, is 1.5 (Bjorkman & Carciofi 2005). Finally, we can obtain the equation for the volume mass density, ρ of an isothermal VDD by considering that the surface density Σ is the vertical integral of the density. This allow us to write ρ in terms of the scale height and the surface density

$$\rho(r,z) = \frac{\Sigma_0}{H\sqrt{2\pi}} \left(\frac{r}{R_{\rm eq}} \right)^{-2} \exp\left[-\frac{z^2}{2\,H^2} \right] \propto \rho_0\, r^{-n}, \tag{3}$$

with $n = 3.5$ and ρ_0 is the base volume density of the disc. In this work we present our results in terms of the number density n_0, which relates to the volume density as $n_0 = \rho_0\, N_A/\mu$, where N_A is Avogadro's number.

2.1 Deviations from a power-law density

The above considerations and the power law approximation of Eq. 3 are valid for an isothermal, steady-state VDD. Real Be discs, however, are rarely either. Be discs are famously variable in many time-scales. They are dependent on injection of mass and AM on their base to exist, and variations on the mass injection rate affect their properties in complex ways. At its most dramatic, if mass injection stops for a long period (larger than the typical viscous timescales), the disc completely dissipates and the Be star is seen as a regular (but fast rotating) B star. The inner disc dissipates faster, falling back into the central star as it is no longer able to support itself without the injection of AM. The outer disc still receives AM from the decaying inner disc, and can therefore survive for longer, but dissipates with time. These disc build-up and dissipation events happen in the viscous diffusion timescale, given by

$$\tau_\nu = \frac{v_{\rm orb}}{\alpha c_s^2}\sqrt{R_{\rm eq}\, r} \sim 20\,\text{years}\,\frac{0.01}{\alpha}\sqrt{\frac{r}{R_{\rm eq}}}, \tag{4}$$

meaning that Be discs can be completely built and lost in timescales of months to years given that estimates of the viscous parameter α put it in the ballpark of a few tenths (Rímulo et al. 2018; Ghoreyshi et al. 2018).

A Be star that is in the process of either building or losing its disc will not have a volume density that follows the $n = 3.5$ prescription. Given their inside-out growth and dissipation, discs that are building-up have n higher than 3.5, as the inner part of the disc fills up faster than the outer part. In dissipation, we have the opposite ($n < 3.5$), as the inner disc is also quicker to be depleted than the outer disc (Haubois et al. 2012, their Figs. 1 and 3). In fact, the situation is even more complex than depicted above, because the models of Haubois et al. (2012) show that n actually varies strongly with the distance to the star (e.g., their Figs. 3 and 6). Vieira et al. (2017) used this to connect their estimates of n for their sample of 80 Be stars to the current state of the disc, with $3.0 < n < 3.5$ being considered a region of disc stability. Most of their sample had $n < 3.5$, suggesting these discs were dissipating at the time of the observations, whereas only 45% of the discs were either in build-up (24%) or stable (21%).

Another factor that can cause n to deviate from 3.5 is the presence of a binary companion. As massive stars, early-type[2] Be stars are inserted in the larger context of massive star multiplicity: around 80% have interactions with a companion in some point of their lives (Sana et al. 2012). Multiplicity fraction decreases with mass (Janson et al. 2012; Sota et al. 2011), but late-type[3] Be stars have been found to have companions as well (e. g., κ Dra – Klement et al. 2022). Oudmaijer & Parr (2010), for instance, finds a binary fraction of 30±8% for Be stars specifically (their method could probe separations from 0.1 to 8 arcsec, and magnitude differences up to 10 mag). The binary fraction among Be stars is not well constrained, with suggestions ranging from 5% (van Bever & Vanbeveren 1997) to nearly 100% (Shao & Li 2014; Klement et al. 2019). Okazaki et al. (2002), in their smoothed particle hydrodynamics simulations of binary Be stars, find that when the companion has a close enough orbit, it tidally affects the disc, which can lead to disc truncation and to the accumulation of matter inside of its orbit, making the radial density falloff much shallower ($n < 3.5$ – Panoglou et al. 2016, Cyr et al. 2017). This accumulation effect is stronger for smaller binary separations, smaller viscosities and larger mass ratios.

---

[2] Spectral classes B0-B3

[3] Spectral classes B4-B9

The radial density exponent can also deviate from the isothermal $n = 3.5$ if the disc has a temperature structure that is highly *non*-isothermal (Carciofi & Bjorkman 2008). As the sound speed in the disc (and hence the viscosity) depends on the temperature, the entire density structure of the disc can change profoundly if T varies either in time or space. For instance, Carciofi & Bjorkman (2008) find that in a non-isothermal disk, albeit steady-state, n can range between 2 and 6 (their Fig. 4). The disc structure also depends on the viscosity parameter α, which may also vary (independently of the temperature) throughout the disc and also in time (Ghoreyshi et al. 2021).

Summarising, n can vary in time according to the dynamical status of the disc and the tidal influence of a companion, and vary radially due to non-isothermality and variations in viscosity. Therefore, the power law density of Eq. 3 is an approximation for the staggering majority of Be stars. At the same time, it is a useful approximation as it allows measuring – via detailed modelling – the (average) disk density slope at a given moment in time, irrespectively of how this slope was realised.

3 THE CENTRAL STAR

Rotation is an important ingredient in the formation, structure and evolution of stars in the MS (e.g., Cranmer 2005; Ekström et al. 2008). Ekström et al. 2012 shows that the evolutionary tracks for rotating and non-rotating hot stars differ significantly, with rotators having chemically enhanced stellar surfaces and enjoying longer MS lifetimes[4] due to rotational mixing bringing more hydrogen to the core (Georgy et al. 2013). These effects are especially relevant for Be stars since they are the fastest rotators in the MS (Cranmer 2005).

The Roche equipotential formalism is frequently used to describe the rotating stellar geometry (Cranmer 1996, and references therein). The star is deformed according to the rotation rate,

$$W = \frac{v_{\rm rot}}{v_{\rm orb}}, \tag{5}$$

where $v_{\rm rot}$ is the rotational velocity at the equator (Rivinius et al. 2013a). For critically rotating stars, $W = 1$. Stars with high values of W (> 0.5), such as Be stars, are subject to rotational deformation (e.g., Collins & Harrington 1966; Maeder 2009), enhanced chemical mixing, and gravity darkening (Collins 1963; von Zeipel 1924). A Be star is therefore flattened along its rotational axis, with hotter (and thus brighter) poles and a dimmed equator. This has a direct consequence on the thermal structure of the disc (e.g., McGill et al. 2011), influencing the observables (Townsend et al. 2004). Therefore, any accurate Be star model must take gravity darkening and oblateness into account.

4 DESCRIPTION OF MODEL GRID

The BeAtlas project arises in the context of grid-based modelling, routinely applied to infer parameters of physical models (e. g., Choi et al. 2016). BeAtlas comprises two systematic grids of hdust models. The *photospheric grid* (Sect. 4.2) covers the typical range of stellar parameters (Sects. 3 and 4.1.1) from spectral types of early A to late O, from non-rotating ($W = 0$) to near-critical rotation. The *disc grid* (Sect. 4.3) contains models of stars surrounded by discs, computed according to the simplified VDD formulation of Sect. 2 and covering the typical range of stellar and disc parameters associated with the Be phenomenon. Details on the synthetic observables included in both grids are given in Sect. 4.4.

4.1 Radiative Transfer Calculations

The models were calculated with the Monte Carlo radiative transfer code hdust (Carciofi et al. 2004; Carciofi & Bjorkman 2006, 2008). This code has been successfully applied in several previous studies to interpret multi-technique observations. Some recent examples are the interferometric study of Achernar (Dalla Vedova et al. 2017), the computation of line profiles of binary Be stars (Panoglou et al. 2018), and the interpretation of optical light curves using the VDD model (Rímulo et al. 2018; Ghoreyshi et al. 2018).

The code accepts arbitrary 3D geometry (i.e., density distribution) and kinematics. The circumstellar chemistry considers atomic hydrogen in full non-LTE and/or dust grains. The implemented gas opacity sources are Thomson scattering, bound-bound, bound-free and free-free absorptions. The code describes the star realistically, including limb darkening, gravity darkening, and rotational flattening according to the Roche model (see details in Sect. 3). Its outputs include the synthetic observables such as the polarised emergent spectrum (both continuum and Hydrogen lines in emission and absorption) and synthetic images.

hdust is based on the Monte Carlo method, that discretises the radiation field in a number of photon packets, here understood as a cohesive ensemble of photons that are launched by the star and interacts with the disc (i.e., is absorbed or scattered). The accuracy of the simulation depends on the number of photon packets used (e.g., Wood et al. 1997).

4.1.1 *Modelling the central star*

The hdust code requires the following information about the central star as input parameters: mass (M), polar radius ($R_{\rm p}$), luminosity (L), rotation rate (W), and gravity darkening parameter (see below). In addition, the emergent spectrum at each position of the photosphere must be specified. For that, we use the model atmospheres from Kurucz (1994), while the limb darkening follows the prescription given by Claret (2000).

The gravity darkening is described by the modified von Zeipel law, in the form $T_{\rm eff} \propto g^{\beta_{\rm GD}}$. We adopt the model presented by Espinosa Lara & Rieutord (2011), where the gravity darkening exponent $\beta_{\rm GD}$ is a function of the rotation rate. In this prescription, the effective temperature $T_{\rm eff}$ on the surface of the star becomes a function of W and the polar angle (colatitude) θ[5], as in Eq. 31 of Espinosa Lara & Rieutord (2011). For a given rotation rate, a model correction factor is found using an iterative numerical procedure, and $\beta_{\rm GD}$ is then estimated by fitting the θ dependent profiles of $T_{\rm eff}$ and g using a power law (see Espinosa Lara 2014, for more details, specially Eq. 3.17). This theoretical approach has been validated in works such as Domiciano de Souza et al. (2014), where the predicted values of the model were compared to interferometric measurements of six rapidly rotating stars. By adopting this prescription for the

---

[4] This is only false when a star is very metal poor, and the dominant effect of rotation is the helium diffusion to the outer envelope, making the star overluminous and thus reducing lifetime (Meynet & Maeder 2002).

[5] The polar angle is the angle between a given point in the stellar surface and its spin axis.

gravity darkening, the number of free parameters for the central star reduces from five to four.

In order to connect the parameters used by HDUST to the stellar physical parameters (age, polar radius and luminosity) in a consistent way, we use the rotating stellar models of Georgy et al. (2013) and Granada et al. (2013), hereafter referred to as the Geneva grid. We selected models with solar metallicity ($Z = 0.014$), according to Grevesse & Sauval (1998). These models cover the mass range from 1.7 to 20 $\mathrm{M}_\odot$ and initial rotation rates from $W = 0$ to $W = 0.998$. Specifically for this work, 20 $\mathrm{M}_\odot$ models were computed to properly cover the high-mass end of the Be phenomenon, following the exact same physical description that the ones in Georgy et al. (2013). The chosen mass range includes all typical masses of known Be stars as well as the transition to late type Oe stars (Negueruela et al. 2004) and to early-A stars. By using the Geneva grid, the number of free parameters for a star reduces from four to three (mass, rotation rate and age).

4.2 BEATLAS: Photospheric Grid

The photospheric grid is applicable for discless (i.e., inactive) Be stars, normal B stars and Bn stars, and contains 660 photospheric models. (11 masses × 10 rotation rates × 6 ages). Each model was computed for 10 inclination angles, so the grid effectively contains 6600 emergent spectra. The grid is summarised in Tab. 1. The stellar mass was chosen in the range 1.7 to 20 $\mathrm{M}_\odot$, typically covering the spectral range from A7 to O8.5. The association between mass and spectral type are based on Martins et al. (2005), Townsend et al. (2004), and Adelman (2004), for O, B and A spectral types, respectively. The rotation rate covers the full range between a non-rotating star ($W = 0$) to a nearly-critically rotating one $W = 0.99$. The chosen steps follow $W_i = 0.99\,(i/N)^{1/2}$ with $i = 0, \ldots, N$ and $N = 10$. As mentioned in Section 4.1.1, there is one specific $\beta_{\rm GD}$ for each rotation rate, with values ranging from $\beta_{\rm GD} = 0.25$ for $W = 0$, and $\beta_{\rm GD} \approx 0.13$ for $W = 0.99$.

In our models, the age of a star is given in terms of its MS lifetime. This lifetime is expressed in the Geneva grid as the amount of H present in the core of the star. In the MS, the age parameter ranges from $t/t_{\rm MS} = 0$ (H fraction $X \approx 72\%$ and He fraction $Y \approx 26\%$) to $t/t_{\rm MS} = 1.0$ ($X \approx 0\%$), where $t/t_{\rm MS}$ represents the fraction of time already spent by the star relative to the time duration from zero-age MS to terminal-age MS. The values for $t/t_{\rm MS}$ shown in Tab. 1 were chosen to better sample the trajectory of the central star along its MS track, as displayed in Fig. 1. From $0 \leq t/t_{\rm MS} \leq 1$, the conversion between $t/t_{\rm MS}$ to real age is mass dependent. Given a mass, a rotation rate and $t/t_{\rm MS}$, the Geneva grid is interpolated to calculate the corresponding $R_{\rm p}$, L and age. This grid has known numerical issues for the models of evolved stars ($t/t_{\rm MS} > 1$), in particular for fast rotators. To sidestep this problem, we included another value for the age parameter, $t/t_{\rm MS} = 1.25$, as an extrapolation of the MS models rather than using the problematic post-MS models. Therefore, this value of $t/t_{\rm MS}$ does not correspond to a real age, but is used to explore parameter ranges (size and luminosity) that are consistent with a star just leaving the MS beyond the ones predicted by the Geneva grid for the MS. The associated values of $R_{\rm p}$ and L are extrapolated using an exponential function. In this manner, we can accommodate possibilities that are not predicted, and not contemplated, by the Geneva MS grid, such as slightly evolved stars.

Finally, the last parameter of the photospheric grid is the inclination angle of the stellar spin axis with respect to the line of sight, i. For i, we chose 10 values, equally spaced in $\cos(i)$. As shown in the example colour-magnitude diagrams of Appendix D, this parameter has an important effect on the spectral energy distribution (SED) as a whole and naturally also on the line profiles.

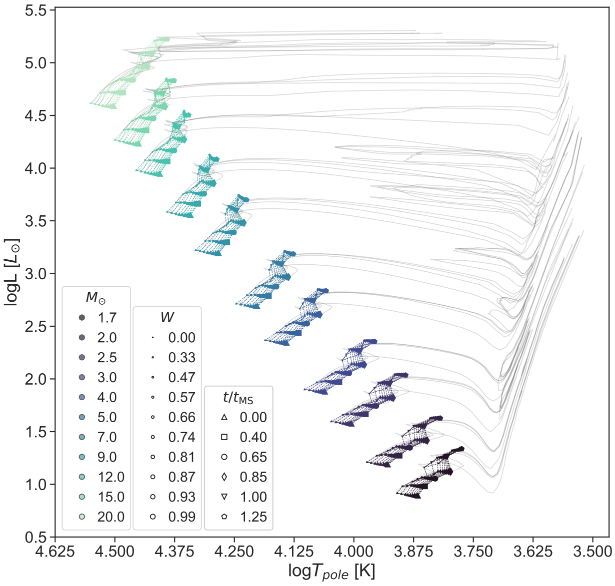

Figure 1. Hertzsprung–Russell diagram comprising the photospheric grid parameters. Masses are indicated by different marker colours. Marker sizes represent different rotation rates W. In grey solid lines, four complete Geneva tracks are showed, corresponding to the initial velocities of $W_{\rm Geneva}$ = 0, 0.769, 0.925 and 0.998 for each stellar mass. Values of $t/t_{\rm MS}$ for each (M, W) pair are connected with dashed lines, following the tracks, indicated by different marker types; the path from ZAMS to TAMS goes from bottom left up to top right.

4.3 BEATLAS: Disc Grid

For the disc grid, the stellar parameters were selected based on the best representation of the Be phenomenon. The mass range lower limit was set at 3 $\mathrm{M}_\odot$ and the upper limit of 20 $\mathrm{M}_\odot$ was unchanged. In total, we chose 10 values of stellar masses for the disc grid. We restricted the number of W values to 5, beginning at $W = 0.50$ up to $W = 0.99$, since no slow rotating Be star is known to exist (see the compilation presented in Rivinius et al. 2013a, their Fig. 9). Also, the age parameter $t/t_{\rm MS}$ was confined to a total of 4 values, including an extrapolated non-physical value of $t/t_{\rm MS} = 1.25$. The only unchanged parameter was the inclination angle. The main reason for the above choices is computation time, as a more complete stellar grid would make computing the disc grid prohibitively expensive.

Following the VDD formulation of Sect. 2, we assume that the radial disc density falloff is a power-law with the exponent, n, as a free parameter (Eq. 3). Further parameters describing the disc are the volume number density (n_0) at the disc base ($r = R_{\rm eq}$) and the disc radius ($R_{\rm D}$). The disc scale-height H follows a simple power-law of the form of Eq. 2. To compute H_0, the disc temperature was set to $T = 0.60\,T_{\rm pole}$ following Carciofi & Bjorkman (2006), and the flaring exponent β was fixed at the isothermal value of 1.5.

For each M value, a grid of n_0 was built with 8 points equally distant in logarithmic space between a fixed lower limit and a mass-dependent upper limit. The latter corresponds to HDUST models con-

Table 1. BeAtlas stellar parameters of the photospheric grid. For each rotation rate, there is only one associated value of the gravity darkening exponent. The non-rotating models are assigned with $\beta_{\rm GD} = 0.25$, and for the critically rotating models $\beta_{\rm GD} \approx 0.13$.

	Parameter	Range	Values
Fundamental parameters			
M	Mass ($\mathrm{M}_\odot$)	1.7 - 20	1.7, 2, 2.5, 3, 4, 5, 7, 9, 12, 15, 20
W	Rotation Rate	0 - 0.99	0.00, 0.33, 0.47, 0.57, 0.66, 0.74, 0.81, 0.87, 0.93, 0.99
$t/t_{\rm MS}$	Stellar Age	0 - 1.25	0, 0.40, 0.65, 0.85, 1, 1.25
$\cos i$	Inclination angle	0 - 1	0, 0.11, 0.22, 0.33, 0.44, 0.55, 0.67, 0.78, 0.89, 1
i	Inclination angle	90 - 0	90.00, 83.68, 77.29, 70.73, 63.90, 56.63, 47.93 , 38.74 , 27.13, 0.
Derived parameters			
ST	Spec. Type	A7 - O8.5	A7, A2, A0, B9.5, B7.5, B6, B3.5, B2.5, B1, B0.5, O8.5
$\beta_{\rm GD}$	Gravity darkening exponent	0.25 - 0.13	0.25, 0.23, 0.21, 0.20, 0.19, 0.18, 0.17, 0.16, 0.15, 0.13

vergence limit, adapted to an analytical approximation, described by:

$$\ln n_0^{\rm upper}(M)\,[\mathrm{cm}^{-3}] = \begin{cases} aM^2 + bM + c, & M \leq 7\,\mathrm{M}_\odot, \\ dM + e, & M > 7\,\mathrm{M}_\odot, \end{cases} \tag{6}$$

where $a = -0.152/M_\odot^2$, $b = 2.51/M_\odot$, $c = 22.09$, $d = 0.14/M_\odot$, and $e = 31.02$. The works of Vieira et al. (2017) and Rímulo et al. (2018) revealed a tendency for massive stars to have much denser discs than their low mass siblings, giving an observational consistency with our convergence limitations. The maximum n_0 value – corresponding to $M = 20M_\odot$ – was chosen to be $n_0 = 5 \times 10^{14}\,\mathrm{cm}^{-3}$, the highest reported in the literature for a B0 star (Carciofi & Bjorkman 2006). For the lower limit we adopted the value of $10^{11}\,\mathrm{cm}^{-3}$ for all stellar masses, which roughly corresponds to the detection limit of an emission feature (however weak) in the Hα line.

The disc radius ranges from 10 to 100 $R_{\rm eq}$. In theory, Be discs can expand to hundreds of stellar radii. However, if the Be is a binary system, the presence of the companion can tidally affect the disc and truncate it. In our grid, the lower limit value of the disc radius corresponds to an estimate for the disc radius of the Be star o Pup, which has the shortest period among all known binary Be stars (Koubský et al. 2012), and thus the smaller known disc radius. On the other hand, the upper limit, 100 $R_{\rm eq}$, corresponds to a disc size for which the disc emission starts to be negligible at all wavelengths considered in the simulation (see Sect. 4.4; and also Vieira et al. 2015).

The n exponent (Eq. 3) range was chosen, according to Vieira et al. (2017), from 1.5 to 4.5. This range is in broad agreement with other studies from the literature (e.g., Waters et al. 1989; Silaj et al. 2014; Touhami et al. 2014). Recall that for an isothermal, steady-state disc, $n = 3.5$. An overview of the parameters of the disc grid is given in Tab. 2.

The disc grid comprises a total of 61 600 models (11 masses × 5 rotation rates × 4 ages × 7 density slopes × 5 disc sizes × 8 values for n_0), each computed for 10 inclination angles, resulting in 616 000 emergent spectra. Given that each complete model can take on average 15 h to be calculated using 64 computing cores, to complete BeAtlas approximately 15 × 61 600 × 64 = 59 million core-h [6] are required, a challenging number even for modern computing standards. We emphasise that the complete disc grid could not be completed for this work. Parts of the disc grid were computed, aiming at bracketing the parameter space needed to study our targets, α Eri and β CMi (Sect. 6 and 7). At the moment, the disc grid is 32% complete.

4.4 Observables

To finish the specification of BeAtlas, we provide a list of observables (e.g., continuum bands, spectral lines, images, etc.). The most efficient way to run hdust is to compute individual runs for each spectral range of interest. To make optimal usage of this feature, we specified 22 spectral bands (first part of Tab. A1) covering all the way from the UV up to the radio. Each band is defined by a minimum and maximum wavelength, the number of spectral bins (i.e., its spectral resolution), their spacing (linear or logarithm), and the number of photon packets.

We are also interested in spectral lines (both in emission and in absorption) in the optical and IR domains. These lines were selected among the most commonly used in the literature (second part of Tab. A1). For some observables we also compute images across pre-defined spectral channels aiming at reproducing interferometric observables. Our definitions include both decommissioned interferometers (e.g., AMBER[7] and MIDI[8]), for which large number of archival observations are available, and current interferometers at ESO (GRAVITY[9] and MATISSE[10]) and Georgia State Unversity's CHARA[11].

5 MCMC SAMPLING

A grid of models, no matter how much science has been put to it, is useless without a statistical engine that explores the parameter space (e.g., Klement et al. 2017b; Rímulo et al. 2018; Bouchaud et al. 2020; Bowman et al. 2020). With this intent, we combine BeAtlas with Bayesian statistics and Monte Carlo Markov Chain (MCMC) methods. The use of Bayesian-MCMC data analysis in astronomy has grown exponentially in recent years due to advances in both computing power and computer science, revolutionising

---

[6] The core-h is a standard unit for measuring computing time in parallel computers, and is equivalent of one hour of computing time in one computing core

[7] `www.eso.org/sci/facilities/paranal/instruments/amber/overview.html`

[8] `www.eso.org/sci/facilities/paranal/decommissioned/midi.html`

[9] `www.eso.org/sci/facilities/paranal/instruments/gravity.html`

[10] `www.eso.org/sci/facilities/develop/instruments/matisse.html`

[11] `www.chara.gsu.edu/`

Table 2. BeAtlas parameters of the disk grid. The values for i are the same as in Tab. 1.

	Parameters	Range	Values
Fundamental parameters			
M	Mass ($\mathrm{M}_\odot$)	3 - 20	3, 3.5, 4, 4.5, 5, 6, 7, 9, 12, 15, 20
W	Rotation Rate	0.50 - 0.99	0.50, 0.75, 0.85, 0.92, 0.99
t/t_{MS}	Stellar Age	0 - 1.25	0, 0.65, 1, 1.25
$\log_{10} n_0$ (lower)	Disc base number density (cm^{-3} - dex)	Fixed	11.0
$\log_{10} n_0$ (upper)	Disc base number density (cm^{-3} - dex)	$M_\odot$-dependent	12.3, 12.6, 12.9, 13.2, 13.4, 13.9, 14.0, 14.2, 14.4, 14.7
R_{D}	Disc radius (R_{eq})	10 - 100	10, 20, 40, 70, 100
n	Number density radial exponent	1.5 - 4.5	1.5, 2.0, 2.5, 3.0, 3.5, 4.0, 4.5
Derived parameters			
ST	Spec. Type	B9.5 - O8.5	B9.5, B9, B7.5, B6.5, B6, B4.5, B3.5, B2.5, B1, B0.5, O8.5
β_{GD}	Gravity darkening exponent	0.21 - 0.13	0.21, 0.18, 0.16, 0.15, 0.13

the way we see data in science (e.g., Sharma 2017, and references therein).

In Bayesian formalism the posterior distribution is defined as

$$p(\Theta, \alpha|D) \propto p(\Theta, \alpha) p(D|\Theta, \alpha), \tag{7}$$

where Θ is a unique set of parameters that describe a model, D is the data and α is the previously known information of the problem. As such, $p(\Theta, \alpha)$ is the *a priori* distribution and $p(D|\Theta, \alpha)$ is the likelihood.

Our goal is to find probability density functions (PDFs) of the parameters that can together describe a Be star given a suitable set of models, observational data and prior information. To do this, we need a code to search through the parameter space, iteratively comparing models to data ($p(D|\Theta, \alpha)$), thus sampling the posterior distribution ($p(\Theta, \alpha|D)$). We use a Python implementation of Goodman & Weare (2010)'s affine-invariant ensemble sampler, the high-performance open source emcee[12] (Foreman-Mackey et al. 2013a). It is an ensemble sampler that follows a variation of the classic Metropolis-Hastings (Metropolis et al. 1953; Hastings 1970) algorithm called stretch move. Being an ensemble sampler, emcee uses many "walkers", who thread along different (but connected) chains to sample the posterior distribution. Every time one of these walkers takes a step, the other walkers are informed. The ensemble thus performs the stretch move together, reaching convergence faster (i.e., in fewer steps along the chain) than a single, lone walker could. In every step and for every walker, a new set of parameters is proposed by emcee. The BeAtlas synthetic observables are interpolated to this new set of parameters using the python scipy function griddata to find the synthetic observables that correspond to these parameters. The synthetic observables are then compared to the data of the target using a likelihood function.

Although the stretch move algorithm will converge for different likelihood functions, the most commonly used one is the χ^2 distribution. The type of likelihood depends on the observational data given to the code. For the SED from the visible to radio (0.39μm, forward), we adopt a logarithmic χ^2 in the form (Robitaille et al. (2007), Eq 6.; Klement et al. (2017b), Eq. 4)

$$\chi^2_{\mathrm{mod}} = \sum_{i=1}^{N} \left[\frac{\log(F_{\mathrm{obs,i}}/F_{\mathrm{mod,i}})}{\sigma_{F_{\mathrm{obs,i}}}/F_{\mathrm{obs,i}}} \right]^2, \tag{8}$$

where $F_{\mathrm{obs,i}}$ are the observed fluxes, $\sigma_{F_{\mathrm{obs,i}}}$ are their errors, and $F_{\mathrm{mod,i}} = F_{\mathrm{mod,i}}(\Theta)$ represents the BeAtlas grid of models described in Section 4 for each wavelength i. The likelihood is

$$\log p(D|\Theta, \alpha) \propto -0.5\, \chi^2_{\mathrm{mod}}. \tag{9}$$

The use of a logarithm χ^2 offers better performance when the data has a large dynamic range: the SED of a Be star from the visible to the radio can vary 6 orders of magnitude in wavelength and 17 orders of magnitude in flux (e.g., the inset plot of Fig. 8). For the UV part of the SED we adopt a simple, non-logarithmic χ^2, because of the smaller wavelength (and dynamical) range, in the form

$$\chi^2_{\mathrm{mod}} = \sum_{i=1}^{N} \left[\frac{F_{\mathrm{obs,i}} - F_{\mathrm{mod,i}}}{\sigma_{F_{\mathrm{obs,i}}}} \right]^2, \tag{10}$$

Thus, if we give the code the complete SED, from UV to radio, as input data, then the two likelihoods are combined by summing the reduced χ^2 of each, and multiplying by the total number of data points in the complete SED. When an Hα profile or polarisation data are the input, the likelihood is also a non-logarithmic χ^2. Similarly to what is done for the complete SED, when we give the code multiple data as input data, the final likelihood is also a sum of their reduced χ^2, each multiplied by the respective number of data points.

The models of BeAtlas cannot be directly compared to observational data: they must first be normalised for the distance of the object and corrected for the interstellar reddening. In our method, we correct for extinction using the prescription of Fitzpatrick & Massa (1999), with both the colour excess, $E(B-V)$, and R_V as free parameters.

One of the reasons for choosing the Bayesian approach is its capacity to combine the data with prior knowledge. In principle any available information on a given target can be used as priors. Common examples are the parallax – widely available thanks to the Gaia and Hipparcos missions (Gaia Collaboration et al. 2016 and Perryman et al. 1997, respectively) – and the inclination angle that may be available from interferometric studies. Another important prior is $v \sin i$ that, however, should be applied with caution as it may become quite insensitive to the stellar rotation rate for large values of W (Townsend et al. 2004). In our study, we have the option to use any, none or all of these three priors (more priors can be added to the code as necessity arises). We define the priors as Gaussian distributions centred in the literature value and with its literature uncertainty as variance. Therefore

---

[12] Available online under the MIT License: `https://github.com/dfm/emcee`

$$\log p_a(\Theta, \alpha) \propto -0.5 \left(\frac{a_{\rm obs} - a_{\rm mod}}{\sigma_{a_{\rm obs}}} \right)^2 , \tag{11}$$

where $a_{\rm mod}$ is the random model value of parameter a generated in each step of the inference. The priors used for each simulation shown here are specified in the text of Sects. 6 and 7.

5.1 Simulation setup

Summarising, the two grids defined in Sect. 4 have distinct applications. The photospheric grid can be used to study discless A to O stars, from non-rotating to fast rotators. Of great relevance is the study of inactive Be stars, for which BeAtlas can directly probe the fundamental parameters without interference from the disc. In this case, the parameters explored by the MCMC simulations are: stellar mass (M), rotation rate (W), age ($t/t_{\rm MS}$), inclination (i), distance (π) and extinction ($E(B-V)$). In the case of active Be stars, the disc grid is used to explore additional parameters: disc base number density (n_0), disc radius ($R_{\rm D}$), and radial density exponent (n). A wide range of observables can be studied, including the SED from the UV up to the radio, continuum linear polarisation and hydrogen line profiles.

There are already published works that used older versions of BeAtlas and our MCMC code (de Almeida et al. 2020; Suffak et al. 2020; Marr et al. 2021; Richardson et al. 2021; Marr et al. 2022), as they have been in development for over 5 years. However, the work we present here is the first critical test of our method, which has undergone major updates in the past year. Therefore, here we apply the method to two well studied Be stars, α Eri (Sect. 6) and β CMi (Sect. 7), to certify that it can accurately recover the fundamental parameters of these stars. All of our simulations have 120 walkers in the ensemble. To ensure convergence, simulations were run until the number of steps reached 50 times the mean autocorrelation time of all parameters, as recommended by Foreman-Mackey et al. (2013b), and until the autocorrelation time of each parameter changed less than 1% between subsequent estimates. Typically, the above implies quite long chains with dozens of thousands of steps, depending on the dataset and grid used. In general, the simulations converge in a matter of hours or days, depending on the complexity of the model. To represent the PDFs obtained using the standard "value ± uncertainty" notation, we chose to use the highest density region (HDR – also called highest probability region, or credible interval) of each PDF in 68%, with the median value of this region as the "best" value for the parameter (Hyndman 1996; Chen et al. 2000). The HDR does not have to be unique and continuous, but can be broken in more than one region, which allows us to explore multiple solutions for non-unimodal distributions. Thus, when a distribution is double-peaked, two sets of "solutions" are considered by us as possible results. Furthermore, using HDR allows for a better representation of skewed distributions.

6 α Eri: PHOTOSPHERIC BeAtlas

6.1 Target Overview

α Eri (α Eridani, Achernar, HD10144, HR472, HIP7588) is the nearest Be star to Earth, at a distance of only 42.8 ± 1.0 pc (π = 23.39 ± 0.57 mas – van Leeuwen 2007). It is well-known also for the drastic deformation it suffers due to its rapid rotation. Being such a close target, it has been the focus of several interferometric and imaging observations in the last decade. With PIONIER data, Domiciano de Souza et al. (2014) imaged the photosphere of α Eri and measured its equatorial rotational velocity ($v_{\rm eq} = 298.8^{+6.9}_{-5.5}$ km/s), equatorial radius ($R_{\rm eq} = 9.16 \pm 0.23\, R_\odot$), inclination ($i = 60.6^{+7.1}_{-3.9}$°), and the gravity darkening exponent ($\beta_{\rm GD} = 0.166^{+0.012}_{-0.010}$). The discovery of its wide binary companion, α Eri B (Kervella & Domiciano de Souza 2007), with a period of 2570.94 ± 0.53 days, ≈ 7 years, and the subsequent analysis of additional observations of Kervella et al. (2022) allowed for a robust estimate of the mass of α Eri A, the Be star, as $5.99 \pm 0.60 M_\odot$. It is also found to be an evolved star, with an estimated core chemical composition of $X \approx 6\%$ and $Y \approx 93\%$.

The viscous disc of Be stars dissipates if matter stops being added to its base, i.e., if the mass ejection from the star ceases. When this happens, the inactive Be star is then perceived just as a fast rotating B star, as most of its class-defining observational traits disappear. α Eri has well-documented inactive phases (e.g., from 1970 to 1975 – Vinicius et al. 2006, and in early 2000s – Rivinius et al. 2013b), where no emission could be detected in its spectra, and several phases where a generally weak emission appears (e.g., between 1980 to 1990 and after 2002). Therefore, data from the inactive periods can be used to study the photospheric emission from α Eri.

6.2 Results

We applied the method described in Sect. 5 for α Eri using the photospheric BeAtlas grid. For the simulations presented here, we used a prior only on the parallax, using the Hipparcos value of 23.39 ± 0.57 mas. Note that there are no Gaia (Gaia Collaboration et al. 2022) estimates for the parallax of α Eri as it heavily saturates the Gaia detectors. R_V is kept fixed at the usual value of 3.1 (Fitzpatrick & Massa 1999).

The data used are UV spectra from the International Ultraviolet Explorer (IUE – obtained from the INES Archive Data Center[13]) from 1989 (a phase of weak disc emission). Only high-dispersion large-aperture IUE spectra were chosen, as they can be flux calibrated. The data was also averaged and binned to match the resolution of the grid. To test the photospheric grid, we use a spectrum taken during one of the well-documented inactive phases. The selected spectrum was the cleanest from the period of the year 2000 inactive phase, from January 11th (Fig. 2), taken with ESO's FEROS (high-res echelle spectrograph, R = 48000), mounted at the 1.52m telescope in the La Silla Observatory. Unfortunately, this spectrum is still crowded with telluric lines and emission due to cosmic rays. The worst of these effects were removed from the spectrum using a sliding box outlier remover routine. The absorption lines C ii 6578.1 and 6582.9 are quite strong: the region affected was also removed from the spectrum for the simulation, as our models do not include carbon lines and could not reproduce this feature. The Hα spectrum is also binned to the resolution of the grid and normalised to velocity space. The systemic velocity is found by fitting an inverted Gaussian to the line wings. The velocity range considered for the analysis is -1000 to 1000 km/s.

To test our method and the constraining capabilities of different observables, we ran three simulations in total, all with a prior on the parallax. For the first simulation only the UV data was used; the corner plot with the PDFs is shown in Fig. 3. On the second simulation, only the Hα profile was modelled; PDFs are shown in

---

[13] `http://sdc.cab.inta-csic.es/cgi-ines/IUEdbsMY`

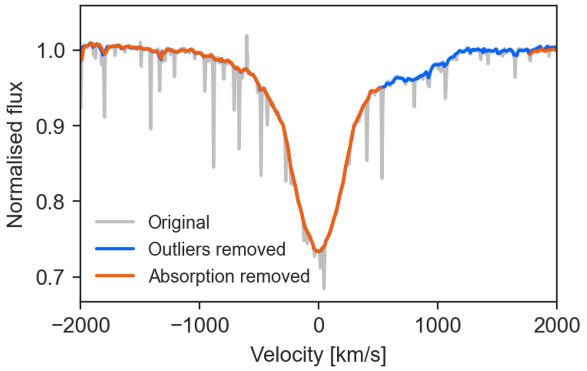

Figure 2. FEROS Hα profile for α Eri, from January 11th, 2000, when the star was inactive. The original profile (grey line) was crowded with telluric lines and cosmic ray features, which were removed (blue line). The C II absorption feature in 6580Å was also removed (orange line).

Fig. 4. Finally, we ran a simulation that considered both the UV and the Hα profile simultaneously (Fig. 5). 2D histograms and Spearman coefficients of all parameters for each simulation are also displayed in Figs. 3, 4 and 5. The results for all three simulations are summarised in Tab. 3.

In Be stars, the UV and Hα emissions arise from completely different physical processes. The UV comes mostly from the central star and therefore is sensitive to the stellar parameters M, W and $t/t_{\rm MS}$. For fast rotators, it may also strongly depend on the inclination of the system. On top of that, the UV spectra is modified by the interstellar reddening and distance.

The UV-only results (PDFs on Fig. 3) present α Eri as a $5.62^{+0.18}_{-0.16} M_\odot$ Be star; the very well defined PDF for the mass agrees with the UV being sensitive to this parameter. They also bring α Eri closer than Hipparcos indicated, at 37.3 pc ($26.0^{+1.36}_{-1.30}$ mas), and tilt the system so the inclination is only about 25.9°, far from the interferometric estimate of 60.6°. We note that for both inclination and distance, the PDFs are broad, and thus the errors on these estimates are large: i.e., the constraining power of the UV on these parameters is not very strong. Even so, the large errors do not account for the discrepancy between these measurements, which means that the UV alone does not constrain the simulation enough to accurately estimate these quantities. Finally, a $t/t_{\rm MS}$ larger than one indicates that a star like α Eri is not well represented by the MS phase of the Geneva grid of evolutionary models.

The Hα profile is sensitive to the stellar parameters and, in the case of fast rotators, to the inclination, but not to the distance (as the profile is normalised) and reddening (as it has negligible effects in the line shape). The Hα-only results (PDFs on Fig. 4) are consistent with these expectations, as the PDF for $E(B-V)$ is flat – i.e., this parameter is undetermined by the simulation –, and the PDF for the distance simply reflects the prior used. The results indicates α Eri as a $6.75^{+0.42}_{-0.53} M_\odot$ Be star, at the end of its MS lifetime, rotating at either $0.56^{+0.07}_{-0.06}$ or 0.76 ± 0.09 of critical.

Comparing the UV- and Hα-only simulations shows that the only relatively well constrained stellar parameters are M and $t/t_{\rm MS}$– albeit with large uncertainties. As discussed in Sect. 4.2, our grid allows for values of $t/t_{\rm MS} > 1$, i.e., the star has left the MS already (from the theoretical perspective of the Geneva models). The result from all our MCMC simulations place α Eri at this point in its evolution. Our extrapolation of the Geneva models for the artificial $t/t_{\rm MS} > 1$ ages is based on the native HDUST parameters actually used to calculate the radiative transfer models, $R_{\rm p}$ and luminosity. Therefore, our result of α Eri as an evolved star is indicative of its larger physical size and brightness rather than its actual age. The case of the rotation rate is interesting: it is the only parameter in our simulations to show a clear double-peaked PDF structure, with two separate HDRs (Hα-only simulation, Fig. 4). The relative strengths of the two peaks indicate that both solutions are likely given the data. If we consider the highest W found for the Hα, it is consistent with the UV-only result. The odd one out is the inclination: it is particularly discrepant between the two sets of results, with the UV-only result suggesting a lower value, inconsistent with previous studies of α Eri. However, the errors are large, as the UV does not constrain the parameter well. But all in all, given the limited data used in each simulation, the results are consistent with each other, excluding the inclination.

We cannot simply chose one set of results over the other. The MCMC method does not know stellar astrophysics; it is bounded by the data and the grid we give to it. What we can do to find the best possible results is to give the code more information to work with, so the parameters can be better constrained. This is where the result for the simulation using both UV and Hα shines (Fig. 5). It is immediately visible that the PDFs for all parameters are thinner, and the uncertainties on the estimates of the parameters are thus smaller (Tab. 3). The residuals in the inset plots also show the models fit both the UV and Hα line profile quite well, indicating that the simulation was successful in describing both data simultaneously.

When we consider both datasets at the same time, a tug-of-war between them is at play. Fig. 6 shows the 2D histogram for the mass and inclination (the two parameters where the UV- and Hα-only simulations are at odds) and for $t/t_{\rm MS}$ and rotation rate (where all models agree) for all three simulations. As shown by the contours, the UV- (in blue) and the Hα-only (in orange) results for M and i only overlap on a small region of the parameter space (in contrast with the $t/t_{\rm MS}$ and W map, where the overlap region is much larger). When given both datasets at once, the UV+Hα simulation converges to the overlap region. For the rotation rate, the peak at $W = 0.56$ found on the Hα simulation disappears, in agreement with the fact that both Hα (considering the second peak) and the UV find a common solution closer to 0.77, which is astrophysically more significant as most known Be stars have rotation rates higher than 0.6 (Rivinius et al. 2013a). The mass is also very well defined by this combined simulation. The mass of a star is notably a difficult parameter to determine in general, and by far the best method for its determination is orbital analysis of visual binaries, where a 2% accuracy is the mass is a very precise result (for example, see Anguita-Aguero et al. 2022). The mass we determine with our method is more properly referred to as a "theoretical" mass, as it depends strongly on the underlying evolutionary model used in our methodology. This example corroborates the intuitive notion that more reliable and significant results should be obtained as more observations are included.

2D histograms and Spearman coefficients in Figs. 3, 4 and 5 give us information on the correlations of each pair of parameter in the simulations. Positive Spearman coefficients indicate positive correlations: the simulation cannot discriminate well between increasing one or decreasing the other correlated parameters. Negative coefficients (anti-correlations) are the opposite: increasing (or decreasing) one parameter or the other has a similar effect on the models. The parameters usually have correlations with more than one other parameter, which in turn correlates to others, creating a feedback that, given the large number of parameters involved, can become quite difficult to gauge. The untangling of these intercon-

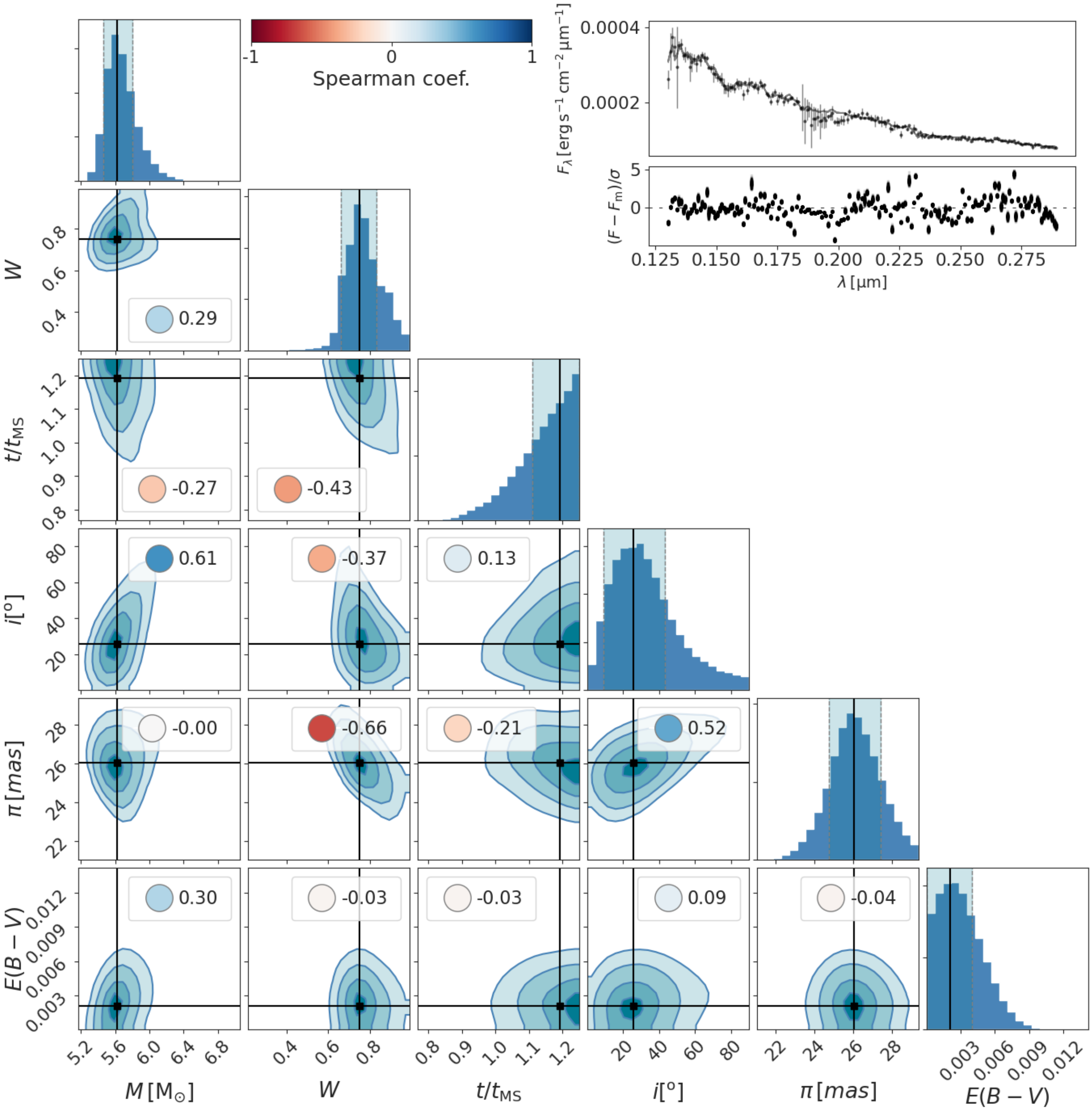

Figure 3. Corner plot of the UV-only simulation of α Eri. The PDFs for each parameter are shown in the main diagonal. The 2D histograms for each pair of parameters are shown in the lower part of the plot. The coloured circles indicate the Spearman coefficient for the correlation between the pairs of parameters (the colour scale are indicated at the top). On the upper inset, the observational data and residuals are plotted. The thin grey lines are a subset of 300 random models sampled by the code.

nections is one the main advantages of our method. In previous works, the correlations affecting the inference of stellar parameters of Be stars were not duly considered, as many parameters would be fixed to simplify the tiresome modelling procedure.

The UV-only simulation (Fig. 3) shows relevant correlations between several parameters. The three stellar parameters are strongly intercorrelated, whereas $E(B-V)$ only correlates significantly with mass, and the distance only with W and i. The inclination has relevant correlations to all stellar parameters and with distance, because changing the inclination of a Be star affects its apparent brightness given the oblateness and gravitational darkening of the star. Changing the distance also increases or decreases the apparent brightness of the star, which connects with W and i again because of the rotational effects on the surface gravity and area of the star. Therefore, we end up with a net of correlations between mass, rotation rate, t/t_MS, inclination and distance that is very difficult to disentangle.

To help understand how the parameters correlate, we show in Fig. 7 the colour-magnitude diagram (CMD) of several models with $M = 5.62 M_\odot$ (our result from the UV-only simulation), for

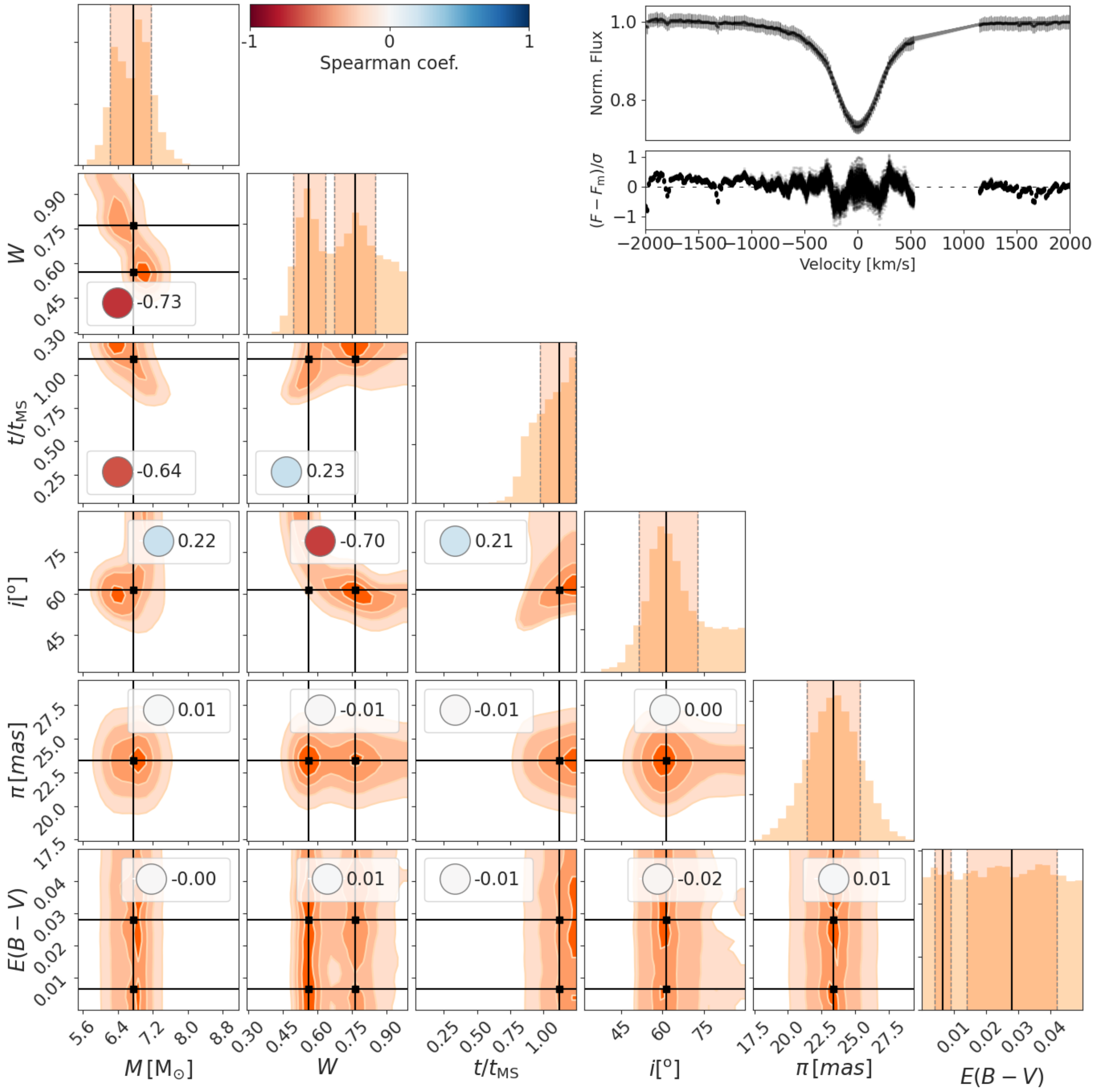

Figure 4. Same as Fig. 3, but for the Hα profile of α Eri.

different values of $t/t_{\rm MS}$, rotation rate and inclination (see Fig. A1 for a version with several masses). The trends seen in the CMD for different families of models showcase the effects of each parameter. Increasing the inclination makes the star dimmer and redder, and increasing $t/t_{\rm MS}$ makes it brighter and bluer: they are positively correlated. However, changing the rotation rate can brighten or dim the star, depending on the inclination angle: for low inclinations, increasing the rotation rate leads to a brighter, but redder, star. Thus, as far as the UV flux is concerned, if W increases, i must decrease to keep the same general flux emission: they are anti-correlated. The cluster of models with different W, $t/t_{\rm MS}$ and i in areas of the CMD of Figs. 7 and A1 show that there is significant degeneracies between the models, making it more difficult for the simulation to discriminate between different parameters.

The relationship between the parameters changes in the Hα-only simulation (Fig. 4). While the inclination still correlates with the three stellar parameters, the distance and reddening are not relevant for this simulation. The rotation rate W now has a strong anti-correlation ($\rho = -0.73$) with the mass, and a weaker positive correlation ($\rho = 0.23$) with the age. These correlations can be explained by the fact that the fast rotation of the star affects the shapes of the photospheric lines via rotational broadening, gravity darkening and a latitude dependent surface gravity. As such, the depth of the line decreases if the star rotates faster, but typically

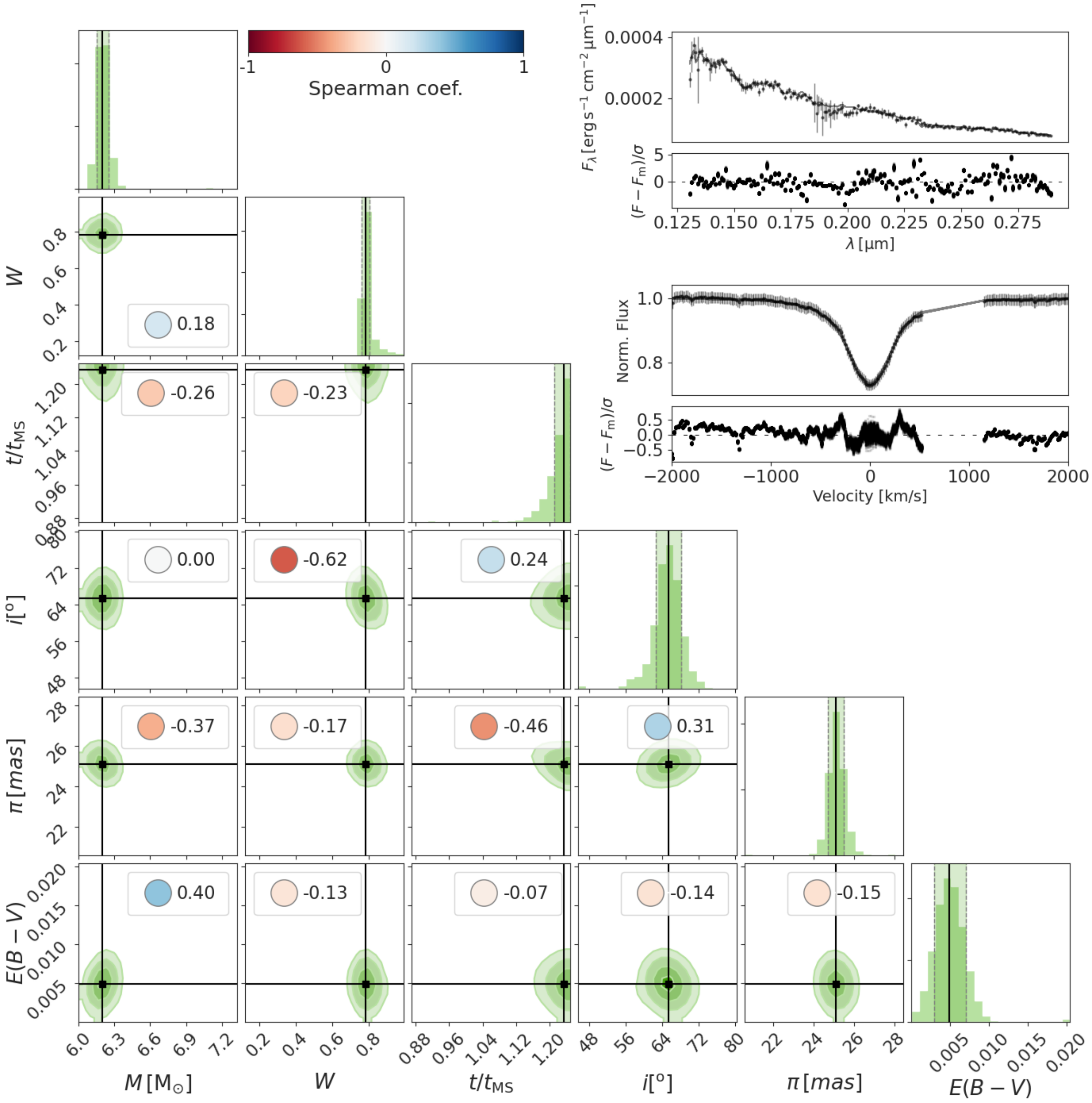

Figure 5. Same as Fig. 3, but for both the UV spectra and Hα profile of α Eri.

increases with decreasing mass (recall that the strongest H lines occur for A-type stars) and increases with decreasing surface gravity (or increasing radius). The inclination and W also have a significant anti-correlation ($\rho = -0.70$). The gravity darkening is more relevant if we can actually "see" the rotation: if the star is pole-on, for the observer it is not rotating at all, and has a less extreme temperature gradient. Therefore, if we decrease the inclination, the simulation pushes for higher rotations so its effects on the line profile are maintained.

The correlation coefficients shown in Fig. 5 are the result of the combined influences of the UV spectrum and the Hα on the simulation. The different values of the coefficients are a reflection of their complicated relationships.

6.3 Discussion

We now compare the results of the UV+Hα simulation for α Eri with the parameters obtained by Domiciano de Souza et al. (2014) and Kervella et al. (2022) (Tab. 3). The mass is remarkably consistent between our work and Kervella et al.'s (the mass was a fixed parameter in the analysis of Domiciano de Souza et al. 2014), even though ours is a theoretical mass, derived from the Geneva models, and theirs is a dynamical mass, derived from interferometric and

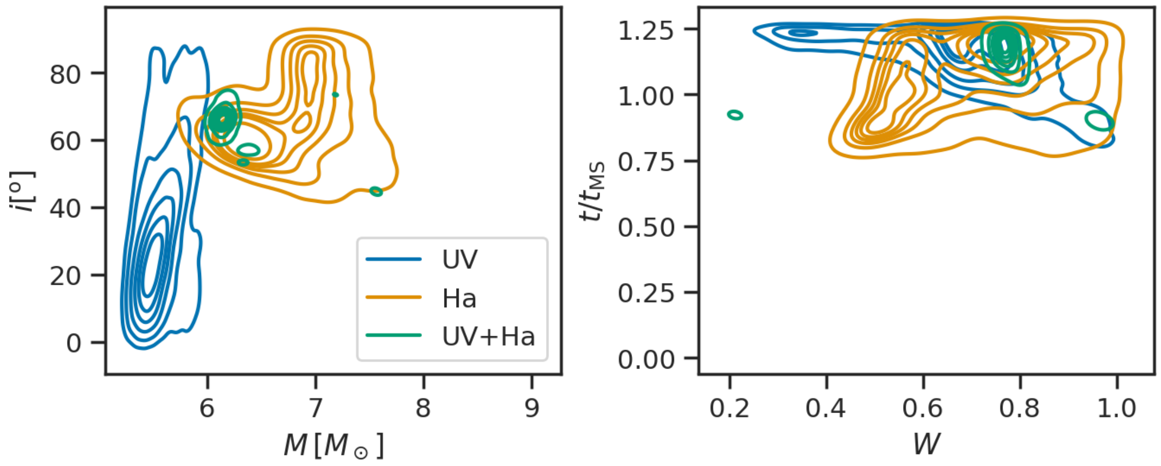

Figure 6. 2D histogram for the mass and inclination and $t/t_{\rm MS}$ and W of α Eri for our three simulations: UV (in blue), Hα (in orange), and UV and Hα combined (in green). Levels correspond to iso-proportions of the density for each distribution.

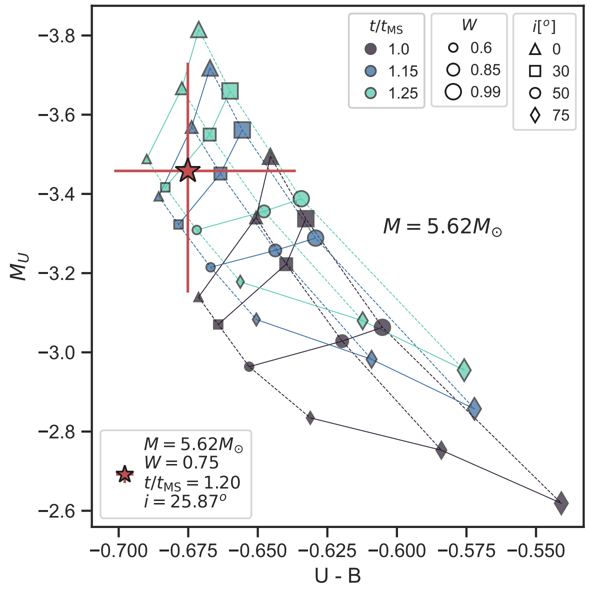

Figure 7. Colour-magnitude diagram for selected models from the Geneva grid. Different markers indicate inclinations, marker size indicate rotation rate W and marker colour indicates $t/t_{\rm MS}$. All models have a mass of $M = 5.62M_\odot$ The red star marks the most likely solution given by the UV-only simulation for α Eri, as per Tab. 3.

spectroscopic determinations of the orbital parameters of this binary system. Kervella et al. (2022) also offers an estimate of the age of α Eri, in agreement with our results that point to a star either at the end of the MS or the early post-MS stages. Another remarkable result is the inclination angle, that agrees well with the interferometric determination of Domiciano de Souza et al. (2014). The three estimates for the luminosity are similar within the errors and our derived distance is largely consistent with the Hipparcos value. The main disagreement is for W: our result ($W \approx 0.77$) suggests a lower rotation rate than found by Domiciano de Souza et al. (2014) ($W \approx 0.84$). Our estimate was constrained mostly by the Hα line profile, whereas Domiciano de Souza et al.'s by the interferometric measurement of the stellar oblateness. The different values of W causes systematic differences between derived parameters such as $R_{\rm p}$, $R_{\rm eq}$ and $\beta_{\rm GD}$. Our estimate for the polar radius, $R_{\rm p} = 5.86^{+0.63}_{-0.55} R_\odot$, coming from the Geneva models, is ~ 14% percent smaller than Domiciano de Souza et al.'s estimate of $6.78R_\odot$. The smaller $R_{\rm p}$ and rotation rates lead to a large discrepancy between our estimate for the equatorial radius and Domiciano de Souza et al.'s.

The causes for these discrepancies between our results and literature lie with the underlying models, assumptions made in each analysis, and the different data used. The results of Domiciano de Souza et al. come from a geometric approach; by measuring the physical shape of the photosphere and the inclination of the rotation axis and assuming a rigid rotator model they obtain their value for $\beta_{\rm GD}$, and then derive W. On the other hand, our model is spectroscopic: the shape of the line is what the code attempts to recreate.

We note that both BeAtlas and Domiciano de Souza et al. (2014) use the rigid rotator approximation. This approach is common when modelling fast rotators, given that neither their interior nor their photosphere have a complete theory that covers all the physical phenomena observed in these stars. Therefore, discrepancies between models and data are possible. In the case of α Eri especially, its Be nature brings further complications. As our Fig. 4 and Fig. 5 of Domiciano de Souza et al. (2014) both show, there are features in the residuals when models are compared to the data. This can be due to physical phenomena that occur in the stellar photosphere that are not considered in the underlying models, or can also be caused by the presence of a weak, residual disc from α Eri's previous active phase.

All in all, our method's ability to recover the fundamental parameters of α Eri using solely the UV spectrum and a single Hα profile is a significant result, even more so as it surpasses previous works in speed and ease. Furthermore, with BeAtlas, the entire parameter space is explored at once, for all parameters, without the computational cost of needing to calculate new models for every Be star we wish to study. The results of our analysis showcases the reliability of BeAtlas for studying inactive Be stars (as well as B and Bn stars), enabling seamless and semi-automatic modelling of numerous targets, with novel statistical robustness.

Table 3. Table summarising the results of our simulations for α Eriand literature estimates of the same parameters. The first six listed parameters are the ones inferred directly from our simulations; the others are derived.

Parameter	UV	Hα	UV + Hα	Domiciano de Souza et al. 2014	Kervella et al. 2022
$M\ [M_\odot]$	$5.62^{+0.18}_{-0.16}$	$6.75^{+0.42}_{-0.53}$	$6.20^{+0.05}_{-0.05}$	$6.1^{\star}$	5.99 ± 0.60
W	$0.75^{+0.08}_{-0.09}$	$0.56^{+0.07}_{-0.06}$ or $0.76^{+0.09}_{-0.09}$	$0.78^{+0.02}_{-0.02}$	0.84	—
$t/t_{\rm MS}$	$1.19^{+0.06}_{-0.08}$	$1.12^{+0.12}_{-0.15}$	$1.24^{+0.02}_{-0.02}$	—	$\approx 0.90^{(a)}$
$i\,[^{\rm o}]$	$25.87^{+17.35}_{-16.74}$	$61.29^{+11.50}_{-9.75}$	$65.35^{+2.79}_{-2.75}$	$60.6^{+7.1}_{-3.9}$	—$^{(b)}$
π [mas]	$26.05^{+1.36}_{-1.30}$	$23.39^{+1.98}_{-2.00}$	$25.10^{+0.39}_{-0.39}$	$23.39 \pm 0.57^{\star}$	$23.39 \pm 0.57^{\star}$
$E(B-V)$	$0.002^{+0.002}_{-0.002}$	$0.007^{+0.002}_{-0.003}$	$0.005^{+0.002}_{-0.002}$	0.00	0.00
$R_{\rm eq}/R_{\rm p}$	$1.28^{+0.07}_{-0.06}$	$1.16^{+0.04}_{-0.03}$ or $1.29^{+0.07}_{-0.06}$	$1.31^{+0.02}_{-0.02}$	1.352	1.39
$R_{\rm eq}\ [R_\odot]$	$7.10^{+0.78}_{-0.72}$	$7.05^{+1.08}_{-0.88}$ or $7.57^{+1.27}_{-1.06}$	$7.68^{+0.21}_{-0.21}$	9.16 ± 0.23	$8.14 \pm 0.26^{(c)}$
$\log(L)\ [L_\odot]$	$3.33^{+0.08}_{-0.09}$	$3.60^{+0.17}_{-0.21}$ or $3.59^{+0.17}_{-0.21}$	$3.50^{+0.02}_{-0.03}$	3.480	3.54 ± 0.05
$\beta_{\rm GD}$	$0.181^{+0.013}_{-0.013}$	$0.207 + 0.008 - 0.010$ or $0.178^{+0.013}_{-0.014}$	$0.176^{+0.003}_{-0.004}$	$0.166^{+0.012}_{-0.010}$	—
$v \sin i$ [km/s]	$127.0^{+95.8}_{-86.3}$	$210.1^{+56.2}_{-50.5}$ or $276.2^{+65.3}_{-65.0}$	$278.8^{+14.5}_{-13.7}$	260.3	—
$\overline{T}^{(d)}_{\rm eff}\ [10^4\ K]$	$1.546^{+0.059}_{-0.061}$	$1.784^{+0.095}_{-0.135}$ or $1.741^{+0.113}_{-0.146}$	$1.645^{+0.018}_{-0.021}$	$1.5^{\star}$	1.5539 ± 0.0438

Notes. (a) The time fraction was estimated based on the same models used in Sect. 4.3 of Kervella et al. 2022, from which the authors evaluated an age of 63 ± 4 Myr. (b) The inclination angle of 30.32 ± 0.35 calculated by Kervella et al. 2022 corresponds to the orbital plane of the system. The misalignment value between the equatorial plane of Achernar A and B of 30^{+7}_{-4} was calculated using i from Domiciano de Souza et al. 2014. (c) This value corresponds to a mean radius estimate fitted by Kervella et al. 2022, and it's not exactly an equatorial radius measurement. (d) In our work and in Domiciano de Souza et al. 2014, $\overline{T}_{\rm eff}$ is an average over the Roche photosphere, while in Kervella et al. 2022 they find an average temperature from spectral fitting using Castelli & Kurucz (2003). ★ Fixed value in their analysis.

7 β CMi: DISC BEATLAS

7.1 Target Overview

β CMi (β Canis Minoris, HD58715, HR2845, HIP36188 – B8Ve) is one of the most stable Be stars known, having been active since its discovery (Merrill et al. 1925), maintaining a stable disc with little variation (Klement et al. 2015). Also nearby (20.17 ± 0.20 mas, van Leeuwen 2007), β CMi was the target of interferometric studies: Quirrenbach et al. (1997) placed a lower limit for the diameter of the Hα emitting region, 13 $R_\odot$, and later Tycner et al. (2005), also through long-baseline interferometric data, found the diameter to be 28.8 ± 5.7 $R_\odot$. β CMi is the first late-type Be star to show signs of non-radial pulsation (Saio et al. 2007); spectrointerferometry and spectroscopy analysis of β CMi provided important confirmation of the Keplerian nature of Be discs (Wheelwright et al. 2012; Kraus et al. 2012).

β CMi was the target of the multi-technique analysis of Klement et al. (2015). This work represents a landmark in the Be literature, as it is still the most comprehensive model of a Be star to date (note that a corrigendum was published, Klement et al. 2017a). One interesting result was the detection of a SED turndown, a steepening in the slope of the SED in the radio, that was successfully modelled by a truncated disc, suggestive of a binary companion (see also Klement et al. 2017b). The authors also find the C IV 1548 line in the spectra of β CMi (not expected for a late-type B star), which they interpret as an indication of a hot, possibly subdwarf (sdB or sdO) companion. Dulaney et al. (2017) detected a companion in the system using radial velocity (RV) analysis, with a period of 170.4 days. The detection was, however, questioned by Harmanec et al. (2019), who noted that the RV signal might be contaminated. Wang et al. (2018) also found no sign of a sdOB secondary when analysing β CMi's UV data. Its status as a binary is therefore still not confirmed.

7.2 Results

We test the disc BEATLAS on β CMi using virtually the same data as Klement et al. (2017b), which is summarised below. Photometric data were combined from the literature using the Virtual Observatory VOSA (Bayo et al. 2008), comprising results of several observers and missions: UBVRI photometry from Ducati (2002); IR photometry from Dougherty et al. (1991), IRAS (Coté & Waters 1987), AKARI/IRC mid-IR all-sky Survey (Ishihara et al. 2010), SST (Su et al. 2006) and WISE (Cutri & et al. 2014); sub-mm and radio data from the VLA (Taylor et al. 1990), JCMT (Waters et al. 1991), IRAM (Wendker et al. 2000), APEX/LABOCA (Klement et al. 2015), CARMA (Klement et al. 2015) and JVLA (Klement et al. 2019). For the UV, data from IUE was used. As for α Eri, only high-dispersion large-aperture observations were selected and the data were averaged and binned to match the resolution of the grid. We also use polarimetric data taken from the Pico dos Dias Observatory, consisting of multi-epoch $BVRI$ linear photopolarimetry (see Klement et al. 2015, for more details). Our polarimetric data includes the dataset used in Klement et al. (2015), but has more recent points as well (Tab. B1).

β CMi can be considered a stable Be star, as its observables imply that the disc has not undergone dissipation or any significant structural changes (such as $m = 1$ waves, which are common for Be stars - see Okazaki 1997) in the past decades. Fig. B1 shows a compilation of 162 spectra from the BeSS database (Neiner et al. 2011) covering 20 years – from 2002 to 2023. The data demonstrates the remarkable stability of β CMi, displaying a root-mean-square (RMS) percentage variance of only 4.87% in the equivalent width (considering the median, $EW_{\rm med} = -3.77$ as the predicted value) and 2.79% in the V/R ratio (considering the predicted value as $V/R = 1$, also the value of the median of the measurements). Therefore, its SED, although comprised of data gathered in different epochs, is considered here as a true snapshot of its emission at a given moment. We also consider that the errors on any given measurement on the SED must be at least 10% of the measured value, as the intrinsic variability of a Be disc over time, even for discs as stable as this, should be accounted for. As indicated by the RMS errors of Hα line measurements, 10% is a cautious and conservative estimate. The polarisation data used for the simulation is an average of all measurements available for each of the 5 filters, and the errors are their median absolute deviation.

Several simulations were calculated for β CMi. We focus first on two of them: a full-SED simulation, with data from UV to radio (0.13 μm to 10 cm) and a polarisation-only simulation that uses the same BVRI polarisation data as Klement et al. (2015). We use a prior on the parallax for all simulations of β CMi. We use Hipparcos' determination, which has a smaller uncertainty and is well validated (van Leeuwen 2007), rather than Gaia DR2's estimate. For the full-SED simulation specifically, we also use a prior on the $v \sin i$ based on the value of Becker et al. (2015): 248 ± 13 km/s. R_V is kept fixed at the usual value of 3.1 (Fitzpatrick & Massa 1999) for all simulations.

Fig. 8 shows the result full-SED simulation for β CMi. The PDFs for all parameters are very well defined, and the residuals indicate that the model was able to describe the data well. The picture of β CMi our results paint is crystal clear: it is a late-type Be star, with an average rotation rate and at a later stage of its MS lifetime. The disc of β CMi is on the low density end for Be stars at large, but at the high end for Be stars with similar spectral types – see Fig. 8 of Vieira et al. (2017). Interestingly, the results suggest a disc that is truncated at around 33 $R_{\rm eq}$ ($\approx 136 R_\odot$), and with radial density exponent n smaller than 3.5, at about 2.8. Inclination, distance, and reddening are well constrained by the simulation.

As for α Eri, the correlations between parameters are complex, especially now that the disc is also being considered: as their non-negligible correlations indicate, stellar and disc parameters are coupled. Previous works for active Be stars do not take this into account, as they fix parameters (usually the stellar ones) when performing their χ^2 minimisation. When a parameter is fixed, its uncertainties are not propagated to the rest of the parameters, causing a chronic underestimation of the errors. In addition, when correlations are ignored and the entire parameter space is not explored simultaneously, there is the danger of missing regions of the parameter space that describe the system more accurately.

To understand the behaviour of the disc BeAtlas simulation and the correlations of the parameters, we must understand how the disc affects the observables. The SED of a Be star originates from three main components: photospheric emission, disc emission (reprocessed from photospheric emission) and disc absorption. The disc of a Be star can be thought of as a pseudo-photosphere that grows with wavelength approximately as (Vieira et al. 2016)

$$R_\lambda^{\rm eff} \propto \lambda^{(u+2)/(2n-\beta-s)} \times \rho_0^{2/2n-\beta-s}\,, \tag{12}$$

where s and u are the exponents of the radial power laws that describe the temperature and Gaunt factor variations, β is the exponent for the scale-height of the disc, as per Eq. 2, and ρ_0 is the base density of the disc, as per Eq. 3. Thus, the size of the pseudo-photosphere relates to the wavelength of the emission, with larger areas being responsible for the emission in larger wavelengths (Carciofi 2011; see also Fig. 13 of Vieira et al. 2015). The disc is then divided in two parts: an optically thick inner disc ($r < R_\lambda^{\rm eff}$) and a thin outer disc ($r > R_\lambda^{\rm eff}$), and the SED emission we measure is a combination of these. As such, we would expect the UV and visible to be more sensitive to flux from the star itself and the innermost disc, while the IR and the radio wavelengths (which originates from larger disc area) from the whole disc.

All three disc parameters are correlated, as all play a role in defining the pseudo-photosphere and thus the disc emission as whole. If n increases, the density profile of the disc becomes steeper and the size of the pseudo-photosphere becomes smaller, which translates in the SED as less flux excess. To remedy this effect, the disc would have to be denser. Indeed, this is the case for the full-SED simulation: n_0 and n have the strongest positive correlation among all parameters ($\rho = 0.78$). The correlation of the disc size with the base density is also quite straightforward: if the disc is smaller, there is a decrease in the overall emission; increasing the base density would counterbalance this effect (the results in Fig. 8 indicate a weaker correlation, $\rho = 0.38$). Similarly for $R_{\rm D}$ and n, as the disc size decreases, the emitting area also decreases, leading to a drop in the flux excess. To balance this, n would have to decrease as well to increase flux excess. In the full-SED simulation, the correlation is positive, as expected, but with a smaller significance ($\rho = 0.29$).

The inclination of the system also greatly affects the emission that reaches the observer. For a Be star seen pole-on, the general effect of the disc is to increase the flux at longer wavelengths, as reprocessed starlight is redirected mostly perpendicularly to the disc plane. For tenuous discs such as β CMi's, this flux excess is almost negligible in the UV, but its significance increases with wavelength so that from the far IR forwards it completely dominates the SED. For edge-on stars, the disc obscures part of the star: if the pseudo-photosphere is small, it can dim the system as a whole, as the disc steals stellar flux, but does not have a large re-emitting area. On the other hand, if the pseudo-photosphere is large, the disc will emit more in redder wavelengths, now brightening the system. In the case of β CMi, its intermediate inclination of 45° means that the stellar flux is partially absorbed and reprocessed by the disc, but still contributes significantly to the SED emission. In our simulation, we found the strongest correlations for i were with the stellar parameters, while only relatively weak correlations exist with the disc parameters, indicating that the geometry and temperature of the star are more affected by the inclination than the geometry and emission of the disc.

As the disc, in some wavelength ranges, has an impact on the flux that can rival the star itself, there are correlations also between stellar and disc parameters. The mass does not correlate significantly with the disc parameters, but the age and W do, in particular $t/t_{\rm MS}$ with $\log n_0$ and n, and W with R_D. The correlations with $t/t_{\rm MS}$ are straightforward. A larger $t/t_{\rm MS}$ implies a larger star and therefore a larger pseudo-photosphere for the same base density; the two parameters are then anticorrelated ($\rho = -0.43$ in Fig. 8); the same principle is valid for the correlation between $t/t_{\rm MS}$ and n ($\rho = -0.27$). The correlations between W and the disc parameters also follow the same logic: larger W implies a larger star and larger pseudo-photosphere, an effect that requires $R_{\rm D}$ to decrease to be counterbalanced ($\rho = -0.16$ in Fig. 8).

The polarisation-only simulation is shown in Fig. C1. The contrast between the results of the full-SED and polarisation-only simulations could not more striking. The latter simulation offers little to no constraint on the central star, but allows for estimating the base density of the disc. This result is expected as the primary factor controlling the polarisation level, other than the geometry, is the total number of scatterers – here, free electrons (Brown & McLean 1977). The polarisation-only simulation highlights a valuable lesson: without knowledge of the central star and on the density exponent n (strongly correlated with $\log n_0$), the simulation was unable to accurately determine the disk parameters that polarisation should be sensitive to. This results indicates that the constraining strength of the polarisation is too weak to distinguish between the models. Thus, only the results from the non-flat PDFs of Fig. C1 were included in Tab. 4. Even so, we note that only the PDF for $\log n_0$ has enough statistical relevance.

7.2.1 *Modelling Different Sections of the SED*

If Be disc emission behaves as a pseudo-photosphere (Sect. 7.2), then this should be apparent in our simulations if only sections of the SED are given to the code as input rather than the full SED. To investigate this, and to study the constraining power of each part of the SED, we separate out data into two sections: one covering the UV, visible and near-IR (0.13 – 5.0 μm) and another from the mid-IR to the radio (5.0 μm onward). The results are shown in Fig. 9 in the form of violin plots. The different colours represent the three sections: UV-NIR (blue), MIR-Radio (orange) and full-SED (green). The corresponding corner plots of these simulations can be found in Fig. C2 and C3. As expected, the PDFs of each parameter change drastically depending on the data used. In the UV-NIR simulation, the stellar parameters are well defined, as expected, while the disc parameters are more scattered, showing broad, sometimes with double-peaked PDFs (blue violins). The opposite happens for the MIR-Radio simulation, where the PDFs for the stellar parameters are all flat, and the disc parameters are more defined (orange violins). The known correlations between both disc and stellar parameters (Sect. 7.2) explain the different behaviours of these simulations. For instance, in the MIR-Radio simulation, the poorly constrained stellar parameters are reflected in the disc parameters. Here, a situation similar to the polarisation arises: although the MIR-Radio section of the SED should be the most effective in constraining the disc parameters, its ability to do so is hindered by the lack of information on the central star.

The differences between the results of the three simulations can also provide us with useful insights into structural changes in the disc. The two discrepant estimates of n by the UV-NIR and MIR-Radio sections, both very well determined by their respective simulations, can be a real effect, indicating that the inner disc is denser, with a less steep radial fall-off, than the outer disc, which has a larger n. These results suggest that the radial slope of the density varies with the distance from the star, and the disc density is thus not well represented by a single power-law; in other words, it deviates from the isothermal steady-state VDD solution. This point will be further discussed below.

7.3 Discussion

β CMi was the target of an in-depth analysis by Klement et al. (2015, 2017b). They calculated a custom grid of HDUST models, keeping the mass and age of the star fixed. These models were compared to UV spectra (used to initially constrain the stellar radius and luminosity), photometric data (according to Klement et al. 2015, the IR data constrained the disc parameters), polarisation (W and β), AMBER spectrointerferometry (i), hydrogen line profiles (used for consistency checks) of β CMi via χ^2 minimisation. Klement et al. (2017b) include new radio data, but the same models were used for comparison. These works therefore provide a very complete view of the star, which made it a good target for testing our method. The abridged results from our simulations and from Klement et al. 2017a,b are on Tab. 4.

The agreement between the results is remarkable, specially considering that our models explored more values for the parameters (mass and age especially), but used fewer data to constrain them. The disc parameters in particular all agree within 1σ, and the inclination and distance are also recovered. The result for $E(B-V)$ is also consistent with the estimate of $E(B-V) = 0.01$ from (Dougherty et al. 1994). The largest discrepancy in between the results is for W, which can be explained by the fact that age has a significant correlation with W ($\rho = -0.55$), and is not explored in Klement et al.'s grid as a free parameter.

Using the SED and priors alone our method is able to recover the inclination of the system within 1σ of the interferometric measurements, which is the most reliable way to estimate this parameter. The base density of the disc and the exponent n are also consistent within 1σ. This result is clear proof of what can be achieved with BeAtlas: finding the fundamental parameters of both the star and the disc, simultaneously, went from being a 2+ years project where a bespoke grid of models had to be calculated and systematically compared to different data, to a ~1 week effort. It is also interesting to note that the result from the full-SED and the polarisation-only simulations also give compatible results for the base density, even though these observables probe different phenomena (free-bound recombination vs. electron scattering) and regions of the disc.

7.3.1 *The SED turndown and denser inner disc of β CMi*

As discussed in Sect. 2, the power-law prescription of the steady-state, isothermal VDD is, although often used in Be literature, an approximation. Inconstant mass and AM feeding rates, viscosity variations, non-isothermal effects and binarity can all lead to density structures where the radial density exponent n is no longer the theoretically predicted value of 3.5.

The viscosity of VDDs is parametrised by the parameter α. In the solution we presented in Sect. 2, it is implied that this parameter is constant both in time and throughout the disc. However, the work of Rímulo et al. (2018) indicates that α can vary, for instance, depending on the status of the disc, being larger during disc formation than during dissipation. Furthermore, Ghoreyshi et al. (2021) finds evidence for an α variable also with radius for the Be star 28 CMa. Our results for the UV-NIR and MIR-Radio simulations (Fig. 9) suggest a smaller n in the inner disc of β CMi, which could be explained by a radially variable α.

Thermal effects in Be discs were studied by Carciofi & Bjorkman (2008) by solving the viscous diffusion and energy balance in the VDD formalism. In this scenario, the effective slope of the disc ranges from 2 to 3 between $1 \lesssim r \lesssim 3\,R_{\rm eq}$, and from 3 to 3.5 for $r \gtrsim 3\,R_{\rm eq}$. Strong effects are only seen for very dense discs; for the less dense disc of β CMi ($\log n_0 = 12.17^{+0.03}_{-0.03}$) it is likely that they, if present, would cause smaller changes in the density slope. Therefore, isothermal effects may also be the cause of the radial variation in n we detect for β CMi.

Klement et al. (2015) reported a steepening of the slope of the SED in the radio region for β CMi. The putative cause of this SED turndown is disc truncation: beyond a certain distance from the star, at the truncation radius, there is a sudden decrease in disc density. As the SED emission is dependant on the area of the emitting region, this density break translates as less flux in longer wavelengths. Our results (Fig. 8, Tab. 4) indicate that the disc of β CMi is truncated at about 34 $R_{\rm eq}$, or about 139 $R_\odot$ assuming $R_{\rm eq} = 4.1\,R_\odot$, in agreement with the values reported by Klement et al. (2015, 2017b) within 1σ. The physical cause of disc truncation is not clear. In the context

Table 4. Table summarising the results of our simulations for β CMiand literature estimates of the same parameters. The first nine listed parameters are the ones inferred directly from our simulations; the others are derived.

Parameter	Full SED	Polarisation	Klement et al. 2017a	Klement et al. 2017b
M [$M_\odot$]	$3.64^{+0.02}_{-0.02}$	—	$3.5^\star$	$3.5^\star$
W	$0.74^{+0.02}_{-0.02}$	—	$\gtrsim 0.98$	1.0
$t/t_{\rm MS}$	$0.71^{+0.02}_{-0.02}$	$0.82^{+0.18}_{-0.31}$	—	—
$\log\, n_0$ [cm^{-3}]	$12.17^{+0.03}_{-0.03}$	$11.83^{+0.31}_{-0.29}$	12.30	$12.22^{+0.30}_{-0.18}$
$R_{\rm D}$ [$R_{\rm eq}$]	$33.66^{+0.93}_{-0.97}$	—	35^{+10}_{-5}	40^{+10}_{-5}
n	$2.83^{+0.04}_{-0.04}$	—	3.0 – 3.5	2.9 ± 0.1
i [$^\circ$]	$46.29^{+1.55}_{-1.54}$	$40.50^{+8.49}_{-9.35}$	43^{+3}_{-2}	$43^\star$
π [mas]	$20.18^{+0.20}_{-0.20}$	—	—	—
$E(B-V)$	$0.026^{+0.002}_{-0.002}$	—	—	$0.01^{+0.02}_{-0.01}$
$R_{\rm eq}/R_{\rm p}$	$1.28^{+0.01}_{-0.01}$	—	1.49	—
$R_{\rm eq}$ [$R_\odot$]	$4.12^{+0.15}_{-0.13}$	—	4.17	4.20
$\log(L)$ [$L_\odot$]	$2.38^{+0.02}_{-0.02}$	—	2.26	2.26 ± 0.01
$\beta_{\rm GD}$	$0.181^{+0.003}_{-0.003}$	—	$0.1367^{+0.0025}_{-0.0013}$	—
$v \sin i$ [km/s]	$221.1^{+6.8}_{-7.3}$	—	270	—
$\overline{T}_{\rm eff}^{(a)}$ [10^4 K]	$1.175^{+0.015}_{-0.016}$	—	1.3740	—

$^{(a)}$ In our work, $\overline{T}_{\rm eff}$ is an average temperature over the Roche photosphere, while in Klement et al. 2017a it represents $T_{\rm eff}$ at the pole. ★ Fixed value in their analysis.

of the VDD model, there are two likely causes: the presence of a close binary companion and disc evaporation by gas pressure (disc ablation was believed to be another possible cause of truncation in the last decade, but more recent works – Kee et al. 2016 and following series – indicate its effect is much more significant in the inner disc than the outer disc.

The radial velocity of a VDD grows with radius, starting with subsonic velocities at the base of the disc (Bjorkman & Carciofi 2005). In principle, a VDD in an isolated (single) Be star should expand indefinitely, ultimately merging with the interstellar medium. Okazaki (2001) showed that once the radial speed of the disc reaches the transonic regime (at the transonic critical radius), the azimuthal velocity is no longer Keplerian, but AM-conserving. This shift occurs because the disc is no longer driven by viscosity, but rather by gas pressure. The critical radius relates to $v_{\rm orb}$ and the sound speed c_s as (Krtička et al. 2011)

$$\frac{R_s}{R_{\rm eq}} = \left[\frac{3}{10+4s}\left(\frac{v_{\rm orb}}{c_s}\right)^2\right]^{\frac{1}{1-s}}, \tag{13}$$

where s is the power-law exponent for the temperature, $T = T_0(R_{\rm eq}/r)^s$. For an isothermal disc, $s = 0$ and the typical values for R_s are about 430 $R_{\rm eq}$ for a B9V star and 350 $R_{\rm eq}$ for a B0V; for β CMi, using our most likely values, $\sim$ 315 $R_{\rm eq}$, much further than our estimate for the truncation radius of β CMi and other Be stars. However, the recent work of Curé et al. (2022) revisits this idea and offers a different solution to the equation of motion. They find that for certain values of line-force parameters and disc temperature, the transonic point can occur much closer to the Be star, at radii smaller than 50 $R_{\rm eq}$. This line of research will be further developed, but it is a possible answer to the truncation of Be discs.

We are then left with the presence of a binary companion as the most likely cause of disc truncation for β CMi. Binarity holds a special importance for Be stars in general. The causes of the spin up of Be stars are still not clear. Three main channels have been proposed for how a B star could acquire this fast rotation. The first is that they are simply born as very fast rotators, and remain so for the rest of their MS lifetime, and being a Be star is an innate characteristic (Zorec & Briot 1997). The second concept is that the star's spin up is a consequence of the stellar evolution along the MS, with the acceleration of the outer layers of the star resulting from contraction of its core (Ekström et al. 2008; Granada et al. 2013). The third option is binary evolution. Pols et al. (1991) considered the possibility that Be stars are formed through the evolution of mass-transfer close binaries. In this scenario there are two intermediate mass interacting stars, with one of them donating mass and AM to its companion. This companion, formerly a regular B star, becomes a Be star, while the donor evolves into a He star (or sub-dwarf O) or a compact object (WD, NS or BH). The existence of a large number of confirmed Be+NS and Be+sdO binaries indicate that this certainly happens. Pols et al. concluded that no more than 60% of the total number of Be stars would be formed this way, while van Bever & Vanbeveren (1997) found a maximum of 20% (and a minimum of 5%).

Several recent works, however, put much more weight in favour of the binary channel. Be stars have a higher fraction of runaways than normal B stars (Boubert & Evans 2018) and are not found in systems with a low mass MS star (Bodensteiner et al. 2020). The results of McSwain & Gies (2005) photometric survey showed that up to 73% of Be stars may be a result of binary mass transfer. de Mink et al. (2013) indicated that the main channel through which massive stars in general are spun-up is binary mass transfer and mergers, and noted that their models produce faster spinning stars than the ones of Pols et al. (1991) and van Bever & Vanbeveren (1997). The fraction of mergers and mass gainers in their simulation was 24.1%, very close to the estimate of the number of Be stars among

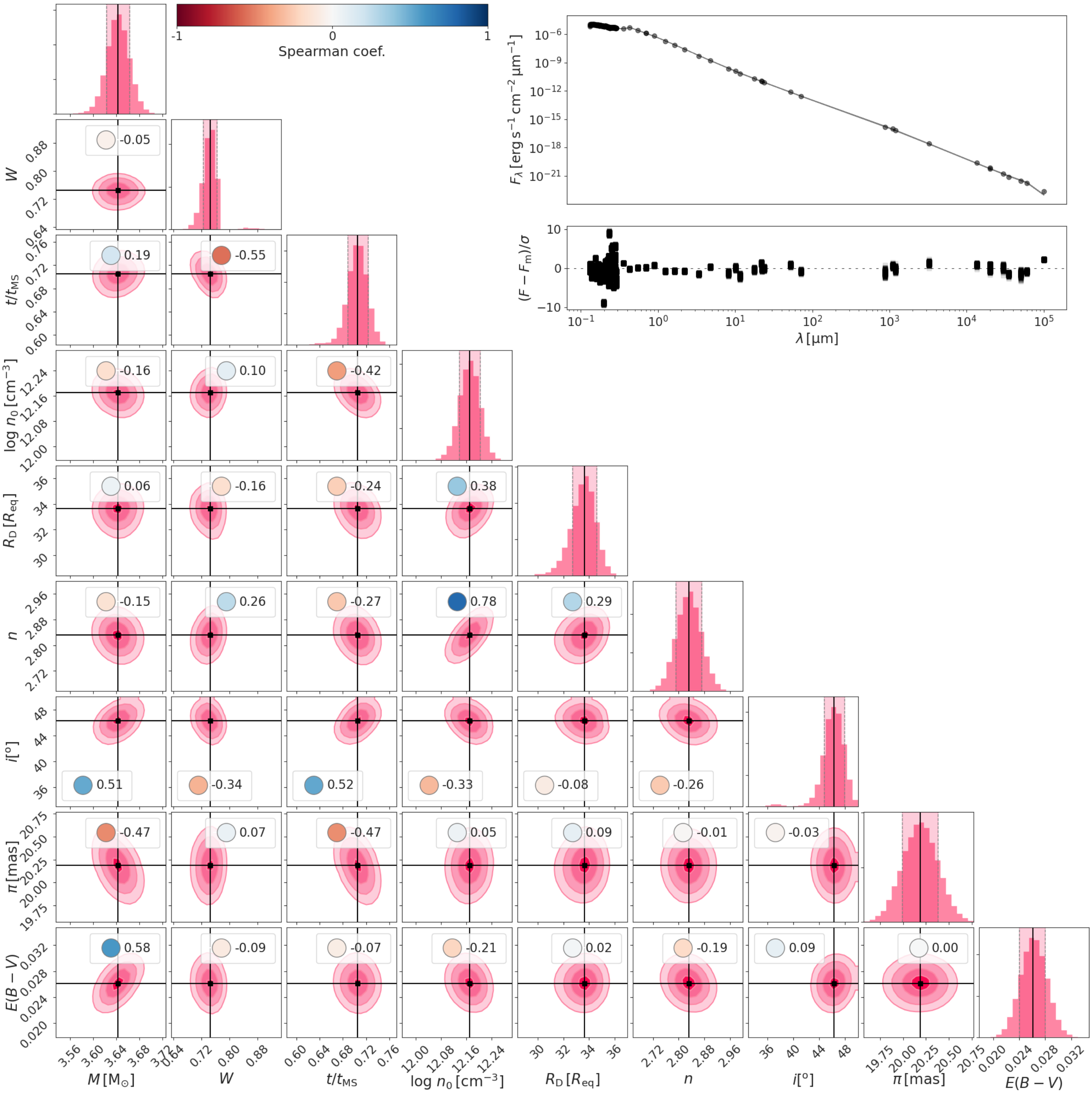

Figure 8. Corner plot of the MCMC run for the SED data of β CMi. The PDFs for each parameter are shown in the main diagonal. The 2D histograms for each pair of parameters are shown in the lower part of the plot. The coloured circles indicate the Spearman coefficient for the correlation between the pairs of parameters. On the upper inset, the observational data and residuals are plotted. The thin grey lines are a subset of 300 of the models sampled by the code.

early-type, non-supergiant B stars (20-30% - Zorec & Briot 1997). Shao & Li (2014) performed a thorough study of the influence of binarity in the birth of Be stars in the Galaxy using population synthesis, finding that fraction of Be stars that are a direct result of binary evolution among B-type stars was around 13–30%, again remarkably close to Zorec & Briot (1997)'s estimate for the Be population among early B-types. It is interesting to note that the only Be star with convincing data *against* the spin-up via binary mass transfer scenario is Achernar (Kervella et al. 2022).

Of particular interest is the work of Klement et al. (2019), which analysed the SEDs of 57 Be stars in search of signs of SED turndown. The authors detected it for all 26 targets with sufficient data coverage (including β CMi); among them are both confirmed and unknown binaries. Thus, the binary fraction among Be star could be as high as 100% if binarity is indeed behind the detected disc truncation.

Assuming a circular, coplanar orbit for the companion, Panoglou et al. (2016) finds in their SPH simulations that the truncation radius of the disc has a 3:1 resonance with the orbit for binary Be stars. No companion was detected for β CMi in the UV (Wang et al. 2018), nor via interferometry (Klement et al., in prep). Summing that to what is implied by the spectroscopic analysis of β CMi

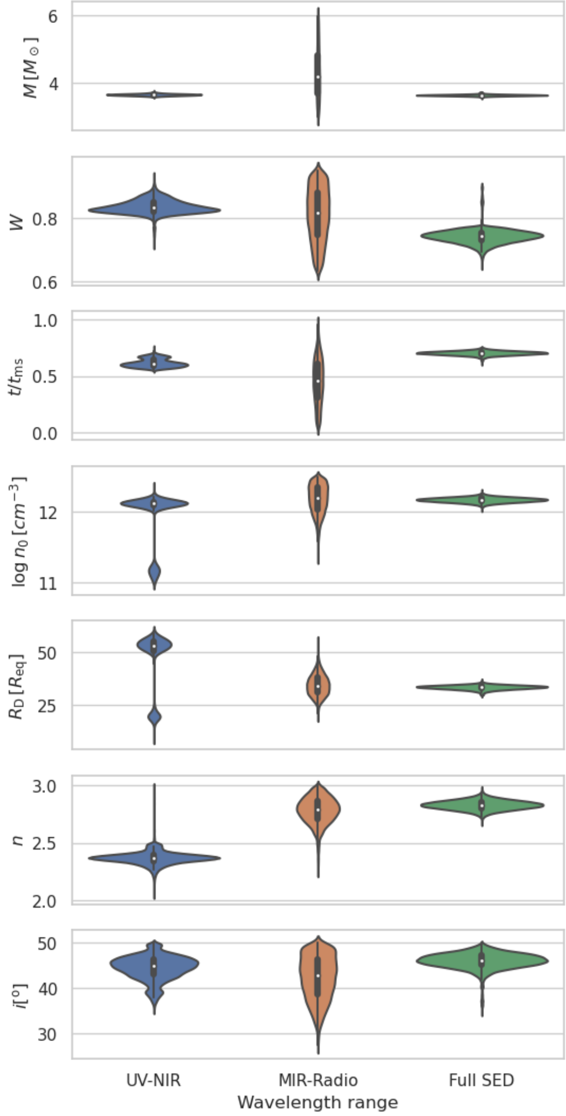

Figure 9. Violin plots showing the results of three MCMC simulations for different SED sections of β CMi. The blue violins represent the PDFs of the parameters for the a section covering the UV, visible and near-IR (UV-NIR – from 0.13 to 5.0 μm - corner plot in Fig. C2); the orange violins for the section from mid-IR to the radio (MIR-Radio – 5.0 μm onward - corner plot in Fig. C3); the green violins are for the simulation considering the entire SED, as also seen in Fig. 8.

(Dulaney et al. 2017; Harmanec et al. 2019), the mass of the companion must be low. Thus, assuming a mass range for the possible companion of $0.5 > M_2 > 0.1\,M_\odot$, our derived truncation radius and that truncation happens at the 3:1 resonance radius, this would place orbital period of the secondary between 280 and 295 days. Dulaney et al. (2017) found a possibly significant period at 170.4 days in their analysis of radial velocity shifts in β CMi spectral lines. It does not match the 3:1 resonance, but lies somewhere between 3:2 and 2:1 resonances if masses below 1.0 $M_\odot$ are considered, and matches 2:1 for $M_2 \approx 1.3 M_\odot$. Assuming our upper ranges for the values of $R_{\rm D}$ and $R_{\rm eq}$, the period of 170.4 days is consistent with a 3:2 resonance for a companion of mass $M_2 \approx 0.1 M_\odot$. We cannot discard the possibility of a possible companion as proposed by Dulaney et al. (2017), but their derived period and mass of the companion (0.42 $M_\odot$) together cannot be reconciled with our truncation radius in terms of its relation with the resonance radius. This relation, however, is also dependant on factors not considered in our analysis, such as the viscosity of the disc and the eccentricity and misalignment of the orbit.

Another effect of binarity, discussed briefly in Sect. 2.1, is the alteration of the radial density slope of the disc. This change is due to the accumulation of matter that occurs as the tidal interaction with the companion star hinders disc growth, resulting in a denser inner disc. How intense the accumulation effect is depends on the separation of the two stars, their mass ratio and the disc viscosity: small orbital separation, large mass ratio and lower viscosity lead to the densest Be discs, with n dropping to values as low as 2.5 (Panoglou et al. 2016).

Thus, the scenario depicted in Sect. 7.2.1 (see Fig. 9), where the slope of the disk density (n) increases with distance from β CMi, is consistent with the predicted accumulation effect observed in SPH simulations and could be interpreted as an indirect evidence of binarity. However, as mentioned earlier, non-isothermal effects may also contribute to similar behaviour, making it challenging to differentiate between the two effects and determine their relative importance.

8 CONCLUSIONS

To fully understand a star, we require knowledge of its photospheric parameters, including $T_{\rm eff}$, $\log\ g$, and others. However, determining these parameters is a complex process that typically involves comparing theoretical models, such as synthetic spectra from model atmosphere calculations, with observations. The analysis is even more challenging for classical Be stars due to their rapid rotation and the presence of their circumstellar viscous Keplerian discs (as discussed in Section 2).

In this work, we present BeAtlas, a grid of synthetic spectra of Be stars. It comprises two systematic grids of models: a purely-photospheric (i.e., discless) grid, and a star + disc grid ("disc grid"), computed according to the VDD formalism. The grid is composed of 616 000 synthetic spectra, calculated using modern stellar evolution models coupled with three-dimensional NLTE radiative transfer calculations. BeAtlas integrates a significant amount of the knowledge accumulated in recent years regarding Be star discs. The grid is used in conjunction with Bayesian MCMC sampling for the determination of fundamental parameters of the star, such as mass, rotation rate, age, and inclination. It also helps determine the properties of the disc, such as disc size, density scale, and density slope, as well as the distance and interstellar reddening of the target. This method efficiently provides PDFs for the modelled parameters and their cross-correlations, even in multi-dimensional parameter spaces. A key advantage of this approach is the use of prior information about the object, which contributes to the inference process.

The power of the combination of Bayesian inference with the BeAtlas grid is made quite clear by our results. As a first test of BeAtlas, we demonstrate that it can be used to perform multi-technique analysis of both active and inactive Be stars. This was done by a detailed study of the active late-type Be star β CMi and an inactive phase of late-type α Eri. These targets were selected because precise determinations for their fundamental parameters are available in the literature. We able to recover literature determinations of most stellar and disc parameters for our targets with good precision. The mass and age of α Eri both agree with the results of Kervella et al. (2022), which used interferometric and spectroscopic data of this binary system. The results for β CMi are notable: with only the SED data as input to our simulation, a complete picture of the star and its disc is recovered, closely matching literature results. For both targets, the distance and inclination are also recovered; for α Eri, the inclination agrees with interferometric measurements. The biggest discrepancies between our results and the literature lie with the rotation rates of both stars, which are less dramatic than the previously reported $> 98\%$ of critical for β CMi (our result is closer to 75%) and 84% for α Eri (against our result of 77%). For β CMi in particular, we recover the disc truncation result of Klement et al. (2015, 2017b), a sign of possible binarity for Be stars. By considering separate sections of the SED in our MCMC sampling, we also find signs that the inner disc of the star is denser than the outer disc, another indicator of binarity. Thus, β CMi is likely in a binary system; whether the companion is indeed the responsible for the signal detected by Dulaney et al. (2017) is not confirmed.

The correlations between all parameters were explored in unprecedented fashion. The net of inter-correlations is complex because Be stars are fast rotators: as evidenced in Figs. 7 and A1, adding rotation as a parameter leads to a multiple degeneracies between the stellar parameters. When we add the disc, whose emission is dependent on its density structure, wavelength considered and observing angle, the true complexity of Be stars is unveiled: if we want to properly study a Be star, the fact that the star and disc are coupled must be taken into account, which our method does seamlessly.

The applications of BeAtlas are numerous. It can be used effectively to find estimates for the fundamental parameters of any given Be or B star with just the SED and Hα line profile, and adding more observables in the simulation (other H lines and polarisation, for instance), will likely increase the accuracy in which the parameters are recovered.

BeAtlas can also be used as a discovery tool: as our method allows for many different combinations of observables and priors, we are able to explore different emitting areas of the disc with more detail, building a more realistic image of Be star disks. Since a model of a Be star can now be made in a matter of hours – as opposed to weeks or months as previously – BeAtlas can also be effectively used to study populations of B and Be stars. Comparing the characteristics of the two populations can reveal the necessary ingredients for the Be phenomenon. In conclusion, we believe BeAtlas has the power to massively upgrade the field of Be stars and help us solve our most pressing questions about these objects.

ACKNOWLEDGEMENTS

This study was financed in part by the “Conselho Nacional de Desenvolvimento Científico e Tecnológico” - Brasil (CNPq) - Finance Code 140171/2015-0. A. C. R. acknowledges support from FAPESP (grant 2017/08001-7), CAPES (grant 88887.464563/2019-00) and DAAD (grant 57552338). A. C. C. acknowledges support from CNPq (grant 311446/2019-1) and FAPESP (grants 2018/04055-8 and 2019/13354-1). P. T. acknowledges support from CAPES (grant 88887.604774/2021-00). M.G. acknowledges support from FAPESP (grant 2018/05326-5). This work made use of the computing facilities of the Laboratory of Astroinformatics (IAG/USP, NAT/Unicsul), whose purchase was made possible by the Brazilian agency FAPESP (grant 2009/54006-4) and the INCT-A. CEJ acknowledges support through the Natural Science and Engineering Research Council of Canada (NSERC). T.H.A. acknowledges support form FAPESP (grants 2018/26380-8 and 2021/01891-2). C.A. and M.C. thanks the support from Centro de Astrofísica de Valparaíso. M.C., C.A. and I.A. acknowledge the support of Fondecyt projects 1190485 and 1230131 and ANID-FAPESP project 2019/13354-1. This work has been possible thanks to the use of AWS-U.ChileNLHPC credits.

Powered@NLHPC: This work was partially supported by the supercomputing infrastructure of the NLHPC[14] (ECM-02). This work was performed using HPC resources from the computing center Mésocentre[15] of CentraleSupélec and École Normale Supérieure Paris-Saclay supported by CNRS and Région Île-de-France. This research was enabled in part by support provided by SHARCNET[16] and the Digital Research Alliance of Canada[17].

This study was granted access to and greatly benefited from the HPC resources of SIGAMM infrastructure (cluster Licallo), hosted by Observatoire de la Côte d’Azur (`crimson.oca.eu`) and supported by the Provence-Alpes Côte d’Azur region, France.

The authors acknowledge the National Laboratory for Scientific Computing (LNCC/MCTI, Brazil) for providing HPC resources of the SDumont[18] supercomputer, which have contributed to the research results reported within this paper.

REFERENCES

Adelman S. J., 2004, in Zverko J., Ziznovsky J., Adelman S. J., Weiss W. W., eds, IAU Symposium Vol. 224, The A-Star Puzzle. pp 1–11, doi:10.1017/S1743921304004314

Anguita-Aguero J., Mendez R. A., Clavería R. M., Costa E., 2022, AJ, 163, 118

Arcos C., Kanaan S., Chávez J., Vanzi L., Araya I., Curé M., 2018, MNRAS, 474, 5287

Baade D., et al., 2016, A&A, 588, A56

Baron D., 2019, arXiv e-prints, p. arXiv:1904.07248

Bayo A., Rodrigo C., Barrado y Navascues D., Solano E., Gutierrez R., Morales-Calderon M., Allard F., 2008, VizieR Online Data Catalog, 349

Becker J. C., Johnson J. A., Vanderburg A., Morton T. D., 2015, The Astrophysical Journal Supplement Series, 217, 29

Bjorkman J. E., Carciofi A. C., 2005, in Ignace R., Gayley K. G., eds, Astronomical Society of the Pacific Conference Series Vol. 337, The Nature and Evolution of Disks Around Hot Stars. p. 75

Bjorkman J. E., Cassinelli J. P., 1993, ApJ, 409, 429

Bodensteiner J., Shenar T., Sana H., 2020, A&A, 641, A42

Borgman J., 1960, Bull. Astron. Inst. Netherlands, 15, 255

Boubert D., Evans N. W., 2018, MNRAS, 477, 5261

Bouchaud K., Domiciano de Souza A., Rieutord M., Reese D. R., Kervella P., 2020, A&A, 633, A78

Bowman W. P., et al., 2020, ApJ, 899, 7

Brown J. C., McLean I. S., 1977, A&A, 57, 141

Brown J. C., Cassinelli J. P., Maheswaran M., 2008, ApJ, 688, 1320

Buscombe W., 1962, Mount Stromlo Observatory Mimeographs, 4, 1

Cannon A. J., Pickering E. C., 1993, VizieR Online Data Catalog, p. III/135A

Carciofi A. C., 2011, in Neiner C., Wade G., Meynet G., Peters G., eds, IAU Symposium Vol. 272, IAU Symposium. pp 325–336 (`arXiv:1009.3969`), doi:10.1017/S1743921311010738

Carciofi A. C., Bjorkman J. E., 2006, ApJ, 639, 1081

Carciofi A. C., Bjorkman J. E., 2008, ApJ, 684, 1374

Carciofi A. C., Bjorkman J. E., Magalhães A. M., 2004, ApJ, 604, 238

Carciofi A. C., et al., 2006, ApJ, 652, 1617

---

[14] `nlhpc.cl`

[15] `mesocentre.centralesupelec.fr`

[16] `sharcnet.ca`

[17] `alliancecan.ca`

[18] `sdumont.lncc.br`

Carciofi A. C., Bjorkman J. E., Otero S. A., Okazaki A. T., Štefl S., Rivinius T., Baade D., Haubois X., 2012, ApJ, 744, L15

Cassinelli J. P., Brown J. C., Maheswaran M., Miller N. A., Telfer D. C., 2002, ApJ, 578, 951

Castelli F., Kurucz R. L., 2003, in Piskunov N., Weiss W. W., Gray D. F., eds, IAU Symposium Vol. 210, Modelling of Stellar Atmospheres. p. A20

Chen M.-H., Shao Q.-M., Ibrahim J. G., 2000, Monte Carlo Methods in Bayesian Computation. Springer New York, doi:10.1007/978-1-4612-1276-8, `https://doi.org/10.1007/978-1-4612-1276-8`

Choi J., Dotter A., Conroy C., Cantiello M., Paxton B., Johnson B. D., 2016, ApJ, 823, 102

Claret A., 2000, A&A, 363, 1081

Collins II G. W., 1963, ApJ, 138, 1134

Collins II G. W., Harrington J. P., 1966, ApJ, 146, 152

Coté J., Waters L. B. F. M., 1987, A&A, 176, 93

Cranmer S. R., 1996, PhD thesis, Bartol Research Institute, University of Delaware

Cranmer S. R., 2005, ApJ, 634, 585

Curé M., Meneses R., Araya I., Arcos C., Peña G., Machuca N., Rodriguez A., 2022, A&A, 664, A185

Cutri R. M., et al. 2014, VizieR Online Data Catalog, 2328

Cyr I. H., Jones C. E., Panoglou D., Carciofi A. C., Okazaki A. T., 2017, MNRAS, 471, 596

Dalla Vedova G., Millour F., Domiciano de Souza A., Petrov R. G., Moser Faes D., Carciofi A. C., Kervella P., Rivinius T., 2017, A&A, 601, A118

Domiciano de Souza A., et al., 2014, A&A, 569, A10

Dougherty S. M., Taylor A. R., Clark T. A., 1991, AJ, 102, 1753

Dougherty S. M., Waters L. B. F. M., Burki G., Cote J., Cramer N., van Kerkwijk M. H., Taylor A. R., 1994, A&A, 290, 609

Ducati J. R., 2002, VizieR Online Data Catalog, 2237

Dulaney N. A., et al., 2017, ApJ, 836, 112

Ekström S., Meynet G., Maeder A., Barblan F., 2008, A&A, 478, 467

Ekström S., et al., 2012, A&A, 537, A146

Espinosa Lara F., 2014, in EAS Publications Series. pp 297–308, doi:10.1051/eas/1569017

Espinosa Lara F., Rieutord M., 2011, A&A, 533, A43

Fitzpatrick E. L., Massa D., 1999, ApJ, 525, 1011

Foreman-Mackey D., Hogg D. W., Lang D., Goodman J., 2013a, PASP, 125, 306

Foreman-Mackey D., Hogg D. W., Lang D., Goodman J., 2013b, PASP, 125, 306

Gaia Collaboration et al., 2016, A&A, 595, A1

Gaia Collaboration et al., 2022, arXiv e-prints, p. arXiv:2208.00211

Georgy C., Ekström S., Granada A., Meynet G., Mowlavi N., Eggenberger P., Maeder A., 2013, A&A, 553, A24

Ghoreyshi M. R., et al., 2018, MNRAS, 479, 2214

Ghoreyshi M. R., Carciofi A. C., Jones C. E., Faes D. M., Baade D., Rivinius T., 2021, ApJ, 909, 149

Goodman J., Weare J., 2010, Communications in Applied Mathematics and Computational Science, 5, 65

Granada A., Ekström S., Georgy C., Krtička J., Owocki S., Meynet G., Maeder A., 2013, A&A, 553, A25

Grevesse N., Sauval A. J., 1998, Space Sci. Rev., 85, 161

Hardorp J., Theile I., Voigt H. H., 1965, Hamburger Sternw. Warner & Swasey Obs., C05, 0

Harmanec P., et al., 2019, ApJ, 875, 13

Hastings W. K., 1970, Biometrika, 57, 97

Haubois X., Carciofi A. C., Rivinius T., Okazaki A. T., Bjorkman J. E., 2012, ApJ, 756, 156

Hiltner W. A., Garrison R. F., Schild R. E., 1969, ApJ, 157, 313

Houk N., Swift C., 1999, Michigan Spectral Survey, 5, 0

Hyndman R. J., 1996, The American Statistician, 50, 120

Ishihara D., et al., 2010, A&A, 514, A1

Janson M., et al., 2012, ApJ, 754, 44

Kee N. D., Owocki S. P., Sundqvist J. O., 2016, preprint, (`arXiv:1602.07874`)

Kervella P., Domiciano de Souza A., 2007, A&A, 474, L49

Kervella P., et al., 2022, A&A, 667, A111

Klement R., et al., 2015, A&A, 584, A85

Klement R., et al., 2017a, Multitechnique testing of the viscous decretion disk model (Corrigendum). I. The stable and tenuous disk of the late-type Be star β CMi, Astronomy & Astrophysics, Volume 607, id.C1, 1 pp., doi:10.1051/0004-6361/201526535e

Klement R., et al., 2017b, A&A, 601, A74

Klement R., et al., 2019, ApJ, 885, 147

Klement R., et al., 2022, ApJ, 940, 86

Koubský P., Kotková L., Votruba V., Šlechta M., Dvořáková Š., 2012, A&A, 545, A121

Kraus S., et al., 2012, ApJ, 744, 19

Krtička J., Owocki S. P., Meynet G., 2011, A&A, 527, A84

Kurucz R., 1994, CD-ROM 19, 20, & 21, Solar abundance model atmospheres for 0,1,2,4,8 km/s. (Cambridge: SAO), 19

Lee U., Osaki Y., Saio H., 1991, MNRAS, 250, 432

Lesh J. R., 1968, ApJS, 17, 371

Levenhagen R. S., Leister N. V., 2006, MNRAS, 371, 252

Maeder A., 2009, Physics, Formation and Evolution of Rotating Stars, doi:10.1007/978-3-540-76949-1.

Marr K. C., Jones C. E., Carciofi A. C., Rubio A. C., Mota B. C., Ghoreyshi M. R., Hatfield D. W., Rímulo L. R., 2021, ApJ, 912, 76

Marr K. C., Jones C. E., Tycner C., Carciofi A. C., Silva A. C. F., 2022, ApJ, 928, 145

Martins F., Schaerer D., Hillier D. J., 2005, A&A, 436, 1049

McGill M. A., Sigut T. A. A., Jones C. E., 2011, ApJ, 743, 111

McSwain M. V., Gies D. R., 2005, ApJS, 161, 118

Meilland A., et al., 2007, A&A, 464, 59

Merrill P. W., Humason M. L., Burwell C. G., 1925, ApJ, 61, 389

Metropolis N., Rosenbluth A., Rosenbluth M., Teller A., Teller E., 1953, Journal of Chemical Physics, 21, 1087

Meynet G., Maeder A., 2002, A&A, 390, 561

Molnar M. R., 1972, ApJ, 175, 453

Negueruela I., Steele I. A., Bernabeu G., 2004, Astronomische Nachrichten, 325, 749

Neiner C., de Batz B., Cochard F., Floquet M., Mekkas A., Desnoux V., 2011, AJ, 142, 149

Okazaki A. T., 1991, PASJ, 43, 75

Okazaki A. T., 1997, A&A, 318, 548

Okazaki A. T., 2001, PASJ, 53, 119

Okazaki A. T., Bate M. R., Ogilvie G. I., Pringle J. E., 2002, MNRAS, 337, 967

Oudmaijer R. D., Parr A. M., 2010, MNRAS, 405, 2439

Panoglou D., Carciofi A. C., Vieira R. G., Cyr I. H., Jones C. E., Okazaki A. T., Rivinius T., 2016, MNRAS, 461, 2616

Panoglou D., Faes D. M., Carciofi A. C., Okazaki A. T., Baade D., Rivinius T., Borges Fernandes M., 2018, MNRAS, 473, 3039

Perryman M. A. C., et al., 1997, A&A, 323, L49

Pols O. R., Cote J., Waters L. B. F. M., Heise J., 1991, A&A, 241, 419

Porter J. M., 1997, A&A, 324, 597

Porter J. M., 1999, A&A, 348, 512

Pringle J. E., 1981, ARA&A, 19, 137

Quirrenbach A., et al., 1997, apj, 479, 477

Richardson N. D., et al., 2021, MNRAS, 508, 2002

Rímulo L. R., et al., 2018, MNRAS, 476, 3555

Rivinius T., Carciofi A. C., Martayan C., 2013a, A&ARv, 21, 69

Rivinius T., Baade D., Townsend R. H. D., Carciofi A. C., Štefl S., 2013b, A&A, 559, L4

Robitaille T. P., Whitney B. A., Indebetouw R., Wood K., 2007, ApJS, 169, 328

Saio H., et al., 2007, ApJ, 654, 544

Sana H., et al., 2012, Science, 337, 444

Secchi A., 1866, Astronomische Nachrichten, 68, 63

Shakura N. I., Sunyaev R. A., 1973, A&A, 24, 337

Shao Y., Li X.-D., 2014, ApJ, 796, 37

Sharma S., 2017, ARA&A, 55, 213

Sigut T. A. A., Jones C. E., 2007, ApJ, 668, 481

Silaj J., Jones C. E., Sigut T. A. A., Tycner C., 2014, ApJ, 795, 82

Sota A., Maíz Apellániz J., Walborn N. R., Alfaro E. J., Barbá R. H., Morrell N. I., Gamen R. C., Arias J. I., 2011, ApJS, 193, 24
Su K. Y. L., et al., 2006, ApJ, 653, 675
Suffak M. W., Jones C. E., Tycner C., Henry G. W., Carciofi A. C., Mota B. C., Rubio A. C., 2020, ApJ, 890, 86
Taylor A. R., Dougherty S. M., Waters L. B. F. M., Bjorkman K. S., 1990, A&A, 231, 453
Touhami Y., et al., 2013, ApJ, 768, 128
Touhami Y., et al., 2014, in Creech-Eakman M. J., Guzik J. A., Stencel R. E., eds, Astronomical Society of the Pacific Conference Series Vol. 487, Resolving The Future Of Astronomy With Long-Baseline Interferometry. p. 395
Townsend R. H. D., Owocki S. P., Howarth I. D., 2004, MNRAS, 350, 189
Tycner C., et al., 2005, ApJ, 624, 359
Tycner C., Jones C. E., Sigut T. A. A., Schmitt H. R., Benson J. A., Hutter D. J., Zavala R. T., 2008, ApJ, 689, 461
Vieira R. G., Carciofi A. C., Bjorkman J. E., 2015, MNRAS, 454, 2107
Vieira R. G., Carciofi A. C., Bjorkman J. E., 2016, in Sigut T. A. A., Jones C. E., eds, Astronomical Society of the Pacific Conference Series Vol. 506, Bright Emissaries: Be Stars as Messengers of Star-Disk Physics. p. 135 (`arXiv:1604.03775`), doi:10.48550/arXiv.1604.03775
Vieira R. G., Carciofi A. C., Bjorkman J. E., Rivinius T., Baade D., Rímulo L. R., 2017, MNRAS, 464, 3071
Vinicius M. M. F., Zorec J., Leister N. V., Levenhagen R. S., 2006, A&A, 446, 643
Wang L., Gies D. R., Peters G. J., 2018, ApJ, 853, 156
Waters L. B. F. M., Boland W., Taylor A. R., van de Stadt H., Lamers H. J. G. L. M., 1989, A&A, 213, L19
Waters L. B. F. M., van der Veen W. E. C. J., Taylor A. R., Marlborough J. M., Dougherty S. M., 1991, A&A, 244, 120
Wendker H. J., Altenhoff W. J., Thum C., 2000, Astronomische Nachrichten, 321, 157
Wheelwright H. E., Bjorkman J. E., Oudmaijer R. D., Carciofi A. C., Bjorkman K. S., Porter J. M., 2012, MNRAS, 423, L11
Wood K., Bjorkman K. S., Bjorkman J. E., 1997, ApJ, 477, 926
Zorec J., Briot D., 1997, A&A, 318, 443
de Almeida E. S. G., et al., 2020, A&A, 636, A110
de Mink S. E., Langer N., Izzard R. G., Sana H., de Koter A., 2013, ApJ, 764, 166
van Bever J., Vanbeveren D., 1997, A&A, 322, 116
van Leeuwen F., 2007, A&A, 474, 653
von Zeipel H., 1924, MNRAS, 84, 684

APPENDIX A: BEATLAS' OBSERVABLES

Table A1. Definition of BeAtlas' observables.

Observable	$\lambda_{\rm min}$ [μm]	$\lambda_{\rm max}$ [μm]	$N_{\rm bins}$	Spacing	$N_{\rm phot}$	Image	Comments
UV	0.1	0.32	210	linear	4.0×10^8	No	Kurucz resolution
SED	0.32	1.05	108	log	1.0×10^9	No	–
J	1.05	1.4	30	linear	1.8×10^8	No	–
H	1.4	1.85	30	linear	1.5×10^8	Yes	PIONIER[1], MIRC[2], R~300
K	1.85	2.45	30	linear	1.5×10^8	Yes	GRAVITY[3], R~4,000
L	2.45	3.9	16	linear	1.0×10^8	Yes	MATISSE[4], R~1,000
M	3.9	8	24	linear	1.5×10^8	Yes	MATISSE, R~550
N	8	13	15	linear	1.0×10^8	Yes	MATISSE, R~250
Q1	13	18	10	linear	2.0×10^7	No	–
Q2	18	25	10	linear	2.0×10^7	No	–
IR35	25	45	10	log	2.0×10^7	No	–
IR65	45	85	10	log	2.0×10^7	No	–
IR100	85	120	10	log	2.0×10^7	No	–
IR160	120	200	10	log	2.0×10^7	No	–
IR300	200	400	10	log	2.0×10^7	No	–
IR600	400	800	10	log	2.0×10^7	No	–
MM	800	1200	10	log	2.0×10^7	No	LABOCA[5], JCMT1/2[6], IRAM[7]
CM07	6000	7500	10	log	2.0×10^7	No	VLA[8]/Q
CM13	11300	16700	10	log	2.0×10^7	No	VLA/K
CM20	16700	25000	10	log	2.0×10^7	No	VLA/Ku
CM30	25000	37500	10	log	2.0×10^7	No	VLA/X
CM60	37500	75000	10	log	2.0×10^7	No	VLA/C

Observable	$\lambda_{\rm c}$ [Å]	R	Spacing	$N_{\rm phot}$	Image	Comments
Hα	6564.61	20,000	linear	1.1×10^9	Yes	CHARA/SPICA[9], R~10,000
Hβ	4862.71	10,000	linear	3.0×10^8	No	–
Hγ	4341.69	6,000	linear	6.5×10^7	No	–
Hδ	4102.89	6,000	linear	6.5×10^7	No	–
Br11	16811.1	6,000	linear	1.0×10^8	No	APOGEE[10]
Br13	16113.7	6,000	linear	1.0×10^8	No	APOGEE
Brγ	21661.178	20,000	linear	2.0×10^8	Yes	AMBER[11], GRAVITY[3]
Pfγ	37405.6	10,000	linear	1.0×10^8	No	–
Hu14	40208.7	10,000	linear	1.0×10^8	No	–
Brα	40522.6	10,000	linear	1.0×10^8	No	–

[1] `www.eso.org/sci/facilities/paranal/instruments/pionier.html`
[2] `www.chara.gsu.edu/instrumentation/mirc`
[3] `www.eso.org/sci/facilities/paranal/decommissioned/midi.html`
[4] `www.eso.org/sci/facilities/develop/instruments/matisse.html`
[5] `www.eso.org/public/teles-instr/apex/laboca/`
[6] `www.eaobservatory.org/jcmt/`
[7] `www.iram-institute.org/`
[8] `www.public.nrao.edu/telescopes/vla/`
[9] `www.chara.gsu.edu/instrumentation/spica`
[10] `www.sdss4.org/dr12/irspec/`
[11] `www.eso.org/sci/facilities/paranal/instruments/amber/overview.html`

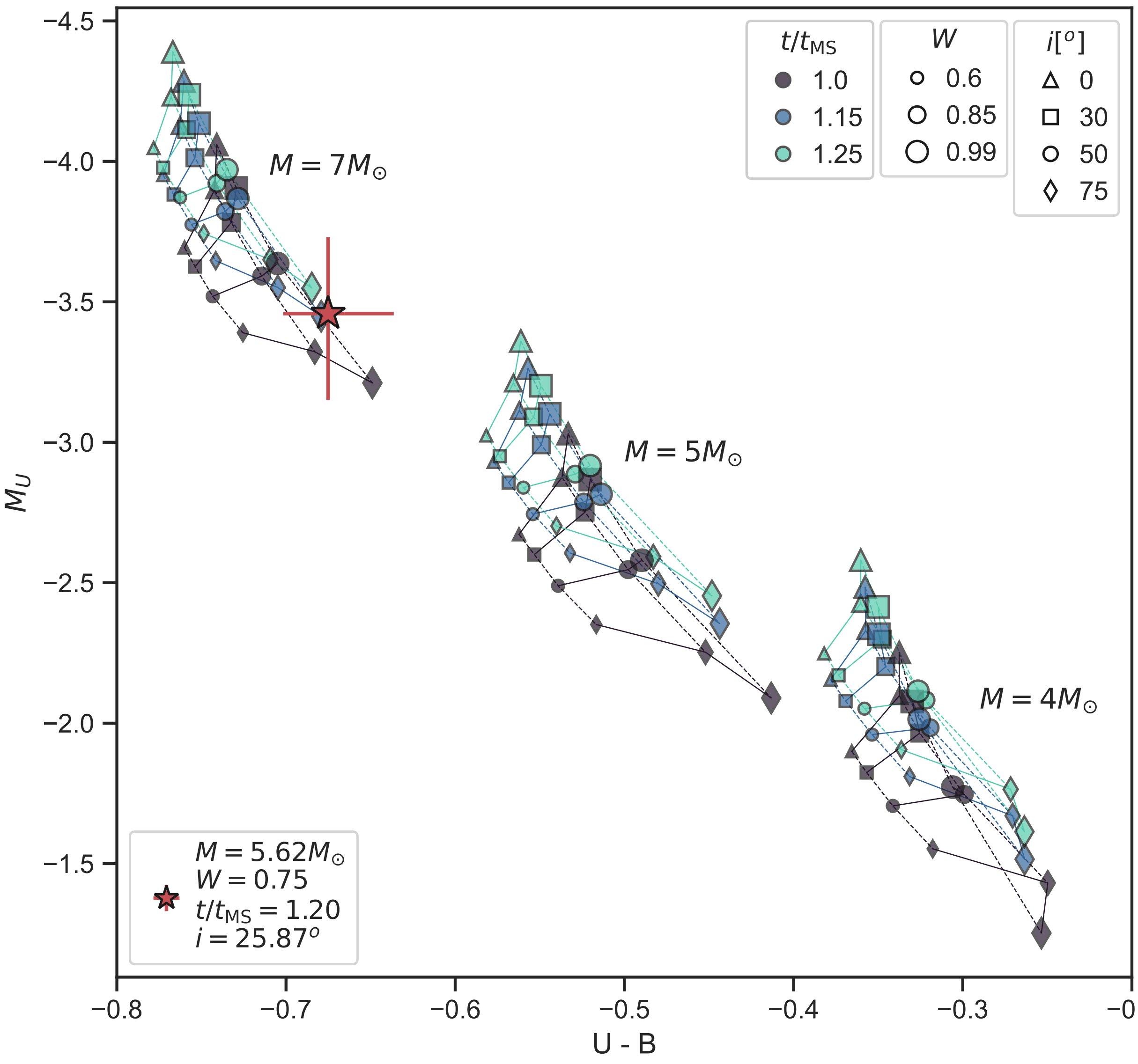

Figure A1. Colour-magnitude diagram for selected models from the Geneva grid for three different masses, from $4M_\odot$ to $7M_\odot$. Different markers indicate inclinations, marker size indicates rotation rate W and marker colour indicates $t/t_{\rm MS}$. The red star marks the most likely solution given by the UV-only simulation for α Eri, as per Tab. 3.

APPENDIX B: β CMi POLARIMETRIC DATA AND Hα PROFILES

Table B1. Polarimetric data from OPD-LNA taken with the IAGPOL polarimeter.

MJD	Filter	$P_{\rm obs}$ [%]	$PA_{\rm Pobs}$	σ_P [%]	σ_{PA}
55855.33	B	0.0365	65.33	0.0038	2.98
55855.34	R	0.0512	88.90	0.0040	2.24
55855.37	I	0.0714	78.06	0.0195	7.82
56022.03	I	0.0488	1.53	0.0151	8.87
56022.04	B	0.0194	72.54	0.0129	19.05
56022.05	V	0.0288	92.40	0.0152	15.12
56022.06	R	0.0425	17.03	0.0171	11.53
56610.19	V	0.0488	3.48	0.0111	6.52
56610.22	I	0.0567	0.00	0.0042	2.12
56610.23	R	0.0526	3.66	0.0242	13.18
56610.25	B	0.0637	1.90	0.0351	15.79
56714.09	V	0.1242	85.81	0.0127	2.93
56726.08	B	0.0601	75.52	0.0260	12.39
56726.09	V	0.0410	75.25	0.0233	16.28
56726.10	R	0.0656	80.67	0.0239	10.44
56726.11	I	0.0379	5.24	0.0209	15.8
56946.28	B	0.0826	86.66	0.0070	2.43
56946.30	V	0.0401	106.55	0.0152	10.86
56946.31	R	0.0601	79.15	0.0084	4.00
56946.32	I	0.0306	1.22	0.0136	12.73
56981.29	V	0.0823	3.00	0.0267	9.29
56981.30	R	0.0624	6.25	0.0089	4.09
56981.30	I	0.0505	12.85	0.0144	8.17

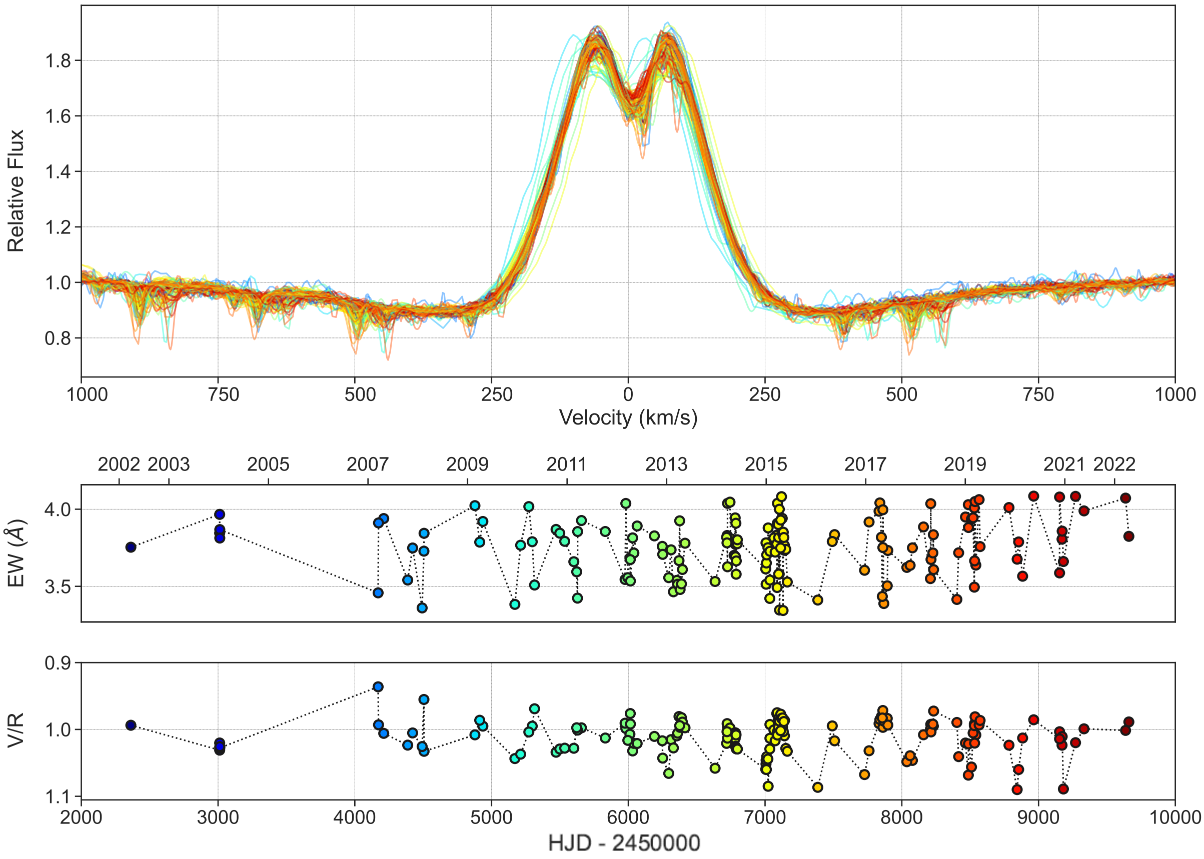

Figure B1. Top panel: Hα profiles from the BeSS database, coloured according to the dates shown in the other panels. Middle panel: Equivalent width (EW) measurements of all profiles. In the top axis, dates are shown in years. Bottom panel: Violet over red ratios (V/R) calculated for all profiles. In the bottom axis, dates are shown in shifted Heliocentric Julian Dates. Both EW and V/R panels share the same time scale.

APPENDIX C: ADDITIONAL CORNER PLOTS

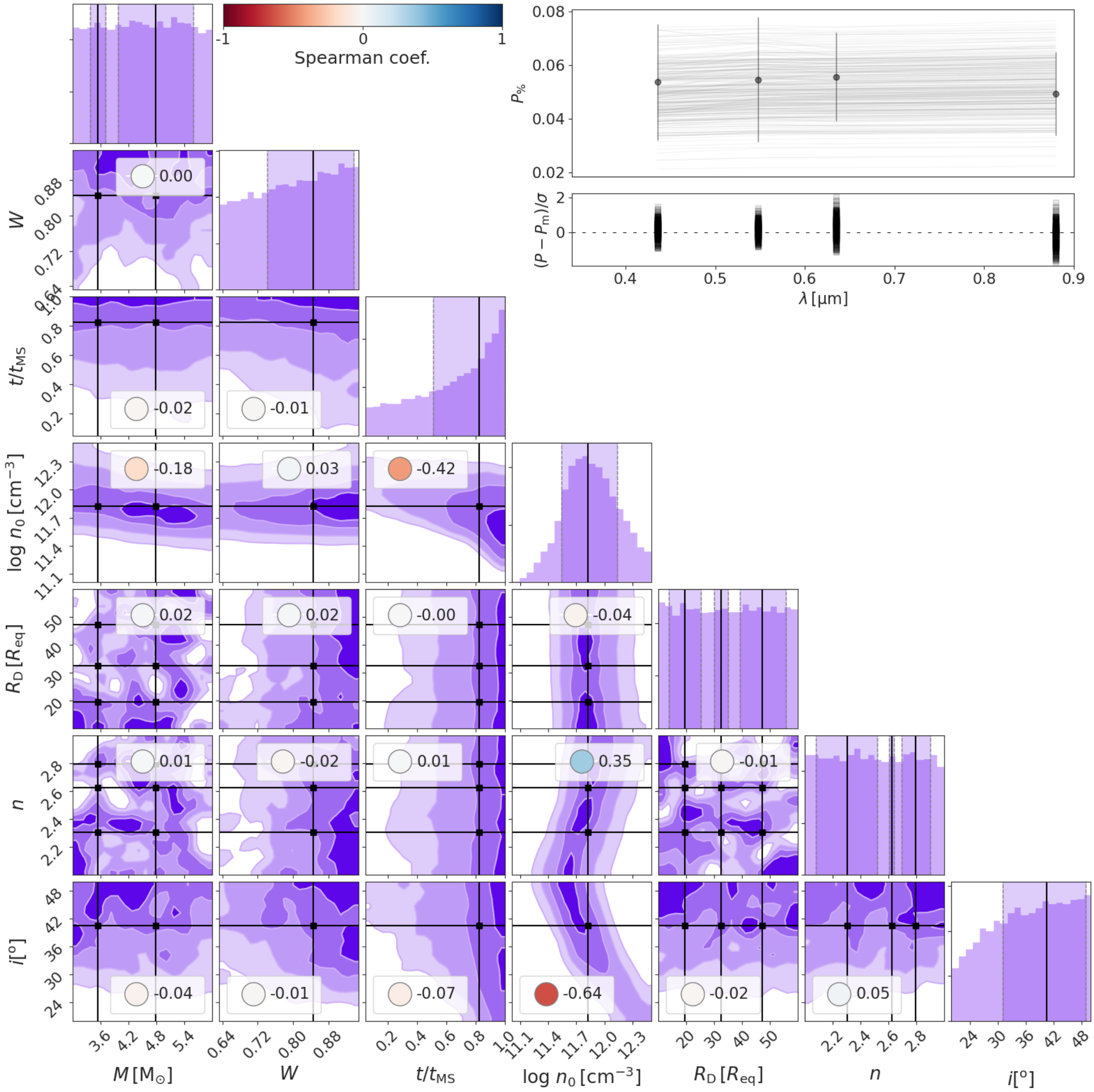

Figure C1. Same as Fig. 8, but for the polarisation data of β CMi.

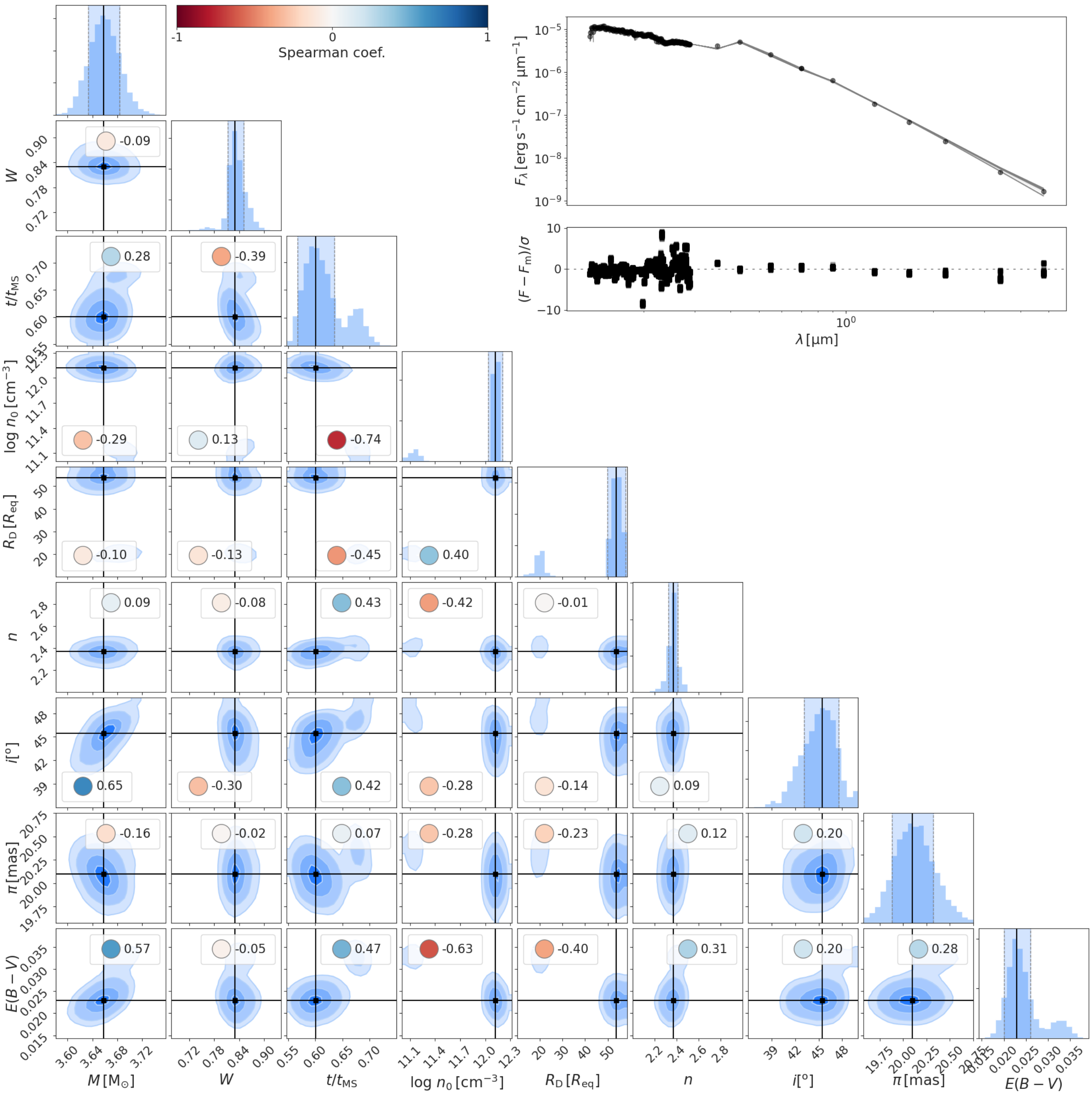

Figure C2. Same as Fig. 8, but for the UV-NIR section of the SED data of β CMi.

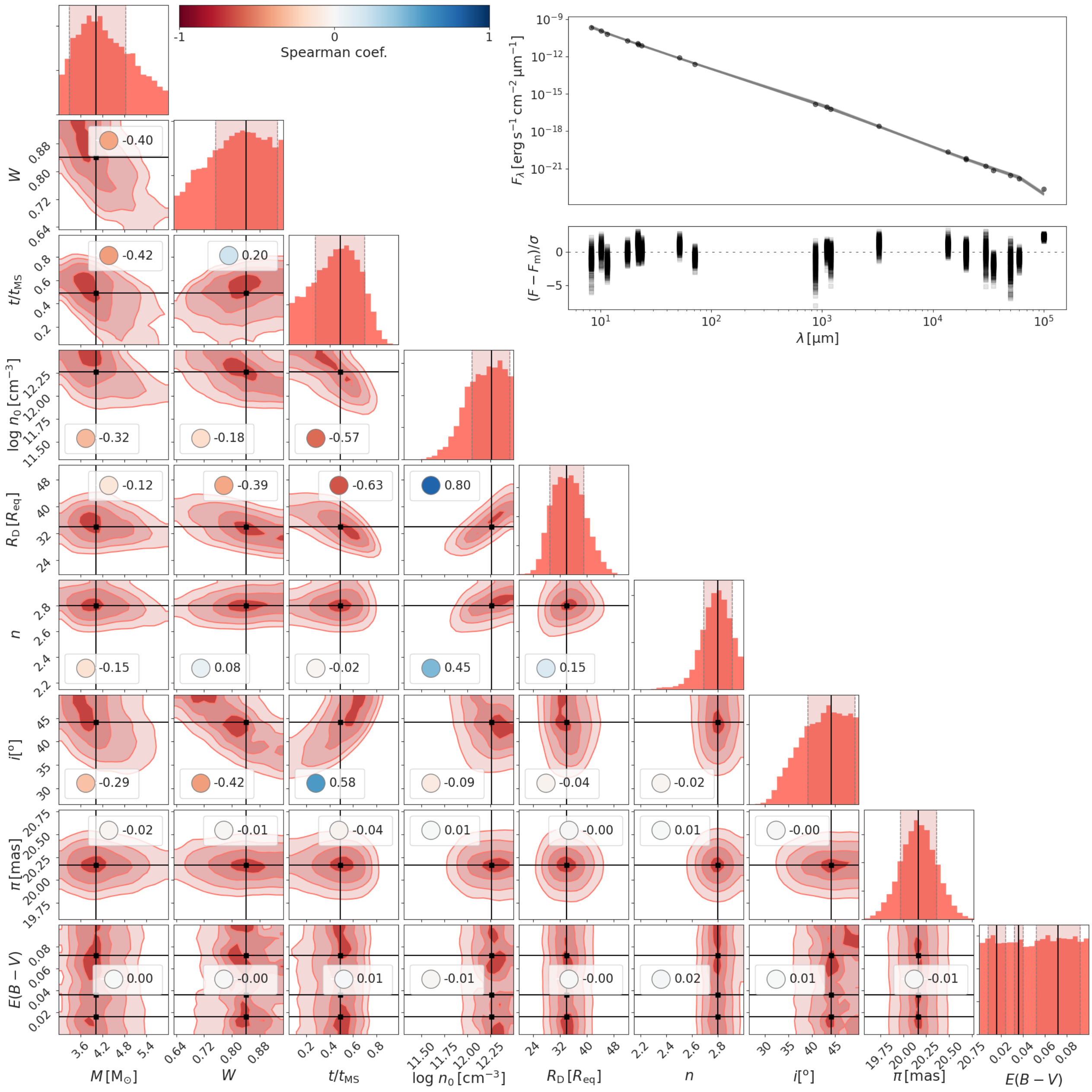

Figure C3. Same as Fig. 8, but for the MIR-Radio section of the SED data of β CMi.

APPENDIX D: PHOTOSPHERIC GRID ON A COLOUR-MAGNITUDE DIAGRAM

[H]

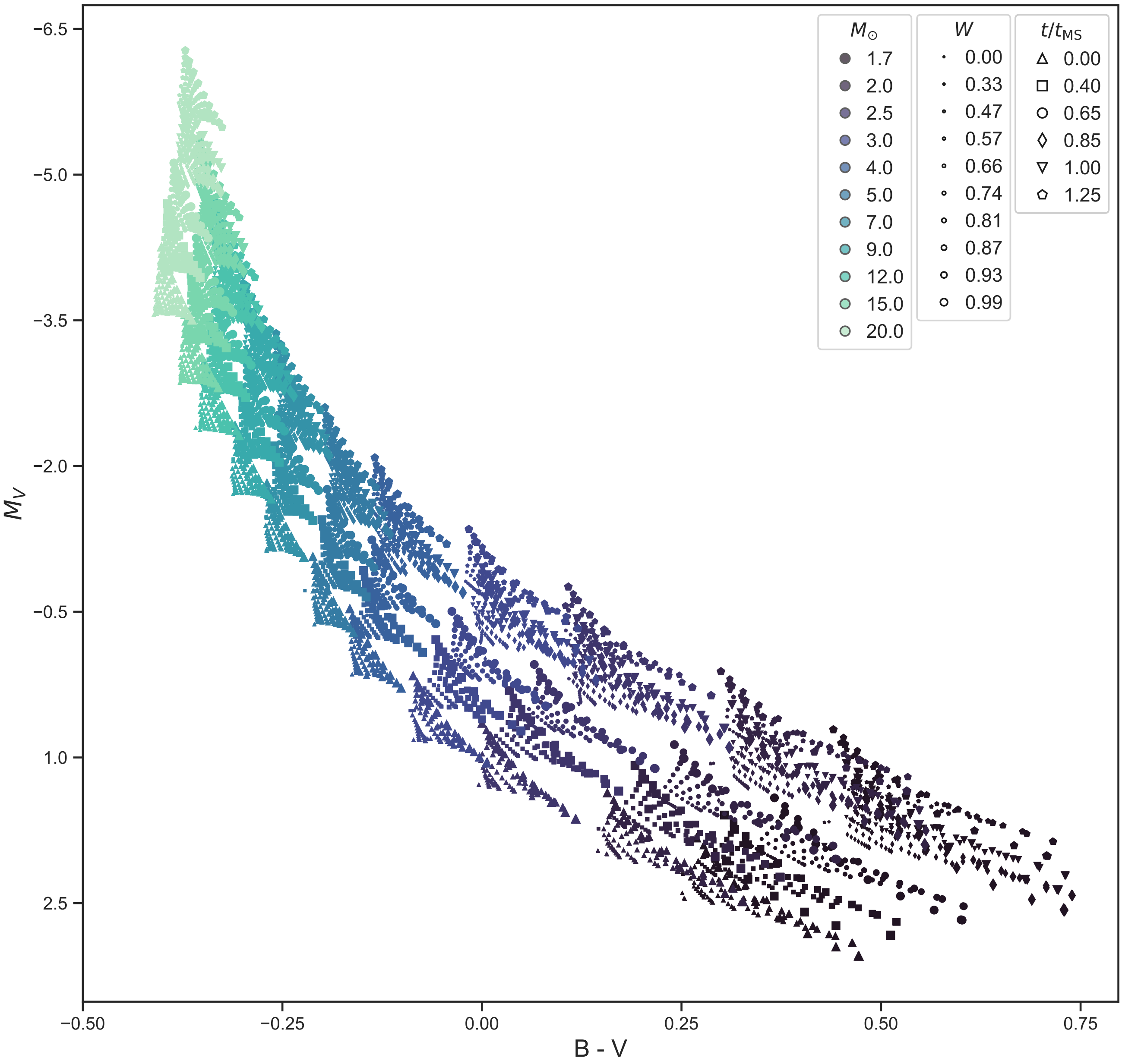

Figure D1. Absolute magnitude $M_V \times$ (B-V) colour-magnitude diagram of the photospheric grid on the Vega system. The configuration of this figure (markers' colours, types and sizes) follows Fig. 1. A significant feature shows up on the observational diagram, which is the cone opening caused by the different inclination angles. Models observed pole-on, when rotating fast, seem brighter, while models observed edge-on seem dimmer and redder.

This paper has been typeset from a TEX/LATEX file prepared by the author.

Appendix C

NGC 330 seen with SAMI paper

Draft version November 25, 2023
Typeset using LaTeX **twocolumn** style in AASTeX631

On the Origin of Fast Rotating Stars.
I. Photometric calibration and results of AO-assisted $BVRI$+Hα imaging of NGC 330 with SAMI/SOAR

Felipe Navarete [1], Pedro Ticiani dos Santos [2], Alex Cavaliéri Carciofi [2] and André Luiz Figueiredo [2]

[1] *SOAR Telescope/NSF's NOIRLab, Avda Juan Cisternas 1500, 1700000, La Serena, Chile*
[2] *Universidade de São Paulo, Instituto de Astronomia, Geofísica e Ciências Atmosféricas,*
Rua do Matão 1226, Cidade Universitária São Paulo-SP, 05508-090, Brazil

ABSTRACT

Hα emission is a clear indicator of circumstellar activity in Be stars, historically employed to assess the classical Be star (CBe) population in young open clusters (YOCs). The YOC NGC 330 in the Small Magellanic Cloud exhibits a large known fraction of Be stars and was selected for a pilot study to establish a comprehensive methodology for identifying Hα emitters in the Magellanic Clouds, encompassing the entire B-type spectral range. Using the SOAR Adaptative Module Imager (SAMI), we investigated the stellar population of NGC 330 using multi-band $BVRI$+Hα imaging. We identified Hα emitters within the entire V-band range covered by SAMI/SOAR observations ($V \lesssim 22$), comprising the complete B-type stellar population and offering a unique opportunity to explore the Be phenomenon across all spectral sub-classes. The stellar radial distribution shows a clear bimodal pattern between the most massive (B5 or earlier) and the lower-mass main-sequence objects (later than B6) within the cluster. The former is concentrated towards the cluster center (showing a dispersion of $\sigma = 4.26 \pm 0.20$ pc), whereas the latter extends across larger radii ($\sigma = 10.83 \pm 0.65$ pc), indicating mass stratification within NGC 330. The total fraction of emitters is $4.4 \pm 0.5\%$, notably smaller than previous estimates from flux- or seeing-limited observations. However, a higher fraction of Hα emitters is observed among higher-mass stars ($32.8 \pm 3.4\%$) than within lower-mass ($4.4 \pm 0.9\%$). Consequently, the putative CBe population exhibits distinct dynamical characteristics compared to the bulk of the stellar population in NGC 330. These findings highlight the significance of the current observations in providing a complete picture of the CBe population in NGC 330.

Keywords: instrumentation: adaptive optics, stars: activity, stars: early-type, stars: emission-line, Be, stars: fundamental parameters, stars: massive, stars: rotation, (galaxies:) Magellanic Clouds

1. INTRODUCTION

Massive stars are known for their intense radiation, strong stellar winds, and sometimes the presence of circumstellar material. These factors can occasionally lead to the emergence of emission lines (mainly hydrogen) in these stars' spectra. Examples include luminous blue variables (LBVs) and Herbig Ae/Be stars, which encompass massive evolved stars and intermediate-mass pre-main-sequence stars, respectively. Studying the Hα emission in these massive stars provides essential insights into their physical properties, evolutionary stages, and circumstellar environments.

In particular, the primary focus of this paper revolves around Classical Be stars (hereafter CBe stars), which earned their name due to the presence of hydrogen emission lines (particularly Hα) in their spectra. CBes are fast-rotating variable stars exhibiting mass ejection episodes from their less-bound equator and decretion disks governed by viscosity (Rivinius et al. 2013). The presence of Hα emission lines in CBes is not merely used to confirm their classification; from spectroscopic studies, the strength and variability of these lines can provide insights into the dynamics and evolution of the disk, as well as the effects of processes such as mass loss, binary interactions, density waves, etc.

Corresponding author: Felipe Navarete
felipe.navarete@noirlab.edu

It has been long recognized that the variability of these stars is remarkably diverse, encompassing a wide range of amplitudes and time scales. For instance, short-term, low-amplitude periodicity from non-radial pulsations are intrinsic to these objects (e.g., Rivinius et al. 2003), and the disk build-up and dissipation phases can extend from days – with outbursts producing detectable flickers (Labadie-Bartz et al. 2022) – to many years, such as κ Draconis (Klement et al. 2022), while ranging from tens of milimagnitudes to more than one magnitude in the visible range. Some systems have also shown periodicity in their long-term variability, such as ω CMa (Ghoreyshi et al. 2021) and HD 6226 (Richardson et al. 2021), while others appear remarkably stable, such as β CMi (see, e.g., Fig. B.1 from Rubio et al. 2023). However, the prevailing scenario is likely unpredictable, leading to intricate and varied light curves. (e.g., Labadie-Bartz et al. 2018).

Fast rotation is a fundamental ingredient for the existence of CBe stars. To date, there are three proposed scenarios to explain the presence of such extreme rotators: *i*) CBe stars are born as fast rotators (Bodenheimer 1971); *ii*) CBe stars are spun up by mass and angular momentum transfer from a binary companion (e.g., Pols et al. 1991, Shao & Li 2014); and *iii*) CBe stars begin their life as slow to moderate rotators, increasing their surface rotation rates along the main sequence (MS) (e.g., Ekström et al. 2008, Georgy et al. 2013). The first two scenarios imply that fast rotation is already present at or close to the Zero Age Main Sequence (ZAMS), while the third one favors a higher incidence of CBe stars towards the end of their MS evolution. It is important to note that these scenarios are not mutually exclusive, and a combination of these processes could contribute to the formation of CBe stars. Discriminating the relative prevalence of each scenario is a key step toward a fuller understanding of the stellar evolution of massive stars, particularly on the impact of binarity/multiplicity effects on the stellar evolution.

Several works have attempted to tackle this problem by studying CBe stars in young open clusters (YOCs). Studying the ratio of CBe stars to the total B star population – referred to as the Be/(B+Be) fraction – in clusters of varying ages is a valid approach to unraveling the formation mechanisms of rapidly rotating stars; however, so far, methodological issues have hampered definite conclusions. One complication is that different works employ different methodologies, making comparisons between results difficult and often leading to conflicting conclusions. For instance, Keller et al. (1999) found that the incidence of CBe stars increases toward the MS turnoff, favoring the evolutionary channel, while Martayan et al. (2006) found several CBe stars of lower masses close to the ZAMS, which favors either the "born as fast rotators" or "binary evolution" scenarios. Additionally, many authors do not adequately consider significant effects that impact CBe star observations, such as gravity darkening and weak Hα emitters. The last factor is often associated with tenuous disks that can lead to SED with Hα emission that fills only partially the absorption profile. These CBe stars with weak disks are quite common (e.g. Vieira et al. 2017) and often difficult to account for as CBes.

Previous studies of CBe stars in stellar clusters estimated the Be/(B+Be) fraction as a function of metallicity (Z) (e.g., Martayan et al. 2006, Martayan et al. 2007) showing evidence that this number grows from about a tenth in the Galaxy to $\approx 35\%$ in the Large Magellanic Cloud (LMC) and can be even higher in the Small Magellanic Cloud (SMC) (Martayan et al. 2010), suggesting a strong Z-dependency of the Be phenomenon.

This paper is the first of a planned series to present consistent observations of YOCs with different ages and metallicities. This first publication aims to describe the technical details of data observation, reduction, and calibration pipelines while also showing the ability of adaptive optics imaging at the 4-m class SOAR telescope to resolve dense cores and provide photometric completeness for the entire B spectral type in the SMC. Furthermore, a preliminary analysis of the YOC NGC 330 is presented.

The paper is structured as follows. Section 2 presents a brief review of NGC 330 and its significance in CBe research. Section 3 describes the observations and subsequent reduction procedures. As follows, Sect. 4 details the photometric calibration procedure and the comparison with external catalogs. Finally, the photometric results and initial analysis of the NGC 330 observations are presented in Sect. 5, and the main conclusions are discussed in Sect. 6.

2. NGC 330

NGC 330 is a young open cluster located at α = 00h 56m 17.6s and $\delta = -72^\circ\,27'\,47''$ (J2000, Rafelski & Zaritsky 2005), within the Small Magellanic Cloud (SMC). NGC 330 was chosen for this pilot study due to its relatively large Be content. It was the subject of intense scrutiny in the last decades, with some stars being photometrically documented over sixty years ago in a survey conducted by Arp (1959). The first detection of CBes in NGC 330 was done by Feast (1972) by spectroscopically measuring the equivalent width of the Hα line (λ=6562.8 Å). Emission line stars, particularly active CBe stars, can be identified using color index information based on the narrow-band Hα filter and another filter encompassing the nearby continuum. For NGC 330, such methodology was first introduced by Grebel & Richtler (1992), providing a significant breakthrough in detecting CBes associated with the YOC. Their Fig. 2 summarizes the adopted classification method through a ($\mathrm{H}\alpha - y$, $b - y$) color-color diagram constructed from broad-band Strömgren *by* filters and a custom narrow-band Hα filter, where active CBes with sufficiently dense disks deviate from the expected MS location. Later, Bessell & Wood (1993) validated the methodology adopted by Grebel & Richtler, observing NGC 330 using VRI+Hα filters.

NGC 330 observations have provided substantial support for various subsequent discoveries. These include a detailed analysis of blue stragglers and evolved stars, comparing photometry with the available evolutionary models at that time (Grebel et al. 1996). Additionally, the application of photometric separation between CBes and normal B-type stars in clusters from the LMC and SMC, including NGC 330, was further explored in works by Keller et al. (1999) and Iqbal & Keller (2013). Other studies delved into the relationship between CBe incidence and metallicity, as discussed in Martayan et al. (2006) and Martayan et al. (2007). Moreover, investigations on stellar variability using OGLE II data were conducted by Schmidtke et al. (2008). More recently, (Bodensteiner et al. 2020) reported the first results from AO-assisted integral-field MUSE spectroscopic observations of the densest region of NGC 330, resolving and classifying a flux-limited sample of B and Be stars and providing an age estimate of the cluster in range of 35 to 40 Myr. At the same time, Patrick et al. (2020) reported an independent assessment of the age of NGC 330 as 45±5 Myr based on the analysis of the evolved red supergiant population of the cluster.

3. OBSERVATIONS AND DATA REDUCTION

Kron-Cousins $BVRI$+Hα imaging observations were carried out at the 4.1-m SOAR telescope (Chile) on January 5th, 2019. We used the SOAR Adaptive Module (SAM, Tokovinin et al. 2016), a GLAO system using a Rayleigh laser guide star at ∼7 km from the telescope to correct the effects of ground-layer atmospheric turbulence. SAM provides corrected images to its internal CCD detector, SAMI (4k × 4k CCD), operating in a 2×2 binned mode, resulting in a plate scale of 91 mas pixel^{-1} over a field-of-view (FOV) of $\sim 3.'1 \times 3.'1$ on the sky.

Individual, long-exposure $BVRI$ images were taken using a three-point dither pattern, separated by 15″ in the E–W direction, with exposure times of 60 s per frame, totaling 180 s per filter. For Hα, three individual exposures of 240 s were obtained (totaling 12 min). Observations included short exposures to avoid saturation of the brightest stars in the FOV. The short exposures were taken in a two-point dither pattern separated by 15″ in the E–W direction, with exposure times of 5 s per frame, totaling 10 s per filter. Table 1 summarizes the SAMI observations.

Table 1. Log of the SAMI observations for NGC 330 made on January 5th, 2019.

Filter	MJD	N_{exp}	t_{exp} (s)	Airmass	Atm. Seeing (″)
B	58488.05261(50)	3	60	1.47	0.54
B	58488.05462(06)	2	5	1.47	0.53
V	58488.04946(50)	3	60	1.46	0.50
V	58488.04823(06)	2	5	1.46	0.47
R	58488.05661(50)	3	60	1.47	0.55
R	58488.05536(06)	2	5	1.47	0.51
I	58488.05968(50)	3	60	1.48	0.49
I	58488.06229(07)	2	5	1.49	0.50
Hα	58488.06650(19)	3	240	1.50	0.54
Hα	58488.06316(06)	2	5	1.49	0.59

Notes: The mean MJD of the observations are provided, and the errors on the last two decimal places are indicated within the parenthesis. The mean atmospheric seeing was obtained from the DIMM monitor installed at Cerro Pachón.

3.1. *Data Reduction*

The data was processed using the SAMI PyRAF-based PySOAR pipeline[1]. Initially, the pipeline creates master bias and master flat-field templates for each filter. Subsequently, the raw images are corrected for overscan, bias-subtracted, and flat-fielded.

The astrometric solution and distortion correction of the field were obtained by comparing the field with reference stars in the USNO-A2 catalog using `SExtractor` and `Scamp` (Bertin et al. 2002), leading to positional errors smaller than $0.''15$. Finally, the individual images were average-combined using `Swarp` (Bertin et al. 2002).

Figure 1 presents false-color RGB maps using the long-exposure $BVRI$+Hα images. The left panel shows the BVI images, exhibiting a few reddened sources in the field. The right panel shows the BR+Hα images. It is possible to identify an extended H II-like structure

---

[1] https://noirlab.edu/science/programs/ctio/instruments/sam/user-guides/reducing-your-sam-images.

to the NW direction of NGC 330, and very red sources associated with a strong Hα emission.

3.2. *PSF photometry*

We extracted the stellar photometry using an automated PSF fitting procedure based on the IDL StarFinder algorithm (Diolaiti et al. 2000).

We used relatively isolated and bright sources to construct the PSF of each $BVRI$+Hα image. Examples of the resulting PSF template for the BVI images are presented in Fig. 2. The PSF models exhibit an extended weak tail towards positive x-axis offsets, a common consequence of the divergence of the tip-tilt loop, according to the instrument manual[2].

Table 2 summarizes the results from the PSF fitting for each filter, showing the extraordinary performance of the AO-assisted observations, achieving angular resolutions as sharp as $0\farcs33$ in the Hα filter.

Table 2. Parameters of the PSF model for SAMI observations and the peak and limiting magnitude for each filter.

Filter	FWHM ($''$)	N_* (short)	N_* (long)	1-σ (ADU)	m_{peak} (mag)	m_{lim} (mag)	σ (mag)
B	0.40	1262	4820	1.86	21.3	22.5	0.06-0.14
V	0.38	2101	7057	2.19	21.7	23.4	0.03-0.18
R	0.35	3255	9464	3.40	22.2	24.2	0.03-0.30
I	0.31	1840	7876	3.58	21.7	22.8	0.04-0.26
Hα	0.33	424	5715	2.05	22.0	23.6	0.09-0.21

Notes: The FWHM was measured for the PSF of each filter. N_* corresponds to the number of sources detected above a 1-σ limit in the short and long exposure frames. σ corresponds to the range of magnitude uncertainties for each filter.

The identification and extraction of the fluxes of the point-like sources were performed by adopting a total of three iterations, considering 3-, 2-, and 1-σ thresholds, and a list of positions (x, y) and instrumental fluxes (in ADU) was obtained for each image. The (x, y) positions were transformed into sky coordinates (RA and Dec) using the astrometric information stored in the header of the images. The instrumental fluxes were corrected to the exposure time of 1 s, and instrumental magnitudes $bvri$+hα[3] were evaluated using a zero point of 25.0 mag.

Figure 3 presents the residuals between the magnitudes extracted from short and long exposure lists for the I-band. The short and long exposure lists were merged, and a final catalog per filter was created as follows. We evaluated a relative zero point (ZP) between the magnitudes from the short and long lists, that is

$$m_{\lambda,\mathrm{short}} = m_{\lambda,\mathrm{long}} + \mathrm{ZP}_\lambda$$

where the ZP per filter are: $\mathrm{ZP}_b = 0.036(12)$ mag, $\mathrm{ZP}_v = 0.015(12)$ mag, $\mathrm{ZP}_r = 0.063(23)$ mag, $\mathrm{ZP}_i = 0.146(26)$ mag, and $\mathrm{ZP}_{h\alpha} = -0.094(25)$ mag. The ZPs were estimated from the data points that are relatively brighter but not saturated in each filter, as indicated by the vertical dashed blue lines in Fig. 3. Sources saturated on the long-exposure images (corresponding to instrumental magnitudes brighter than 12.0, 13.5, 13.4, 13.7, and 13.7 mag in $BVRI$+Hα filters, respectively) were retrieved from the short-exposure list. Fainter sources were obtained from the long-exposure list. We adopted the mean instrumental magnitude value for all the other detections identified in both lists. Finally, the individual filters were cross-matched one by one, assuming a maximum separation of $0\farcs3$, resulting in a final list of 10220 entries with detections in at least one filter, and 4430 entries with magnitudes detected in all five filters.

4. SAMI PHOTOMETRY

4.1. *Photometric calibration*

We implemented a *stellar template fitting* methodology for the photometric calibration of the SAMI $BVRI$+Hα photometry, following a similar procedure adopted for the *Southern Photometric Local Universe Survey* (S-PLUS Almeida-Fernandes et al. 2022). The method consists of calibrating the instrumental magnitudes using a library of synthetic photometry, calculated with a grid of atmospheric stellar models and an external photometric reference catalog covering the same region of the sky. The complete calibration process was developed in Python, using functions from the `AstroPy` and `SciPy` libraries. The following sequence outlines the process:

1. A list of sources with available magnitudes in the external and the SAMI catalogs is used as input. The external reference catalog serves as a source of pseudo-standard stars.
2. The photometric spectral energy distribution (SED) of every star from the list is fitted using the synthetic library, finding a representative model. As atmospheric models provide surface fluxes instead of absolute fluxes, the fitting is performed using a set of color indices (e.g., $g-r$, $r-z$, etc.);
3. A mean magnitude difference (representing every filter from the external catalog) between the best model and the corresponding star is determined;

---

[2] SAM Operator's Manual in https://noirlab.edu/science/programs/ctio/instruments/sam/support-staff.

[3] By definition, lower case and capital letters denote instrumental and calibrated magnitudes, respectively.

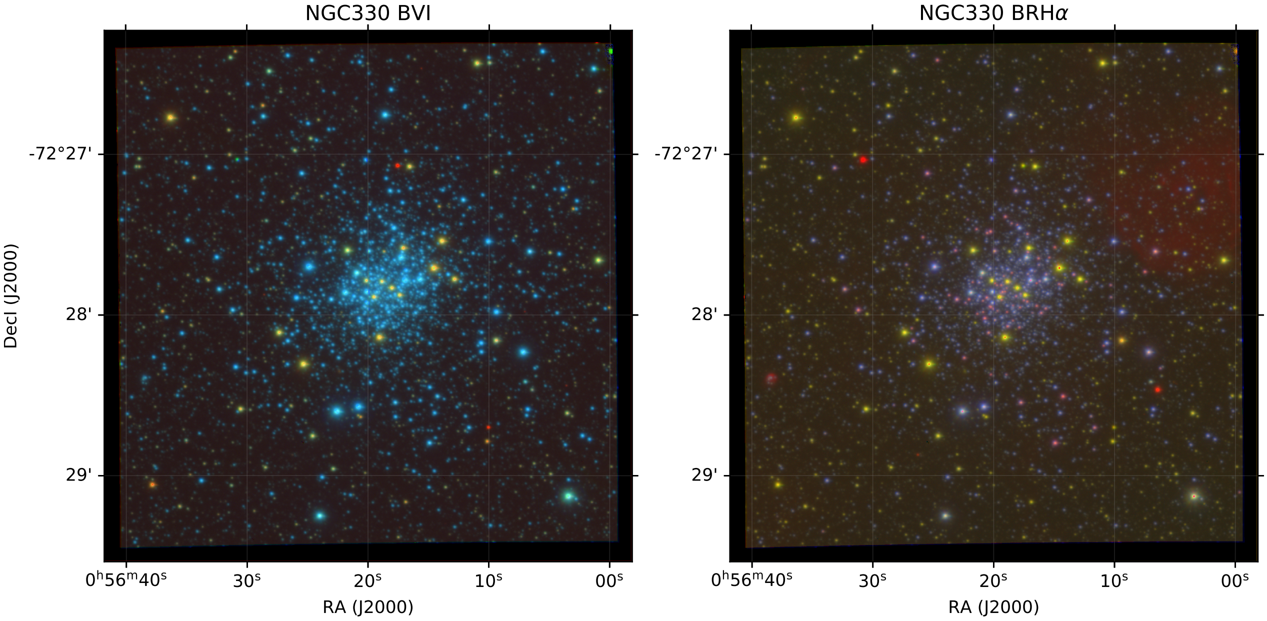

Figure 1. False-color SAMI images of NGC 330 based on the long-exposure frames. Left: BVI image (blue: B, green: V, red: I). Right: BRHα image (blue: B, green: R, red: Hα). Both images have a $3\farcm1 \times 3\farcm1$ field-of-view, centered at $\alpha = 00\text{h}\,56\text{m}\,20.0\,\text{s}$ and $\delta = -72^\circ\,27'\,51\farcs67$ (J2000). North is up, and east is to the left.

4. The SAMI magnitudes are then predicted using the stellar model. The residuals between the predicted and instrumental magnitudes are used to infer a photometric ZP for every filter;

5. A final ZP of every filter is estimated based on the residuals obtained in item (4), as presented in Fig. 4, and applied for every star in the SAMI catalog.

One of the main advantages of this approach is the avoidance of transformation equations (especially for narrow-band filters). Moreover, it treats extinction as a separate and independent parameter, mapped by convolving the synthetic spectra with a range of R_V and $E(B-V)$ values.

In this method, the ZP system inevitably aligns with the external catalog. Therefore, as a necessary condition for obtaining a precise photometric calibration, the spectral coverage of the external catalog must be similar to or broader than that from the observations.

We used the synthetic spectral library of Coelho (2014), which provides model SEDs ranging from 0.13 to 10 μm, with resolutions of $\Delta \log \lambda = 8 \times 10^{-4}$ and a wide range of stellar parameters: effective temperature (T_{eff}) from 3,000 to 25,000 K, surface gravity from $\log(g) = -0.5$ to $+5.5$ (in steps of 0.5 dex), and metallicity (Z) from $Z = 0.0017$ to 0.049 in a custom set of 12 chemical mixtures (for more details, see Table 1 of Coelho 2014).

We adopted the SkyMapper DR1.1 (Wolf et al. 2018) as the external reference catalog, combining an excellent photometric coverage of the southern hemisphere in the SLOAN/SDSS $uvgriz$ filters, providing magnitudes in the AB system and covering a broader spectral range than our observations.

We cross-matched the SAMI coordinates with SkyMapper, using a maximum radius threshold of $0\farcs3$ between the catalogs, resulting in a total of 204 common sources in both catalogs, out of which 82 exhibit magnitudes detected in all six $uvgriz$ filters.

The library of synthetic photometry was constructed as follows. Each spectrum of the atmospheric library was reddened by following the Cardelli et al. (1989) extinction law with a fixed value of $R_V = 3.1$, and assuming 22 different $E(B-V)$ values ranging between 0 and 1.0 mag. Next, the reddened spectra were convolved with the transmission curves of the filters from both the external catalog and the SAMI sets. This process generated a list of 11 magnitudes ($BVRI$+Hα + $uvgriz$) for each synthetic spectrum.

The application of the *stellar template fitting* procedure is divided into external and internal calibration steps, explained as follows.

4.1.1. *External calibration*

The external calibration procedure compares the external catalog with each atmospheric model by computing eight color indices based on the SkyMapper filter set (e.g., $u-v$, $g-i$, etc). The best match between the syn-

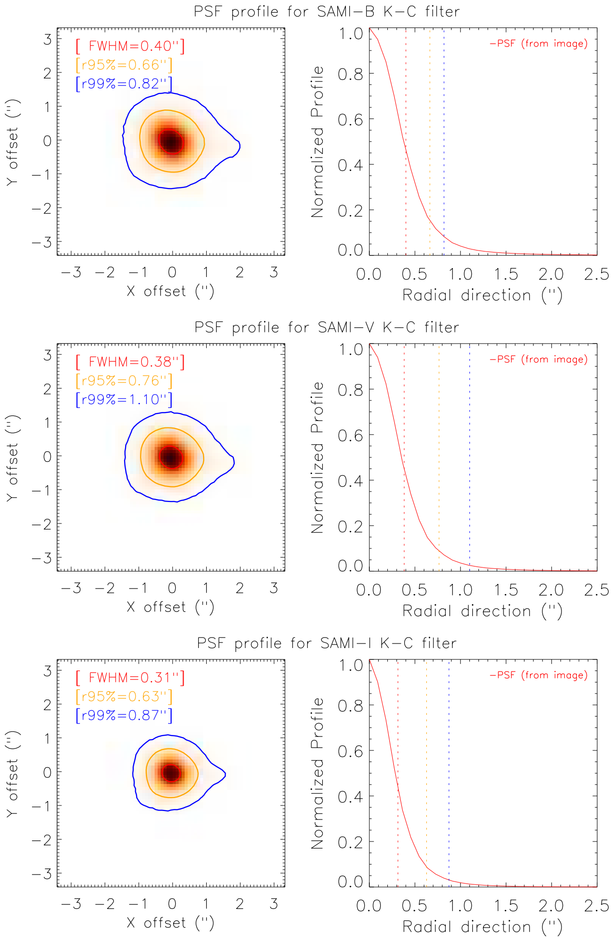

Figure 2. PSF models for the SAMI *BVI*-band images for NGC 330. *Left panel:* two-dimensional profile of the PSF overlaid by the FWHM (red contour), and the radii containing 95% (orange) and 99% (blue) of the enclosed fluxes, respectively. *Right:* radial profile of the PSF. The vertical dashed lines indicate the FWHM (red), and the radii containing 95% (orange) and 99% (blue) of the enclosed flux.

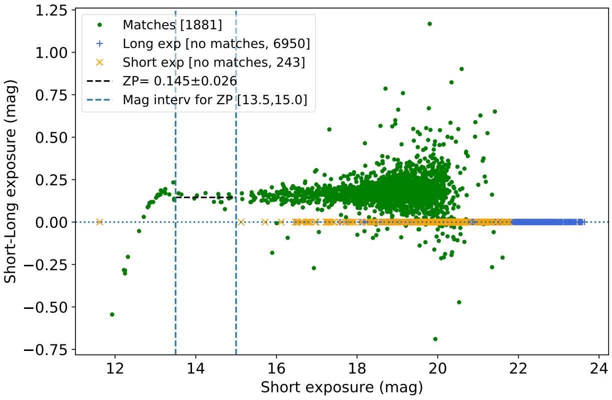

Figure 3. Distribution of residuals between the instrumental magnitudes from short- and long-exposure images for the *I*-band filter. The zero-point offset between short- and long-exposure magnitudes (ZP=0.145±0.026 mag, indicated by the horizontal dashed black line) was estimated from the points located within the vertical dashed blue lines. Saturated sources ($\lesssim$ 13.5 mag) were retrieved from the short-exposure list only.

thetic library and the catalog is selected through a χ^2 minimization process, where the χ^2 value is computed from the contribution of every color index (C_i) in the form:

$$\chi^2 = \sum_{i=1}^{8} \left(\frac{\mathrm{C_{i,model}} - \mathrm{C_{i,ext}}}{\mathrm{e_{C_{i,ext}}}} \right)^2 , \tag{1}$$

where $\mathrm{e_C}$ is the uncertainty of the color index given by $\mathrm{e_C} = (\mathrm{C1}^2 + \mathrm{C2}^2)^{1/2}$, where C1 and C2 represent the magnitudes of $\mathrm{e_C}$. The best-fitting model configuration for a specific source is determined by the minimum value of χ^2 among all possible models considered for that source.

To filter out unrealistic matches between the external catalog and the models, we introduced a parameter termed the *mean photometric offset* (μ_Δ) and its corresponding error (σ_{μ_Δ}), explained as follows. For each target, we computed the difference between the magnitude from the external catalog ($m_{\rm ext}$) and the one from the best-fitted model ($m_{\rm best\,model}$) as:

$$\Delta m_i = m_{i,\rm ext} - m_{i,\rm best\,model} \quad \text{for } i \in uvgriz\,, \tag{2}$$

Following the definition of μ_Δ and σ_{μ_Δ} as the mean and standard deviation of Δm_i values across all six *uvgriz* filters, we established that a suitable fit should display consistent Δm_i values for all filters. Consequently, σ_{μ_Δ} should approach zero. Hence, we only regarded fits as satisfactory for sources exhibiting $\sigma_{\mu_\Delta} \leq 0.15$ mag.

The predicted magnitudes for each source, derived from the best model magnitude value in the external catalog and applied to the SAMI filters ($m_{\rm pred}$) were evaluated as:

$$m_{i,\rm pred} = m_{i,\rm best\,model} + \mu_\Delta \quad \text{for } i \in BVRI\text{+H}\alpha \tag{3}$$

The photometric zero point offset for each filter ($\mathrm{ZP}_{\mathrm{ext},i}$) was inferred from the residuals between the instrumental magnitude ($m_{\rm inst}$) and the predicted magnitude ($m_{\rm pred}$) of the sources from the external catalog:

$$\mathrm{ZP}_{\mathrm{ext},i} = m_{i,\rm inst} - m_{i,\rm pred} \quad \text{for } i \in BVRI\text{+H}\alpha. \tag{4}$$

The outcome of Eq. (4) is a distribution of ZP values, as presented in Fig. 4. For each filter, the distribution exhibits a defined peak containing the bulk of the sources and an extended tail of outliers toward positive values. An outlier-resistant Gaussian fit was performed on each histogram, and the mean external ZP and its error ($\sigma_{\rm ZP}$)

correspond to the Gaussian μ and σ, respectively. Given that the fitting procedure excludes outliers, the associated error is relatively low (e.g., see the last plot for the Hα filter).

Finally, the calibrated SAMI magnitudes ($m_{\rm ext}$) and their errors ($\sigma_{\rm ext}$) were obtained by applying the fitted ZPs as:

$$\left.\begin{aligned} m_{i,\rm ext} &= m_{i,\rm inst} - {\rm ZP}_i \\ \sigma_{i,\rm ext} &= \sqrt{\sigma^2_{i,\rm inst} + \sigma^2_{{\rm ZP}_i}} \end{aligned}\right\} \text{ for } i \in BVRI\text{+H}\alpha, \quad (5)$$

In principle, Eq. (5) yields suitable calibrated magnitudes for scientific purposes. However, the photometric calibration can be improved through an internal calibration step, as explained below.

4.1.2. *Internal calibration*

The internal calibration is very similar to the previous procedure but uses the externally calibrated SAMI catalog as input, replacing the external reference catalog. As a consequence, this step is significantly time-consuming. However, the internal calibration step enables us *i*)to validate the successful application of the external calibration procedure to the SAMI magnitudes; and *ii*) to obtain the extinction and atmospheric parameters from the best-fitted model for all the sources in the externally calibrated photometric catalog.

In short, each source is matched against the synthetic magnitude library, and a χ^2 minimization procedure is obtained for five color indices based on the broad-band $BVRI$ filters, following a similar approach as outlined in Eq. (1). The *internal mean photometric offset* ($\mu_{\Delta,\rm int}$) and its error ($\sigma_{\mu_{\Delta,\rm int}}$) were evaluated in the same way as the external calibration procedure. In this case, $\sigma_{\mu_{\Delta,\rm int}}$ serves as an indicator of the quality of fit between the calibrated magnitudes and their corresponding counterparts in the synthetic photometric library: values closer to zero signify well-fitted models, while larger values indicate poorer fits. Then, the internally-calibrated magnitudes ($m_{\rm pred}$) of the source are calculated as:

$$m_{i,\rm pred} = m_{i,\rm best\,model} + \mu_{\Delta,\rm int} \text{ for } i \in BVRI\text{+H}\alpha. \quad (6)$$

Similarly to the external calibration method, an internal zero-point offset (${\rm ZP}_{\rm int}$) can be evaluated from the distribution of the residuals between $m_{i,\rm inst}$ and $m_{i,\rm pred}$, as presented in Fig. 5. For successful calibrations, all ${\rm ZP}_{\rm int}$ values are expected to be close to zero, and therefore, no internal calibration is necessary. For cases where the ZP is larger than its error, the internal calibration process is a necessary step, providing a better match between the external reference catalog. In such cases, the internal ZPs need to be accounted for in the calibration process as follows:

$$\left.\begin{aligned} m_{i,\rm int} &= m_{i,\rm ext} - {\rm ZP}_{{\rm int},i} \\ e_{i,\rm int} &= \sqrt{e^2_{i,\rm ext} + e^2_{i,{\rm ZP}_{\rm int}}} \end{aligned}\right\} \text{ for } i \in BVRI\text{+H}\alpha. \quad (7)$$

Indeed, Fig. 5 illustrates that histograms of the broadband $BVRI$ filters are centered around zero with relatively small errors ($\lesssim 0.01$ mag). This observation signifies the successful application of the photometric calibration to the SAMI photometry. Consequently, the internal calibration procedure can be omitted as it does not improve the overall results.

Unlike the other filters, the zero point of the Hα filter exhibits both the largest deviation from zero (ZP = 0.056 mag) and the largest error ($\sigma_{\rm ZP} = \pm 0.083$ mag). Given that the Hα filter serves as an indicator of stellar activity processes (including disk emission from Be stars), we do not expect it to have the same dispersion observed in the broad-band $BVRI$ filters. In fact, the Hα residuals exhibit a bimodal distribution where most of the sample is centered at zero, and a smaller fraction is concentrated around -3 mag. This indicates the bulk of Hα fluxes is consistent with the synthetic models, as expected for normal stars, but a significant number of sources exhibit Hα fluxes larger than predicted by the synthetic models. This is an important output from the internal calibration method, allowing us to identify the sources with Hα excess.

4.2. *Calibrated SAMI magnitudes*

Table 3 presents the calibrated SAMI photometric results obtained from the external calibration procedure (Sect. 4.1.1), together with the stellar parameters from Coelho (2014), delivered by the internal calibration (Sect. 4.1.2). The uncertainties of the calibrated magnitudes range from 0.03 to 0.30 mag for the $BVRI$ filters, and from 0.02 to 0.19 mag for the Hα filter. The full list of the photometric results is available online.

To compare the photometry with the expected brightness of the stars in the SMC, we derived synthetic $BVRI$+Hα magnitudes of rotating stellar models from O9 to A7-type MS stars. This was achieved by convolving BeAtlas photospheric grid of models (Rubio et al. 2023), with the proper transformations to place them on the AB system.

The photospheric BeAtlas spectrum is characterized by four parameters: the stellar mass (M), the rotation rate W ($v_{\rm rot}/v_{\rm orb}$, Rivinius et al. 2013) the MS lifetime fraction ($t/t_{\rm MS}$), and the stellar inclination angle with respect to the line-of-sight (i).

To establish the correspondence between each spectral type (ST) to mass (M), we adopted the spectral type versus Mass (ST-M) relation from Schmidt-Kaler

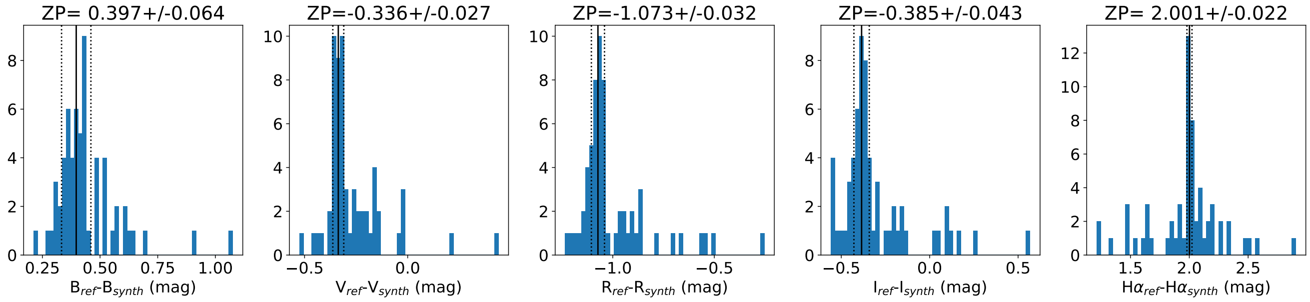

Figure 4. Distribution of residuals between the observed and synthetic model magnitudes of the external reference catalog. The external photometric zero-point (ZP) was estimated through an outlier-resistant Gaussian fitting procedure. The ZP and the 1-σ error bars (indicated at the title of each plot) are shown as the filled and dashed vertical lines, respectively.

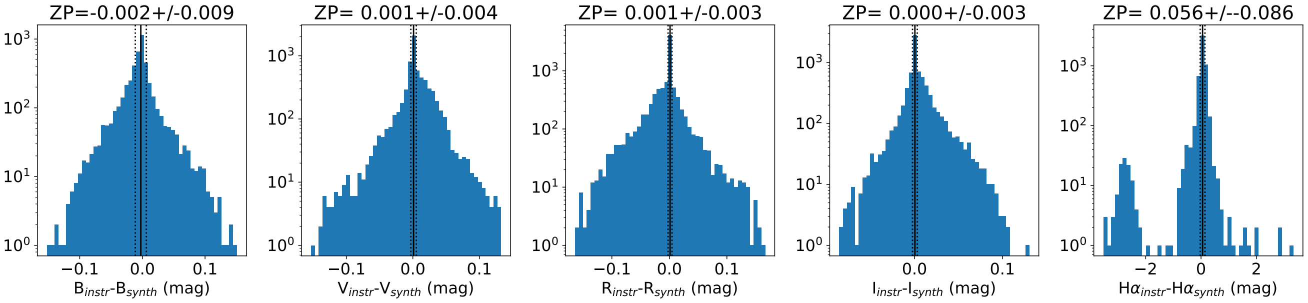

Figure 5. Distribution of residuals between the observed and synthetic model magnitudes of the SAMI magnitudes (internal calibration). The y-axis is shown on a logarithmic scale. A full description of the plots is given in Fig. 4.

Table 3. Calibrated $BVRI$+Hα SAMI photometry for NGC 330, the associated physical parameters from the internal calibration method and the photometric classification of the source.

ID	RA (deg)	Dec (deg)	N$_{\rm filt}$	B (mag)	V (mag)	R (mag)	I (mag)	$H\alpha$ (mag)	E_{B-V} (mag)	$T_{\rm eff}$ (K)	log(g) (dex)	Fe/H (dex)	α	$\sigma_{\mu_{\Delta,int}}$ (mag)	Type
1	14.070568	−72.463074	5	12.494(64)	12.619(29)	12.815(40)	13.048(51)	12.769(21)	0.000	9250	2.0	−0.5	0.4	0.0002	MS
2	14.094029	−72.476657	5	12.523(64)	12.535(29)	12.652(40)	12.834(51)	12.636(21)	0.000	7750	2.0	0.0	0.0	0.0048	MS
3	14.014281	−72.485452	5	12.671(64)	12.339(29)	12.180(40)	12.167(51)	12.123(21)	0.000	6250	4.5	−1.0	0.4	0.0133	MS
4	14.103593	−72.461670	5	12.741(64)	12.920(29)	13.164(40)	13.460(51)	13.104(21)	0.025	13000	4.0	0.0	0.0	0.0007	MS
5	14.091106	−72.464351	5	12.972(64)	13.050(29)	13.207(40)	13.426(51)	13.220(21)	0.025	10000	1.5	−1.0	0.4	0.0046	MS
6	14.065419	−72.462967	5	13.017(64)	13.107(29)	13.284(40)	13.484(51)	13.300(21)	0.000	8500	1.5	−1.0	0.0	0.0013	MS
7	14.071939	−72.460710	5	13.032(64)	13.116(29)	13.274(40)	13.484(51)	13.305(21)	0.025	10000	1.5	−1.0	0.4	0.0016	MS
8	14.086628	−72.476189	5	13.069(64)	13.238(29)	13.491(40)	13.814(51)	13.435(21)	0.000	12250	4.5	0.2	0.4	0.0048	MS
9	14.083651	−72.464272	5	13.120(64)	13.220(29)	13.426(40)	13.682(51)	13.536(21)	0.050	12250	4.5	0.0	0.0	0.0014	MS
10	14.087173	−72.462312	5	13.254(64)	13.223(29)	13.261(40)	13.358(51)	13.268(21)	0.000	7000	1.0	−1.0	0.0	0.0100	MS

Notes: Only the first 10 rows of the table are shown. The full table is available online. The columns are: (1) Index (2–3) Right ascension and declination (in degrees, J2000); (4–8) B, V, R, I and Hα magnitudes and their uncertainties on the last two decimal digits; (9) Total color excess; (10) Effective temperature; (11) Stellar surface gravity; (12) Stellar metallicity; (13) Stellar α exponent; (14) Internal mean photometric offset error; (15) Photometric classification of the source: (F) Foreground objects, (RGB) evolved stars consistent with $>$ 100 Myr PARSEC isochrones, (MS) Main Sequence stars with no clear Hα excess, (Ha) Stars with Hα excess and selected through Eq. 8, (wHa) Stars associated with Hα $-R < 0$, but not selected through Eq.. 8 (therefore, weak H-alpha emitters), (SG) bright objects compatible with blue/red super giants ($B - I > 0.5$ and $V < 16$) (–) objects associated with incomplete photometry (N$_{filt} < 5$) or that did not fall into any of the previous classification types.

(1982) for B-type stars, with Adelman (2004) and Martins et al. (2005) for A- and O-type stars, respectively.

As an effort to obtain the potential magnitude range for each ST, we set the rotation rate W to its maximum value ($W = 0.99$), as the largest range in brightness occurs when the star is critically rotating and is observed either pole-on ($i = 0°$) or edge-on ($i = 90°$). As for the stellar age, we computed $t/t_{\rm MS}$ under the assumption that NGC 330 has an age of $t = 35$ Myr (Bodensteiner et al. 2020). For stars earlier than B3, the magnitude range was estimated considering objects at the TAMS ($t/t_{\rm MS} = 1.0$), as these objects cannot exist in the MS considering the expected age of NGC 330 and the single stellar evolution scenario.

Given that the BeAtlas spectra are dereddened and flux-calibrated for a 10 pc distance, we adopted the values of $E(B-V) = 0.11$ mag and $d = 57.5$ kpc (Milone et al. 2018), with the extinction law as described by Fitzpatrick (1999) with $R_V = 3.1$ mag. Table 4 lists the expected magnitude range for $BVRI$+Hα filters for the spectral types O9, A0, A2, A7, and all B subtypes.

Table 4. Expected magnitude range for normal O-, B- and A-type stars in the SMC, including the effects of fast rotation.

ST	B	V	R	I	Hα
O9	12.9-13.8	13.2-14.0	13.4-14.2	13.8-14.5	13.5-14.2
B0	13.4-14.2	13.6-14.4	13.9-14.6	14.2-14.9	13.9-14.7
B1	14.7-15.5	14.9-15.7	15.2-16.0	15.5-16.3	15.3-16.0
B2	14.9-15.8	15.2-16.0	15.4-16.2	15.8-16.5	15.5-16.2
B3	15.4-16.2	15.7-16.4	15.9-16.7	16.2-16.9	16.0-16.7
B4	16.0-16.8	16.2-17.0	16.5-17.2	16.8-17.5	16.5-17.2
B5	16.7-17.5	16.9-17.7	17.2-17.9	17.5-18.2	17.2-18.0
B6	17.9-18.7	18.1-18.7	18.3-19.1	18.6-19.3	18.4-19.1
B7	18.5-19.4	18.7-19.5	18.9-19.7	19.1-19.9	19.0-19.7
B8	18.9-19.7	19.0-19.8	19.2-20.0	19.5-20.2	19.3-20.1
B9	19.3-20.2	19.4-20.2	19.6-20.4	19.9-20.6	19.7-20.5
A0	19.8-20.7	19.8-20.7	20.0-20.8	20.2-21.0	20.1-20.9
A2	20.4-21.4	20.4-21.4	20.6-21.5	20.8-21.6	20.7-21.6
A7	20.8-22.0	20.8-21.8	21.0-21.9	21.1-22.0	21.1-22.0

The distribution of the calibrated SAMI photometry per filter is presented in Fig. 6. The magnitudes for all filters follow an IMF-like distribution with maximum frequency at 21.3 (B), 21.8 (V), 22.2 (R), 22.0 (I), and 21.6 (Hα), which serves as a proxy for evaluating the photometric completeness limit of the observations. The completeness of all filters is at least one magnitude fainter than the expected limit for B-type stars (B9, indicated by the green shaded area). The B and Hα filters exhibit the shallowest completeness limit, roughly consistent with the expected faintest brightness for A2 stars. This result highlights that the adopted instrumental setup provides sufficient depth to properly identify all OB and early A-type stars at the distance of the SMC.

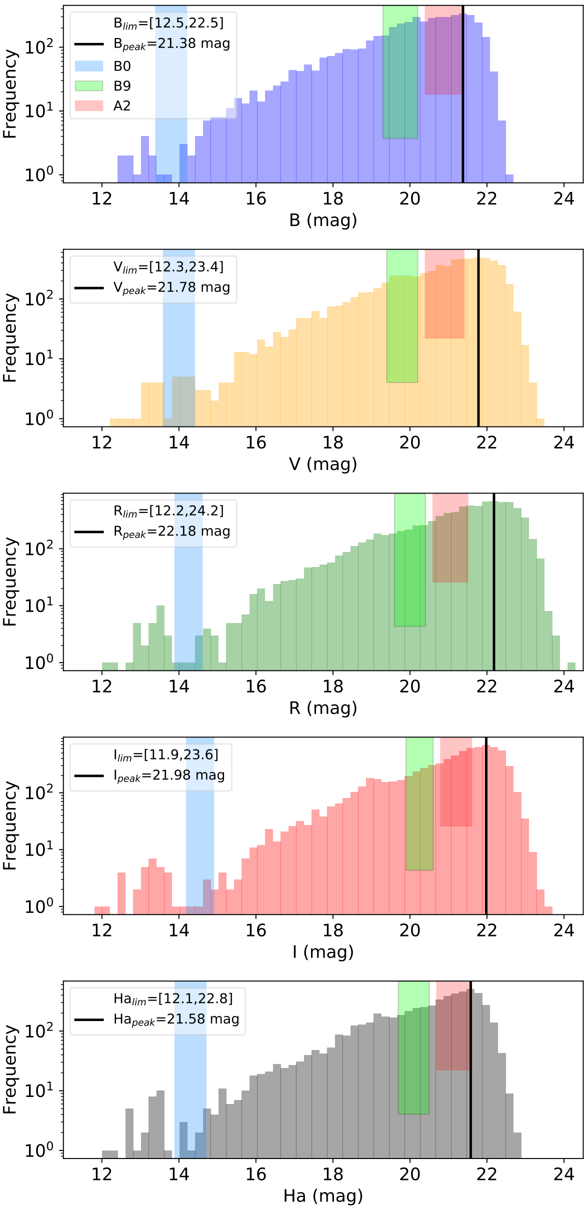

Figure 6. Photometric completeness for the $BVRI$+Hα filters of SAMI observations. Each histogram is sampled with a bin of 0.1 mag, from 11.5 to 24 mag. The vertical dashed line indicates the peak of the distribution. The brightest and faintest object detected on each filter is indicated on the label. We show the expected magnitude intervals for B0 (blue), B9 (green), and A2 stars (orange) for each filter.

4.3. *Comparison with published catalogs*

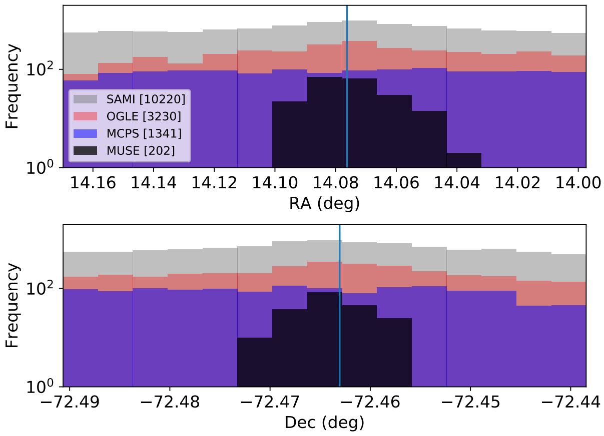

Figure 7. Distribution of sources in the NGC 330 FOV from the SAMI catalog (grey), and the external catalogs (red: OGLE, blue: MCPS, black: MUSE) in the RA (top panel) and declination directions (bottom). The number of sources from each catalog is indicated on the label. The vertical blue line indicates the central coordinates of NGC 330.

We validated the outcomes of our photometric calibration, as detailed in Sect. 4.1, by cross-referencing the results with three previously published catalogs: the Optical Gravitational Lensing Experiment (OGLE-II, Udalski et al. 1998), the Magellanic Clouds Photometric Survey (MCPS, Zaritsky et al. 2004), and the AO-assisted MUSE observations from Bodensteiner et al. (2020). For the cross-matching procedure, we adopted a maximum separation of 0.″5 for the seeing-limited OGLE and MCPS positions and 0.″3 for the AO-assisted MUSE positions, leading to a sample of 3230 (OGLE), 1341 (MCPS), and 250 (MUSE) sources with SAMI counterparts.

Figure 7 presents the spatial distribution of the sources of the SAMI catalog and the published catalogs (red: OGLE; blue: MCPS; black: MUSE) along the RA (top panel) and declination (bottom) directions. Far from the cluster's center, OGLE and MCPS exhibit a relatively constant distribution of sources in both RA and DEC directions. An overdensity of OGLE sources is observed towards the cluster's central position, which is not evident for the MCPS, indicating that OGLE has a better completeness towards NGC 330 than MCPS. MUSE observations are limited for $V \leq 18.5$ mag objects, located within a considerably smaller $\sim 1' \times 1'$ FOV around the cluster's center. Consequently, MUSE covers a limited area, capturing a relatively smaller number of targets than the other catalogs.

Figure 8 displays the cumulative distribution function of the distance of the nearest neighbor in each of the four catalogs. This metric represents the likelihood of a single object in one catalog being matched with one or multiple sources from another catalog, holding particular significance when comparing catalogs derived from seeing-limited observations (such as OGLE and MCPS) with those from adaptive optics-assisted observations (like MUSE and SAMI), particularly in crowded areas like the central region of the cluster. This quantity also relates to the depth of the images, as fainter targets detected in one catalog might be absent in another. Consequently, the probability of cross-matching multiple objects from a higher-resolution catalog (e.g., SAMI) with a single object from a catalog with a coarser resolution increases as this distance gets larger. For instance, a single and bright object in the seeing-limited OGLE or MCPS catalogs can be resolved into multiple and fainter objects detected in SAMI images. The minimum distance corresponds to 1.″04 for MCPS, and 0.″40 for OGLE and MUSE. A minimum separation of 0.″08 is observed for SAMI, indicating a significant gain in resolution and depth from the AO-assisted observations.

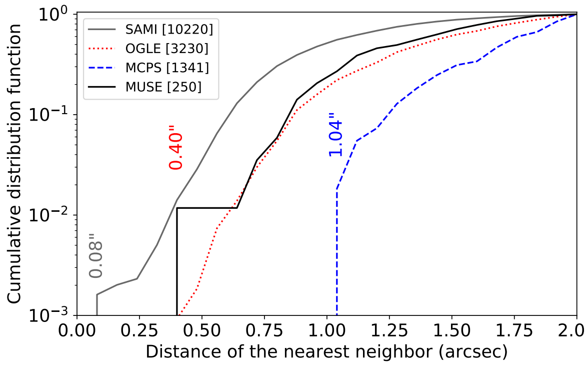

Figure 8. Comparison of the distance of the nearest neighbor from different photometric catalogs: SAMI (filled grey curve), OGLE (dotted red), MCPS (dashed blue), MUSE (filled blue). The curves represent the cumulative distribution function of the quantity, starting at zero and progressing towards one. The total number of objects in each respective catalog is indicated on the plot. The minimum separation between the sources of each catalog is indicated in the plot.

We now compare the calibrated BVI magnitudes with those from the OGLE catalog to check the reliability of our photometric calibration. OGLE magnitudes in the Vega system were converted to the AB system, and comparisons were made for sources brighter than 20 mag in all the BVI filters. The OGLE catalog was primarily selected given that, among the three published catalogs, OGLE exhibits the deepest completeness of sources in the same FOV of SAMI observations (Fig. 7) and displays a relatively small minimum separation of closest neighbors (0.″4, Fig. 8). For completeness, the com-

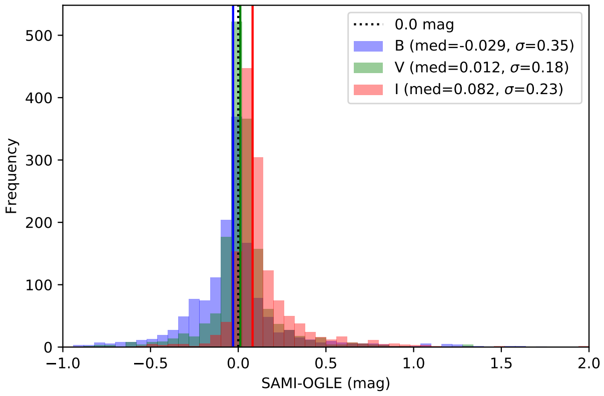

Figure 9. Distribution of residuals between BVI magnitudes from SAMI and OGLE catalogs. Filled vertical lines indicate the median values of the distributions, while the dashed line is placed at $x = 0$. The median value and 1-σ width (68%) of each distribution are indicated in the label.

parison between SAMI photometry and the MCPS and MUSE catalogs is presented in Appendix A.

The distribution of the residuals between SAMI and OGLE magnitudes are presented in Fig. 9. The residuals are distributed around 0 mag with 1-σ widths smaller than 0.4 mag in all filters. Despite the relatively large widths, the comparison with OGLE gives the most symmetric results among the three external catalogs. Two factors can explain the extended tails in the distributions: *i*) deblending of multiple sources, as we are comparing photometry from AO-assisted observations with coarser seeing-limited catalogs; and *ii*) intrinsic variability among sources in the sample (e.g., CBes), given the significant time gaps between the observations.

The results from this section and Appendix A indicate that the adopted calibration method is robust and consistent with the published catalogs, providing calibrated AB magnitudes, ranging between ∼12 and ∼24 mag, for all $BVRI$+Hα filters.

4.4. *Identification of foreground sources from Gaia DR3*

We took advantage of the astrometric stellar parameters from Gaia Data Release 3 (Gaia DR3, Gaia Collaboration et al. 2023) to identify and remove Galactic foreground sources in the SAMI FOV. Initially, we cross-matched the SAMI catalog with Gaia DR3, leading to a list of 2866 sources with Gaia counterparts. Given our photometric completeness extending beyond Gaia DR3, the faintest objects associated with a Gaia DR3 counterpart exhibited magnitudes reaching $V \lesssim 22.0$ mag, about ~ 1.5 mag brighter than the faintest objects detected by SAMI (cf. Table 2 and Fig. 6).

Subsequently, we implemented the following selection criteria:

- Removal of sources associated with large Renormalized Unit Weight Error values, RUWE > 1.4 (Lindegren et al. 2021), keeping only those associated with a good astrometric solution;
- Removal of sources exhibiting parallaxes with nominal values smaller than 1-σ; and
- Selection of sources exhibiting parallax values $|\varpi| \geq 0.1$ mas, much larger than the expected parallax value for the SMC, $\omega_{\rm SMC} \approx 0.016$ mas, estimated from the distance of $d_{\rm SMC} = 62.44$ kpc (Graczyk et al. 2020).

Employing the above procedure resulted in 849 confirmed foreground objects (≈ 8% of the SAMI catalog), which were excluded from the results and analysis presented in the next section.

5. RESULTS

5.1. *Photometric analysis of NGC 330*

We used the calibrated BVI photometry, excluding foreground objects, to construct the C-M diagram presented in Fig. 10. PARSEC (Bressan et al. 2012) evolutionary tracks for ages ranging from 10 to 800 Myr are overlaid with distinct colors to assist the analysis. The isochrones were scaled to the distance of the SMC ($m - M = 18.97$ mag, Milone et al. 2018) and a $A_V = 0.2$ mag reddening vector, assuming the Cardelli et al. (1989) extinction law with $R_V = 3.1$, is overlaid.

Most sources are located on the main sequence at $B - I \lesssim 0$ mag, while a considerable fraction of targets exhibit redder colors ($B - I > 0.3$ mag). Sources brighter than $V = 16$ mag are consistent with a population of main sequence (for $B - V < 0$ mag) and evolved objects ($B - V \gtrsim 0$ mag) with ages between 20 and 60 Myr. The right panel shows that the top-brightest sequence of stars is consistent with the 10 Myr isochrone (dark blue), assuming $A_V = 0.2$ mag (indicated by the reddening vector). Targets at $V \sim 15$ mag and $B - I \sim 2$ mag are consistent with a relatively older population with ages between 50 and 60 Myr (yellow isochrone). We also observe a relatively large fraction of stars located to the right of the main sequence (see details on the right panel), which are likely objects associated with Hα excess at the expected position of CBe stars.

Fainter targets exhibiting larger $B - I$ values represent an older population of evolved stars in the Red Giant Branch (RGB) phase and, therefore, are clearly not associated with the young cluster. We identified

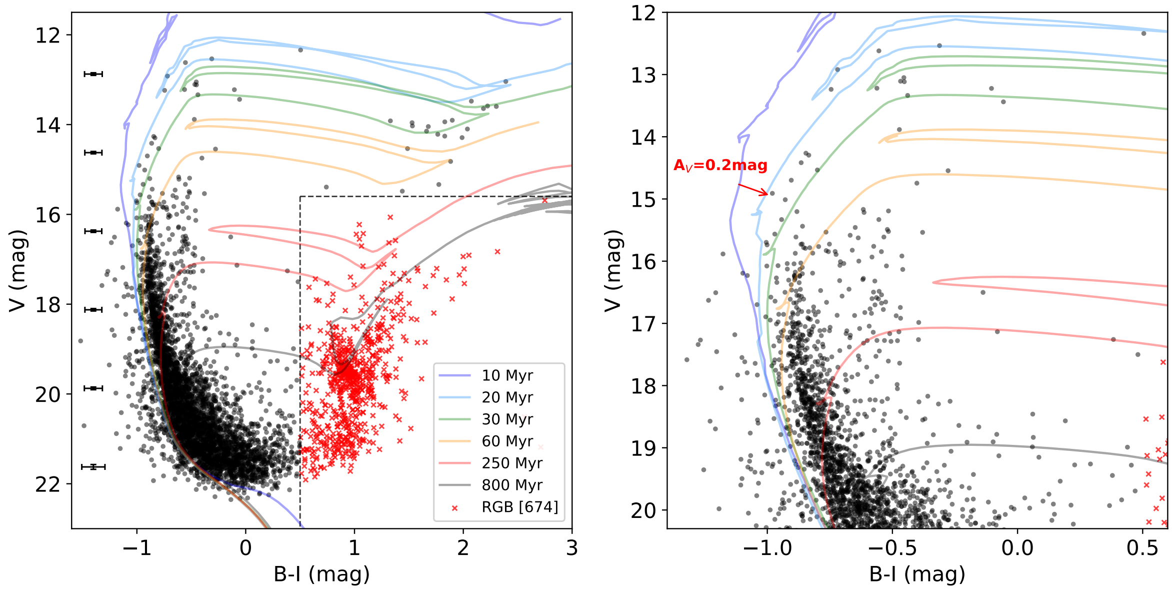

Figure 10. Color-magnitude diagram based on the SAMI photometry for NGC 330. PARSEC evolutionary tracks for ages between 10 and 800 Myr are overlaid in different colors. Red × symbols within the black dashed lines are likely associated with an old stellar population, consistent with the 250-800 Myr isochrones. The black error bars indicate the typical errors of the points as a function of the y-axis. The right panel shows a zoomed view of the main sequence. The red arrow indicates the direction of the reddening vector, assuming $A_V = 0.2$ mag.

674 sources fainter than $V = 15.5$ mag and exhibiting $B - I > 0.5$ mag (shown as red × symbols). These sources were not filtered out based on their Gaia DR3 parameters, suggesting they are either foreground Galactic objects or field stars from the SMC with poor astrometry (see Sect. 4.4) and will therefore be omitted from further analysis. A mixture between young main sequence and older stars leaving the main sequence is likely observed for $V \gtrsim 18$ mag, making it difficult to disentangle different populations solely based on color-criteria selections.

The same C-M diagram is presented in Fig. 11 (left), with each point color-coded based on its H$\alpha - R$ color index, taking into advantage the calibrated Hα and R photometry. This color index is a variation of the $R-$Hα index, often adopted as a proxy for selecting Hα emitters in the SMC (e.g., Keller et al. 1999; Iqbal & Keller 2013), which may include stars undergoing the Be phenomenon, Red Supergiants (RSGs), Blue Supergiants (BSGs), and possibly active young stellar objects (YSOs). We further compare the expected V-magnitude range for B0, B9, and A2 stars listed in Table 4 as shaded regions over the diagram.

A total of 1419 sources exhibiting Hα excess (that is, H$\alpha - R < 0$ mag) are shown as green to blue points in the C-M diagram. The visual inspection of the C-M diagram suggests four main groups of Hα emitters:

1. The bulk of Hα emitters (blue points) are located to the right of the main sequence at $B-I < 0$ mag, spread around the expected V-band magnitudes for B-type stars (indicated by the blue and green regions) and consistent with the expected loci of CBes (e.g., Keller et al. 1999 and Iqbal & Keller 2013);

2. Several Hα emitters are detected to the left of the main sequence, aligning with the expected position of blue stragglers or mergers (e.g., Dresbach et al. 2022); and

3. A third group corresponds to red and evolved objects stars ($V > 15.5$, $B - I > 0.6$) located within the RGB region defined in Fig. 10, for which 407 of 459 objects ($88.7 \pm 4.4\%$) exhibit H$\alpha - R < 0$. The behavior for more evolved objects to exhibit a relatively large Hα excess compared to typical MS stars has been previously observed in earlier studies of NGC 330 (e.g., see Fig. 1 from Keller et al. 1999 and Fig. 2 from Iqbal & Keller 2013) and other clusters (e.g., NGC 6752, Bailyn et al. 1996).

4. We note a significant number of sources with a positive H$\alpha - R$ color in the faintest region of the MS ($V \gtrsim 20$ mag). Considering the shallower photometric completeness of the Hα filter (~ 21.7 mag, Fig. 6) in comparison to the R filter (~ 22.2 mag),

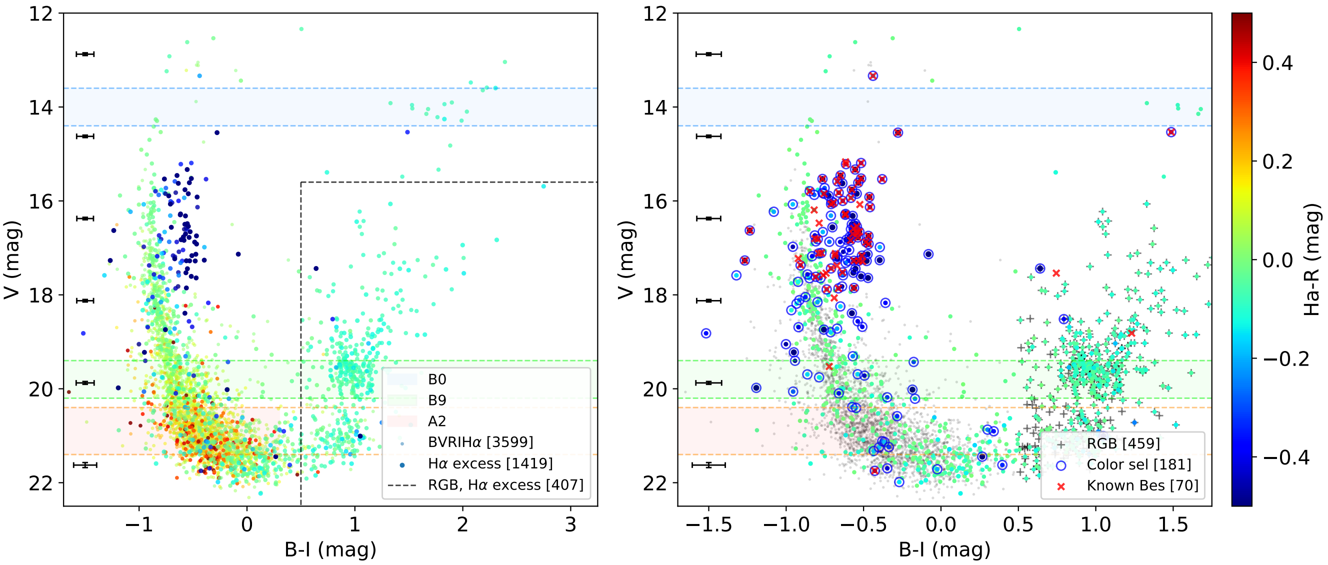

Figure 11. (left) V vs $B-I$ color-magnitude diagram of NGC 330 with SAMI photometry. The points are color-coded using the $\mathrm{H}\alpha-R$ color index. The total number of sources with Hα excess ($\mathrm{H}\alpha-R<0$) is indicated on the label. The number of old stars (located within the black dashed lines) with Hα excess is also indicated. The expected magnitude intervals for B0 (blue), B9.5 (green), and A2 stars (red) are represented by the shaded regions. The black error bars on the left indicate the typical errors of the points as a function of the y-axis. (right) An inset of the color-magnitude diagram highlighting the sources exhibiting Hα excess. The points associated with $\mathrm{H}\alpha-R<0$ are color-coded, while points with $\mathrm{H}\alpha-R>0$ are indicated as smaller black dots. Red × symbols correspond to known CBe stars from previous works, and blue circles indicate the Hα emitters selected through the color selection criterion (see text). Black + symbols indicate stars in the RGB phase (unlikely members of NGC 330).

it is possible that these positive $\mathrm{H}\alpha-R$ values could be a result of a signal-to-noise effect.

5.2. *Selection of* Hα *emitters*

Previous studies (e.g., Keller et al. 1999; Iqbal & Keller 2013) adopted R–Hα versus $V-I$ diagrams to identify active CBes in NGC 330. By adopting a simple color selection criteria, they were able to separate objects exhibiting clear Hα excess from normal stars, thus excluding the bulk of main sequence stars and the cooler evolved objects. Although both studies have made significant contributions to identifying CBe stars in the SMC, their findings were limited by the following observational aspects:

1. Their photometric analysis was based on seeing-limited observations (1″.5–2″.0), not sufficient to disentangle and resolve the stellar population in the innermost and crowded central region of the cluster;
2. Both works limited their sample to relatively bright stars ($V<17.5$ mag for Keller et al. 1999 and $V<18.0$ mag for Iqbal & Keller 2013);
3. Arbitrary zero-points were adopted for the R–Hα color index (so that normal MS stars had R–Hα≈ 0).

Leveraging the superior spatial resolution provided by the adaptive optics AO-assisted SAMI observations, we have reevaluated the color selection criteria utilized previously. This reassessment was undertaken to validate our ability to identify both known and new Hα emitters (active CBes) within NGC 330.

We first cross-matched the positions of known CBe stars with the SAMI catalog, leading to a total of 70 unique objects, from which 47, 31 and 23 are from Keller et al. (1999, K99), Iqbal & Keller (2013, I18), and Martayan et al. (2007, M07), respectively (12 objects are in common with K99 and I13, while four objects are unique from M07). They are indicated as red × symbols in Figs. 11 (right) and 12.

The overall distribution of the points in Fig. 12 exhibits a clear concentration of targets with positive $\mathrm{H}\alpha-R$ values, consistent with main sequence stars with $V-I\sim0$ mag) and evolved red objects at $V-I\gtrsim 0.5$ mag (which is also consistent with the position of most of the sources classified as RGB sources). The sources exhibiting Hα excess, however, have $V-I$ colors ranging from -2.0 (to the left of the MS) to 1.0 mag (to the right of the MS). As expected, almost all known CBe stars (red × symbols) are located at the top of the C-C diagram, exhibiting negative $\mathrm{H}\alpha-R$ values. Only three targets exhibit $\mathrm{H}\alpha-R\approx0$ mag values: two are

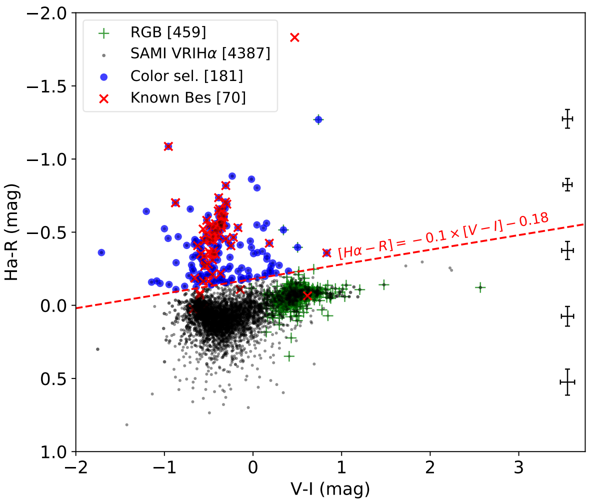

Figure 12. H$\alpha - R$ vs. $V - I$ color-color diagram for NGC 330. Red × symbols correspond to known CBe stars from previous works (see text). Blue circles indicate the Hα emitters selected through the color selection criterion defined by the dashed red line. Green + symbols display stars in the RGB phase (not associated with NGC 330). The black error bars indicate the typical errors of the points as a function of the H$\alpha - R$ color.

located within the MS objects, and one is found within the RGB sequence at $V - I \approx 0.5$ mag.

To expand the selection of similar objects exhibiting Hα excess, we adopted the following color selection criterion:

$$(\mathrm{H}\alpha - R) = -0.10 \cdot (V - I) - 0.18\,, \qquad (8)$$

indicated as the red line in Fig. 12, such that objects with (H$\alpha - R$) smaller than the above criterion for a given ($V - I$) are considered to have Hα excess. This color selection criterion identified 181 sources exhibiting Hα excess, represented by the blue circles in the C-C diagram from Fig. 12. This criterion roughly lies between the color selection criteria established by Keller et al. (1999)[4] and Iqbal & Keller (2013)[5]. Moreover, it also considers the higher quality and the deeper photometric depth achieved by SAMI observations compared to the previous works.

Naturally, the adoption of Eq. 8 led to a much smaller number of objects than by just selecting all sources exhibiting negative H$\alpha - R$ values (1419, Fig. 11). In addition, it correctly identifies most of the known CBe stars (67 of 70), excluding the majority of evolved objects to the right of the MS (indicated as green + symbols). The three known CBe stars not selected by the color criterion of Eq. (8) are located within the MS locus. This is expected, given the long-term variability of CBe stars. In a time scale of a decade, some stars may have dissipated their disks (entirely or partially) with a corresponding reduction of their Hα excess.

The right panel of Fig. 11 highlights the sources associated with negative Hα $-R$ indices, and also shows the known CBe stars and the objects selected through the color criterion from Eq. (8). The known CBe stars are relatively bright objects ($V \lesssim 18$ mag), given the flux-limited nature of the previous observations. The sources selected using Eq. (8) are observed over the full range of V-band magnitudes (i.e., luminosities). A total of 137 Hα emitters selected through the color criteria exhibit $V < 20.3$ mag, corresponding to stars earlier or equal to B9. The remaining 44 sources exhibit $20.3 < V \lesssim 22.5$ mag, as expected for lower mass objects with spectral types ranging from early to mid-A stars.

The exact nature of these low-mass stars associated with Hα excess is difficult to assess. At least for some of them, the Hα excess is spurious due to the larger photometric errors in the Hα filter. However, eight sources exhibit positive $B - I$ indices, consistent with objects leaving the MS through the red-giant branch (RGB).

According to the color selection criterion, most of the bright Hα emitters ($V \leq 20.3$ mag) are located to the right of the MS, together with most of the known CBe stars from previous works. About 16 Hα emitters (including two known CBe stars) are identified to the left of the MS ($B - I \lesssim -1$ mag), corresponding to stellar mergers or blue stragglers candidates. Only four Hα emitters are associated with $B - I$ values larger than 0.5 mag, three are likely old RGB sources, and the brightest one ($V = 14.535 \pm 0.026$ mag) corresponds to a known binary system (Martayan et al. 2007).

5.3. *Comparison with MUSE*

The recent MUSE observations of the central region of NGC 330 (α = 00h 56m 16.8s, $\delta = -72° 27' 47''$, FOV$\sim 63'' \times 63''$) reported by Bodensteiner et al. (2020) offers an excellent opportunity to compare spectroscopic and photometric results.

First, we selected all the 1242 objects from the SAMI catalog that lie within the MUSE FOV (from here on, it will be referred to as the "SAMI subsample"). Fig. 13 presents the photometric completeness of this subsample, confirming that it is also complete within the expected magnitude ranges for B-type stars in all filters. For instance, the photometric completeness for the V

---

[4] H$\alpha - R \approx -0.05 \cdot (V - I) - 0.33$, in AB magnitudes

[5] H$\alpha - R \approx -0.15 \cdot (V - I) - 0.04$, in AB magnitudes

band is at $V = 20.94$ mag, about ~ 2.5 mag deeper than the $V = 18.5$ mag limit reached by Bodensteiner et al. (2020). A total of 334 sources with SAMI photometry are brighter than $V = 18.5$ mag (referred to as the "bright subsample"), while 908 are fainter than the photometric limit adopted throughout their analysis.

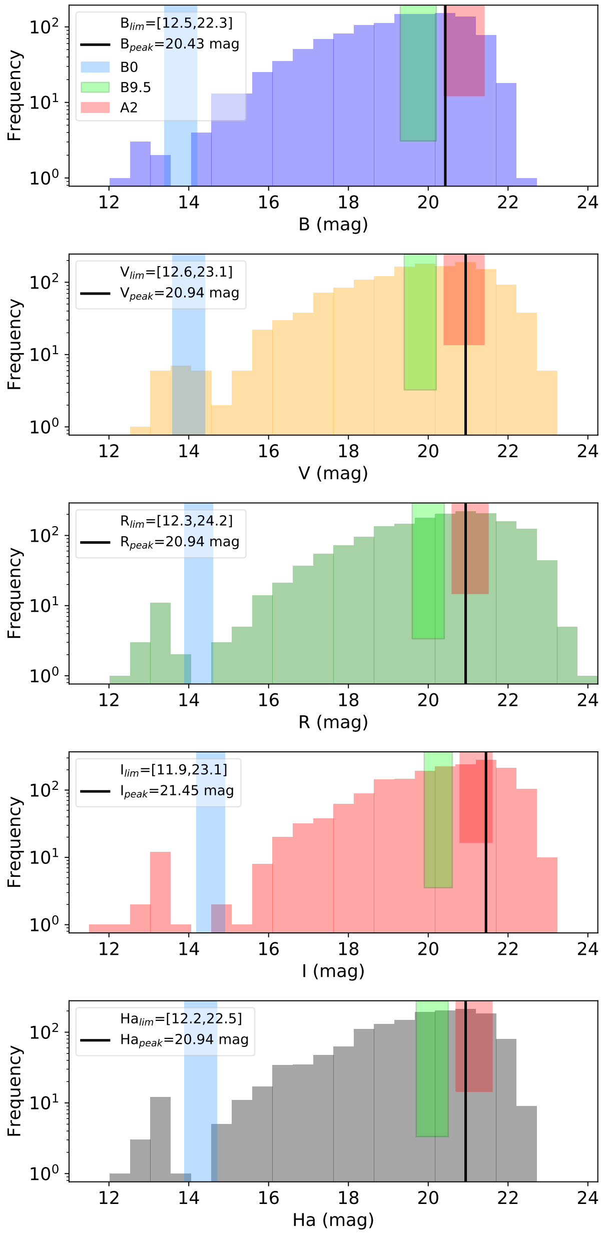

Figure 13. Same as Fig. 6 but for a smaller FOV of 1′×1′ centered at α = 00h 56m 16.9s, $\delta = -72°27'48.7''$, and bins of 0.4 mag comprising the same magnitude range.

A cross-match between the SAMI catalog with the objects listed in Table D.1 of Bodensteiner et al. (2020) resulted in a total of 250 targets with measurements in all five filters (henceforth "MUSE subsample"). From these, 73, 163, and 14 were classified by Bodensteiner et al. as Be, normal B, and giants (RSG, BSG), respectively.

To identify the Hα emitters within the MUSE FOV, we applied the same selection criterion from Fig. 12 on the SAMI (1242 sources) and the MUSE subsamples (250 sources). The results are presented in Fig. 14.

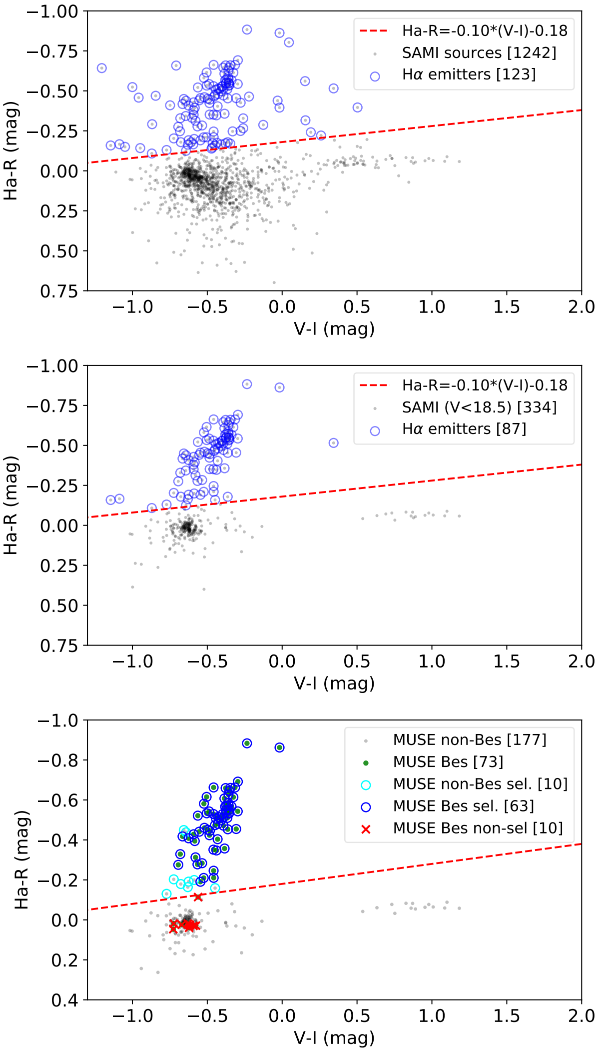

Figure 14. Same as Fig. 12 but for a smaller FOV of 63″×63″ centered at α = 00h 56m 16.9s, $\delta = -72°27'48.7''$. Top panel: 1242 sources with SAMI photometry. Middle: flux-limited ($V \leq 18.5$ mag) subsample of the SAMI sources. Bottom: 250 MUSE objects detected on the SAMI catalog. Open blue circles correspond to the Hα emitters selected through the color selection criterion of Eq. 8, shown as dashed red lines. Open cyan circles correspond to non-Be MUSE objects exhibiting Hα excess. Red × symbols indicate spectroscopic confirmed CBe stars not showing Hα excess.

A total of 123 Hα emitters were selected among the 1242 SAMI sources within the MUSE FOV, corresponding to $10 \pm 1\%$[6] of the sample. This fraction is much smaller than the $32 \pm 3\%$ reported by Bodensteiner et al. (2020) based on a flux-limited sample of stars. The bright subsample ($V < 18.5$ mag) of SAMI sources provides a direct comparison with their results. Here, a total of 87 Hα emitters were identified. A fraction of $27 \pm 3\%$ Hα emitters was observed after the exclusion of 16 giant stars located on the right side of the diagram ($V - I > 0.5$ mag, middle panel of Fig. 14). Finally, 63 CBe stars + 10 non-CBe stars from the MUSE sample exhibited Hα excess from 250 targets. By excluding the giants located on the right side of the diagram (14), we end up with a fraction of $31 \pm 4\%$ of Hα emitters for the MUSE samples, which is in good agreement with the findings from Bodensteiner et al. (2020, $32 \pm 3\%$).

The analysis of the flux-limited SAMI subsample led to a similar fraction of CBe stars ($27 \pm 3\%$) as that obtained from spectroscopic MUSE observations ($32 \pm 3\%$). Despite that, the deeper SAMI photometry allowed us to identify a significant number of fainter Hα emitters, consistent with late-type CBe stars. As the population of normal stars increases exponentially as a function of the mass (and the V-band magnitude), the total fraction of active CBe stars with clear Hα emission decreases toward late-B stars, reaching $10 \pm 1\%$ when considering all stars exhibiting $V \leq 22$ mag.

5.4. *Fraction of* Hα *emitters versus normal stars*

The C-M diagrams of Fig. 11 show that Hα emitters are found over a wide range of luminosities ($12 < V \lesssim 22.0$ mag). This range is wider than that expected for B-type stars ($13.6 \leq V \leq 20.2$ mag), indicating the SAMI photometry is deep enough to identify all CBe stars exhibiting strong enough Hα emission within NGC 330.

By taking advantage of the deeper photometric completeness of SAMI photometry, we can now obtain a complete census of the fraction of Hα emitters stars versus normal MS stars associated with NGC 330. For the analysis presented in this section, we selected a total of 3318 sources exhibiting $B - I < 0.5$ mag, i.e., excluding the bright evolved objects and the RGB sources (see Fig. 10).

The next subsections present the analysis of the fraction of Hα emitters as a function of *i*) the distance from the center of NGC 330, and *ii*) the spectral type of B stars.

5.4.1. *Radial distribution of* Hα *emitters in NGC 330*

We investigated the surface density of Hα emitters as a function of the distance from the cluster's center (assuming as central coordinates α = 00h 56m 16.9s, $\delta = -72^\circ\,27'\,48''$). For reference and comparison, we also computed the surface density of MS objects (sources exhibiting $B - I < 0.5$ mag and not selected using Eq. (8)), dividing them into higher- and lower-mass MS stars with respect to $V \leq 18.0$ mag (corresponding to the transition between B5 and B6 stars) to look for evidence of mass stratification within the cluster. The distance of 57.5 kpc to the SMC was adopted (Milone et al. 2018) to convert the angular projected distances from arcseconds to parsecs.

The resulting curves are presented in the top panel of Fig. 15, showing the number of sources per parsec^2, evaluated at concentric rings from 0 to 140$''$, in steps of 5$''$ (solid lines). For comparison, the cumulative distribution function (CDF) of the total number of stars as a function of the projected distance is shown as the dashed lines in the same plot.

The surface density of the sources with available SAMI photometry (filled grey curve) shows a cusp pattern towards the center of the cluster, decreasing towards larger radii. The CDF (dashed grey curve) reaches 50% at a radius of 16.8 pc ($\sim$60$''$), which is about 75% smaller than the radius of the cluster reported by Glatt et al. (2010, indicated by the horizontal filled black line). The lower-mass MS stars exhibit a similar surface density profile (black curve), and the CDF of the total number of low-mass stars reaches 50% at a projected distance of 17.2 pc (62$''$), roughly following the CDF of the MS+Hα sample (in grey). The higher-mass MS stars (blue curve), however, exhibit a much more compact distribution, indicating that massive stars are preferably located within the inner region of the cluster (the CDF reaches 50% at 6.4 pc (23$''$). Finally, the Hα emitters (red curves) exhibit a similar distribution as that observed for the high-mass MS stars, and its CDF reaches 50% at 6.6 pc (24$''$) distance. These results suggest that the Hα emitters and the massive stellar populations are likely confined within the inner region of the cluster.

The middle panel of Fig. 15 shows the fraction of Hα emitters, i.e., Hα/(MS+Hα), as a function of the distance to the cluster's center. The data suggests a significant increase in the proportion of Hα emitters towards the center, in agreement with the surface density results above. About 50% of all Hα emitters and > 50% of the higher-mass MS stars are concentrated within a circle of 6.6 pc (24$''$) radius, whereas only $\sim$ 10% of the lower-mass MS objects are found within the same area. Such distinct distribution between higher- and lower-mass ob-

---

[6] The fractional errors shown throughout the manuscript were derived using a Poisson distribution, i.e., $\sigma_{\rm Be} = N_{\rm Be}^{1/2}/N_{\rm total}$.

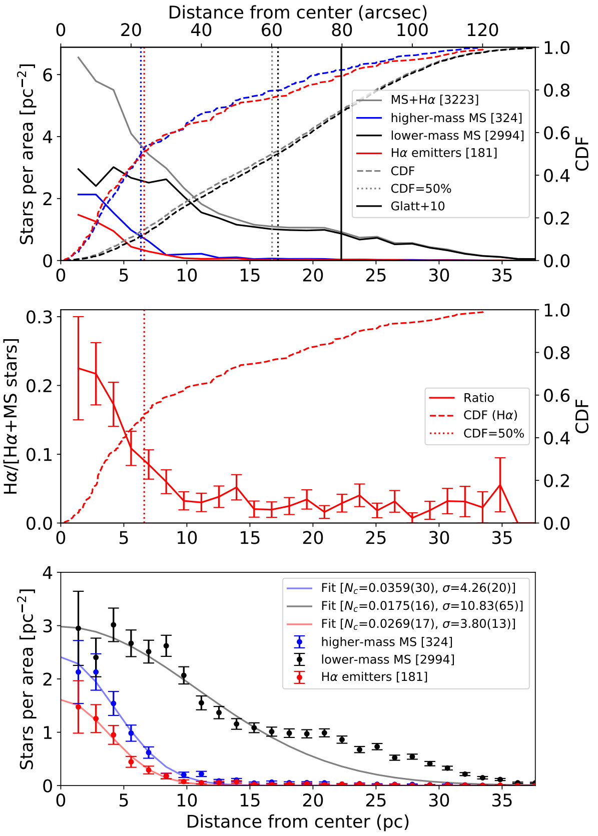

Figure 15. Top panel: Surface density (number of sources per area) of normal MS stars (the filled blue curve indicates higher-mass objects associated with $V \leq 18$ mag, and fainter, lower-mass objects by the filled black curve), Hα emitters (filled red), and the total number MS and Hα emitters (filled grey) as a function of the distance from the center of NGC 330. The values were calculated for concentric rings around the central coordinates of the cluster in steps of 5″. The dashed curves indicate the cumulative distribution function of the quantities, while the dotted curves indicate the distance corresponding to CDF = 0.5. For reference, the vertical filled black line indicates the 1.′33 cluster radius from Glatt et al. (2010). Middle: The Hα emitter fraction as a function of the distance from the center of NGC 330 (solid line). The uncertainties are indicated by the error bars. For comparison, the CDF for Hα emitters is indicated by the dashed curve. Bottom: Three-dimensional Gaussian fit model to the surface density of Hα emitters (red), higher- (blue) and lower-mass MS stars (black). The best parameters for each curve (N_c, σ) are indicated on the label.

jects corresponds to a clear evidence of mass segregation within NGC 330.

The stellar surface density measurements can be used to infer the physical properties of the cluster, for example, providing valuable information about the structure, density profile, and dynamical characteristics, offering insights into the formation and evolution of stellar systems and populations. Taking the analysis a step further, we transformed the surface density information mentioned earlier into volume density. This conversion assumes that the stars exhibit a spatial distribution following a three-dimensional Gaussian distribution, as detailed in Appendix B). For this analysis, we can estimate the stellar density at the center of the cluster (in stars pc^{-3}) and the characteristic scale (i.e., standard deviation, σ) of the stellar population (in pc).

The bottom panel of Fig. 15 presents the observed stellar density of the MS stars and Hα emitters as a function of the projected distance from the center of the cluster, together with the best three-dimensional Gaussian fit. We observe a reasonably good fit for all datasets for $r \lesssim 15$ pc, indicating that the model can reproduce the observed spatial stellar distribution. This simple model better fits the observed dataset with greater accuracy when compared to, e.g., simplified King profiles often adopted for young stellar clusters (e.g. Bonatto & Bica 2009; Hetem & Gregorio-Hetem 2019). Therefore, adopting this profile is encouraging and warrants testing with other young stellar clusters. The characteristic scale for the lower-mass MS stars is $\sigma = 10.83 \pm 0.65$ pc, while the σ values are relatively shorter for the higher-mass and Hα emitters (4.26 ± 0.20 and 3.80 ± 0.13 pc, respectively). These results show unequivocally that the Hα emitters and the most massive stars are preferably located in a more compact region from the center of the cluster. At the same time, low-mass MS objects are observed towards larger distances.

In addition, the central density for high-mass MS and Hα emitters corresponds to $N_c = (35.9 \pm 0.30) \cdot 10^{-2}$ pc^{-3} and $(26.9 \pm 0.17) \cdot 10^{-2}$ pc^{-3}, respectively, while the the density of lower-mass MS stars is relatively lower, $N_c = (17.5 \pm 0.16) \cdot 10^{-2}$ pc^{-3}. These estimates quantitatively support i) the existence of a significant mass stratification within NGC 330, and ii) that Hα emitters are preferably found towards the inner region of the cluster.

5.4.2. *Fraction of* Hα *emitters as a function of the Spectral Type*

We further investigated the fraction of Hα emitters as a function of the V-band magnitude (i.e., spectral type) to assess its distribution vs. stellar mass within NGC 330 and in the adjacent stellar field. We defined two sub-samples of normal MS stars and Hα emitters exhibiting with $B - I < 0.5$ mag (therefore excluding older objects). This selection led to 3397 highly probable members located within the radius of NGC 330, $r = 1.33'$ (Glatt et al. 2010). In an effort to examine the B-type stars associated with Hα emission, we selected a subset of 858 sources exhibiting V-band magnitudes within the range expected for B0-B9 stars (from Table 4. Additionally, 1631 sources were identified at greater distances from the cluster's center, which are more likely to be field stars. We adopted the Main Sequence Turn Off point (MSTO) as $V = 15.92$ mag (in AB magnitudes) from Iqbal & Keller (2013), equivalent to the age of NGC 330 estimated as $\log(\mathrm{age}) = 7.4$ dex (~ 25 Myr) from Glatt et al. (2010). The results are presented in Fig. 16.

The top left panel of Fig. 16 presents the distribution of the normal MS stars (blue bars) and Hα emitters (red) as a function of their V-band magnitude. For comparison, the associated spectral sub-types are also indicated in the plots, using the mean value of the magnitudes listed in Table 4. The sources are distributed across a wide range of brightness ($12 \leq V \leq 22.5$), covering the entire magnitude interval expected for B-type stars. While the number of normal MS objects increases towards late-type objects following a power law (i.e., IMF-like), the distribution of Hα emitters peaks at V between 15.5 and 18 mag (B1-B5 stars), and the bulk of Hα emitters is slight offset towards fainter magnitudes than the MSTO for NGC 330. A total of 152 Hα emitters are observed within the entire V-band magnitude range, corresponding to a fraction of 4.4±0.5% of Hα emitters (Hα/[Hα +MS]) with $V \lesssim 22.5$ mag.

The bottom left panel of Fig. 16 shows the fraction of Hα emitters as a function of the V-band magnitude. As observed on the top panel, the largest fraction of Hα emitters is also found for V-band magnitudes between 15 and 18 mag, consistent with B1-B5 stars. The distribution reaches a peak of $60 \pm 14\%$ at $V \sim 15.5$ mag, corresponding to early B-type objects (B1-B3) close to the MSTO, in agreement with findings from previous seeing-limited results from Iqbal & Keller (2013).

The fraction of Hα emitters decreases to values smaller than 10% for $V > 18$ mag (i.e., for spectral sub-types later or equal to B6). Despite the smaller fraction observed towards fainter objects, the total number of sources with Hα excess (top panel) is remarkable, indicating a considerable number of late-B type stars exhibiting Hα emission, a result absent in previous works due to the relatively faint nature of such objects. To properly compare our statistics with previous works, we adopted $V = 18.0$ mag (corresponding to B5-B6 stars) as a limit to estimate the fraction of Hα emitters for higher- and lower-mass stars (indicated as HM and LM in the legend of the figure). Such division led to a fraction of 31.9±3.3% of Hα emitters for stars more massive than B5-B6, and $1.8 \pm 0.2\%$ for lower mass objects.

A similar behavior is observed when restricting the analysis towards the expected magnitudes for B-type stars ($13.6 \leq V \leq 20.2$, from Table 4), as indicated by the middle panels in Fig. 16. For such sub-sample, the Hα emitter fraction reaches a peak of $60 \pm 15\%$ for B2 stars at the limit of the MSTO, decreasing towards late-type objects. The fractions are slightly larger than observed for the full sample (left panel), reaching $32.8 \pm 3.4\%$ and $4.4 \pm 0.9\%$ for the higher- and lower-mass samples, respectively. The higher fraction of Hα emitters towards the more massive stellar population agrees with the previous results from Bodensteiner et al. (2020), while the lower fraction towards lower-mass objects is an interesting new result, indicating a small but significant fraction of active stars towards the lower mass limit of B-type stars.

For completeness, the top right panel of Fig. 16 presents the distribution of Hα emitters and MS stars for the field stars. The MS stars exhibit a similar IMF-like distribution as observed on the top left panel, with very few bright (e.g., massive) objects exhibiting $V < 18$ mag. This is expected as massive stars (at the top of the IMF) are less likely to be isolated stars, i.e., unbound to the cluster. Only 22 of the 1631 sources at larger radii from NGC 330 are Hα emitters. While most of them are fainter than $V = 21$ mag, only four are brighter than $V = 18$ mag. Consequently, low-count statistics at the high-mass end likely affect the fraction of Hα emitters, as indicated by the bottom right panel of Fig. 16. The integrated high-mass fraction ($11.8 \pm 5.9\%$) is about three times lower than observed towards NGC 330, while the fraction remains at ~1% values for the lower-mass objects.

6. DISCUSSION AND CONCLUSIONS

This work reported the first multi-band photometric study of a stellar cluster in the Magellanic Clouds in the broad-band $BVRI$ and narrow-band Hα filters with sufficient photometric depth to investigate its massive stellar population up to A-type stars ($V \approx 22$ mag). The unprecedented quality of AO-assisted SAMI/SOAR observations allowed us to resolve the stellar population of NGC 330 at scales of $\gtrsim 0.''1$ in all five filters, and to identify Hα emitters throughout the entire B-type stellar population, providing an excellent opportunity to investigate the Be phenomenon and the occurrence of CBe stars across all spectral sub-classes.

We first established a photometric calibration based on a *stellar template model fitting* methodology to calibrate all $BVRI$+Hα filters of the SAMI catalog, delivering photometric errors smaller than 0.3 mag for sources at the 23-mag limit using less than a hundred known objects. As a direct consequence of using stellar template models, we also obtained the corresponding stellar

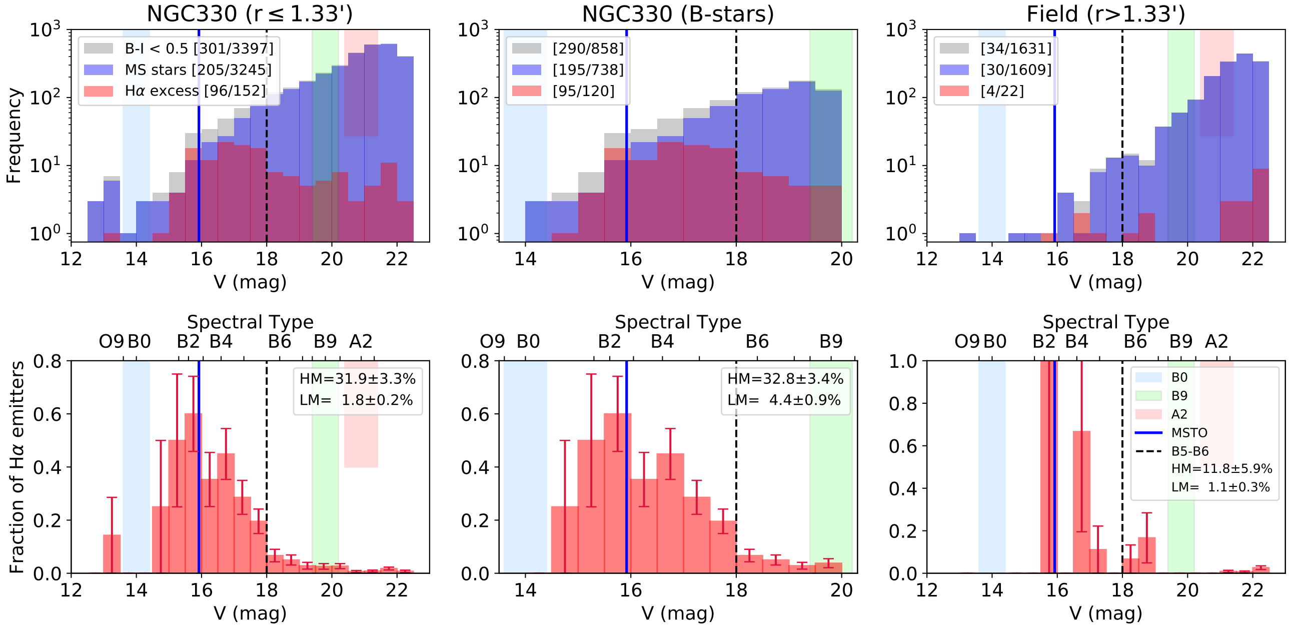

Figure 16. Top panels: Distribution of normal MS stars and Hα emitters as a function of the V-band magnitude. From left to right, we show the total number of stars within a $1\farcm33$ radius from the center of NGC 330, the B-type star candidates in NGC 330, and the total number of stars in the field ($r > 1\farcm33$). The expected magnitude intervals for B0 (blue), B9 (green), and A2 stars (red) are indicated by the shaded regions. The vertical filled blue line indicates the MSTO ($V = 15.92$) for NGC 330, and the vertical dashed black lines divide the sample into higher- (HM) and lower-mass stars (LM) using $V = 18.0$ mag as reference. The values on the legend correspond to the number of sources brighter than $V = 18.0$, and the total number of sources, respectively. Bottom: the ratio of Hα emitters a function of the V-band magnitude for the same subsamples presented in the top panel. The upper axis indicates the mean V-band magnitude for each spectral type listed in Table 4. The ratio of Hα emitters for the HM and LM subsamples are indicated on each panel. The error bars correspond to the fractional errors for each bin.

parameters for each object, and these findings will be utilized in an upcoming publication.

The astrometric information from the Gaia DR3 catalog was used to identify and filter out 849 foreground objects in the line-of-sight of NGC 330. In addition, using a simple inspection of PARSEC evolutionary tracks, we identified 674 old Red Giant Branch stars that are unlikely to be associated with the young stellar cluster, removing them from further analysis. The online version of Table 3 presents the classification of the full SAMI catalog.

Through the adoption of a color selection criterion based on color indices, we successfully identified 181 Hα emitters within the NGC 330 field. Among these sources, 137 are brighter than $V < 20.2$ mag, corresponding to stars equal to or earlier than B9. This count surpasses by a factor of two the previously reported number of Hα emitters in literature, based on similar selection criteria (Keller et al. 1999; Iqbal & Keller 2013). The remaining 44 Hα emitters correspond to fainter, lower-mass objects within the magnitude range of $20.2 < V \lesssim 22.5$ mag.

We conducted a comparison between the AO-assisted SAMI observations and the recent MUSE observations reported by Bodensteiner et al. (2020). Our focus was on the identical sky region, and we restricted our sample to match their magnitude limit ($V < 18.5$ mag). Based on spectroscopic classification, Bodensteiner et al. identified a total of 82 stars (2 Oe and 80 Be) leading to a Be fraction of Be/(B+Be) = 32±3%. Using our adopted color selection criterion (Eq. 8), we identified 87 stars in our magnitude-limited sample, leading to a fraction of Hα emitters of 27 ± 3%, in good agreement with the previous study.

Further comparison was made with the previous seeing-limited works of Keller et al. (1999) and Iqbal & Keller (2013), who analyzed the fraction of CBe stars for a flux-limited sample of objects exhibiting $V < 17$ mag. Keller et al. (1999) reported that the fraction of CBe stars reaches a maximum of 80% at V between 15.0 and 15.5 mag (consistent with B1-B2 objects), decreasing towards fainter objects. Their findings are very similar to the results presented in Fig. 16. In addition, Iqbal & Keller (2013) found the fraction of Hα emitters peaks at the MSTO ($V \sim 16$ mag), at 40% (see their Fig. 4). Although their fraction is smaller than observed from the SAMI observations (see below), our observations also match the peak of CBe stars closer to the MSTO (cf. their Fig. 4). In addition, the existence of stars above the MSTO can only be explained by binary interaction or rapid rotation, therefore explaining the significantly large fraction of CBe stars for stars earlier than B2-B3.

Our comprehensive sample enables us to construct a detailed perspective of the Hα-emitting population in NGC 330. We demonstrate that Hα emitters are found across a broader range of magnitudes than that expected for B stars, signifying that Hα emitters are found across the late O up to A spectral subtypes.

An analysis of the radial spread of the stars in the cluster revealed that the surface density distribution of normal MS stars is clearly bimodal: the higher-mass stars (arbitrarily defined as the ones brighter than $V = 18$ mag, roughly earlier than B6) are concentrated in the inner part of the cluster. In contrast, the lower-mass ones are spread over a much larger volume. Furthermore, the Hα emitting stars are spatially correlated with the higher-mass ones. From the above, and further supported by Fig. 16, two important conclusions may be drawn: 1) the Hα emitters are much more frequent among the higher-mass subsample, reaching a peak value of almost 60% for B2 stars; 2) the stellar content of the cluster clearly displays mass stratification, with the higher-mass ones (presumably also with a high binary content, e.g., Sana et al. 2014) occupying a much smaller effective volume. The current analysis offers a more robust confirmation of mass stratification within NGC 330 compared to earlier space-based HST observations indicating similar evidence (e.g., Sirianni et al. 2002; Gouliermis et al. 2004).

When the whole main-sequence population is considered (removing the stars with $B - I > 0.5$ mag), we found a Hα/(Hα+MS) ratio of $4.4 \pm 0.5\%$. This is much lower than the fraction of CBe stars reported by Keller et al. (1999, $34 \pm 8\%$) and Iqbal & Keller (2013, 16.6%). The reason is apparent from Fig. 16, which shows that the total number of stars rises quickly towards later spectral types while the number of Hα emitters drops sharply. When we restrict the analysis to the B-stars (middle panels of Fig. 16), the fraction increases to $14.0 \pm 1.3\%$, but is still much lower than the magnitude-limited estimates from the previous works. The fraction of Hα emitters significantly increases when restricting the analysis towards the stars brighter than $V = 18$ mag (corresponding to B5-B6 stars), showing Hα fractions around 32%, which is consistent with the fraction of CBe stars reported by Bodensteiner et al. (2020, $32 \pm 3\%$).

The photometric analysis presented in this work is biased towards Hα emitters with relatively strong H$\alpha - R$ excess (Fig. 12). Such Hα excess may unequivocally be associated with CBes that were active at the time of the observations and, thus, possessed large and dense disks. Conversely, we expect that weak Hα emitters or quiescent CBe stars with proper spectroscopic classification from Bodensteiner et al. (2020) are generally not selected by the color criterion. Indeed, ten of the CBe stars classified by those authors do not satisfy Eq. 8 (indicated as red × symbols in Fig. 14). In contrast, ten of their B-type stars are clear Hα emitters in our sample (indicated as open cyan circles in the same figure).

Despite the large dispersion on the fraction of Hα emitters as a function of mass, a significant number of individual Hα emitters are observed over the entire range of magnitudes shown in Fig. 16. On the premise that Hα emission is a clear indicator of CBe activity, this evidence shows that CBe stars coexist regardless of their main sequence lifetime fraction (t/t_{MS}), supporting that the Be phenomenon observed in NGC 330 is unlikely to be mainly ruled by evolutionary phases (such as core contraction), in agreement with the findings from Iqbal & Keller (2013); Keller et al. (1999).

Even though the telltale signature of the Be phenomenon is Hα emission, estimating the $\mathrm{Be}/(\mathrm{B} + \mathrm{Be})$ fraction using only photometry is a challenging task, as there are many foreseeable situations in which Be stars will not display a detectable H$\alpha - R$ color excess. For instance, during the early (late) stages of disk construction (dissipation) the line emission can be too weak. Also, some CBe stars only develop tenuous disks at times (e.g., Vieira et al. 2017). Finally, many CBes are seen without any traces of disks for extended periods of time. One classical example is δ Sco, which was considered a normal B-type star for over a century, but grew a disk in the year 2000 that lasts to this day (Suffak et al. 2020).

From the above it follows that the real $\mathrm{Be}/(\mathrm{B} + \mathrm{Be})$ fraction will always be higher than the observed Hα emitter fraction in young clusters. One way to improve estimates of the CBe content is to consider observations at different epochs. For instance, when considering the MUSE objects with available SAMI photometry from Fig. 14, ten spectroscopically classified Be stars do not show Hα excess. In contrast, 63 Be stars and ten B stars are identified as Hα emitters. When considering all these 83 objects, the lower limit of the $\mathrm{Be}/(\mathrm{B} + \mathrm{Be})$ fraction would slightly rise from $31 \pm 4\%$ to $35 \pm 4\%$.

In the following paper of this series, a new methodology will be presented, taking into account the complexities of CBe stars to create realistic stellar populations and their ensuing photometry to obtain a much better estimate of the CBe content of NGC 330, without the know biases outlined above.

The work of F. N. is supported by NOIRLab, which is managed by the Association of Universities for Research in Astronomy (AURA) under a cooperative agreement with the National Science Foundation. P. T. acknowledges support from CAPES (grant 88887.604774/2021-00). A. C. C. acknowledges support from CNPq (grant 311446/2019-1) and FAPESP (grants 2018/04055-8 and 2019/13354-1). A. F. acknowledges support from CAPES (grant 88882.332925/2019-01) and FAPESP (grant 2023/06539-0). This work made use of the computing facilities of the Laboratory of Astroinformatics (IAG/USP, NAT/Unicsul), whose purchase was made possible by the Brazilian agency FAPESP (grant 2009/54006-4) and the INCT-A. Based on observations obtained at the Southern Astrophysical Research (SOAR) telescope, which is a joint project of the Ministério da Ciência, Tecnologia e Inovações (MCTI/LNA) do Brasil, the US National Science Foundation's NOIRLab, the University of North Carolina at Chapel Hill (UNC), and Michigan State University (MSU).

Facilities: SOAR(SAMI)

Software: Astropy (Astropy Collaboration et al. 2013, 2018), SciPy (Virtanen et al. 2020), IDL

REFERENCES

Adelman, S. J. 2004, in The A-Star Puzzle, ed. J. Zverko, J. Ziznovsky, S. J. Adelman, & W. W. Weiss, Vol. 224, 1–11, doi: 10.1017/S1743921304004314

Almeida-Fernandes, F., SamPedro, L., Herpich, F. R., et al. 2022, MNRAS, 511, 4590, doi: 10.1093/mnras/stac284

Arp, B. H. 1959, AJ, 64, 254, doi: 10.1086/107929

Astropy Collaboration, Robitaille, T. P., Tollerud, E. J., et al. 2013, A&A, 558, A33, doi: 10.1051/0004-6361/201322068

Astropy Collaboration, Price-Whelan, A. M., Sipőcz, B. M., et al. 2018, AJ, 156, 123, doi: 10.3847/1538-3881/aabc4f

Bailyn, C. D., Rubenstein, E. P., Slavin, S. D., et al. 1996, ApJL, 473, L31, doi: 10.1086/310382

Bertin, E., Mellier, Y., Radovich, M., et al. 2002, in Astronomical Society of the Pacific Conference Series, Vol. 281, Astronomical Data Analysis Software and Systems XI, ed. D. A. Bohlender, D. Durand, & T. H. Handley, 228

Bessell, M. S., & Wood, P. R. 1993, in New Aspects of Magellanic Cloud Research, ed. B. Baschek, G. Klare, & J. Lequeux, Vol. 416, 271, doi: 10.1007/3-540-56432-2_206

Bodenheimer, P. 1971, ApJ, 167, 153, doi: 10.1086/151014

Bodensteiner, J., Sana, H., Mahy, L., et al. 2020, A&A, 634, A51, doi: 10.1051/0004-6361/201936743

Bonatto, C., & Bica, E. 2009, MNRAS, 397, 1915, doi: 10.1111/j.1365-2966.2009.14877.x

Bressan, A., Marigo, P., Girardi, L., et al. 2012, MNRAS, 427, 127, doi: 10.1111/j.1365-2966.2012.21948.x

Cardelli, J. A., Clayton, G. C., & Mathis, J. S. 1989, ApJ, 345, 245, doi: 10.1086/167900

Coelho, P. R. T. 2014, MNRAS, 440, 1027, doi: 10.1093/mnras/stu365

Diolaiti, E., Bendinelli, O., Bonaccini, D., et al. 2000, A&AS, 147, 335, doi: 10.1051/aas:2000305

Dresbach, F., Massari, D., Lanzoni, B., et al. 2022, ApJ, 928, 47, doi: 10.3847/1538-4357/ac5406

Ekström, S., Meynet, G., Maeder, A., & Barblan, F. 2008, A&A, 478, 467, doi: 10.1051/0004-6361:20078095

Feast, M. W. 1972, MNRAS, 159, 113, doi: 10.1093/mnras/159.2.113

Fitzpatrick, E. L. 1999, PASP, 111, 63, doi: 10.1086/316293

Gaia Collaboration, Vallenari, A., Brown, A. G. A., et al. 2023, A&A, 674, A1, doi: 10.1051/0004-6361/202243940

Georgy, C., Ekström, S., Granada, A., et al. 2013, A&A, 553, A24, doi: 10.1051/0004-6361/201220558

Ghoreyshi, M. R., Carciofi, A. C., Jones, C. E., et al. 2021, ApJ, 909, 149, doi: 10.3847/1538-4357/abdd1e

Glatt, K., Grebel, E. K., & Koch, A. 2010, A&A, 517, A50, doi: 10.1051/0004-6361/201014187

Gouliermis, D., Keller, S. C., Kontizas, M., Kontizas, E., & Bellas-Velidis, I. 2004, A&A, 416, 137, doi: 10.1051/0004-6361:20031702

Graczyk, D., Pietrzyński, G., Thompson, I. B., et al. 2020, ApJ, 904, 13, doi: 10.3847/1538-4357/abbb2b

Grebel, E. K., & Richtler, T. 1992, A&A, 253, 359

Grebel, E. K., Roberts, W. J., & Brandner, W. 1996, A&A, 311, 470, doi: 10.48550/arXiv.astro-ph/9512143

Hetem, A., & Gregorio-Hetem, J. 2019, MNRAS, 490, 2521, doi: 10.1093/mnras/stz2698

Iqbal, S., & Keller, S. C. 2013, MNRAS, 435, 3103, doi: 10.1093/mnras/stt1502

Keller, S. C., Wood, P. R., & Bessell, M. S. 1999, A&AS, 134, 489, doi: 10.1051/aas:1999151

Klement, R., Baade, D., Rivinius, T., et al. 2022, ApJ, 940, 86, doi: 10.3847/1538-4357/ac98b8

Labadie-Bartz, J., Carciofi, A. C., Henrique de Amorim, T., et al. 2022, AJ, 163, 226, doi: 10.3847/1538-3881/ac5abd

Labadie-Bartz, J., Chojnowski, S. D., Whelan, D. G., et al. 2018, AJ, 155, 53, doi: 10.3847/1538-3881/aa9c7e

Lindegren, L., Klioner, S. A., Hernández, J., et al. 2021, A&A, 649, A2, doi: 10.1051/0004-6361/202039709

Martayan, C., Baade, D., & Fabregat, J. 2010, A&A, 509, A11, doi: 10.1051/0004-6361/200911672

Martayan, C., Frémat, Y., Hubert, A. M., et al. 2006, A&A, 452, 273, doi: 10.1051/0004-6361:20053859

Martayan, C., Frémat, Y., Hubert, A.-M., et al. 2007, A&A, 462, 683, doi: 10.1051/0004-6361:20065076

Martins, F., Schaerer, D., & Hillier, D. J. 2005, A&A, 436, 1049, doi: 10.1051/0004-6361:20042386

Milone, A. P., Marino, A. F., Di Criscienzo, M., et al. 2018, MNRAS, 477, 2640, doi: 10.1093/mnras/sty661

Patrick, L. R., Lennon, D. J., Evans, C. J., et al. 2020, A&A, 635, A29, doi: 10.1051/0004-6361/201936741

Pols, O. R., Cote, J., Waters, L. B. F. M., & Heise, J. 1991, A&A, 241, 419

Rafelski, M., & Zaritsky, D. 2005, AJ, 129, 2701, doi: 10.1086/424938

Richardson, N. D., Thizy, O., Bjorkman, J. E., et al. 2021, MNRAS, 508, 2002, doi: 10.1093/mnras/stab2759

Rivinius, T., Baade, D., & Štefl, S. 2003, A&A, 411, 229, doi: 10.1051/0004-6361:20031285

Rivinius, T., Carciofi, A. C., & Martayan, C. 2013, A&A Rv, 21, 69, doi: 10.1007/s00159-013-0069-0

Rubio, A. C., Carciofi, A. C., Ticiani, P., et al. 2023, Monthly Notices of the Royal Astronomical Society, stad2652, doi: 10.1093/mnras/stad2652

Sana, H., Le Bouquin, J. B., Lacour, S., et al. 2014, ApJS, 215, 15, doi: 10.1088/0067-0049/215/1/15

Schmidt-Kaler, T. 1982, Intrinsic colors and visual absolute magnitudes (calibration of the MK system): Datasheet from Landolt-Börnstein - Group VI Astronomy and Astrophysics · "Stars and Star Clusters", 2B, Springer-Verlag, Berlin, doi: 10.1007/10201975_2

Schmidtke, P. C., Chobanian, J. B., & Cowley, A. P. 2008, AJ, 135, 1350, doi: 10.1088/0004-6256/135/4/1350

Shao, Y., & Li, X.-D. 2014, The Astrophysical Journal, 796, 37, doi: 10.1088/0004-637X/796/1/37

Sirianni, M., Nota, A., De Marchi, G., Leitherer, C., & Clampin, M. 2002, ApJ, 579, 275, doi: 10.1086/342723

Suffak, M. W., Jones, C. E., Tycner, C., et al. 2020, ApJ, 890, 86, doi: 10.3847/1538-4357/ab68dc

Tokovinin, A., Cantarutti, R., Tighe, R., et al. 2016, PASP, 128, 125003, doi: 10.1088/1538-3873/128/970/125003

Udalski, A., Szymanski, M., Kubiak, M., et al. 1998, VizieR Online Data Catalog, J/AcA/48/147

Vieira, R. G., Carciofi, A. C., Bjorkman, J. E., et al. 2017, MNRAS, 464, 3071, doi: 10.1093/mnras/stw2542

Virtanen, P., Gommers, R., Oliphant, T. E., et al. 2020, Nature Methods, 17, 261, doi: 10.1038/s41592-019-0686-2

Wolf, C., Onken, C. A., Luvaul, L. C., et al. 2018, PASA, 35, e010, doi: 10.1017/pasa.2018.5

Zaritsky, D., Harris, J., Thompson, I. B., & Grebel, E. K. 2004, AJ, 128, 1606, doi: 10.1086/423910

APPENDIX

A. COMPARISON BETWEEN SAMI PHOTOMETRY AND EXTERNAL CATALOGS

For completeness of the results exhibited in Sect. 4.3, the comparison between the SAMI photometry and the external catalogs from MCPS and MUSE is presented as follows.

A.1. *MCPS*

We compared the calibrated BVI magnitudes with those from the MCPS catalog for sources brighter than 20 mag for all filters. The residuals between SAMI and MCPS magnitudes are presented in the left panel of Fig. 17.

The residuals peak around 0 mag, exhibiting an extended tail towards positive values. Therefore, the 1-σ widths of the distributions are relatively larger than those observed for OGLE (see Fig. 9). According to Fig. 8, the minimum distance of the nearest neighbor for MCPS is $1''.04$, the largest value observed among all the other photometric catalogs, suggesting that a single and bright object in MCPS is likely resolved into multiple and fainter objects in SAMI observations, explaining the positive residuals as observed in Fig. 17.

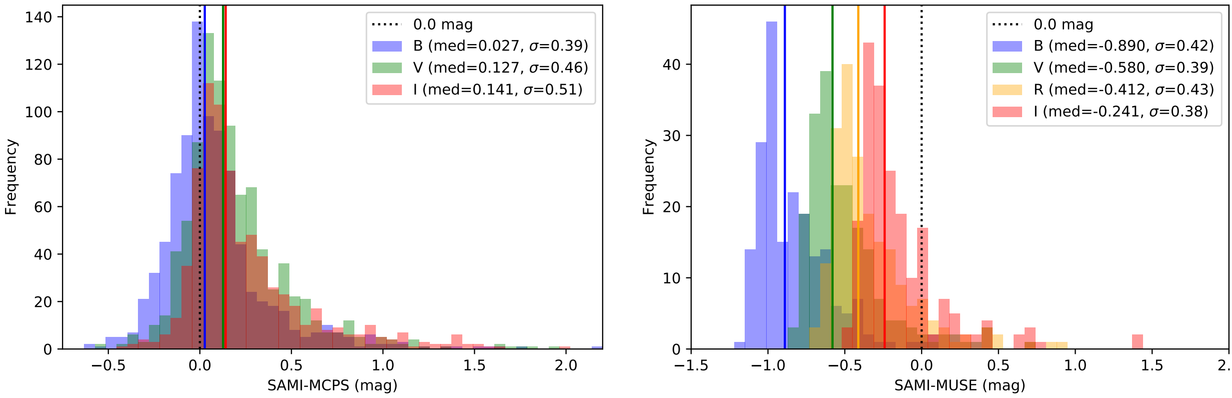

Figure 17. Left panel: Residuals between SAMI and MCPS photometry. Right panel: Residuals between SAMI and MUSE photometry. The full description of the plots is given in Fig. 9.

A.2. *MUSE*

The right panel of Fig. 17 presents the residuals between the $BVRI$ magnitudes from SAMI and MUSE photometry. The synthetic MUSE photometry was obtained by extracting the one-dimensional spectrum of the objects and convolving them with the SAMI filter transmissions. The distribution of the photometric residuals exhibits a systematic negative offset towards the bluest filters, ranging from -0.241 mag for the I-band to -0.89 mag to the B-band. Given that the comparison between OGLE (Sect. 4.3) and MCPS (Appendix A.1) do not exhibit any systematic divergence, we speculate that a zero-point correction on the flux-calibrated MUSE datacube can be the cause of such large offsets.

B. A THREE-DIMENSIONAL GAUSSIAN MODEL FOR THE STELLAR DENSITY

The formula for a 3D Gaussian function in cylindrical coordinates is given by:

$$n(r,\phi,z) = N_{\rm c}\cdot\exp\left(-\frac{r^2}{2\sigma_r^2}-\frac{z^2}{2\sigma_z^2}\right)\,, \tag{B1}$$

where it was assumed, for simplicity, symmetry around the z-axis. N_c is the density of stars (stars pc^{-3}) at the cluster's center. Further assuming that the observer is placed along the z-axis, and that the standard deviations along the r and z directions are the same (i.e., $\sigma_r=\sigma_z=\sigma$), we have that the observed superficial density of stars, $\Sigma(r)$ (in pc^{-2}), at a distance r from the cluster's center is

$$\Sigma(r) = \int_{-\infty}^{\infty} n(r,\phi,z)dz\int_0^{2\pi}d\phi = (2\pi)^{3/2}N_{\rm c}\cdot\sigma\cdot\exp\left(-\frac{r^2}{2\sigma^2}\right)\,. \tag{B2}$$